Berichte des Instituts für Geophysik
der Ruhr-Universität Bochum
Reihe A
Nr. 56

Andreas Kemna

Tomographic Inversion of Complex Resistivity

Theory and Application

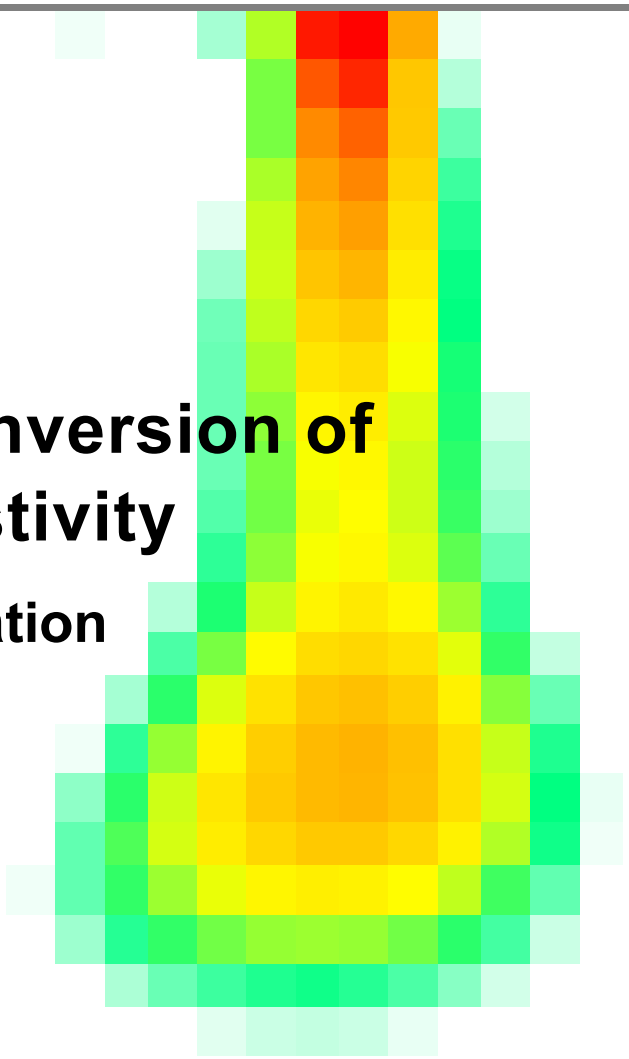

DER ANDERE VERLAG

Tomographic Inversion of Complex Resistivity - Theory and Application

Die Deutsche Bibliothek – CIP-Einheitsaufnahme

Kemna, Andreas:
Tomographic inversion of complex resistivity : theory and application / Andreas Kemna.-
Osnabrück : Der Andere Verl., 2000
(Berichte des Institutes für Geophysik der Ruhr-Universität Bochum :
Reihe A ; Nr. 56)
Zugl.: Bochum, Univ., Diss., 2000
ISBN 3-934366-92-9

© Copyright 2000 by Der Andere Verlag, 49074 Osnabrück
Der Andere Verlag, Kollegienwall 22A, 49074 Osnabrück
Tel. (0541) 20 20 125, Fax (0541) 20 20 127
E-Mail: talkto@der-andere-verlag.de
Internet: http://www.der-andere-verlag.de
ISBN 3-934366-92-9

Berichte des Instituts für Geophysik
der Ruhr-Universität Bochum

Reihe A
Nr. 56

Andreas Kemna

Tomographic Inversion of Complex Resistivity

Theory and Application

Der Andere Verlag
Osnabrück 2000

Die vorliegende Arbeit wurde von der Fakultät für Geowissenschaften der Ruhr-Universität Bochum als Dissertation im Fach Geophysik zur Erlangung des Grades eines Doktors der Naturwissenschaften anerkannt.

Erster Gutachter:	Prof. Dr. Dr. h.c. Dresen
Zweiter Gutachter:	Prof. Dr. Rüter (DMT, Essen)
Fachfremder Gutachter:	Prof. Dr. Chakraborty
Gutachter ohne Benotung:	Dr. Binley (Lancaster University)

Tag der Disputation: 7. Juli 2000

DANKSAGUNG

Die vorliegende Arbeit wäre nicht möglich gewesen ohne die bereitwillige Unterstützung zahlreicher Personen und Institutionen, die mir in den letzten fünf Jahren in dankenswerter Weise zuteil wurde.

An erster Stelle ist sicherlich die Deutsche Montan Technologie GmbH (DMT, Essen) zu nennen, bei der die Arbeit innerhalb der heutigen Abteilung Geologie und Ingenieurgeophysik des Geschäftsbereichs GeoTec in weiten Teilen entstand. Für die grundsätzliche Befürwortung der Thematik sowie die Bereitstellung eines Arbeitsplatzes, der mir die notwendigen Freiräume zu deren Bearbeitung bot, bin ich insbesondere dem heutigen Geschäftsbereichsleiter Herrn Dr. Eiko Räkers zu großem Dank verpflichtet. Überdies bedanke ich mich bei ihm für den jahrelangen Zuspruch und das entgegengebrachte Vertrauen. Für die angenehme Arbeitsatmosphäre sei allen Kolleginnen und Kollegen herzlich gedankt. Insbesondere möchte ich Paul Althaus, Heinrich Dyballa, Dr. Rolf Elsen, Ralf Fritschen, Renate Müller, Uwe Niedereichholz und Anna Plaschke nennen, die mich seit meinem Beginn bei DMT vor neun Jahren stets unterstützt und mir hilfsbereit zur Seite gestanden haben.

Die Arbeit wurde fachlich von Herrn Prof. Dr. Dr. h.c. Lothar Dresen (Ruhr-Universität Bochum) betreut, wofür ich mich hiermit ausdrücklich bedanke. Obwohl ich aufgrund meiner Tätigkeit bei DMT nur sporadisch am Institut für Geophysik der Ruhr-Universität Bochum präsent sein konnte, setzte er sich – wann immer nötig – für meine Belange fürsorglich und beharrlich ein. Seine direkte und unkomplizierte Art schätze ich sehr. Herrn Prof. Dr. Horst Rüter (DMT) sei für die Übernahme des Korreferats gedankt.

Mein ganz besonderer Dank gebührt Herrn Dr. Andrew Binley (Lancaster University, England). Unsere enge und freundschaftliche Zusammenarbeit in den letzten vier Jahren hat wesentlich zum Gelingen dieser Arbeit beigetragen. In zahlreichen fruchtbaren Diskussionen und durch seine vielen wertvollen Anregungen und Kommentare hat er mein Verständnis thematischer Aspekte geschärft, mich stets motiviert und Begeisterung für neue Ideen geweckt. Besonders möchte ich ihm für die gründliche Durchsicht des Manuskripts, für seine zahlreichen nützlichen Verbesserungsvorschläge sowie für sprachliche Korrekturen danken. Ohne seine Unterstützung wäre die Arbeit wahrscheinlich nicht in englischer Sprache verfasst worden und somit einer breiteren Leserschaft erschließbar.

Wesentliche Teile dieser Arbeit wurden im Rahmen von Forschungsprogrammen der Europäischen Union gefördert. So wurde der entwickelte Inversionsalgorithmus in

seinen Grundzügen während eines mit Mitteln des ‚European Groundwater Research Programme' (Zeichen ERB CHRX CT92 0074) finanzierten Forschungsaufenthaltes an der Lancaster University im Jahre 1996 implementiert und getestet. Die Feldanwendung zur Charakterisierung der Untergrundsituation eines kontaminierten Standortes war Bestandteil des Projekts ‚Detecting and locating non-aqueous phase contaminants in soils by three geophysical methods', welches im Rahmen des ‚European Environment & Climate Programme' (Zeichen ENV4 CT95 0079) in Kooperation zwischen DMT, dem Institut Français du Pétrole (IFP, Paris, Frankreich) und der Universität zu Köln durchgeführt wurde. Insbesondere bedanke ich mich an dieser Stelle bei den Mitarbeitern des IFP für die Bereitstellung von relevanten Bohrprotokollen und Laborergebnissen.

Hinsichtlich der Feldanwendung zur Exploration einer Sulfidlagerstätte möchte ich der Metal Mining Agency of Japan (MMAJ, Tokio, Japan) meinen Dank aussprechen, die mir freundlicherweise die Rohdaten der Messung zur Bearbeitung zur Verfügung stellte. Herr Hiroyuki Katayama half mir geduldig bei Fragen zum Datenformat und versorgte mich bereitwillig mit allen notwendigen Informationen. Herrn Prof. Dr. Keeva Vozoff (V&A Pty. Ltd., Australien) sei gedankt für sein Engagement im Vorfeld, ohne das die erfolgreiche Zusammenarbeit mit der MMAJ nicht zu Stande gekommen wäre.

ACKNOWLEDGMENTS

This thesis would not have been possible without the willing and able support of numerous persons and institutions that I have been fortunate enough to meet during the last five years.

First mention must be given to the company Deutsche Montan Technologie GmbH (DMT, Essen, Germany), where much of the work for this thesis was carried out within the Geology and Engineering Geophysics Department, in the GeoTec Division. For supporting the thesis in principle and providing a job that offered the opportunity to work on it as necessary, I am particularly obliged to the present head of the division Dr. Eiko Räkers. Moreover, I thank him for his long-standing encouragement and trust in me. For providing me with a pleasant working environment, I want to thank all my colleagues warmly. In particular I would like to mention Paul Althaus, Heinrich Dyballa, Dr. Rolf Elsen, Ralf Fritschen, Renate Müller, Uwe Niedereichholz, and Anna Plaschke, who have always been supportive and ready to help since my start at DMT nine years ago.

The thesis was supervised by Prof. Dr. Dr. h.c. Lothar Dresen (Ruhr University Bochum, Germany), for which I thank him herewith specially. Although I could only be sporadically present in the Geophysics Department at the Ruhr University Bochum due to my placement at DMT, he interceded – whenever necessary – carefully and persistently on behalf of my interests. His direct and uncomplicated manner I appreciate very much. Prof. Dr. Horst Rüter (DMT) I thank for acting as the second examiner.

My particular thanks are due to Dr. Andrew Binley (Lancaster University, England). Our close and friendly cooperation in the last four years contributed essentially to the success of this thesis. In numerous fruitful discussions and also by his many valuable suggestions and comments, he has sharpened my comprehension of thematic aspects, always motivated me, and aroused enthusiasm for new ideas. Especially I wish to thank him for his thorough inspection of the manuscript, his numerous useful suggestions for improvements, as well as for grammatical corrections. Without his support the thesis would probably not have been written in English and thus opened to a wider public.

Sponsorship of essential parts of this thesis was granted from research programmes within the European Community. The developed inversion algorithm was mainly implemented and tested during a research visit at Lancaster University in 1996, which was funded by means of the ‘European Groundwater Research Programme’

(reference ERB CHRX CT92 0074). The field application for the characterization of the subsurface situation at a contaminated site was part of the project 'Detecting and locating non-aqueous phase contaminants in soils by three geophysical methods', which was conducted within the framework of the 'European Environment & Climate Programme' (reference ENV4 CT95 0079) in cooperation between DMT, the Institut Français du Pétrole (IFP, Paris, France), and the University of Cologne (Germany). At this point, I particularly thank the colleagues at IFP for providing relevant borehole logs and laboratory results.

Regarding the field application for the exploration of a sulfide deposit I wish to express my thanks to the Metal Mining Agency of Japan (MMAJ, Tokyo, Japan), who kindly provided the raw data of the survey for processing. Hiroyuki Katayama helped me patiently with questions on data format and supplied me willingly with all necessary information. Prof. Dr. Keeva Vozoff (V&A Pty. Ltd., Australia) I thank for his commitment in the start-up phase, without which the successful cooperation with the MMAJ would have not been achieved.

Düsseldorf
April 2000

Andreas Kemna

CONTENTS

1 Introduction 1

1.1 Background 1

1.2 Motivation and Objectives 2

1.3 Structure 4

1.4 Notational Remarks 6

2 Principles of Complex Resistivity in Geophysics 7

2.1 Introduction 7

2.2 Physical Fundamentals 8

2.3 Petrophysical Understanding of Complex Resistivity 11

2.3.1 Electrolytic Conductivity 11

2.3.2 Interfacial Conductivity 12

2.3.3 Electronic Conductivity 15

2.4 Relaxation Models 16

2.4.1 Relaxation Time 16

2.4.2 Cole-Cole Model 17

2.4.3 Constant-Phase-Angle Model 19

2.5 Field Measurements and Related Quantities 20

2.5.1 General Considerations 21

2.5.2 Classic IP Parameters 22

2.5.3 Complex Resistivity Measurements 25

2.6 Practical Applications 28

2.6.1 Mineral Exploration 28

2.6.2 Hydrogeological and Environmental Applications 31

2.7 Discussion and Conclusions 38

3 Modeling and Inversion Theory 41

3.1 Introduction 41
3.1.1 Review of IP Inversion Approaches 42
3.1.2 Conclusion 44
3.2 Forward Problem 45
3.2.1 Basic Equations 46
3.2.2 Boundary Conditions 47
3.2.3 Singularity Removal 48
3.2.4 Numerical Solution by Finite-Element Method 49
3.2.5 Sensitivity Computation 52
3.2.6 Inverse Fourier Transform 54
3.2.7 Modeling Examples 54
3.3 Inverse Problem 58
3.3.1 Inversion Approach 58
3.3.2 Parameters and Data 60
3.3.3 Numerical Solution 63
3.3.4 Regularization Parameter and Step-Length Damping 67
3.3.5 Robust Inversion 68
3.3.6 Final Phase Improvement 70
3.4 Summary 71

4 Synthetic Model Examples 73

4.1 Contaminant Plume Model 73
4.2 Horizontal Layer Model 82
4.3 Mineralization Zone Model 90
4.4 Summary 98

5 Field Applications 101

5.1 Environmental Site Characterization 102
5.1.1 Site Description 102
5.1.2 Electrode Setup and Data Acquisition 104
5.1.3 Inductive Coupling Removal 106
5.1.4 Inversion Procedure 112
5.1.5 Inversion Results 113

5.1.6 Cole-Cole Analysis 119
5.1.7 Hydraulic Permeability Estimation 123
5.1.8 Summary 126
5.2 Mineral Exploration 128
5.2.1 Site Description 128
5.2.2 Electrode Setup, Data Acquisition, and Inversion Procedure 130
5.2.3 Inversion Results 133
5.2.4 Summary 138

6 Summary and Conclusions 141

References 147

Appendices 159

A: Grain Size Sorting and Cole-Cole Exponent 159
B: Rearrangement of Finite-Element Functional 160
C: Evaluation of Inverse Fourier Integral 161
D: Parameterization of Model Roughness 163
E: Derivation of Complex Normal Equations 164
F: Variation of Regularization Parameter 165
G: Cole-Cole Model Fitting 166

List of Symbols and Abbreviations 171

1 INTRODUCTION

1.1 BACKGROUND

The investigation of the earth's subsurface is of general interest in many areas of socio-economic or environmental relevance. Whereas formerly the pure exploitation of the earth – e.g., in terms of water or minerals – has been the primary motivation, today the earth's protection and a responsible dealing with its natural resources plays an important role. For instance, the contamination of the subsurface soil and ground water from anthropogenic sources (wastes, chemicals, fuels, etc.) represents a serious problem endangering both human health and the environment. Applied geophysics provides effective tools to investigate such subsurface problems, either non-invasively from the surface or by the aid of boreholes. Main tasks in this regard include the localization, discrimination, and/or identification of structural characteristics in the underground.

Electrical methods belong to the fundamental techniques employed in applied geophysics. From the early beginning of this discipline, their great potential has been recognized for the investigation of the underground. The success of geoelectrical methods originates from the fact that minerals and rocks often exhibit distinct specific electrical properties which, in turn, correlate closely with the structural characteristics of interest. Electrical properties may be either investigated passively, as in the self-potential method, or actively by impressing a current onto the ground, as in the resistivity and induced polarization (IP) methods. The latter ones normally operate at relatively low measurement frequencies, typically less than 10 Hz, where – in contrast to electromagnetic methods – inductive effects can be ignored. Whereas the more commonly used resistivity method investigates the primary conduction phenomena in terms of signal amplitudes, in the IP method secondary polarization effects are measured in terms of time-domain discharge curves or frequency-domain phase shifts. This extension of the standard resistivity technique has been proven to provide important, complementary information on the subsurface in various applications. Due to the long-standing history and continuing development of the resistivity method, it is not attempted here to give a representative list of references. Instead, it is referred to the large number of standard textbooks on the subject in general (see, e.g., Telford et al., 1990). Recommendable reviews with emphasis on IP, however, include the work

by Wait (1959), Madden and Cantwell (1967), Bertin and Loeb (1976), and Sumner (1976).

Since the first applications of the resistivity method, numerous significant improvements have taken place concerning instrumentation, field techniques, data processing, and interpretation, and the method has now become an advanced exploration tool routinely employed for the solution of various subsurface problems. Standard applications include, for instance, ground-water prospecting, mineral exploration (typically in conjunction with IP), and any near-surface investigations related to hydrogeology and engineering geology (see, e.g., Ward, 1990). However, the advent of new imaging techniques in the last decade, such as electrical resistivity tomography (ERT), has opened the applicability of the method also to particular hydrogeological and environmental problems often associated with only subtle electrical contrasts. These techniques are based on sophisticated numerical inversion algorithms which yield detailed images of the electrical properties in the subsurface. In principle, they may be employed with arbitrary electrode arrangements, for example in a typical borehole to borehole (crosshole) geometry. In recent years, ERT has been successfully applied, for instance, to analyze fluid flow in porous and fractured sediments (e.g., Daily et al., 1992; Binley et al., 1996; Slater et al., 1996; Slater et al., 1997), to detect and map subsurface contaminant plumes (e.g., Daily et al., 1995; Ramirez et al., 1996), and to monitor contaminant remediation processes (e.g., Ramirez et al., 1993; Daily and Ramirez, 1995; LaBrecque et al., 1996c). As indicated by the large number of publications occurring each year on both theoretical aspects of ERT and related field applications (see, e.g., the last years' SAGEEP proceedings[1]), today there is a broad acceptance of the technique, and its practical value, especially for hydrogeological and environmental site characterization, is beyond question.

1.2 MOTIVATION AND OBJECTIVES

The ultimate basis for a reasonable interpretation of geophysical data is a sufficient knowledge of the relationship between the observed physical parameters and underlying structural characteristics. In the resistivity and IP methods, the principal pore-scale mechanisms in rocks responsible for the macroscopic electrical phenomena are known for a long time (as for IP, see, e.g., Marshall and Madden, 1959). Electrolytic conduction through the pore solution principally represents a purely resistive (i.e., in-phase) contribution to the bulk conductivity of a rock. On the other hand, interfacial conduction mechanisms, incident to electrical double layers at the

[1] Proc. Symp. Application of Geophysics to Engineering and Environmental Problems, Environ. Eng. Geophys. Soc.

grain surfaces, or abrupt changes in the conduction mode (e.g., from electrolytic to electronic in mineralized rocks) may give rise to IP effects and, thus, reactive (i.e., out of phase) conductivity components. Mathematically, the electrical rock properties may be conveniently described by a frequency-dependent complex resistivity, comprising magnitude and phase.

In the last three decades, extensive research has been conducted to gain insight into the complex resistivity characteristics of mineralized and, more recently, sedimentary rocks, with a view to the utilization thereof in mineral exploration, hydrogeological, and environmental applications. Besides the possibility of mineral discrimination, complex resistivity has been found to provide valuable information about the structural and hydraulic nature of porous media and fluids contained within such media. With the availability of appropriate relaxation models, such as the Cole-Cole model, in particular the quantitative spectral analysis of complex resistivity has become possible, which reveals additional material characteristics. Today, from the growing petrophysical understanding of electrical phenomena, for the complex resistivity method various new and promising perspectives of tremendous practical relevance arise. Envisaged applications include, for instance, contaminant detection and identification (e.g., Vanhala et al., 1992; Börner et al., 1993; Vanhala, 1997) or the estimation of hydraulic permeability (e.g., Börner et al., 1996; Sturrock et al., 1999).

Unfortunately, the proven relations between electrical and structural characteristics are not readily available at the field scale, where acquired data usually are of *apparent* rather than *intrinsic* nature. Therefore, it is generally desired to invert any measured data set, given for example in form of a geoelectrical pseudosection, to some representative image of the subsurface prior to a further analysis. Unlike in the conventional resistivity method, where efficient imaging techniques – such as ERT – are now widely available (see Section 1.1), similar inversion schemes for complex resistivity are still lacking – in particular with respect to spectral applications. The undisputed demand for such schemes (see Ward et al., 1995), however, initiated this thesis in 1995.

In view of the situation outlined above, the main objective of the present thesis is the development of a new, sophisticated, flexible and robust algorithm for complex resistivity tomography. With such an inversion procedure, lab-proven relations between (spectral) complex resistivity and intrinsic structural characteristics may be effectively utilized also at the field scale. By this, the benefits of high-resolution imaging and improved source characterization possibilities are intimately combined. Accordingly, the approach may enable access to both geometrical origin and structural cause of the observations in complex resistivity surveys. Besides the theory underlying the numerical implementation of the algorithm, however, the extensive examination of the method's suitability and efficiency in the various fields of potential application is likewise within the scope of this thesis. For this purpose, relevant synthetic models as well as typical field examples are considered in much detail. Particular objectives in

this regard include (i) the adaptation of an effective procedure to remove inductive coupling from broad-band, tomographic complex resistivity field data, (ii) the field application of the method for hydrocarbon contaminant detection in a sedimentary environment, (iii) the analysis of spectral inversion results with respect to relaxation time and grain size characteristics, and (iv) the tomographic estimation of hydraulic permeability from field data inversion results. In addition, numerous related aspects are addressed – not only to supply the reader with necessary or useful supplementary information, but also to embed the principal objectives of the thesis in a more general context. Note finally that for reasons of simplicity, this thesis is essentially restricted to the consideration of two-dimensional complex resistivity surveys – which are still the most common practice today. Extension to three-dimensional analysis is, however, straightforward.

As a whole, by providing a comprehensive treatment on the subject, the thesis is intended to contribute substantially to the elucidation of the possibilities and limitations of tomographic complex resistivity inversion with respect to both theory and application.

1.3 STRUCTURE

In order to provide a reasonable basis for the development of the new complex resistivity inversion scheme and its application to both synthetic model and field data examples, in the first part of this thesis (Chapter 2) the principles of complex resistivity in geophysics are briefly reviewed. Starting from physical fundamentals, the petrophysical origin of the observed phenomena is recalled, and commonly employed relaxation models for their spectral description are outlined. Subsequently, general aspects related to resistivity and IP field measurements are addressed, inclusive of the various descriptive parameters that may be deduced, followed by an overview of possible applications of the method for mineral exploration, hydrogeological, and environmental purposes.

The second part of the thesis (Chapter 3) presents the theory of both modeling and inversion parts of the developed tomography scheme. For the solution of the forward problem, comprising the calculation of the complex potential distribution for an arbitrary (two-dimensional) complex conductivity distribution and a given (point) current source, the flexible finite-element technique is adopted. In this context, several aspects affecting accuracy and efficiency of the implementation are considered in detail, such as boundary conditions, singularity removal, or computation of the sensitivities with respect to the individual element conductivities. The solution of the inverse problem, on the other hand, is based on a well-established regularized inversion approach in which the model distribution is subject to a smoothness

constraint. In this thesis, however, the approach is extended to a new, complex form, as to directly account for the given complex parameters and data in the inversion algorithm. The involved optimization problem is solved by means of a combination of an iterative Gauss-Newton scheme and the conjugate-gradient method. In addition, efficient procedures are incorporated capable of overcoming any numerical problems incident to particular data noise characteristics.

Subsequent to the theory chapter, the developed tomographic inversion scheme is extensively tested on different synthetic models (Chapter 4). Three models are presented which are chosen as to represent typical situations that may be encountered in realistic applications. By the first model, simulating a subsurface pollution scenario involving two different contaminant plumes, the general inversion behavior is examined, in particular with respect to data noise. The second model features a horizontal layer case typical for a clastic sedimentary environment. Here, particular objectives are the investigation of anisotropic model smoothing and the general impact of borehole separation on image quality in crosshole complex resistivity tomography. A dipping mineralization zone model completes the synthetic studies. Unlike the other model examples, however, here different structural elements are supplied with full spectral Cole-Cole (relaxation) properties reflecting the associated rock type characteristics. By applying the developed algorithm successively to single-frequency data extracted from a multifrequency data set and, subsequently, fitting a Cole-Cole model to the individual model cell inversion results, the capability is examined of recovering spectral Cole-Cole parameters in a tomographic way.

In the last part of the thesis (Chapter 5), two case histories of complex resistivity tomography are considered to eventually demonstrate the usefulness of the proposed inversion procedure in practical applications. The first field survey was conducted for the purpose of environmental site characterization at a kerosene-contaminated jet fuel depot. Since spectral data were acquired up to relatively high frequencies, an efficient inductive coupling removal scheme is described which was applied to the data prior to inversion. In addition to the interpretation of the recovered complex resistivity images, a Cole-Cole analysis of the spectral inversion results is performed and evaluated with respect to the subsurface characteristics and, moreover, an attempt is made at the tomographic estimation of hydraulic permeability. To complete the demonstration, a field survey for mineral exploration is presented, which was conducted over a sulfide deposit in the Broken Hill area, Australia. In conjunction, both field data examples prove the universality and efficiency of the developed complex resistivity tomography method.

1.4 NOTATIONAL REMARKS

In principle, standard notation is employed throughout the thesis (see, e.g., Sheriff, 1991).

Complex quantities are not explicitly marked to avoid unnecessary labeling. In general, the type of a symbol – i.e., real or complex – is mentioned when it is introduced. Otherwise the type should be clear from the context.

For analogous reasons, identical symbols are used in the time domain and the frequency domain. Again, however, the meaning is clear from the context. In ambiguous situations, the domain is indicated implicitly by adding the corresponding dependence on either time t or (angular) frequency ω.

The Latin and Greek alphabets are limited. Therefore, it is sometimes inevitable – if strange denotations shall be omitted – to use one and the same symbol for two different quantities. In such situations, the actual meaning is usually indicated earlier, unless being obvious. Also, the corresponding quantities seldom occur within the same context.

For simplicity, partial derivatives $\frac{\partial}{\partial \ldots}$ are sometimes abbreviated by $\partial_\ldots$, in particular with respect to the three Cartesian space coordinates x, y, and z.

Note that a complete list of the symbols and abbreviations used in this thesis is given subsequent to the Appendices.

2 PRINCIPLES OF COMPLEX RESISTIVITY IN GEOPHYSICS

2.1 INTRODUCTION

Electrical conduction (charge transport) and polarization (charge separation) belong to the fundamental physical properties of material media. The media of interest in geoscientific disciplines dealing with the earth's crust are basically minerals and rocks. Rocks are generally characterized by a complex internal structure, a variety of processes on numerous spatial and temporal scales are responsible for their electrical behavior. Therefore, the comprehensive understanding of the electrical phenomena occurring in rocks has always been (and still is) a challenging task for petrophysicists. To date, however, the principal underlying mechanisms are well-known, and an adequate mathematical description of the electrical rock properties, at least on a macroscopic scale, has been developed. Herein, the descriptive physical parameter of both conduction and polarization phenomena at lower frequencies (i.e., less than 10 kHz) is the complex conductivity, or its reciprocal, complex resistivity. As a complex number with both magnitude and phase, it fully describes the electrical response of a rock to an electrical excitation and, thus, characterizes its electrical behavior.

The understanding of the physics of rocks provides the basis for the interpretation of geophysical data in various fields of applied geophysics (like exploration, engineering or environmental geophysics) and, thus, plays a key role in the successful investigation of the underground. Electrical conduction and polarization phenomena are utilized in the geoelectrical methods of direct current (DC) resistivity and induced polarization (IP), respectively. A combination and extension of both represents the complex resistivity method, synonymous with the spectral IP (SIP) method. Here, besides the virtual conduction and polarization effects, their change with frequency of the employed electrical input signal (normally a square or sine wave) is measured. Since the spectral (i.e., frequency-dependent) behavior reveals many structural characteristics of the subsurface, the complex resistivity method is particularly helpful for source characterization and discrimination in various geophysical applications.

The following sections give an overview of the principles of complex resistivity phenomena in rocks and their importance in geophysics as being of interest within the

scope of this thesis. First, relevant physical fundamentals are discussed, and the concept of complex conductivity as the descriptive quantity of low-frequency electrical properties is introduced (Section 2.2). The petrophysical origin of the phenomena is outlined next (Section 2.3), followed by the presentation of the basic relaxation models being in use for the quantitative description of the spectral behavior of complex resistivity (Section 2.4). Then, the principles of complex resistivity field measurements are reviewed, including the various descriptive parameters that may be deduced (Section 2.5). Finally, the possible applications of the complex resistivity method in mineral exploration, as well as for hydrogeological and environmental purposes are shown (Section 2.6). The chapter ends with a brief discussion and some concluding remarks regarding the integration of the subsequent, main part of this thesis (Section 2.7).

2.2 PHYSICAL FUNDAMENTALS

In general, electromagnetic phenomena within material media are macroscopically described by Maxwell's equations. According to these, the total electric current density

$$\nabla \times \mathbf{H} = \mathbf{j} + \partial_t \mathbf{D} + \mathbf{j}_s \tag{2.1}$$

is composed of conduction currents $\mathbf{j}$, displacement currents $\partial_t \mathbf{D}$, and any source currents $\mathbf{j}_s$, where $\mathbf{H}$ and $\mathbf{D}$ denote the magnetic field and the dielectric displacement, respectively. Assuming a linear, isotropic, and time-invariant medium, in the frequency domain the constitutive relations, coupling $\mathbf{D}$ and $\mathbf{j}$ with the electric field $\mathbf{E}$, take the simplified form

$$\begin{aligned} \mathbf{j} &= \sigma(\omega)\mathbf{E}\,, \\ \mathbf{D} &= \varepsilon(\omega)\mathbf{E}\,, \end{aligned} \tag{2.2}$$

where the former relation represents Ohm's law. In the equations (2.2), σ and ε are the electrical conductivity and the dielectric permittivity, respectively, which describe the electrical properties of the considered medium as scalar functions of the angular frequency ω. In the most general case, σ and ε are, however, nonlinear tensor functions of temperature, pressure, etc., but the assumptions above are justified in so far as the simple macroscopic description (2.2) predicts the observed phenomena in many situations.

As Fuller and Ward (1970) state, the constitutive relations (2.2) are each entirely analogous to the input-output relation of a linear system, and hence, one can interpret the corresponding electrical parameters in the frequency domain as transfer functions.

The equivalent time-domain formulation of, for instance, Ohm's law is given by the convolution integral

$$\mathbf{j}(t) = \int_0^\infty \sigma(t')\,\mathbf{E}(t-t')\,dt' \,, \tag{2.3}$$

where, in adoption of linear-system theory's terminology, $\sigma(t)$ is the impulse response of the conductive system. In eq. (2.3), the lower integration bound zero expresses the fundamental principle of causality, which requires that $\sigma(t)$ is zero for $t < 0$. At a time t only the electric field *prior* to that time determines the current density, or in other words, no output before input. For causal systems, the transfer function and the impulse response are related through the Laplace transform[1] according to

$$\sigma(\omega) = \mathcal{L}\left\{\sigma(t)\right\}. \tag{2.4}$$

Since the actually measurable physical quantities $\mathbf{j}(t)$ and $\mathbf{E}(t)$ in eq. (2.3) are real, and consequently, also $\sigma(t)$ is real, from the representation of $\sigma(\omega)$ in eq. (2.4) directly follows that, in general, the conductivity must be complex and frequency-dependent. This means that the electric field and the conduction current density are not necessarily in-phase, in accordance with the fact that all macroscopic conduction phenomena are microscopically caused by the motion of charge carriers (molecules, ions, atoms, electrons), which obviously need a certain time to respond to an applied electric field.

Most physical systems are stable, i.e., for a bounded input (e.g., a step-function voltage excitation) also the corresponding output is bounded. This property forces the transfer function to have no singularities. For stable systems, a general restriction on the complex conductivity is directly placed by the afore-mentioned principle of causality. It can be shown that the real and the imaginary part of conductivity must be Hilbert transforms of each other.[2] Explicitly, it is (e.g., Fuller and Ward, 1970)

$$\sigma(\omega) = \sigma_\infty + \frac{\mathrm{i}}{\pi} P \int_{-\infty}^{\infty} \frac{\sigma(\omega')}{\omega' - \omega}\, d\omega' \,, \tag{2.5}$$

where σ_∞ is the high-frequency asymptote of $\sigma(\omega)$, i is the imaginary unit, and P indicates the evaluation of the integral in terms of the Cauchy principal value, i.e., exclusion of the singular point $\omega' = \omega$. An empirically found spectral behavior $\sigma(\omega)$

---

[1] For causal systems, the Laplace transform is formally equivalent to the Fourier transform extended to complex-valued arguments.

[2] The corresponding dispersion relations are known as Kramers-Kronig relations and were initially derived for the dielectric permittivity.

must necessarily obey eq. (2.5). Its validity is independent of the underlying microscopic conduction and polarization mechanisms.

Within the preceding considerations $\mathbf{E}$ was treated as the system's input causing an output $\mathbf{j}$. Of course, it is also possible to describe conduction phenomena vice versa in terms of a voltage response to a current input, as discussed by Shuey and Johnson (1973). In the latter case, the complex electrical resistivity $\rho(\omega)$, which is the reciprocal of $\sigma(\omega)$, acts as the descriptive transfer function of the system. Moreover, as a matter of principle, all the fundamental aspects discussed above, though formulated for conductivity, also apply similarly to the dielectric permittivity $\varepsilon(\omega)$, relating the electric displacement to the electric field. An extensive treatment of this matter is found in Böttcher and Bordewijk (1978).

For a sinusoidal time dependence $e^{i\omega t}$ of the considered fields, from eqs. (2.1) and (2.2), one obtains for the total current density

$$\nabla \times \mathbf{H} = \left(\sigma(\omega) + i\omega\varepsilon(\omega)\right)\mathbf{E} + \mathbf{j}_s \,, \tag{2.6}$$

where both σ and ε are frequency-dependent complex quantities. Obviously, there is some ambiguity in dividing the physically decisive term $\sigma + i\omega\varepsilon$ into two separate complex quantities σ and ε. For this reason, it is sometimes suggested to attribute the real part of $\sigma + i\omega\varepsilon$ entirely to conductivity and the imaginary part entirely to permittivity (e.g., Wait, 1982). Others renounce a distinction between conductivity and permittivity at all, in favor of either a generalized complex conductivity $\sigma + i\omega\varepsilon$ or a generalized complex permittivity $\varepsilon - i\sigma/\omega$ (e.g., Kulenkampff, 1994).

Within the scope of this thesis only electrical properties of rocks at frequencies less than 10 kHz are of interest. At this scale the observed delay of the response to an impressed excitation is caused by polarization effects which involve the movement of charge carriers over distances up to the order of centimeters. According to Pelton et al. (1983), such charge is more appropriately labeled as *free* rather than *bound*, and consequently, the corresponding phenomena are more correctly referred to as conductive (or resistive) rather than dielectric. However, the distinction between free and bound charge, or correspondingly, between conduction and displacement currents within rocks is problematic and rather artificial since the motion of charge carriers is always influenced in some way by existing bonding forces (Fuller and Ward, 1970; Kulenkampff, 1994). This fact will become more comprehensible when regarding the underlying conduction and polarization mechanisms, which are addressed in the next section.

In agreement with Pelton et al. (1983), in the following $\sigma(\omega)$, or respectively $\rho(\omega)$, is always considered to be complex, and its imaginary part shall account for any polarization effects occurring within rocks at the lower frequency scale. An inherent advantage of this convention is that the use of abnormally large values of permittivity

is avoided, which would be required otherwise to explain the observed effects quantitatively. Therefore, also the quasi-static approximation $\omega|\varepsilon|/|\sigma| \ll 1$ holds for normal earth materials if $f = \omega/2\pi < 10\,\text{kHz}$, and the conventional displacement currents within the total current density (2.6) can be neglected. Thus, taking the divergence of eq. (2.6) finally yields

$$\nabla \cdot \left(\sigma(\omega)\mathbf{E}\right) + \nabla \cdot \mathbf{j}_s = 0\,, \tag{2.7}$$

which will be the basis of the modeling algorithm described in Chapter 3.

2.3 PETROPHYSICAL UNDERSTANDING OF COMPLEX RESISTIVITY

In the following, the general concepts of electrical conduction and induced polarization mechanisms within rocks shall be summarized since they are essential for the understanding and interpretation of complex resistivity measurements. A comprehensive representation of this topic is given, for instance, in the reviews of Olhoeft (1981) and Ward (1990), and more recently, in the textbook by Schön (1996). It may be noted, however, that a full understanding of the electrical properties of rocks on the basis of a microscopic theory is still one of the major objectives of current research in petrophysics (Kulenkampff, 1994).

According to Ruffet et al. (1995), a rock can be considered as a three-component system, consisting of grains, pores (which might be fluid-filled), and the corresponding interfaces. The electrical bulk properties of a rock depend on both the individual properties of these constituents and their geometrical arrangement, i.e., the microstructure, within the rock. In most cases (particularly for silicates and carbonates), the conduction through the solid rock matrix is negligible, and mainly electrolytic as well as interfacial conduction takes place through the pore solution and along the pore (or grain) surfaces, respectively. However, for rocks containing certain minerals (e.g., sulfides), also electronic semi-conduction or even metallic conduction phenomena must be taken into account.

2.3.1 ELECTROLYTIC CONDUCTIVITY

The pore spaces of natural rocks are more or less filled with water, which contains various ions of dissolved salts. Electrolytic conduction is based on the movement of these ions through the aqueous solution in connected pore spaces. This *normal* mode of conduction may be described by an electrolytic conductivity σ_{el} as a contribution to the bulk conductivity of the whole formation σ.

The observed proportionality between σ_{el} and the conductivity of the pore solution σ_w is empirically found to be dependent on the porosity Φ and the water saturation S_w according to Archie's law (1942)

$$\sigma_{el} = \frac{\Phi^m}{a}\,\sigma_w\,S_w^n\,. \tag{2.8}$$

In eq. (2.8), m and n are usually referred to as the cementation exponent and the saturation exponent, respectively, and a is a proportionality constant. The quantity $F = a/\Phi^m$ represents the so-called formation factor. The real parameters a, m, and n; typically of the order of $a \approx 1$, $m \approx 2$, and $n \approx 2$; are mainly controlled by the pore space geometry (constrictivity, tortuosity)[3] and, thus, contain additional information about rock texture. Details are given in Schön (1996), who also tabulated numerical values for these parameters documented in the literature, for different rock types. Obviously, σ_w, and consequently also σ_{el}, increases with increasing ion concentration in the pore solution due to the higher number of potential charge carriers. Moreover, σ_w is dependent on the mobility of the ions and, therefore, on the viscosity and the temperature of the fluid.

Within an electrolyte each ion is surrounded by an inversely charged ionic cloud. This cloud lags behind its central ion when the latter moves in response to an applied electric field, resulting in a braking Coulomb force due to an asymmetric charge distribution. Consequently, the electrolytic conductivity increases with increasing frequency of the impressed field, since the ionic cloud lacks more and more time to build up the braking charge distribution and, correspondingly, the overall mobility of ions increases (see, e.g., Falkenhagen, 1971). Strictly speaking, this ionic polarization process causes σ_w to be complex. However, for the lower frequency range ($f < 10\,\text{kHz}$), the involved phase lag is virtually zero, and σ_w may be regarded as a real-valued quantity. In this sense, the electrolytic conductivity (2.8) represents an exclusively ohmic contribution to the bulk conductivity σ.

2.3.2 INTERFACIAL CONDUCTIVITY

Besides electrolytic conduction, controlled by pore volume properties as outlined in the previous section, a second component contributing to the overall conductivity is given by the interface conductivity σ_{int}, mainly controlled by pore surface properties. This additional mode of conduction was first detected for reservoir rocks bearing a significant content of clay minerals (Patnode and Wyllie, 1950). The origin of the

[3] The constrictivity describes the cross-sectional variations of the pore channels, while the tortuosity is an implicit measure of the length of the pore channels within a certain rock volume.

interfacial conductivity lies in the electrical double layer which is formed at the interface between electrically charged grain surfaces and the electrolyte.

Due to certain characteristics within the crystal lattice (isomorphous ion substitution, imperfections), to some extent most solid rock particles possess *fixed* electric charges on their surfaces. In addition, depending on the chemical environment provided by the chemistry of the pore fluid, *variable* surface charges may exist in terms of unsatisfied valence charges. In particular clay minerals exhibit significantly, negatively charged surfaces on these accounts (see, e.g., Yong et al., 1992) and, hence, play an important role regarding surface conductivity phenomena. The negative surface charges attract cations from the pore solution and, in electrokinetic equilibrium of diffusion and Coulombic interaction, the so-called double layer is formed. It consists of the negatively charged particle surface, an immediately adjacent fixed layer of adsorbed cations (Stern layer), and a diffuse layer of mobile cations characterized by an exponentially decreasing concentration with distance from the surface (Grahame, 1947).

The cations of the diffuse layer are loosely held to the surface and, therefore, can be easily exchanged for other cations (cation exchange)[4] and implicitly add to the *normal* ion concentration within the electrolyte. This phenomenon constitutes an additional mode of ohmic conduction, consequently referred to as ohmic interface conductivity. Moreover, the existence of the double layer is responsible for the so-called membrane polarization, a polarization mechanism arising within porous rocks under the influence of an electric field in the low-frequency range. This polarization phenomenon is mathematically described by an imaginary component of the (therefore complex) interface conductivity, which is also referred to as capacitive interface conductivity.

Membrane polarization is based on the different mobility of cations and anions within the pore solution in the vicinity of a double layer (Ward and Fraser, 1967). Whereas, in the presence of an electric field, the cations can readily pass through the diffuse layer via the process of cation exchange, the anions are blocked by the corresponding cationic cloud and, consequently, accumulate within the pore passages (see Figure 2.1). In this sense, the double layer acts as an ion-selective membrane. The magnitude of the resulting polarization also depends on the pore channel geometry. Obviously, the influence of the double layer on ion mobility increases with decreasing pore radius, which involves stronger polarization effects in constricted pore paths (Ogilvy and Kuzmina, 1972). It may be emphasized that the occurrence of membrane polarization is not only restricted to porous rocks containing clay minerals, but is

[4] The maximum number of exchangeable cations within the double layer defines the so-called cation exchange capacity (CEC).

inherent to any rocks exhibiting minerals with charged surfaces (e.g., silicate minerals).

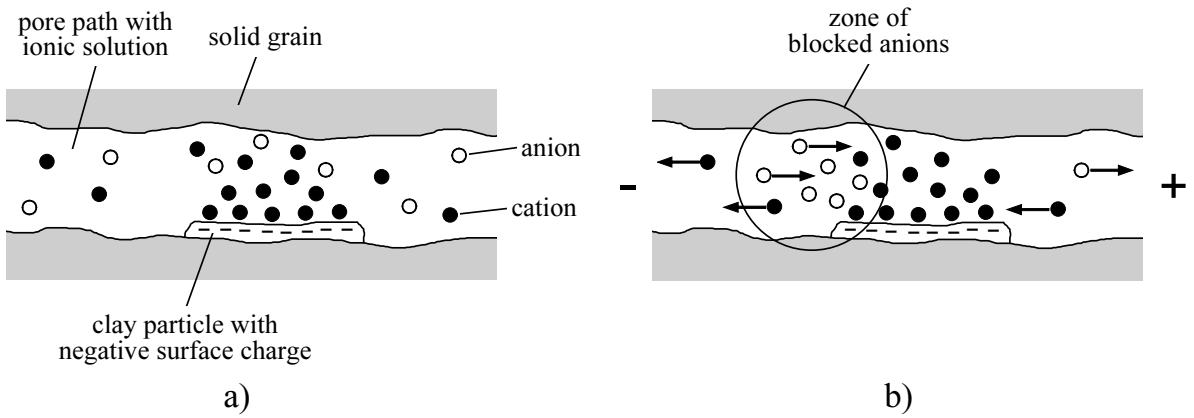

Figure 2.1: Origin of membrane polarization in porous rocks containing clay minerals. a) Distribution of ions within the pore solution under the influence of a negatively charged clay particle, forming an electrical double layer. b) Accumulation of anions, blocked by the cationic cloud of the double layer, in the presence of an electric field. After Ward and Fraser (1967).

For sedimentary rocks, both ohmic and capacitive part of interface conductivity are found to be directly proportional to the specific internal surface area of the rock (Rink and Schopper, 1974; Börner and Schön, 1991) and, thus, contain important additional information about its textural characteristics. According to Börner et al. (1996), the complex interface conductivity may be expressed as

$$\sigma_{\text{int}} = \frac{h(\sigma_{\text{w}})\, S_{\text{por}}}{F}\, S_{\text{w}}^{\nu}\left(1 + \text{i}\, l\right), \tag{2.9}$$

where $h(\sigma_{\text{w}})$ is a real (and generally nonlinear) function of salinity, S_{por} is the specific surface area related to the pore volume, and F and S_{w} are again formation factor and water saturation, respectively. The parameter $l = \text{Im}(\sigma_{\text{int}})/\text{Re}(\sigma_{\text{int}})$ accounts for the actual separation of σ_{int} into real and imaginary part, it generally varies between 0.01 and 0.15 (Börner et al., 1996). Recent investigations indicate that the saturation exponent ν in eq. (2.9) correlates with that of σ_{el} in eq. (2.8) according to $n - \nu \approx 1$ (Schopper et al., 1997).

The two components electrolytic and interfacial conductivity can be described as a parallel conductor system with a total conductivity $\sigma = \sigma_{\text{el}} + \sigma_{\text{int}}$ (Waxman and Smits, 1968). However, since σ_{el} may be regarded as a real quantity, interfacial electrical properties are directly accessible via the measurement of the quadrature component of σ.

2.3.3 ELECTRONIC CONDUCTIVITY

In the previous sections a possible conduction through the solid rock matrix itself was not considered. However, a non-negligible contribution to the overall conductivity on this account arises in the presence of such minerals that electrically act as semi-conductors or metallic conductors. These include almost all sulfides (e.g., pyrite), some oxides (e.g., magnetite), as well as metals (e.g., native copper) and graphite. The corresponding conduction mechanism is referred to as electronic since the current is carried by free electrons. The occurrence of electronic conduction can cause a significant increase of the bulk conductivity of a mineralized rock, depending on the kind and amount of mineralization.

As a matter of fact, the geometrical arrangement of electronic conducting minerals within the host rock is inherently related to the type of mineralization, which can be either well-disseminated, forming connected veinlets, or even massive. Except for the extreme latter case, in order for a current to flow through a mineralized rock, charge must necessarily be carried across the interfaces between the mineral grains and an ionic solution in the rock pores. At these interfaces the conduction mode changes from electronic to electrolytic, and the required charge-transfer is accomplished by either electrochemical reactions (e.g., oxidation, reduction) or capacitive coupling (Marshall and Madden, 1959). The two mechanisms are usually referred to as the faradaic and the non-faradaic path, respectively. At any interface between an electronic conductor and an electrolyte an electrical double layer (see Section 2.3.2) is formed due to an existing potential drop across the interface (Grahame, 1947). The complex electrochemical and electrokinetic processes (Wong, 1979; Klein et al., 1984) related to both faradaic and non-faradaic charge transfer at the mineral-solution interface involve the accumulation of ions within the corresponding diffuse layer in the pore fluid, which constitutes a polarization opposed to the applied electric field (Ward and Fraser, 1967). This polarization mechanism, resulting from the occurrence of electronic conducting minerals, is called electrode polarization. The magnitude of electrode polarization is generally much greater than that of membrane polarization, being discussed in the previous section.

Electrode polarization phenomena play an important role concerning the electrical characteristics of mineralized rocks at the lower frequency scale. They give rise to a complex-valued conductivity which contains useful information about rock structure and texture. Details on this are addressed in Section 2.6, dealing with practical applications of complex resistivity measurements.

2.4 RELAXATION MODELS

In the previous section the conduction and polarization mechanisms within rocks which give rise to the experimentally observed phenomena were briefly reviewed. However, in order to characterize the frequency dependence of electrical properties, a quantitative description of their spectral behavior is desired. An appropriate mathematical model, relating descriptive petrophysical parameters of rock type to measurable *spectral* quantities, is the basis of any practical application of the complex resistivity method related to source discrimination.

There exist numerous different approaches to accomplish the above requirement. They are mainly based on electrochemical interaction theory (e.g., Marshall and Madden, 1959), general relaxation theory (Jonscher, 1981), and more recently, adaptation of fractal concepts (Le Méhauté and Crépy, 1983) and cluster theory (Dissado and Hill, 1984). A representative overview of the various model descriptions is given in Pelton et al. (1983), Kulenkampff (1994), and Ruffet et al. (1995). It is not the purpose here to provide a comprehensive review or evaluation of all these approaches. Instead, only the basic, simple, and therefore widely used relaxation models shall be presented in order to illustrate the spectral characteristics of the complex electrical resistivity of rocks in principle. Even if some of these models from a theoretical point of view inherently lack physical justification (Jonscher, 1981; Ruffet et al., 1991), they are quite attractive in practice since they fit the observations in many cases as far as certain rock types are concerned.

As mentioned earlier, the electrical properties may be described in terms of either conductivity or resistivity. However, the following formulation uses resistivity for two reasons. First, resistivity behaves qualitatively similar to dielectric permittivity, for which most of the relaxation models were originally derived, and second, its usage is more common in the geophysical community when referred to geoelectrical exploration methods.

2.4.1 RELAXATION TIME

The simplest form of relaxation is represented by the classic Debye model, describing orientational dipole polarization in simple, viscous dielectrics. Starting from an existing polarization $\mathbf{P}$ due to the occurrence of an electric field in the past, in the absence of this field the decrease of $\mathbf{P}$ at a time t is proportional to the value of $\mathbf{P}$ at that instant, i.e.,

$$\partial_t \mathbf{P}(t) = -\frac{1}{\tau}\,\mathbf{P}(t)\,, \tag{2.10}$$

where the proportionality constant implicitly defines a characteristic time constant of the process, the relaxation time τ. Equation (2.10) implies an exponential decay $\mathbf{P}(t) \sim \mathrm{e}^{-t/\tau}$. The corresponding permittivity transfer function is obtained by means of Laplace transform of the impulse response. For the problem above it results[5]

$$\varepsilon(\omega) = \varepsilon_\infty + \frac{\varepsilon_0 - \varepsilon_\infty}{1 + \mathrm{i}\,\omega\tau}, \tag{2.11}$$

where it was taken into account that ε_0 and ε_∞ are the real, finite, and non-zero asymptotes of permittivity at low and high frequency, respectively.

Equation (2.11) represents the contribution of a *single* relaxation time to the transfer function $\varepsilon(\omega)$. In the general case, there might occur other relaxation processes due to different physical or chemical mechanisms, each related to a characteristic time constant or even a large spectrum of time constants. Therefore, it is reasonable to extend eq. (2.11) to account for any arbitrary continuous distribution of relaxation times $g(\tau')$:

$$\varepsilon(\omega) = \varepsilon_\infty + \left(\varepsilon_0 - \varepsilon_\infty\right) \int_0^\infty \frac{g(\tau')\,d\tau'}{1 + \mathrm{i}\,\omega\tau'}. \tag{2.12}$$

Obviously, the general expression (2.12) reduces again to the Debye model (2.11) for the choice $g(\tau') = \delta(\tau' - \tau)$, where δ denotes the Dirac delta function.

2.4.2 COLE-COLE MODEL

Cole and Cole (1941) suggested a slight, but important extension of Debye's formula (2.11) to explain experimental observations on various dielectrics. Their model was later adopted by Pelton et al. (1978a) to describe complex resistivity spectra of mineralized rocks over the frequency range 10 mHz to 10 kHz. In terms of resistivity, the empirical Cole-Cole model is given by

$$\rho(\omega) = \rho_\infty + \frac{\rho_0 - \rho_\infty}{1 + \left(\mathrm{i}\,\omega\tau\right)^c}, \tag{2.13}$$

in which c is the so-called Cole-Cole exponent, varying between 0.1 and 0.6 for most mineralized rocks, with a mean value near 0.25 (Pelton et al., 1978a). Analogous to eq. (2.11), the real values ρ_0 and ρ_∞ designate the low- and high-frequency asymptotes, where $\rho_0 > \rho_\infty$ since $|\rho(\omega)|$ is a decreasing function of frequency.

---

[5] Note that $\mathcal{L}\left\{\mathrm{e}^{-t/\tau}\right\} = \tau/\left(1 + \mathrm{i}\,\omega\tau\right)$ (e.g., Abramowitz and Stegun, 1984).

Figure 2.2 shows the magnitude and phase behavior of the Cole-Cole relaxation model as well as the corresponding distribution of relaxation times $g(\tau')$, which was calculated according to formulas given in Böttcher and Bordewijk (1978). From Figure 2.2 it is obvious that a small value of c accounts for a broad frequency dispersion, related again to a broad distribution of relaxation times. The phase spectrum shows a maximum, $-\varphi_{peak}$, in the dispersive region, which occurs at a frequency

$$\omega_{peak} = \left(\frac{\rho_0}{\rho_\infty}\right)^{1/2c} \frac{1}{\tau}, \tag{2.14}$$

inversely proportional to the time constant τ (e.g., Pelton et al., 1983). Thus, especially the phase curve provides distinct information about the characteristic time scale of the relaxation process.

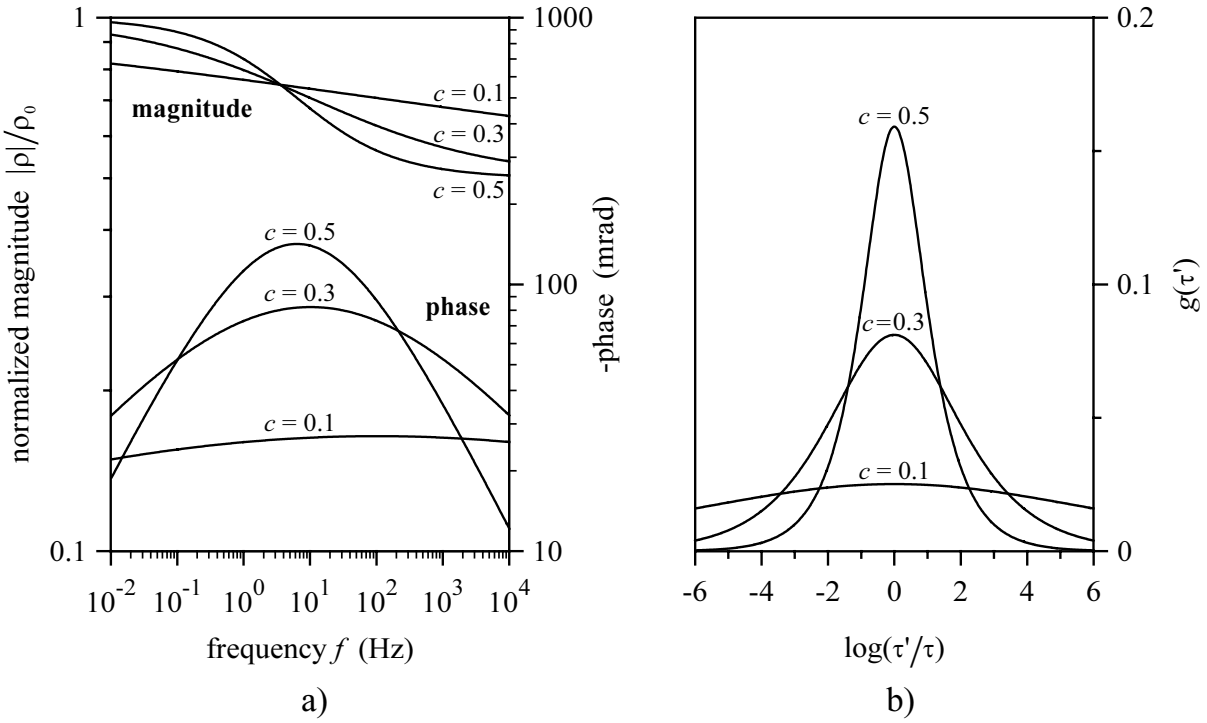

Figure 2.2: a) Magnitude and phase curves for the Cole-Cole relaxation model (2.13) with $\rho_\infty = \rho_0/2$, $\tau = 0.05$ s, and c varying from 0.1 to 0.5. b) Distributions of the relaxation times τ', normalized by τ, corresponding to the Cole-Cole spectra shown in a).

As Pelton et al. (1978a) state, a phenomenological explanation of the Cole-Cole relaxation of mineralized rocks may be given in terms of a simple equivalent electrical circuit representing the pore geometry. The circuit analog is composed of two parallel conduction paths: pore passages that are blocked by electronic conducting minerals and unblocked pore passages. Whereas the unblocked path behaves purely resistive,

the blocked path consists of a complex impedance of the form $(\mathrm{i}\omega X)^{-c}$, simulating the mineral-solution interface,[6] in series with an additional resistance attributing to the electrolytic conduction through the pore solution itself. A similar circuit model was already considered by Marshall and Madden (1959) and Madden and Cantwell (1967) to explain complex resistivity measurements on various mineralized rocks.

The equivalent time-domain formulation of eq. (2.13) as well as further variations and generalizations of the Cole-Cole model are discussed in Böttcher and Bordewijk (1978), Pelton et al. (1983), and Wait (1984).

2.4.3 CONSTANT-PHASE-ANGLE MODEL

Laboratory measurements on a variety of sedimentary rocks have shown that both real and imaginary part of complex conductivity in the range from 1 mHz to 1 kHz obey a nearly identical frequency dependence, following a simple power law (Börner and Schön, 1991; Börner et al., 1993). In complex notation, the corresponding spectral behavior of resistivity may be expressed as

$$\rho(\omega) = \rho_\mathrm{n} \left(\frac{\omega_0}{\mathrm{i}\omega} \right)^b , \tag{2.15}$$

in which ρ_n is the magnitude of resistivity at a reference frequency ω_0. The exponent b characterizes the frequency dependence and is of the order of $0 < b < 0.05$ (Börner and Schön, 1991). The model (2.15) exhibits a steady decrease of resistivity magnitude with increasing frequency, similar to the Cole-Cole model (2.13) for a small exponent c, and a constant phase angle over the whole frequency range, obviously given by[7]

$$\varphi(\omega) = -\frac{\pi}{2} b . \tag{2.16}$$

Therefore, eq. (2.15) is customarily referred to as the model of constant phase angle (CPA). A constant-phase-angle behavior was already observed by Van Voorhis et al. (1973) for porphyry copper mineralization, by Vinegar and Waxman (1984) for shaly sands, and by Lockner and Byerlee (1985) for granite and sandstone samples.

A microscopic interpretation of the CPA model goes back to Dissado and Hill (1984), who explained an identical frequency dependence of the permittivity of certain

---

[6] For $c = 0.5$, the expression $(\mathrm{i}\omega X)^{-c}$ is identical to the so-called Warburg impedance, which follows an inverse square-root frequency dependence and is characteristic for conduction mechanisms involving diffusive processes (Grahame, 1952).

[7] Note that within this thesis φ always denotes the phase of complex resistivity. The phase of the corresponding conductivity is $-\varphi$.

dielectrics, the so-called anomalous low-frequency dispersion, on the basis of a cluster description of the structural ordering within the underlying material. It is of interest to note that Liu (1985) derived exactly the same frequency dependence for the impedance of a rough interface between two materials showing different conduction modes (e.g., metallic and electrolytic) by considering a fractal equivalent circuit. Accordingly, the frequency exponent b is directly related to the fractal dimension and, hence, to the geometry of the rough interface. In this context, the validity of the CPA model (2.15) for porous rocks may be interpreted as an indication of a fractal character of the pore space geometry. In fact, Pape et al. (1987) showed that the internal surface of clastic sediments is properly described by a self-similar fractal model, their so-called pigeon-hole model. As discussed by Kulenkampff (1994), the fractal character dominates the pore structure up to a scale approximately designated by the effective hydraulic radius, which represents the lower bound of pore radii responsible for the transport properties of a sediment.

Laboratory and, in particular, field measurements of complex resistivity inevitably cover only a limited frequency range, sometimes less than three decades. Therefore, it might be difficult to distinguish between a constant-phase-angle behavior and a Cole-Cole model exhibiting a broad frequency dispersion since the latter is characterized by a relatively flat phase spectrum. Such an ambiguity results from a lack of spectral information in cases when relaxation processes with a sufficiently broad distribution of relaxation times are present. For instance, Wong (1979) explained one of the 'constant'-phase spectra measured by Van Voorhis et al. (1973) on mineralized rocks by means of an electrochemical model exhibiting a broad and inconspicuous phase maximum, which resulted in an excellent fit of the observations. Also Börner (1991) documented the existence of a slight phase maximum superimposed on a constant-phase response for several sandstone samples. However, in uncertain situations the simplest model description, i.e., the CPA model (2.15), should be the most preferable.

2.5 FIELD MEASUREMENTS AND RELATED QUANTITIES

Generally, field measurements of ground resistivity and induced polarization (IP) are performed using a four-electrode array consisting of two separate dipoles, one for current injection and one for measuring the resulting electric field in the subsurface in terms of potential differences. In principle, resistivity and IP measurements may be carried out in the time domain or in the frequency domain. Whereas in the former method the voltage decay with time after switch-off of an impressed current pulse is observed, the latter measures the (phase-shifted) voltage response to a periodic sinusoidal or square-wave current input with frequency. However, in practice, also the

time-domain current waveform is periodically repeated, and the measured discharge curves are being stacked, in order to improve the signal-to-noise ratio. Therefore, with modern instruments which fundamentally digitize the entire signals in real-time using high sampling rates (up to tens of kHz), the underlying data acquisition in both methods actually becomes similar (Frangos, 1990), and the remaining essential differences between time- and frequency-domain measurements may be the deduced descriptive parameters.

2.5.1 GENERAL CONSIDERATIONS

In the frequency domain, the measured voltage $V(\omega)$ due to a current input $I(\omega)$ depends upon the transfer impedance of the ground for the given electrode locations, $Z(\omega)$, and the transfer function of the receiver system, $R(\omega)$, according to $V(\omega) = R(\omega) Z(\omega) I(\omega)$. Customarily, the impedance $Z(\omega)$ is being assigned to an apparent complex resistivity $\rho_a(\omega)$ by means of multiplication by a (real-valued) geometric factor G which accounts for the geometrical arrangement of the four electrodes. Thus, the measured voltage can be written as

$$V(\omega) = R(\omega) \rho_a(\omega) I(\omega) / G \,, \tag{2.17}$$

or, equivalently in the time domain,

$$V(t) = R(t) * \rho_a(t) * I(t) / G \,, \tag{2.18}$$

where $*$ denotes convolution. Both time- and frequency-domain formulations are directly related through the Fourier (or Laplace) transform provided that the IP phenomenon is linear. However, they are entirely equivalent, i.e., exactly convertible into each other, only if information on all frequencies and times is available. This requirement is certainly not met for practical field applications. Because of the simpler form of the corresponding mathematical relations in the frequency domain (multiplication instead of convolution), $\rho_a(\omega)$ is usually the preferred quantity to be deduced from the measurements, also with regard to a further processing of the data.

As an example of a field recording, Figure 2.3 shows a transmitted current waveform and the corresponding voltage response measured with a crosshole dipole-dipole electrode array. The digital recording may be referred to as a time-domain measurement since a square wave with 50 % duty cycle[8] was applied, which enables the evaluation of the transient discharge curve during the off-periods of current injection. If only peak amplitudes are of interest, or the signals are supposed to being

[8] The duty cycle denotes the proportion of time in which current is delivered by the transmitter during a complete waveform cycle.

transformed into the frequency domain anyway, usually a 100 % duty-cycle waveform is used because of its inherent advantage in terms of signal strength.

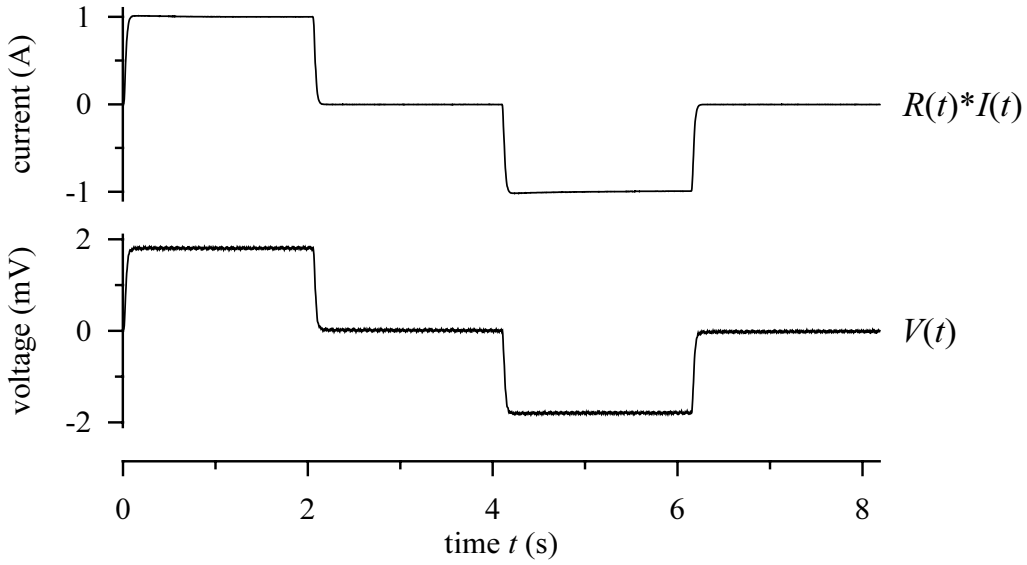

Figure 2.3: Example of a time-domain measurement, showing transmitted current waveform (top) and received voltage signal (bottom). For current input a 50 % duty-cycle square wave with pulse length $T = 2.048\,\mathrm{s}$ was used. The data were digitally recorded with the RESECS resistivity meter by DMT[9] using a sampling rate of 250 Hz. Note that both signals are affected by a time-domain receiver response $R(t)$ due to the application of an analog low-pass filter, appropriate to reduce power-line noise before digitization.

The following sections treat first, for completeness, the classic time- and frequency-domain IP parameters including the interrelations between them, and second, the general spectral formulation in terms of complex resistivity. Details on IP instrumentation and aspects related to this matter are found in Sumner (1976) and Frangos (1990). Various sources of noise (e.g., telluric and cultural noise) and distortion (e.g., capacitive and inductive wire coupling) that may affect complex resistivity measurements are discussed in Sumner (1976) and Ward (1990).

2.5.2 CLASSIC IP PARAMETERS

Within this section the following notational convention is met. Normally, *apparent* quantities (like ρ_a in the previous section) are indicated by an additional subscript in order to stress the distinction from the corresponding *intrinsic* or *true* property of the ground. For simplicity, this indication is dropped in the following since exclusively apparent parameters are considered.

---

[9] Deutsche Montan Technologie GmbH, Essen, Germany.

CHARGEABILITY

In the time-domain IP method the observed voltage response does not instantaneously drop off to zero when the applied charging current is switched off, but to a certain value V_s, referred to as the secondary voltage, depending on the polarization properties of the ground. Based on this quantity, Seigel (1959) introduced a descriptive parameter for IP, the chargeability

$$m = \frac{V_s}{V_p}, \tag{2.19}$$

as the ratio of V_s to the primary voltage V_p being reached just before current shut-down. However, this *zero-time* chargeability is difficult to determine for field measurements, and usually the corresponding average value along some part of the subsequent discharge curve is evaluated instead, that is the *integral* chargeability

$$M = \frac{1}{(t_2 - t_1)V_p} \int_{t_1}^{t_2} V(t)\, dt\,. \tag{2.20}$$

Unfortunately, M is also referred to as simply chargeability, and thus, terminology is not unambiguous in this context.

In a first approximation, M may be linearly related to the resistivity phase at a reference frequency ω_0, i.e.,

$$M \sim -\varphi(\omega_0)\,, \tag{2.21}$$

where the corresponding proportionality constant in particular depends upon the chosen integration limits t_1 and t_2 in eq. (2.20). On the basis of a valid relaxation model, however, the constant can be deduced by relating its time- and frequency-domain formulations via the Laplace transform (see Section 2.2). For the CPA model (2.15) with frequency exponent b, for instance, the voltage response due to N_p alternating pulses of a square-wave current with 50 % duty cycle and pulse length T is given by (Kemna et al., 1997)

$$V(t) \approx V_p \sum_{k=0}^{N_p-1} (-1)^{N_p-k} \left[(t + 2kT)^b - (t + T + 2kT)^b \right]. \tag{2.22}$$

From eqs. (2.20) and (2.22), the proportionality constant of relation (2.21) is easily found by numerical evaluation of $M(\varphi)$ for the relevant range of $\varphi = -(\pi/2)b$ and subsequent straight-line fitting. Values for a specific definition of M, the so-called Newmont standard, are also given in Nelson and Van Voorhis (1973).

FREQUENCY EFFECT

In the frequency-domain method the IP effect is commonly described by the so-called frequency effect

$$FE = \frac{\rho_0 - \rho_\infty}{\rho_\infty}, \tag{2.23}$$

which is the normalized difference between the asymptotic resistivity magnitudes at zero and infinite frequency. It may also be given as a percent frequency effect $PFE = 100\ FE$. However, for practical reasons, instead of the asymptotes ρ_0 and ρ_∞, customarily the respective magnitudes $|\rho(\omega_1)|$ and $|\rho(\omega_2)|$ at some defined frequencies $\omega_1 < \omega_2$ (e.g., separated by one decade) are used to determine FE.

Both descriptive parameters m and FE are easily interrelated via the initial- and final-value theorems of Laplace transforms (Wait, 1959), yielding

$$m = \frac{FE}{1 + FE} = \frac{\rho_0 - \rho_\infty}{\rho_0}. \tag{2.24}$$

Note that the theoretical relationship (2.24) only represents a rough approximation in practice, because it assumes an infinitely long charging current in the time domain as well as an infinite frequency spacing in the frequency domain.

The frequency effect may also be referred to a small frequency spacing $\Delta\omega$ around a reference frequency ω_0, corresponding to a variation in resistivity magnitude $\Delta|\rho|$ around $\rho_n = |\rho(\omega_0)|$, that is

$$FE(\omega_0) = -\frac{\Delta|\rho|}{\rho_n}. \tag{2.25}$$

As stated in Section 2.2, the real and the imaginary part of resistivity are intimately connected with each other through the Hilbert transform as a consequence of the principle of causality. Equivalent dispersion relations can also be derived for the pair magnitude and phase. From these it can be deduced (e.g., Wait, 1984) that in the first approximation

$$\varphi(\omega_0) \approx \frac{\pi}{2} \frac{d\ln(|\rho|/\rho_n)}{d\ln(\omega/\omega_0)}, \tag{2.26}$$

i.e., at any frequency the resistivity phase is directly proportional to the slope of resistivity magnitude as a function of frequency on double logarithmic scales. Moreover, from eqs. (2.25) and (2.26), it is readily seen that approximately

$$FE(\omega_0) \sim -\varphi(\omega_0). \tag{2.27}$$

In this sense, a single-frequency phase measurement is equivalent to magnitude measurements at two frequencies required to determine the differential frequency effect (Zonge et al., 1972).

METAL FACTOR

A further parameter, mainly used in mineral exploration applications, is the metal factor (or metal conduction factor)

$$MF = \frac{PFE}{\rho_0}, \tag{2.28}$$

going back to Marshall and Madden (1959). This quantity has been found to be less dependent upon the bulk resistivity of mineralized rocks and, hence, more diagnostic concerning the amount of mineralization than the original frequency effect (Hallof, 1964). This observation is obvious from the following consideration.

Let σ denote the complex conductivity with magnitude $|\sigma| = \rho_0^{-1}$ and phase $-\varphi$ corresponding to the metal factor (2.28). Since, from relation (2.27), $PFE \sim -\varphi$ and $\varphi \approx \sin\varphi$ for the observed small phase angles in the IP method, it follows that

$$MF \sim |\sigma| \sin(-\varphi) = \mathrm{Im}(\sigma). \tag{2.29}$$

In this way, the metal factor is implicitly related to the imaginary part of the complex conductivity, being attributed to the polarization phenomena occurring at the mineral-solution interfaces in mineralized rocks, and consequently, it is separated from an electrolytic conduction in the pore spaces.

2.5.3 COMPLEX RESISTIVITY MEASUREMENTS

In the complex resistivity method, also referred to as spectral IP (SIP) method, the fundamental quantities of interest are magnitude $|\rho(\omega)|$ and phase $\varphi(\omega)$ (or the equivalent real and imaginary part) of complex resistivity as functions of frequency. Their measurement allows the subsequent description of the frequency dependence by means of appropriate relaxation models (see Section 2.4) and, thus, may provide access to important petrophysical characteristics of the ground. In contrast to the previously discussed standard IP parameters, a formulation in terms of frequency-dependent complex resistivity is more general as it directly represents the underlying physical property responsible for the observed phenomena.

Most modern IP instruments, either providing time- or frequency-domain data, first of all supply a repetitive square-wave current to the ground, resulting in a voltage response digitally recorded in the time domain. Afterwards, magnitude and phase at the fundamental frequency of the square wave are calculated, or even the entire spectral content of the received signal may be analyzed. However, the usage of a

pulse-train waveform holds some inherent limitations on the valuable frequency band due to its specific spectral characteristics.

In general, the recorded periodic time series $V(t)$, being sampled at intervals Δt with N_s samples per period, can be represented by the Fourier series

$$V(t) = \sum_{k=-\infty}^{\infty} c_k \, e^{i k\omega_0 t} \ , \tag{2.30}$$

with the complex Fourier coefficients

$$c_k = \frac{1}{N_s} \sum_{i=0}^{N_s-1} V(i\Delta t) \, e^{-i k\omega_0 i\Delta t} \tag{2.31}$$

given at the discrete frequencies $k\omega_0$, where $\omega_0 = 2\pi/N_s\Delta t$ denotes the fundamental frequency of the waveform. The values of the corresponding discrete Fourier transform are obtained by rescaling the Fourier coefficients according to

$$V(k\omega_0) = N_s \, \Delta t \, c_k \ . \tag{2.32}$$

In order to illustrate the spectral characteristics of a square wave and the problems involved regarding wide-band complex resistivity measurements, Figure 2.4 shows the spectral analysis of the time-domain recording from Figure 2.3.

Figure 2.4a exhibits the fact that a square wave contains only odd harmonics with their amplitude inversely proportional to the harmonic number (see, e.g., Sumner, 1976). According to eq. (2.17), the sought magnitude and phase spectra of $\rho_a(\omega)$ are obtained by dividing the *output* spectrum $V(\omega)$ by the *input* spectrum $R(\omega)I(\omega)$ at the corresponding discrete frequencies. It is seen from Figure 2.4b that the phase spectrum is being distorted in the range $\log(\omega/\omega_0) > 1.5$, which is due to the lack of spectral energy at higher frequencies. This is in accordance with Soininen (1984), who concludes on the basis of a numerical analysis that alternating pulse-train measurements do not provide spectral phase information from a wide frequency band, but only from the limited band 1 to 1.5 decades above the employed fundamental frequency.

Accordingly, it is seldom possible in practice to determine unambiguous relaxation model parameters (e.g., Cole-Cole parameters), describing the frequency behavior of $\rho(\omega)$ over several decades, from a conventional pulse-train measurement (Tombs, 1981). Extracted descriptive model parameters (Johnson, 1984; Lewis, 1985) do inevitably refer to a relatively narrow frequency band, and any higher-frequency spectral behavior might at best be extrapolated by means of assuming the broad-band validity of the adopted relaxation model.

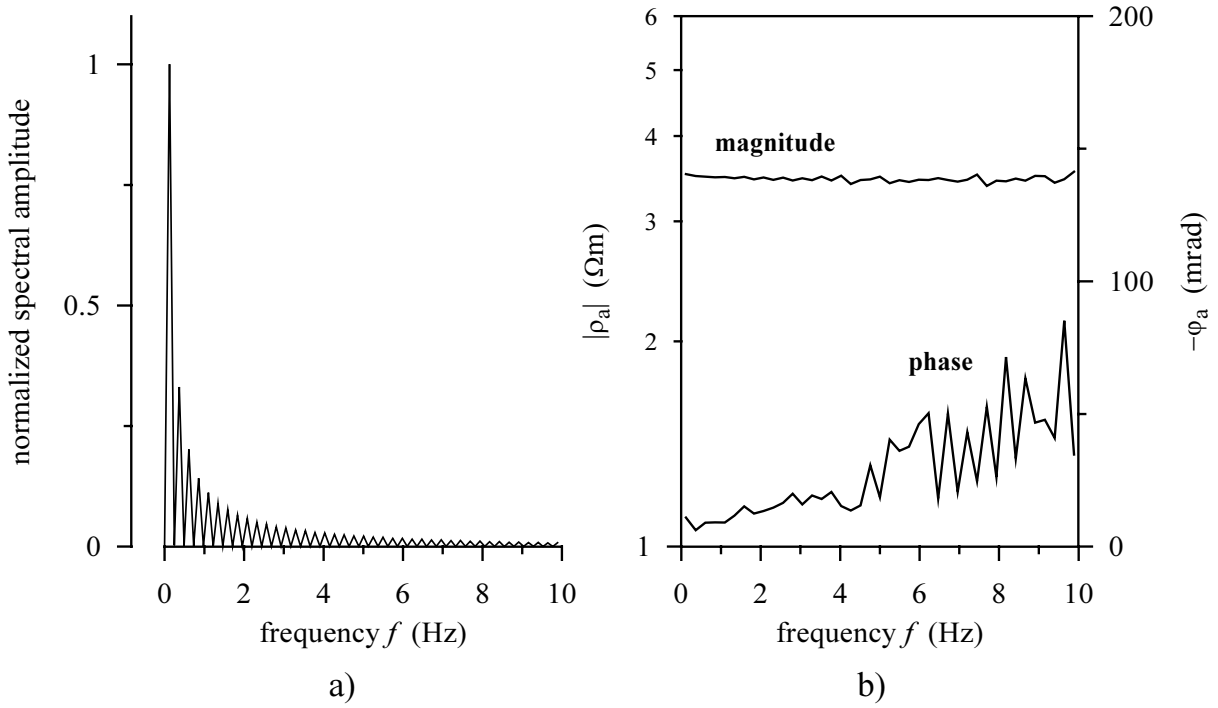

Figure 2.4: Spectral analysis of the time-domain recording shown in Figure 2.3. a) Amplitude spectrum of the recorded current signal, describing the spectral content of the applied square wave. b) Magnitude and phase spectra of the corresponding apparent complex resistivity. Note that the complex resistivity spectra are only evaluated at frequencies where spectral information is available, that is the fundamental frequency of the square wave, $f_0 \approx 0.122$ Hz, and its odd harmonics kf_0 $(k = 1, 3, 5, \ldots)$.

From the preceding discussion it is obvious that the only way getting reasonable wide-band complex resistivity data using a pulse-train current excitation, is to repeat the measurements with different fundamental frequencies of the applied waveform. However, even though the signals are actually recorded in the time domain, these kind of measurements should be more appropriately referred to as frequency-domain measurements. A corresponding field data example, again measured with a crosshole dipole-dipole array, shows Figure 2.5. Plotted are magnitude and phase of apparent complex resistivity measured at altogether eight single fundamental frequencies, covering a range of nearly six decades. It may be noted that the increase of phase lag for frequencies greater than 10 Hz is due to inductive coupling and, thus, must not be attributed to IP phenomena in the ground.

The general theory of inductive coupling effects as occurring in IP measurements is reviewed in Wait (1959) and Sumner (1976). More details on this matter are given in Section 5.1.3 within the context of the presented complex resistivity field surveys, when the employed technique for the removal of inductive coupling effects is discussed.

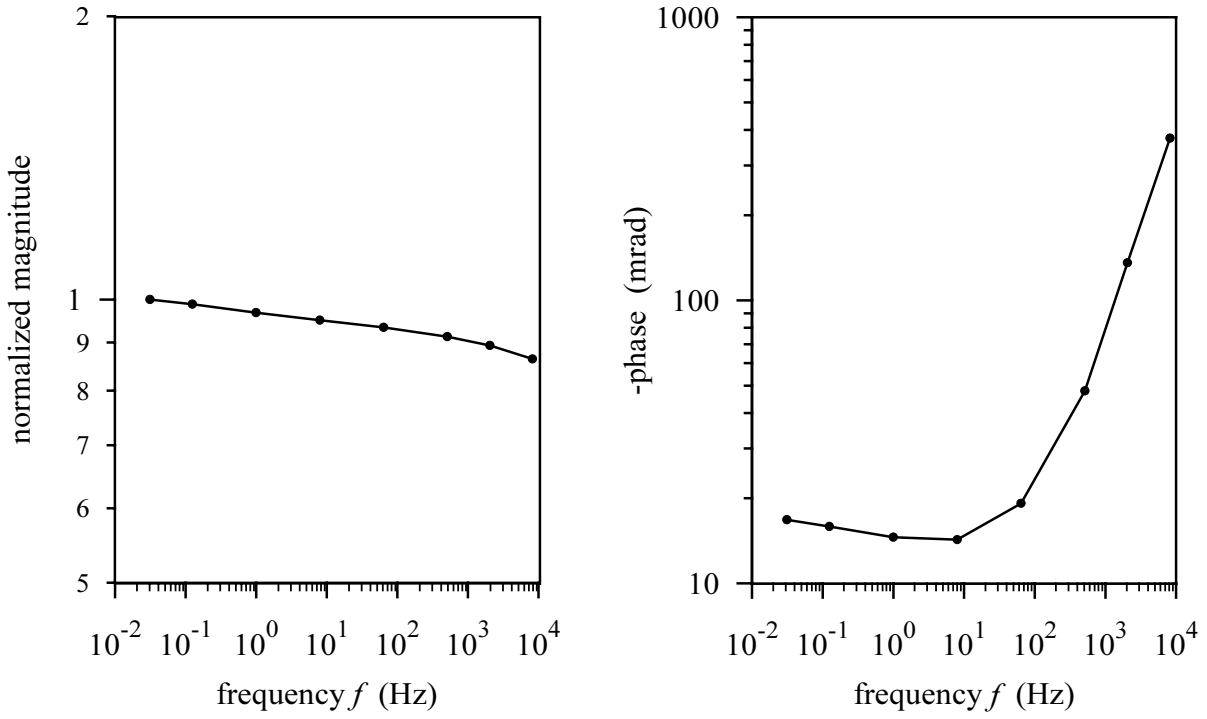

Figure 2.5: Example of wide-band frequency-domain measurements, showing normalized magnitude (left) and phase (right) spectra of apparent complex resistivity. The data were measured at eight frequencies ranging from 2^{-5} Hz to 2^{13} Hz using the ZT-30 transmitter and GDP-32 receiver by ZERO[10].

2.6 PRACTICAL APPLICATIONS

From the underlying mechanisms of conduction and polarization phenomena within rocks (see Section 2.3) it is clear that there exists a strong relation of the observed effects to the inner structure and texture of rocks in terms of mineral composition, grain size, pore space geometry, and pore fluid characteristics. These relations build the basis of any practical applications of the complex resistivity method, either used for mineral exploration, hydrogeological, or environmental purposes. The following sections give a brief overview of the petrophysical information that can be derived from complex resistivity measurements in the different fields of application.

2.6.1 MINERAL EXPLORATION

From the beginning of its development the IP method has been proved to be an effective tool in mineral prospecting (e.g., Bleil, 1953; Marshall and Madden, 1959).

[10] Zonge Engineering and Research Organization, Inc., Tucson, USA.

The main objectives in mining applications are to determine the location and extent of mineralized zones within a host rock and, in addition, to classify both grain size and concentration of the polarizable minerals, and to characterize the type of mineralization. All this information is essential for the discrimination between uneconomic and exploitable geological materials. A quantitative approach to the tasks above was introduced by Pelton et al. (1978a). Based on in-situ complex resistivity measurements over a broad frequency range on various mineral deposits, they showed that the IP response of mineralized rocks closely conforms to the Cole-Cole relaxation model (2.13) and, moreover, that the corresponding Cole-Cole parameters correlate with different structural and textural characteristics.

In general, the amplitude of the IP response of mineralized rocks is directly proportional to the concentration of the electronic conducting minerals. For the Cole-Cole model, a measure of the IP amplitude is given by the absolute value of the phase peak φ_{peak}. Consequently, $|\varphi_{peak}|$ may provide useful information about the amount of ore minerals within a deposit. Marshall and Madden (1959) suggested use of the metal factor (2.29), comprising both IP amplitude and bulk conductivity, to differentiate between disseminated, veined (i.e., fracture filling), and massive sulfide mineralization.

IP source	time constant (s)				
	10^{-2}	10^{-1}	1	10	100
background (non-metallic)					
gold deposits with dissem. sulfides					
bedded lead-zinc deposits					
porphyry copper deposits					
massive pyritic sulfides					
magnetite-related ultramafics					
pyrrhotite-related deposits					

Table 2.1: Characteristic τ values of typical IP sources in mineral exploration. After Seigel et al. (1997).

The most important descriptive parameter in the Cole-Cole model is found to be the time constant τ. It is directly related to the spatial scale at which the polarization processes take place and, accordingly, increases with increasing grain size of the electronic conducting particles. Since it may vary over more than six orders in magnitude for different types of mineralized rocks (typically ranging from 10^{-3} to 10^{3} s), τ is particularly diagnostic with respect to source discrimination. Table 2.1 shows the characteristic range of τ values for typical IP sources being of interest in mineral exploration. As pointed out by Pelton et al. (1978a), the differences in the time constant arise substantially from mineral texture and not from mineral composition. Generally, the time constant of disseminated mineralization is smaller than that of net-

textured mineralization, which again exhibits smaller τ values than veined or massive mineralization (Pelton et al., 1978a; Vanhala and Peltoniemi, 1992; Seigel et al., 1997). Based on this, mineral differentiation is possible in many situations by means of analyzing the measured complex resistivity spectra with respect to τ. For instance, Pelton et al. (1978a) were able to discriminate massive sulfides from graphite, pyrrhotite from magnetite, and disseminated from veined porphyry mineralization. However, by considering the time constant alone, it might be difficult to distinguish, for example, between fine-grained sulfide responses and non-metallic polarization responses caused by clayey or zeolitic materials (Nelson et al., 1982).

A quantitative relation between the time constant τ and the (mean) grain size of the mineralized particles, in the following denoted by r_{grain}, was derived by Wait (1982) on the basis of a simple physical model describing disseminated mineralization. From this, the proportionality

$$\tau \sim \left(\rho_0 \, r_{\text{grain}}\right)^2 \tag{2.33}$$

can be deduced, where ρ_0 is the (zero-frequency) magnitude of the corresponding bulk resistivity. Strictly speaking, relation (2.33) is valid for diffusion-limited systems, where the mineral-electrolyte interface behaves like a pure Warburg impedance (e.g., Olhoeft, 1985). Based on both theoretical data calculated from the electrochemical model by Wong (1979) and experimental data documented in the literature for different mineralized rocks, Olhoeft (1985) determined the relation between τ in s and r_{grain} in m to be

$$\tau \approx 3 \cdot 10^5 \; r_{\text{grain}}^2 \; , \tag{2.34}$$

which is in accordance with relation (2.33) for a certain range of resistivities. However, Pelton et al. (1978a) note that the time constant not only depends upon the mean grain size but also on the mineral concentration in the rock.

In addition to the time constant τ, another important parameter in the spectral IP method is the Cole-Cole exponent c, related to the distribution of relaxation times and, thus, to the particle size distribution of the mineralized rock (e.g., Wong, 1979). The largest values of c $(0.5 < c < 1)$ are found for rocks containing disseminated mineralized grains uniform in size, as well as for rocks with veined or massive mineralization (Luo and Zhang, 1998). Rocks that are characterized by a sporadic or sparsely disseminated matrix exhibit moderate values $(0.4 < c < 0.6)$, whereas for highly mineralized, inhomogeneous rocks, the smallest values are observed $(0.2 < c < 0.4)$. In this way, it is possible to discriminate polarizable bodies according to their structure using the exponent c. In particular, c can be used to distinguish a local rich orebody from surrounding mineralized rocks (Luo and Zhang, 1998).

Comprehensive case histories dealing with the application of the spectral IP method to various mineral exploration problems can be found in Fink et al. (1990), Seigel et al. (1997), and Luo and Zhang (1998).

Finally, it may be noted that the complex resistivity method is not only effective for mineral prospecting, but also seems to be a promising tool in petroleum exploration, particularly when combined with conventional seismic surveys (Sternberg and Oehler, 1990; Sternberg, 1991). The origin of IP anomalies related to oil and gas reservoirs lies in the formation of secondary pyrite when, first, the hydrocarbons are able to migrate from the reservoir into overlying porous host rocks and, second, a sufficient amount of sulfate and iron is present in the overburden, causing certain chemical reactions to take place. These petrophysical and geochemical requirements are, however, met in many situations (Luo and Zhang, 1998).

2.6.2 HYDROGEOLOGICAL AND ENVIRONMENTAL APPLICATIONS

More than four decades ago, Vacquier et al. (1957) pointed out the usefulness of the IP method as a supplement to standard resistivity surveys in ground-water prospecting. In particular, they recognized that the rate of voltage decay in time-domain IP measurements is principally influenced by the grain size and that, based on this, the estimation of the hydraulic conductivity of an aquifer might be possible. Later, Ogilvy and Kuzmina (1972) investigated the dependence of the IP response on particle size distribution, moisture content, and salinity more thoroughly and applied the method to detect ground-water accumulations in clay-sand environments, evaluate ground-water salinity, and differentiate soil with respect to lithology. Also Iliceto et al. (1982) reported on the interrelation between the shape of the time-domain discharge curve and the granulometric characteristics of fine sediments and suggest its utilization in lithotype identification. Dudás et al. (1991) found a qualitative relationship between resistivity magnitude, percent frequency effect, and the dominant grain size by means of a nomogram representation of data measured over unconsolidated sediments. An overview of the published applications of conventional IP surveys to hydrogeological problems can be found in Draskovits et al. (1990).

All the investigations referred to above do not take the spectral character of complex resistivity into account, but are restricted to the analysis of IP amplitude in terms of either chargeability or frequency effect. It was particularly Olhoeft (e.g., Olhoeft, 1985) followed by Vanhala and colleagues (e.g., Vanhala et al., 1992; Vanhala and Soininen, 1995) starting to focus on the applicability of spectral IP measurements to assess texture, mineralogy, moisture content, and electrolyte composition of loose sediments. They demonstrated that especially from the shape of the phase spectrum important petrophysical conclusions may be drawn.

As outlined in Section 2.3.2, the origin of the IP effect in porous sediments lies in the ion exchange reactions taking place in the presence of electrically charged particle surfaces. Since the cation exchange capacity is largest for clay minerals (e.g., montmorillonite, kaolinite), the clay content is an important factor in the formation of the IP response. In addition, the width of the pore spaces, inherently related to the grain size distribution, affects the magnitude of membrane polarization. For larger grain sizes (coarse sands, gravels), the free electrolyte paths with pure ohmic conduction dominate over ion-selective paths, resulting in a decrease of IP amplitude. This fact is illustrated in Figure 2.6, reproduced from Vanhala (1997), where resistivity phase measurements are plotted against the mean grain size for a variety of soil samples. Accordingly, the highest polarizability is observed for sandy silts and fine sands. The decrease in the phase shift for smaller grain sizes (clayey silts, clays) can be related to both the migration of the corresponding relaxation phenomena towards higher frequencies (Vanhala, 1997) and the increasing dominance of the ohmic interface conduction mode inherent to clay minerals (Schön, 1996). The distribution in Figure 2.6 is similar to results already presented by Iliceto et al. (1982) and Dudás et al. (1991). The phase lag typically decreases with increasing moisture content as well as increasing ion concentration in the pore solution since the influence of both saturation and salinity on electrolytic conductivity σ_{el} is stronger than on interface conductivity σ_{int} (see Section 2.3).

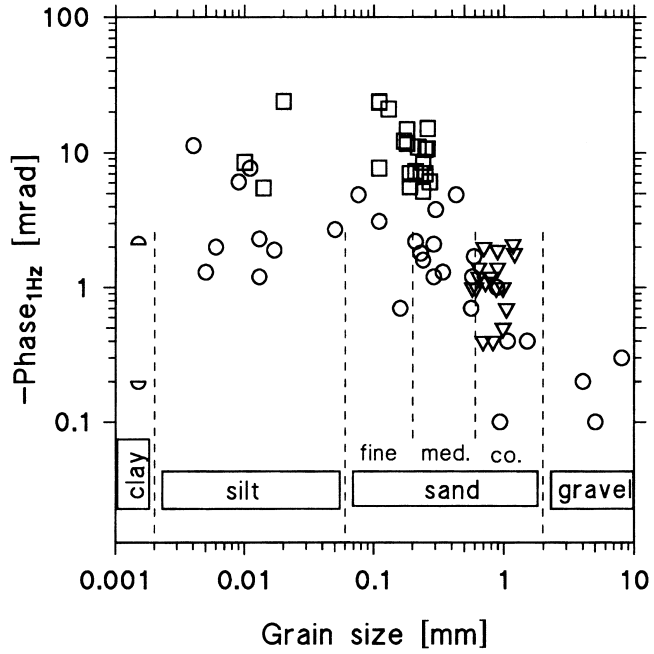

Figure 2.6: Resistivity phase measurements at 1 Hz frequency on various soil samples against the respective mean grain size. As a whole, the measurements indicate the typical distribution of the low-frequency IP effect of loose sediments as a function of grain size. After Vanhala (1997).

Also for clastic sedimentary rocks, on principle, each relaxation phenomenon gives rise to a maximum in the phase spectrum. By means of a Cole-Cole model description, the corresponding time constant may be related to the mean grain size analogous to eq. (2.34), i.e.,

$$\tau \sim r_{\text{grain}}^2 \ . \tag{2.35}$$

Such a proportionality is in fair accordance with SIP and granulometric measurements conducted by Vanhala (1997) on various silt samples. However, it may be noted that the proportionality constant significantly differs from that in eq. (2.34), which was found for certain mineralized rocks. Moreover, relation (2.35) implicitly assumes a rather narrow grain size distribution, for which r_{grain} is not only a mean value but the actual predominant grain size. For wider grain size distributions (e.g., tills), the phase maxima originated from relaxation phenomena at different spatial scales may 'overlap' and add up to a phase spectrum which is nearly constant over a broad range of frequencies. Further, since membrane polarization is mainly controlled by pore surface properties, relaxation phenomena are not only related to the grain size distribution but also to the pore size distribution and the pore surface structure. Beyond the effective hydraulic radius the pore space of clastic sediments exhibits a fractal character (e.g., Kulenkampff, 1994). Although hydraulically ineffective, this part of the pore space may contribute to the formation of the IP response, which can result in a flat phase spectrum as well. Therefore, as already mentioned in Section 2.4.3, the assignment of a unique time constant via the Cole-Cole model might not be appropriate in certain cases, and rather the CPA model (2.15) should be adopted to describe the spectral IP behavior.

The close connection between the frequency-dependent IP response and the underlying pore space geometry can be utilized to estimate one of the most important hydrogeological parameters, the hydraulic permeability, from complex resistivity measurements. This is addressed in the following paragraph.

ESTIMATION OF HYDRAULIC PERMEABILITY

The hydraulic permeability, K, with dimension $[\mathrm{L}^2]$, characterizes the ability of a medium to transmit a fluid.[11] On the basis of a simple capillary tube model describing the pore channels, the Kozeny-Carman equation relates K to the effective hydraulic capillary radius of the pores, r_{eff}, and the formation factor F according to (e.g., Pape et al., 1982)

---

[11] In hydrogeology, often the hydraulic conductivity K_{f} is used, which already takes the viscosity and density of water as the single pore fluid into account. It has the dimension $[\mathrm{L\,T^{-1}}]$.

$$K = \frac{r_{\text{eff}}^2}{8F} . \tag{2.36}$$

Expressing eq. (2.36) in terms of porosity Φ via Archie's law yields the simple relation

$$K \sim \Phi^m r_{\text{eff}}^2 , \tag{2.37}$$

with m being the cementation exponent.

However, by considering systematic grain packings, Berg (1970) derived a more adequate relationship for sedimentary rocks[12], which in particular takes the influence of grain size sorting into account:

$$K = 0.3\, \Phi^{5.1}\, r_{\text{grain}}^2\, \mathrm{e}^{-\Delta_{\ln r}} . \tag{2.38}$$

Herein, K is in darcies, r_{grain} is the median grain size in μm, and $\Delta_{\ln r}$ is a measure of the spread of the grain size distribution on logarithmic scale. The permeability reduction factor $\mathrm{e}^{-\Delta_{\ln r}}$ is attributed to the increasing effect of the smaller pore sizes with decreasing grain size sorting.

The effective hydraulic radius of porous rocks is approximately of the order of the largest present pore radii, which again are determined by the size of the smallest grains (e.g., Kulenkampff, 1994). On the basis of their fractal rock model (Pape et al., 1987), Pape and Schopper (1988) give an empirical relationship between r_{eff}, r_{grain}, and Φ as

$$r_{\text{eff}}^2 \sim \Phi^{5.1/(3-D)}\, r_{\text{grain}}^2 , \tag{2.39}$$

where $D \geq 2$ is the fractal dimension of the pore surface. For consolidated sandstones, Pape et al. (1987) found $D = 2.36$, but it may be smaller for loose sediments with a smoother pore space structure.

Now, provided that the spectral response in complex resistivity measurements exhibits a characteristic time constant τ (in the form of a recognizable phase maximum), from the relations (2.35), i.e., $\tau \sim r_{\text{grain}}^2$, and, for instance, (2.37) and (2.39), a proportionality

$$K \sim \frac{\tau}{F^u} \tag{2.40}$$

---

[12] A recommendable review on different permeability estimation models for sedimentary rocks can be found in Nelson (1994).

is readily deduced. Accordingly, the exponent u depends upon the surface fractal dimension D and the cementation exponent m. Note, however, that D and m are strongly interrelated.

An alternative relationship is analogously obtained when starting from eq. (2.38). Since it is plausible to relate the spread of the grain size distribution to the Cole-Cole exponent c according to $\Delta_{\ln r} \approx 1/c$ (see Appendix A), it results

$$K \sim \frac{\tau}{F^{u'}} \, \mathrm{e}^{-1/c} \, . \tag{2.41}$$

The exponent $u' = 5.1/m < u$ should typically vary between 2.5 and 4 for consolidated and unconsolidated rocks, respectively.

Whereas a proportionality $K \sim F^{-u}$ is well known and numerously reported in the literature (e.g., Schön, 1996), the relation $K \sim \tau$ is in accordance with Pape and Vogelsang (1996). They state that an appropriate characteristic relaxation time, which they derived from the shape of the decay curve in time-domain IP measurements, can be regarded as a measure of the rock's permeability. The additional incorporation of the spread of the grain size distribution via the Cole-Cole exponent, as realized in eq. (2.41), was recently also proposed by Sturrock et al. (1999) with a view to permeability estimation.

Obviously, in addition to the time constant and the frequency exponent, also the formation factor is accessible via complex resistivity measurements. Substitution of the electrolytic conductivity $\sigma_{\mathrm{el}} = \mathrm{Re}(\sigma) - \mathrm{Re}(\sigma_{\mathrm{int}})$ (see Section 2.3.2) into Archie's law (2.8) yields

$$F = \frac{\sigma_{\mathrm{w}} \, S_{\mathrm{w}}^{n}}{\mathrm{Re}(\sigma) - \mathrm{Im}(\sigma)/l} \, , \tag{2.42}$$

which may be evaluated at the frequency ω_{peak}, where the phase maximum occurs[13]. Therefore, by means of the proportionality (2.40) or (2.41), changes in electrically measurable quantities can be related to changes in hydraulic permeability.

As emphasized in the previous paragraph, the fractal microstructure of the pore space may give rise to relatively flat phase spectra, where the adoption of the Cole-Cole model would yield uncertain time constants. In such cases, the spectral IP response should be described by the CPA model (2.15) instead. However, this

[13] Note that the variation in the formation factor (2.42) due to a typical Cole-Cole frequency dependence of σ is, at the most, of the same order as the uncertainty related to the separation of $\mathrm{Re}(\sigma)$ into electrolytic and interfacial contributions by means of the parameter l.

provides another approach for the estimation of hydraulic permeability, suggested by Börner et al. (1996), as outlined below.

Taking the fractal character of the pore surface properly into account, Pape et al. (1987) derived a modified Kozeny-Carman equation, the so-called Paris equation, relating K, F, and the surface area to pore volume ratio, S_{por}, according to

$$K \sim \frac{1}{F\, S_{\text{por}}^{2/(3-D)}}, \tag{2.43}$$

or explicitly for consolidated sedimentary rocks with $D = 2.36$,

$$K = \frac{475}{F\, S_{\text{por}}^{3.1}}, \tag{2.44}$$

provided that K is in darcies and S_{por} in μm^{-1}. For porous sediments with a CPA response, Börner et al. (1996) experimentally found a direct relationship between S_{por} and the imaginary component of conductivity at the reference frequency $\omega_0/2\pi = 1\,\text{Hz}$:

$$S_{\text{por}} = 86\ \text{Im}\big(\sigma(\omega_0)\big), \tag{2.45}$$

where again S_{por} is in μm^{-1}, and σ is in mS/m. Hence, using the modified Kozeny-Carman equation (2.44) together with the equations (2.42), for $\sigma(\omega_0)$, and (2.45), the permeability can be estimated from complex resistivity data.

First applications of the latter approach to field measurements have shown that the electrically determined permeability values compare reasonably well with those obtained from grain size analyses at corresponding rock samples (Börner et al., 1996; Weller and Börner, 1996). However, it seems that a major difficulty in the successful application of the procedures described above is the correct estimation of the surface fractal dimension D (Sturrock et al., 1998 and 1999), which occurs within the exponent of both relations (2.40) and (2.43). Not to mention, of course, the necessity of performing high-quality, accurate complex resistivity measurements over a broad frequency range.

CONTAMINATION PROBLEMS

Olhoeft (1985) suggested the application of the complex resistivity method also to environmental problems such as the characterization of contaminated sites (industrial/municipal landfills, hazardous waste sites, fuel storage sites, etc.). In many situations either inorganic or organic contaminants, or combinations of both, are

present causing measurable changes in the conduction and polarization properties of the ground.[14]

Most inorganic contaminants are soluble and, thus, give rise to an increase of the ion concentration in the subsurface pore water. The corresponding increase of the electrolytic conductivity is mostly distinct enough to be detected by conventional DC resistivity measurements (e.g., Stollar and Roux, 1975; see also the review by Nobes, 1996). The general influence of inorganic contaminants (e.g., chlorides) on complex resistivity spectra of sedimentary rocks is discussed, for instance, in Börner et al. (1993), Vanhala (1996), and Frye et al. (1998). It is of interest to note that the virtual shape of the spectra, however, seems to be rather independent of the pore fluid chemistry.

On the other hand, many organic liquids are immiscible with water[15] and, consequently, constitute an additional, separate phase in the pore space, which principally affects the interfacial electrical properties of the soil or rock (Börner et al., 1993). The resulting change, normally a decrease, in ohmic (in-phase) conductivity is often found to be relatively small and, in particular, may be masked by the much larger effect of inorganics in the case of combined contamination. However, the influence of organic substances on the interfacial polarization processes may result in an IP signature that is accessible by means of complex resistivity measurements. In this way, not only the detection of organic contamination might be possible, but also the distinction between inorganic and organic contaminant constituents.

In order to investigate the electrical effects caused by different types of organic contaminants (organic chemicals, mineral oils) more thoroughly, in the past years many researchers conducted complex resistivity laboratory measurements either on artificially contaminated soil or rock samples or on field samples from contaminated sites. For organic contamination in a clayey environment, Olhoeft (1986) reports an increase of the IP phase shift. Subsequent complex resistivity and infrared spectroscopic measurements on toluene-contaminated montmorillonite samples indicate that this effect is due to the adsorption of organic cations onto the clay surfaces, catalyzing certain polymerization processes (King and Olhoeft, 1989). These clay-organic reactions cause a reduction of the cation exchange capacity, resulting in an increased conductivity phase angle. Vanhala et al. (1992) describe spectral IP effects caused by toluene, heptane, and ethylene glycol in glacial tills. They conclude that the underlying electrochemical reactions may be of similar nature as in clay environments. Börner et al. (1993) conducted complex resistivity measurements on clean and organic-contaminated clay and sandstone samples. Whereas, accordingly, oil

---

[14] A comprehensive classification of soil and ground-water contaminants as well as the various sources of contamination can be found in Yong et al. (1992) and Fetter (1999).

[15] Such contaminants are referred to as non-aqueous phase liquids (NAPLs).

causes an increase of IP amplitude in clays (qualitatively similar to Olhoeft's results), in sandstones the opposite effect is observed. However, the resistivity spectra of benzene-contaminated sandstones again exhibit an increase of phase lag. Soininen and Vanhala (1996) as well as Vanhala (1997) investigate the effect of waste and motor oil on the phase spectrum of glacial sediments (sands, tills). Compared to the clean samples, in general, the oil-contaminated samples show a weaker IP response. An explanation could be that the oil detaches ions from the particle surfaces to the electrolyte (Vanhala, 1997).

Although various published results differ in the observed effects from those mentioned above, particularly with respect to organic-contaminated field sites (e.g., Towle et al., 1985; de Lima and Araujo, 1996), all investigations proved the fact, that the spectral IP response of soils and rocks is measurably influenced by both inorganic and organic contamination. However, it must be emphasized that the utilization of the SIP method in contamination field studies essentially depends upon the natural IP variations present in the ground. Since, in addition, many organic contaminant plumes change with time due to a variety of processes (e.g., volatilization, biodegradation, reactions between contaminant constituents) (Olhoeft, 1992), in practice, the detection, delineation, migration monitoring, or characterization of subsurface contamination might be a complicated task.

2.7 DISCUSSION AND CONCLUSIONS

In the previous sections the principles of complex resistivity phenomena in rocks, aspects related to their description by geophysical measurements and, finally, possibilities for their utilization to investigate structural characteristics of the subsurface, either in mineral exploration, or for hydrogeological and environmental purposes, were discussed. The general usefulness of conventional IP measurements for the characterization of the earth's electrical properties, as a complement to standard DC resistivity surveys, has been recognized for a long time. However, the investigation of the spectral IP behavior, at first in mineralized rocks, occurred after the adequate improvement of measurement technology in the seventies; a development forced by the mineral industry at that time. The capability of performing phase measurements with an accuracy of less than 1 mrad for frequencies below 1 kHz (e.g., Olhoeft, 1985; Vanhala and Soininen, 1995) also built the basis for the subsequent application of the SIP method in sedimentary environments, involving much weaker IP responses, starting from the middle of the eighties.

To date, investigations on samples in the laboratory have still been in the foreground, with researchers concentrating on the actual connection between intrinsic structural characteristics and the resulting spectral IP signature to prove the general

applicability of the method with respect to source characterization and discrimination; i.e., addressing the question "*what* is causing the observations?". In this context, the pioneering work of Olhoeft (1985) must be mentioned. He demonstrated that the different principal electrochemical processes responsible for the observed effects in the various applications are basically distinguishable from their complex resistivity spectra. These water-mineral interactions include oxidation-reduction reactions in the presence of electronic conducting minerals, ion-exchange reactions involving clay or zeolite minerals, and reactions involving organic materials (particularly clay-organic reactions).

In addition to source characterization, however, the interpretation of geophysical field data involves the requirement of spatial localization and delineation of corresponding objects or structural features within the subsurface; i.e., the question "*where* is the origin of the observed effects?" needs to be addressed. In field surveys where certain a-priori information about the nature of the geophysical target, and hence the cause of the observations, is available anyway, the question of geometrical assignment might even be of major importance. Complex resistivity field measurements, first of all, do only provide apparent values of the electrical quantities of interest. Since these do not directly reflect the true, intrinsic subsurface conditions, but represent averaged (and often highly distorted) values from a large underground volume (depending on the measurement geometry, the electrode configuration, and the electrical properties of the underground itself), it is generally desirable to determine the underlying complex resistivity distribution from the observations by means of numerical inversion techniques.

So far, the application of the SIP method to field studies has been mainly limited to either the interpretation of spectral parameters in terms of simple pseudosections (e.g., Seigel et al., 1997), the inversion of mere time-domain chargeability (e.g., Oldenburg and Li, 1994), or the inversion of spectral parameters on the basis of simple, rigid underground models, for instance described by one or two polarizable targets in a homogeneous background medium (e.g., Luo and Zhang, 1998). Whereas sophisticated inversion schemes have been developed in recent years to image the subsurface distribution of conventional DC resistivity, there is still a lack of similar tools for the inversion of spectral complex resistivity (Ward et al., 1995).

For this reason, the main objective within the scope of this thesis was the development of an appropriate complex resistivity inversion algorithm which is, first, capable of handling finely parameterized underground models (a requirement to enable the representation of basically arbitrary distributions of complex resistivity) and, second, suitable to be applied to spectral (i.e., frequency-domain) complex resistivity field data. Such an inversion procedure obviously provides the possibility to utilize the relations between electrical and petrophysical parameters proven in the laboratory also at the field scale. It thus enables access to both key issues outlined above, *geometrical* origin and *structural* cause of the observations, and is therefore of

considerable importance for the interpretation of complex resistivity field measurements in any practical application.

The theory of both the corresponding forward modeling and the actual inverse solution, as the two inherent components of any inversion scheme, are presented in the next chapter.

3 MODELING AND INVERSION THEORY

3.1 INTRODUCTION

Modern resistivity inversion algorithms are usually characterized by a fine and regular parameterization of the earth into a relatively large number of pixels. This allows the representation of basically arbitrary distributions of resistivity by assigning each pixel an individual resistivity value. In order to overcome the difficulties with respect to ill-posedness and nonuniqueness inherent in large-scale, underdetermined resistivity inverse problems, the resulting system of equations must be regularized by additional constraints. This requirement is normally accomplished by solving the system as an optimization problem, where a given model objective function (e.g., the model roughness) is minimized subject to adequately satisfying the data.

Following the terminology in other scientific disciplines dealing with image reconstruction, such finely parameterized resistivity inversion schemes are now customarily referred to as *tomographic*, especially when the underlying electrode setup is designed to surround the target as much as possible, as for example in crosshole arrangements. Accordingly, the whole methodology comprising both specific data acquisition and processing is often shortly referred to as electrical resistivity tomography (ERT). However, when using these terms one should bear in mind that the data in geoelectrical surveys, as inherent in any potential method, are more or less influenced by the entire space and, by far, do not represent simple projections along raypaths as it is assumed in the classic tomographic sense.

As outlined at the end of the previous chapter, the complex resistivity method for geophysical investigations at the field scale still lacks of appropriate inversion tools. Although a few approaches to the subject do exist in the geophysical literature, most of them have certain restrictions regarding a flexible, tomographic model parameterization and regularization on the one hand, or the descriptive IP quantity being used within the inversion on the other hand. In the following, the basic concepts of the IP inversion algorithms published so far shall be briefly reviewed in order to point out their respective limitations.

3.1.1 REVIEW OF IP INVERSION APPROACHES

Most previous algorithms for the inversion of IP data make use of Seigel's formulation to model the IP effect in terms of chargeability. Accordingly, the presence of a polarizable body with intrinsic chargeability m ultimately gives rise to a decreased effective conductivity $\sigma_{ip} = (1-m)\sigma_{dc}$, where σ_{dc} is the original DC (i.e., real-valued) conductivity (Seigel, 1959). From the definition of chargeability in eq. (2.19) it is easily shown that any observed apparent chargeability m_a can then be computed by two separate, conventional DC forward modelings applied to both original and altered conductivity distribution according to

$$m_a = \frac{f_{dc}(\sigma_{ip}) - f_{dc}(\sigma_{dc})}{f_{dc}(\sigma_{ip})}, \tag{3.1}$$

where f_{dc} represents the forward mapping operator. For a given parameterization of the earth into M cells or blocks with intrinsic DC conductivity $\sigma_{dc\,j}$ and chargeability m_j, the linearization of eq. (3.1) yields (Seigel, 1959)

$$m_a \approx \sum_{j=1}^{M} \frac{\partial \ln \sigma_{dc\,a}}{\partial \ln \sigma_{dc\,j}} m_j , \tag{3.2}$$

where $\sigma_{dc\,a}$ denotes the observed, real-valued apparent conductivity corresponding to m_a. The determination of chargeability by means of eq. (3.2), also referred to as perturbation technique, requires the a-priori knowledge of the underlying conductivity distribution. As a consequence, IP inversion algorithms that are based on this technique inevitably work in two steps. Firstly, a pure nonlinear DC resistivity inversion is carried out, and subsequently, a linear, single-step inversion is performed to obtain the intrinsic chargeabilities from eq. (3.2).

The fact that the perturbation technique requires only a simple DC modeling routine was responsible for its implementation in an early, Marquardt-type IP inversion scheme by Pelton et al. (1978b).[1] However, due to the lack of today's computer facilities and performance, they used precomputed resistivity pseudosections to model apparent chargeability values. Therefore, their algorithm was basically restricted to simple prism models and surface electrode arrays.

It was not before the early nineties that LaBrecque (1991) implemented the perturbation approach within a smoothness-constrained (Occam's style) tomographic IP inversion algorithm, which allows both a much finer model space parameterization as well as the use of borehole electrodes. In particular, the algorithm was applied to

[1] Unless otherwise stated, all modeling and inversion algorithms quoted in this section presume 2D underground models.

crosshole data from controlled experiments in a sediment-filled test basin in order to investigate fluid flow in the unsaturated zone (Schima et al., 1993). A similar IP inversion scheme was presented by Iseki and Shima (1992). They applied it to real crosshole field data and, by this, demonstrated the efficiency of combined resistivity and IP tomography for the characterization of oil reservoirs. Subsequent applications include the mapping of an active fault from surface IP measurements (Hasegawa et al., 1996).

Many computational aspects related to the inversion of chargeability by means of the perturbation technique were investigated in detail by Oldenburg and Li (1994). They designed a more general and flexible model objective function to be minimized, which allows an easy incorporation of any additional (e.g., geological) information or bias towards certain model characteristics. Moreover, they compared three different procedures to implement Seigel's IP formulation within the inversion process. These range from using the simplified relationship (3.2) in a linear inverse problem, to a full nonlinear inversion directly based on eq. (3.1). Comprehensive case histories comprising the application of their algorithm to surface field data can be found in Yuval and Oldenburg (1996) and Oldenburg et al. (1997). Recently, Li and Oldenburg (1997) extended the inversion code from 2D to 3D and, in addition, studied the joint use of surface and borehole data.

Finally, Beard et al. (1996) realized a relatively fast IP inversion algorithm, again based on the linear relation (3.2), by implementing a low-contrast approximation to efficiently solve the DC forward problem.

The fundamental restriction of all these approaches with respect to the concept of complex resistivity is their formulation in chargeability. Obviously, this single time-domain parameter, describing exclusively the voltage drop at the time of current shut-down, does not allow the extraction of any spectral information on the IP response. Strictly speaking, it is not even a quantity actually delivered by any conventional IP measurement. Also the crude application of the perturbation technique to complex resistivity data is not plausible from a theoretical point of view. For instance, it does in no way account for the inherent coupling of magnitude and phase, i.e., of conduction and polarization, as expressed in the underlying physical relationship described by eq. (2.7).

An obvious approach to overcome the above-mentioned restrictions is to start directly from eq. (2.7) to model magnitude and phase of apparent complex resistivity on the basis of an entirely complex-valued arithmetic. Such a modeling algorithm provides exactly those quantities that are actually being measured in the frequency domain and, in particular, takes the inherent coupling of magnitude and phase as a complex number properly into account.

This approach was first suggested by Weller et al. (1996a), who implemented it within a finite-difference modeling code, which again was integrated into a tomographic inversion scheme (Weller et al., 1996b). However, though the complex modeling technique is supposed to be more adequate for the interpretation of complex resistivity data than the perturbation technique, the inversion approach by Weller et al. (1996b) still lacks several important achievements of today's inversion theory. They adopted the simultaneous iterative reconstruction technique (SIRT), which was originally developed for linear tomographic problems like X-ray imaging. Although, in general, numerically stable and converging to some reasonable model also in the nonlinear resistivity case, SIRT offers no possibilities to bias the inversion process towards certain model characteristics, i.e., it allows no controlled regularization. Furthermore, its flexibility regarding an incorporation of individual data weighting terms, a fundamental requirement to handle noisy field data, is limited. The application of the complex SIRT algorithm to single-frequency data measured in an experimental tank yielded only unconvincing images of resistivity phase, which were not used for any further interpretation (Weller et al., 1996b). As Weller et al. (1996b) state, a probable reason was the insufficient electrical isolation of the tank's metal casing, affecting many of the phase measurements.

To round off the review of documented IP inversion approaches, the recent work of Daily et al. (1998) must be mentioned. They conducted spectral IP measurements in a crosshole experiment to monitor the migration of a free product, dense non-aqueous phase liquid (DNAPL) contamination within a sandy environment. They obtained tomographic images of the spectral variation in resistivity magnitude by inverting a frequency-effect-type quantity, which permits the application of a DC inversion algorithm. However, in terms of mapping spectral characteristics in the electrical signature of the contaminant plume their attempt was of limited success since, unfortunately, the actual frequency dispersion was of the same order as the measurement accuracy (Daily et al., 1998).

3.1.2 CONCLUSION

The preceding discussion on currently available IP inversion schemes manifests the lack of an appropriate algorithm adopting the concepts of modern inversion theory for the tomographic interpretation of complex resistivity measurements. In this thesis an attempt is made to close this gap by combining the respective advantages of the different approaches proposed so far within a newly developed inversion algorithm.

The basis of the algorithm is the direct modeling of apparent complex resistivity in the frequency domain via the use of complex arithmetic. In contrast to, for instance, the finite-difference implementation by Weller et al. (1996a), the finite-element technique is chosen here, because of its inherent advantages with respect to a flexible model discretization (e.g., easy incorporation of topography, irregular electrode

positions). Furthermore, a flexible, efficient, and robust regularized inversion scheme, which has been extensively applied and continuously improved in various DC resistivity inversion codes (e.g., Oldenburg et al., 1993; LaBrecque et al., 1996a), is adapted and extended to the use of complex-valued parameters and data, in order to solve the inverse problem directly for complex, frequency-domain resistivity. An inherent benefit of such an approach is that it yields both resistivity magnitude and phase simultaneously by running a single complex inversion.

It may be noted that the general concept of the complex resistivity inversion was already published in Kemna and Binley (1996) in association with this thesis.

Before the various aspects related to the solution of the complex inverse problem are addressed in Section 3.3, in Section 3.2 the solution of the corresponding forward problem by means of the finite-element technique is presented.

3.2 FORWARD PROBLEM

For the solution of the resistivity forward problem in 2D or 3D environments there exist various numerical techniques like the integral-equation method, the finite-difference method, or the finite-element (FE) method. A comprehensive overview of this matter can be found in Hohmann (1988). The FE technique is usually preferred if a great flexibility with respect to the geometrical shape of topography, interfaces, or other geological structures as well as the source and receiver locations is desired. Since within this thesis the general applicability of the developed inversion algorithm to nearly arbitrary geological structures and electrode arrangements is considered as one of the major objectives, the FE method has been chosen.

In the following sections the FE method is adapted to the modeling of complex electric potentials as a part of the complex resistivity inversion scheme. However, two basic assumptions are made in order to substantially reduce the overall computational expense.

First, for the purpose of this thesis it is assumed that the region of interest may be represented as a 2D complex resistivity distribution. In practice, 3D data processing also requires specific 3D data acquisition, which involves a comparatively large amount of field work and thus considerable costs. Therefore, today many surveys are still performed along 2D sections and approximate 3D images are rather created by interpolating between several parallel 2D lines (e.g., Dahlin and Loke, 1997). The limitations of a 2D approach depend upon the actual strike length of the geophysical target. However, the electrical response of a body only a few times as long in the strike direction as extended within the considered plane may be already equivalent to that of a 2D body (e.g., Hohmann, 1990), justifying 2D modeling and inversion in many

situations (e.g., LaBrecque et al., 1996b). Of course, the presented forward and inverse problem solutions might be analogously extended to 3D applications.

Second, because of the tremendous numerical simplification within the forward modeling, all inductive effects are assumed to be negligibly small, i.e., for the magnetic induction $\mathbf{B}$ the fundamental assumption

$$\partial_t \mathbf{B} = 0 \tag{3.3}$$

is made. This consequently implies that either the considered frequencies are sufficiently low or, at least, that any inductive coupling response is removed from the complex resistivity data prior to inversion using appropriate removal techniques. The latter issue is addressed in more detail within Chapter 5, dealing with true field data.

3.2.1 BASIC EQUATIONS

From eq. (3.3) directly follows that (in the absence of magnetic sources) the electric field is curl-free and thus can be written as $\mathbf{E} = -\nabla\phi$, with a scalar complex potential ϕ. Therefore, eq. (2.7) ultimately becomes the well-known Poisson equation

$$\nabla \cdot \big(\sigma(\omega)\nabla\phi(\omega)\big) - \nabla \cdot \mathbf{j}_s(\omega) = 0\,. \tag{3.4}$$

Note that although formally equivalent to the conventional DC resistivity problem, eq. (3.4) is actually evaluated at a certain frequency ω. However, the explicit notation of this frequency dependence is being dropped in the following for simplicity.

Since any particular electrode configuration can be realized via appropriate superposition, here only a single electrode current source needs to be considered. This shall be represented as a point source at $\mathbf{r}_s = (x_s, y_s, z_s)$, i.e.,

$$\nabla \cdot \mathbf{j}_s = -I\,\delta(\mathbf{r} - \mathbf{r}_s)\,. \tag{3.5}$$

By convention, a real (zero-phase) current I and $y_s = 0$ is assumed.

Even for a 2D complex conductivity distribution $\sigma(x,z)$, the electric potential $\phi(x,y,z)$ due to a point source is 3D. However, the problem can be reduced to pure two dimensions by transformation into the wavenumber domain with respect to the strike direction y. Since $\phi(x,y,z)$ is even in y, this may be performed by the simple Fourier cosine transform

$$\tilde{\phi}(x,k,z) = 2\int_0^\infty \phi(x,y,z)\cos(ky)\,dy\,, \tag{3.6}$$

where $\tilde{\phi}$ and k are, respectively, transformed complex potential and real wavenumber. Now, application of the transform (3.6) to Poisson's equation (3.4) with source term (3.5) results in the 2D Helmholtz equation (e.g., Hohmann, 1988)

$$\partial_x\left(\sigma\partial_x\tilde{\phi}\right)+\partial_z\left(\sigma\partial_z\tilde{\phi}\right)-\sigma k^2\,\tilde{\phi}+I\,\delta(x-x_\mathrm{s})\,\delta(z-z_\mathrm{s})=0\,, \tag{3.7}$$

which has to be solved for given boundary conditions

$$\sigma\partial_n\tilde{\phi}+\beta\,\tilde{\phi}=0\,, \tag{3.8}$$

where n denotes the outward normal and the complex parameter β defines the type of boundary condition. Once the potentials $\tilde{\phi}(x,k,z)$ are calculated for a range of discrete k values, the inverse Fourier transform

$$\phi(x,y,z)=\frac{1}{\pi}\int_0^\infty\tilde{\phi}(x,k,z)\cos(ky)\,dk \tag{3.9}$$

is applied to get $\phi(\mathbf{r})$.

3.2.2 BOUNDARY CONDITIONS

ERT surveys are generally conducted from both the earth's surface and boreholes, defining a vertical 2D plane. The corresponding model geometry is characterized by homogeneous Neumann boundary conditions, i.e., $\beta=0$, at the surface (no current flow in the normal direction) and mixed boundary conditions, i.e., $\beta\neq0$, at those boundaries confining the considered region within the half-space (see Figure 3.1 in Section 3.2.4). In the following, these two types are referred to as *surface* and *half-space* boundaries, respectively.

Due to their much easier implementation, most early resistivity modeling algorithms impose homogeneous Dirichlet conditions on the half-space boundaries, i.e., $\tilde{\phi}=0$ (corresponding to $|\beta|=\infty$). This consequently requires the usage of large modeling grids, extending far to sides and depth from the actual region of interest, in order to keep related modeling errors at an acceptable level. However, here an approach first suggested by Dey and Morrison (1979) is used instead, where an adequate, finite value for β on the half-space boundaries is determined via the asymptotic behavior of the potential for a homogeneous half-space. Such a mixed (or asymptotic) boundary condition enables the usage of comparatively small grids and, thus, reduces the overall computational requirements for the modeling.

For a point source in a homogeneous half-space with complex conductivity σ_0, the analytic solution of the 2D Helmholtz equation (3.7) in the source-free region is

$$\tilde{\phi}_\mathrm{p}=\frac{I}{2\pi\sigma_0}\left(\mathrm{K}_0(kr_-)+\mathrm{K}_0(kr_+)\right), \tag{3.10}$$

where K_0 denotes the modified Bessel function of order zero. In eq. (3.10), r_- and r_+, the radial distances from any point to the source and its image (in the case $z_\mathrm{s} \neq 0$), respectively, are given by

$$r_- = \sqrt{(x - x_\mathrm{s})^2 + (z - z_\mathrm{s})^2}\ ,\ r_+ = \sqrt{(x - x_\mathrm{s})^2 + (z + z_\mathrm{s})^2}\ . \tag{3.11}$$

Assuming now, in a first approximation, also for the inhomogeneous case $\sigma(x,z)$ an asymptotic behavior of the transformed potential on the half-space boundaries according to

$$|\widetilde{\phi}| \sim \left(\mathrm{K}_0(kr_-) + \mathrm{K}_0(kr_+)\right), \tag{3.12}$$

from the condition (3.8), an expression for the boundary parameter β can be easily derived using the derivative property of the modified Bessel function. It results

$$\beta = \sigma k\, g\ , \tag{3.13}$$

with the real factor

$$g = \frac{\mathrm{K}_1(kr_-)\,\partial_n r_- + \mathrm{K}_1(kr_+)\,\partial_n r_+}{\mathrm{K}_0(kr_-) + \mathrm{K}_0(kr_+)}\ . \tag{3.14}$$

In eq. (3.14), K_1 is the modified Bessel function of first order.

3.2.3 SINGULARITY REMOVAL

It is obvious that an accurate numerical solution of the partial differential equation (3.7) near the source is problematic because of the singularity of the delta function. However, the singularity may be removed (e.g., Lowry et al., 1989) by splitting the transformed potential into *primary* and *secondary* parts according to

$$\widetilde{\phi} = \widetilde{\phi}_\mathrm{p} + \widetilde{\phi}_\mathrm{s}\ , \tag{3.15}$$

where $\widetilde{\phi}_\mathrm{p}$ is the analytic solution for a homogeneous half-space σ_0, given in eq. (3.10). The secondary potential $\widetilde{\phi}_\mathrm{s}$ describes the perturbation of the primary potential $\widetilde{\phi}_\mathrm{p}$ due to inhomogeneities within the conductivity distribution.

The Helmholtz equation corresponding to mere $\widetilde{\phi}_\mathrm{p}$ is

$$\partial_x\left(\sigma_0\,\partial_x\widetilde{\phi}_\mathrm{p}\right) + \partial_z\left(\sigma_0\,\partial_z\widetilde{\phi}_\mathrm{p}\right) - \sigma_0\,k^2\,\widetilde{\phi}_\mathrm{p} + I\,\delta(x - x_\mathrm{s})\,\delta(z - z_\mathrm{s}) = 0\ , \tag{3.16}$$

with boundary conditions

$$\sigma_0\,\partial_n\widetilde{\phi}_\mathrm{p} + \beta_0\,\widetilde{\phi}_\mathrm{p} = 0\ . \tag{3.17}$$

Now, subtracting eq. (3.16) from eq. (3.7) and subsequently substituting eq. (3.15) results in a new Helmholtz equation for the secondary potential $\tilde{\phi}_s$:

$$\partial_x\left(\sigma\partial_x\tilde{\phi}_s\right)+\partial_z\left(\sigma\partial_z\tilde{\phi}_s\right)-\sigma k^2\tilde{\phi}_s+\partial_x\left(\Delta\sigma\partial_x\tilde{\phi}_p\right)+\partial_z\left(\Delta\sigma\partial_z\tilde{\phi}_p\right)-\Delta\sigma k^2\tilde{\phi}_p=0\,, \tag{3.18}$$

with $\Delta\sigma=\sigma-\sigma_0$. Because of eq. (3.13) and hence also $\beta_0=\sigma_0 k g$, the new boundary conditions

$$\sigma\partial_n\tilde{\phi}_s+\beta\tilde{\phi}_s=0 \tag{3.19}$$

are directly found from the equations (3.8), (3.15), and (3.17). Note that eq. (3.19) has exactly the same form as the original boundary condition (3.8).

The advantage of solving the modified differential equation (3.18) for $\tilde{\phi}_s$ instead of the original equation (3.7) for $\tilde{\phi}$ lies in the fact that the delta function has been replaced by a new source term containing only the primary potential $\tilde{\phi}_p$, which can be calculated analytically. This singularity removal prevents comparatively large errors in the numerical solution of the differential equation near the electrodes (e.g., Lowry et al., 1989). Once eq. (3.18) is solved, the sought total potential $\tilde{\phi}$ is found again from eqs. (3.15) and (3.10).

3.2.4 NUMERICAL SOLUTION BY FINITE-ELEMENT METHOD

In this section the linear FE equations for the solution of the complex Helmholtz equation (3.18) subject to the boundary conditions (3.19) are derived. Besides the generalization to complex arithmetic, the presented derivation differs from previously published resistivity FE modelings (Coggon, 1971; Rijo, 1977; Pridmore et al., 1981; Queralt et al., 1991) since it takes explicitly mixed boundary conditions and singularity removal into account.

A common approach to solve problems by means of finite elements is the variational method. It starts with the equivalent formulation of the underlying partial differential equation as a variational stationarity problem by means of some variational principle. Pridmore et al. (1981) and Jin (1993) formulated a generalized variational principle that is applicable to problems involving complex operators (like, e.g., the electromagnetic problem). Adopting this for the complex resistivity problem, it is easily shown that the sought solution $\tilde{\phi}_s$ of eq. (3.18), subject to eq. (3.19), makes the complex functional

$$\mathrm{F} = \iint_A \left\{ \tfrac{1}{2}\sigma\left[\left(\partial_x \widetilde{\phi}_\mathrm{s}\right)^2 + \left(\partial_z \widetilde{\phi}_\mathrm{s}\right)^2\right] + \tfrac{1}{2}\sigma k^2 \widetilde{\phi}_\mathrm{s}^2 \right.$$
$$\left. - \left[\partial_x\left(\Delta\sigma\,\partial_x \widetilde{\phi}_\mathrm{p}\right) + \partial_z\left(\Delta\sigma\,\partial_z \widetilde{\phi}_\mathrm{p}\right) - \Delta\sigma k^2 \widetilde{\phi}_\mathrm{p}\right] \widetilde{\phi}_\mathrm{s} \right\} dx dz + \oint_C \tfrac{1}{2}\beta \widetilde{\phi}_\mathrm{s}^2 \, ds \tag{3.20}$$

stationary. In eq. (3.20), A and C are the considered region in the x,z-plane and its boundary (with arc length s), respectively. Note that for the complex problem, the stationarity requirement $\delta\mathrm{F} = 0$ cannot directly correspond to the minimization of a physical quantity (e.g., the energy) as it is true in the real case (Coggon, 1971).

After discretization into N_e finite elements A_j with constant complex conductivity σ_j and N_b finite boundary elements C_j with constant complex parameter β_j (see Figure 3.1), the functional (3.20) can be written as (see Appendix B)

$$\mathrm{F} = \sum_{j=1}^{N_\mathrm{e}} \left\{ \tfrac{1}{2}\sigma_j \iint_{A_j} \left[\left(\partial_x \widetilde{\phi}_\mathrm{s}\right)^2 + \left(\partial_z \widetilde{\phi}_\mathrm{s}\right)^2\right] dx dz + \tfrac{1}{2}\sigma_j k^2 \iint_{A_j} \widetilde{\phi}_\mathrm{s}^2 \, dx dz \right.$$
$$\left. + \Delta\sigma_j \iint_{A_j} \left[\left(\partial_x \widetilde{\phi}_\mathrm{p}\right)\left(\partial_x \widetilde{\phi}_\mathrm{s}\right) + \left(\partial_z \widetilde{\phi}_\mathrm{p}\right)\left(\partial_z \widetilde{\phi}_\mathrm{s}\right)\right] dx dz + \Delta\sigma_j k^2 \iint_{A_j} \widetilde{\phi}_\mathrm{p}\, \widetilde{\phi}_\mathrm{s} \, dx dz \right\} \tag{3.21}$$
$$+ \sum_{j=1}^{N_\mathrm{b}} \left(\tfrac{1}{2}\beta_j \int_{C_j} \widetilde{\phi}_\mathrm{s}^2 \, ds + \Delta\beta_j \int_{C_j} \widetilde{\phi}_\mathrm{p}\, \widetilde{\phi}_\mathrm{s} \, ds \right),$$

with $\Delta\sigma_j = \sigma_j - \sigma_0$ and $\Delta\beta_j = \beta_j - \sigma_0 k g_j$, where g_j is the real factor given in eq. (3.14), evaluated at the middle of the respective boundary element. A reasonable value for the complex reference conductivity σ_0 can be obtained from the mean of the elements' log conductivities weighted according to the element size.

At the earth's surface the homogeneous Neumann boundary condition $\beta_j = 0$ is applied. For the half-space boundary elements a mixed condition $\beta_j = \sigma_{\kappa j} k g_j$ according to eq. (3.13) is imposed, where $\sigma_{\kappa j}$ is the conductivity of the κ_j-th domain element adjacent to the j-th boundary element.

Within each element a linear approximation of the function $\widetilde{\phi}_\mathrm{s}$, determined by the values at its nodes $\widetilde{\phi}_{\mathrm{s}i}$, is used. Thus, the continuous distribution $\widetilde{\phi}_\mathrm{s}(x,k,z)$ is replaced by the approximate discrete solution $\widetilde{\Phi}_\mathrm{s} = \left(\widetilde{\phi}_{\mathrm{s}1}(k), \ldots, \widetilde{\phi}_{\mathrm{s}N_n}(k)\right)^\mathrm{T}$, with N_n as the total number of nodes. For the primary potential $\widetilde{\phi}_\mathrm{p}(x,k,z)$ the same discretization is adopted, defining the discrete vector $\widetilde{\Phi}_\mathrm{p} = \left(\widetilde{\phi}_{\mathrm{p}1}(k), \ldots, \widetilde{\phi}_{\mathrm{p}N_n}(k)\right)^\mathrm{T}$.

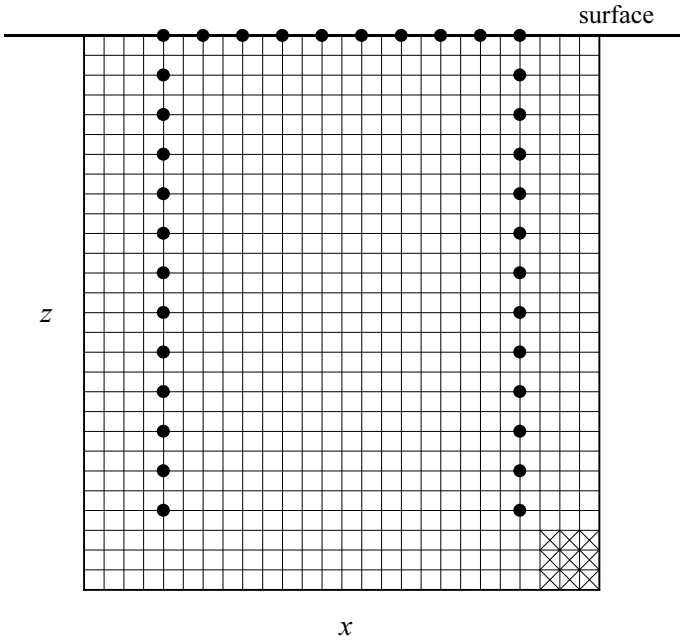

Figure 3.1: Example of a finite-element mesh as being used within this thesis for a typical ERT geometry with both surface and borehole electrodes (indicated by the solid circles). Whereas each rectangular cell represents an area of constant conductivity, the actual elemental discretization within each cell is indicated in the bottom right corner of the grid.

Taking the discretization of the transformed potential into account, the individual integrals occurring in the functional (3.21) can be evaluated analytically, yielding quadratic forms analogous to the corresponding real-valued problem (see, e.g., Schwarz, 1991). These contributions to the total integral are expressed via real, symmetric $N_\mathrm{n} \times N_\mathrm{n}$ matrices $\mathbf{S}_{1j}, \mathbf{S}_{2j}, \mathbf{S}_{3j}$, commonly known as element matrices,[2] i.e.,

$$\begin{aligned} \mathrm{F} = \sum_{j=1}^{N_\mathrm{e}} \Big(& \tfrac{1}{2}\sigma_j \, \widetilde{\Phi}_\mathrm{s}^\mathrm{T} \, \mathbf{S}_{1j} \, \widetilde{\Phi}_\mathrm{s} + \tfrac{1}{2}\sigma_j \, k^2 \, \widetilde{\Phi}_\mathrm{s}^\mathrm{T} \, \mathbf{S}_{2j} \, \widetilde{\Phi}_\mathrm{s} + \Delta\sigma_j \, \widetilde{\Phi}_\mathrm{p}^\mathrm{T} \, \mathbf{S}_{1j} \, \widetilde{\Phi}_\mathrm{s} \\ & + \Delta\sigma_j \, k^2 \, \widetilde{\Phi}_\mathrm{p}^\mathrm{T} \, \mathbf{S}_{2j} \, \widetilde{\Phi}_\mathrm{s} \Big) + \sum_{j=1}^{N_\mathrm{b}} \Big(\tfrac{1}{2}\beta_j \, \widetilde{\Phi}_\mathrm{s}^\mathrm{T} \, \mathbf{S}_{3j} \, \widetilde{\Phi}_\mathrm{s} + \Delta\beta_j \, \widetilde{\Phi}_\mathrm{p}^\mathrm{T} \, \mathbf{S}_{3j} \, \widetilde{\Phi}_\mathrm{s} \Big). \end{aligned} \tag{3.22}$$

Finally, applying the stationarity requirement $\delta\mathrm{F} = 0$ yields the complex linear system of equations

$$\mathbf{S} \, \widetilde{\Phi}_\mathrm{s} = \mathbf{b} \,, \tag{3.23}$$

---

[2] The individual element matrices for the complex resistivity problem are exactly the same as for the corresponding real problem. Their explicit form, as being used within this thesis, is given in Kemna (1995).

with the symmetric (i.e., nonhermitian), diagonally dominant, and sparse FE matrix

$$\mathbf{S} = \sum_{j=1}^{N_\mathrm{e}} \sigma_j \left(\mathbf{S}_{1j} + k^2 \mathbf{S}_{2j} \right) + \sum_{j=1}^{N_\mathrm{b}} \beta_j \mathbf{S}_{3j} \tag{3.24}$$

and the right-hand side vector

$$\mathbf{b} = -\left[\sum_{j=1}^{N_\mathrm{e}} \Delta\sigma_j \left(\mathbf{S}_{1j} + k^2 \mathbf{S}_{2j} \right) + \sum_{j=1}^{N_\mathrm{b}} \Delta\beta_j \mathbf{S}_{3j} \right] \widetilde{\Phi}_\mathrm{p} \,. \tag{3.25}$$

The above system of equations is solved by means of a complex version of the Cholesky decomposition

$$\mathbf{S} = \mathbf{L}\,\mathbf{L}^\mathrm{T} \,, \tag{3.26}$$

where $\mathbf{L}$ is a complex lower triangular matrix. Obviously, the solution is then easily obtained from the equations

$$\mathbf{L}\,\mathbf{c} = \mathbf{b} \,, \;\; \mathbf{L}^\mathrm{T}\,\widetilde{\Phi}_\mathrm{s} = \mathbf{c} \tag{3.27}$$

by forward and backward substitution, respectively. In this thesis, an efficient and stable numerical implementation of the Cholesky algorithm according to Schwarz (1991) is used, which particularly exploits the banded structure of the FE matrix $\mathbf{S}$.

3.2.5 SENSITIVITY COMPUTATION

Like within any inversion algorithm making use of gradient information, the partial derivatives with respect to the model parameters, the so-called sensitivities, must be known. A very efficient and therefore common approach to compute sensitivities in resistivity and electromagnetic inversion problems is based on the principle of reciprocity (for the latter it is referred to, e.g., Geselowitz, 1971 and Tripp et al., 1984). Independent of the number of model parameters, it requires the successive solution of the forward problem for individual sources at each receiver position being involved in the underlying data set. However, in ERT applications, where every electrode acts as both current injection point and potential measurement point, the forward problem has to be solved for each electrode position anyway and, hence, sensitivities can be obtained with little extra effort.

Within this thesis the model parameters are represented by the complex conductivities of the different finite elements. Consequently, unlike in real-valued inversion problems, here the derivatives of complex functions with respect to complex numbers are of interest, i.e., the sensitivities themselves become complex.

An elegant way of deriving an appropriate sensitivity expression via reciprocity starts directly from the linear FE equations (e.g., Rodi, 1976; Oristaglio and Worthington, 1980). Substituting eqs. (3.24) and (3.25) into the matrix equation (3.23) and subsequently taking the derivative with respect to the complex conductivity of the j-th domain element, it is easily shown that

$$\mathbf{S}\,\frac{\partial\widetilde{\Phi}}{\partial\sigma_j} = -\left(\mathbf{S}_{1j} + k^2\,\mathbf{S}_{2j}\right)\widetilde{\Phi}\,. \tag{3.28}$$

Note that although the boundary-element parameters β_j in the expression (3.24) may be determined with the help of the conductivity values of the respective adjacent cells, virtually, they must not be considered as domain-element parameters. Therefore, the derivative $\partial\mathbf{S}/\partial\sigma_j$ within the right-hand side of eq. (3.28) includes no contribution on this account.

A further remark on the general complex differentiability of the discrete complex potential values in $\widetilde{\Phi}$ may be added. Obviously, from eq. (3.24), it is $\partial\mathbf{S}/\partial\mathrm{Im}(\sigma_j) = \mathrm{i}\,\partial\mathbf{S}/\partial\mathrm{Re}(\sigma_j)$. Hence, from eq. (3.28), it is readily seen that each function $\widetilde{\phi}_i(\sigma_j)$ fulfills the Cauchy-Riemann conditions

$$\frac{\partial\,\mathrm{Re}(\widetilde{\phi}_i)}{\partial\,\mathrm{Re}(\sigma_j)} = \frac{\partial\,\mathrm{Im}(\widetilde{\phi}_i)}{\partial\,\mathrm{Im}(\sigma_j)}\,,\quad \frac{\partial\,\mathrm{Im}(\widetilde{\phi}_i)}{\partial\,\mathrm{Re}(\sigma_j)} = -\frac{\partial\,\mathrm{Re}(\widetilde{\phi}_i)}{\partial\,\mathrm{Im}(\sigma_j)} \tag{3.29}$$

and, thus, is actually analytic (i.e., complex differentiable).

From the analogy of eq. (3.28) with the original FE matrix equation for the (total) potential, the sensitivity $\partial\widetilde{\phi}_{i,l}/\partial\sigma_j$, corresponding to a potential $\widetilde{\phi}_{i,l}$ at node i due to a source at node l, can be represented as a superposition of potentials $\widetilde{\phi}_{i,m}$ originated from 'fictitious' sources at the nodes m of the j-th domain element (e.g., Sasaki, 1989). By the principle of reciprocity, the values $\widetilde{\phi}_{i,m}$ can be expressed via potentials $\widetilde{\phi}_{m,i}$ at the nodes m due to a current I_i at node i. Analogous to the DC resistivity problem (e.g., Kemna, 1995), for the complex sensitivity the expression ultimately results in:

$$\frac{\partial\widetilde{\phi}_{i,l}}{\partial\sigma_j} = -\frac{1}{I_i}\sum_m\sum_n a_{j\,mn}\,\widetilde{\phi}_{m,i}\,\widetilde{\phi}_{n,l}\,, \tag{3.30}$$

where the double sum is made over all nodes m, n of the respective element, and $a_{j\,mn}$ is the m,n-th element of the matrix $\mathbf{S}_{1j} + k^2\,\mathbf{S}_{2j}$. From eq. (3.30), the sensitivities are simply obtained by a weighted sum of complex potential products.

3.2.6 INVERSE FOURIER TRANSFORM

For the purpose of this thesis all electrodes are assumed to lie in a plane perpendicular to the strike direction y. Therefore, the complex potential needs to be calculated at $y = 0$ only, and the inverse Fourier transform (3.9) simplifies to a pure integration of the transformed potential values:

$$\phi_i = \frac{1}{\pi} \int_0^\infty \tilde{\phi}_i(k)\, dk\,. \tag{3.31}$$

The numerical evaluation of the integral in eq. (3.31) is based on a combination of Gaussian quadrature and Laguerre integration as suggested by LaBrecque et al. (1996a). The result is an expression

$$\phi_i = \sum_n w_n\, \tilde{\phi}_i(k_n)\,, \tag{3.32}$$

with different abscissa k_n, for which the complex linear system of equations (3.23) has to be solved, and some real weights w_n. Details on the procedure can be found in Appendix C.

Finally, the complex voltage V_i of any arbitrary electrode configuration is obtained by appropriate superposition of calculated potential values, i.e., $V_i = \sum \phi_{im}$, or with eq. (3.32),

$$V_i = \sum_m \sum_n w_n\, \tilde{\phi}_{im}(k_n)\,. \tag{3.33}$$

It is obvious that the order of inverse Fourier transform and superposition can be interchanged because of the linearity of both operations.

The corresponding sensitivities are calculated in an analogous way from eq. (3.30), i.e.,

$$\frac{\partial V_i}{\partial \sigma_j} = \sum_m \sum_n w_n \frac{\partial \tilde{\phi}_{im}}{\partial \sigma_j}(k_n)\,. \tag{3.34}$$

3.2.7 MODELING EXAMPLES

To prove the validity of the implemented complex resistivity FE modeling algorithm, computed results for various 2D earth models have been extensively compared against both analytic solutions and results from other numerical modeling codes. As a demonstration, in this section modeled pole-pole sounding curves for magnitude and phase of apparent complex resistivity over a horizontal three-layer model are presented. The test model is adopted from Weller et al. (1996a) since their modeling

algorithm, although based on finite differences, is comparable to the one presented in the preceding sections. In addition, the distribution of the complex electric potential due to a subsurface current source in the presence of a polarizable body is shown, in order to illustrate the fundamental difference between in-phase and quadrature component field patterns.

POLE-POLE SOUNDING OVER THREE-LAYER MODEL

The horizontally layered earth model designed by Weller et al. (1996a) is characterized by a conductive, polarizable layer embedded in a homogeneous half-space. The model geometry and the corresponding complex resistivity values in terms of magnitude and phase are shown in Figure 3.2.

The reciprocity principle is exploited to calculate pole-pole sounding curves from the modeled complex potential values for a single current injection point at the surface. Since the sounding shall comprise electrode spacings varying over more than three decades, the employed model discretization into 60×30 rectangular cells is characterized by logarithmically increasing cell sizes to depth and both sides, starting from the current source position in the center. The discretization is identical to that used by Weller et al. (1996a), allowing a fair comparison of their results with those obtained herein by the developed FE algorithm.

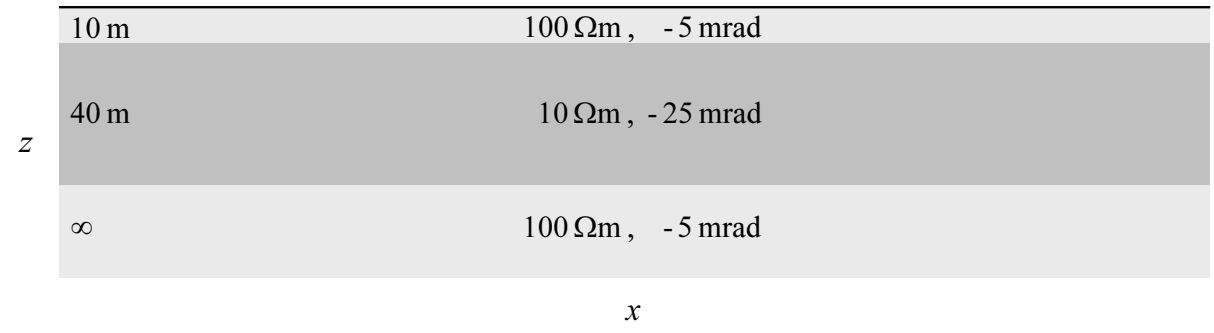

Figure 3.2: Parameters of the horizontal three-layer model.

The modeled sounding curves of magnitude and phase of apparent complex resistivity are shown in Figure 3.3. For comparison, the 'exact' solution, calculated by a linear filter method according to Anderson (1979), and the corresponding deviations of the FE results are included. Note that the symbols directly represent the grid nodes of the discretization in the horizontal direction.

According to Figure 3.3b, the errors in the FE solution for spacings up to 1000 m are less than 1 % for resistivity magnitude and less than 0.2 mrad for resistivity phase. Even for the largest spacings (where the grid boundary is reached) the errors clearly stay below 3 % and 1 mrad, respectively. Note that the perfect fit for nodes directly

neighboring the current source must be attributed to singularity removal, whereas the usage of mixed boundary conditions is responsible for the fair accordance even towards the boundaries of the grid.

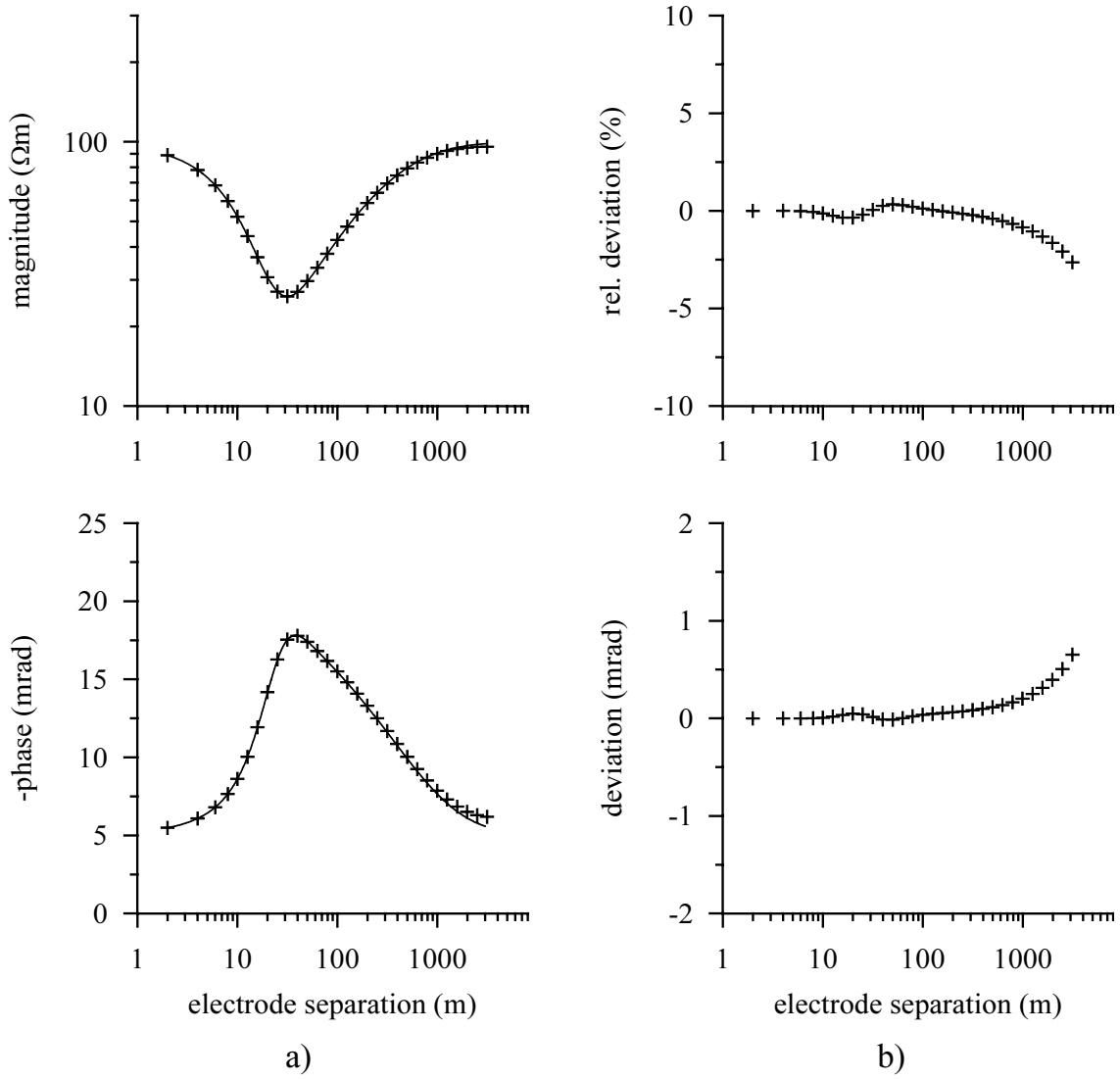

Figure 3.3: Modeling results for a pole-pole sounding over the three-layer model shown in Figure 3.2. a) Modeled curves of magnitude (top) and phase (bottom) of apparent complex resistivity using the developed FE algorithm (symbols) and an exact linear filter method (solid curves). b) Corresponding deviations of the FE solution from the exact solution.

RESPONSE OF A POLARIZABLE BODY

The second modeling example is intended to recall the fundamental characteristics of the complex potential field pattern in the presence of a polarizable body. For clearness, a single subsurface electrode is used as the current source. The simple model consists of a purely polarizable 2D block in a homogeneous half-space. Figure 3.4 shows the

modeling result for in-phase and quadrature component of the complex potential in the plane through the source point perpendicular to the strike direction.

The field pattern of the real component exhibits the well-known distribution for a subsurface source in a homogeneous half-space. This in-phase potential principally depends upon the distance from the current source, as taken into account by the geometric factor. Note that the assumed mixed boundary conditions at the bottom and the sides of the grid are exact for the homogeneous in-phase problem, i.e., the equipotentials intersect the boundary in the correct angle. The quadrature component represents an exclusively secondary potential originated at polarization dipoles within the polarizable body (notice the dipole character of the equipotentials). The pattern is therefore affected by both the location (and shape) of the anomaly and the current source position.

In particular, from Figure 3.4 it is obvious that for arbitrary electrode configurations (e.g., crosshole arrangements) the observation of negative IP responses, i.e., a positive phase of the apparent complex resistivity, is not unusual, even if intrinsically absent (since physically unreasonable).

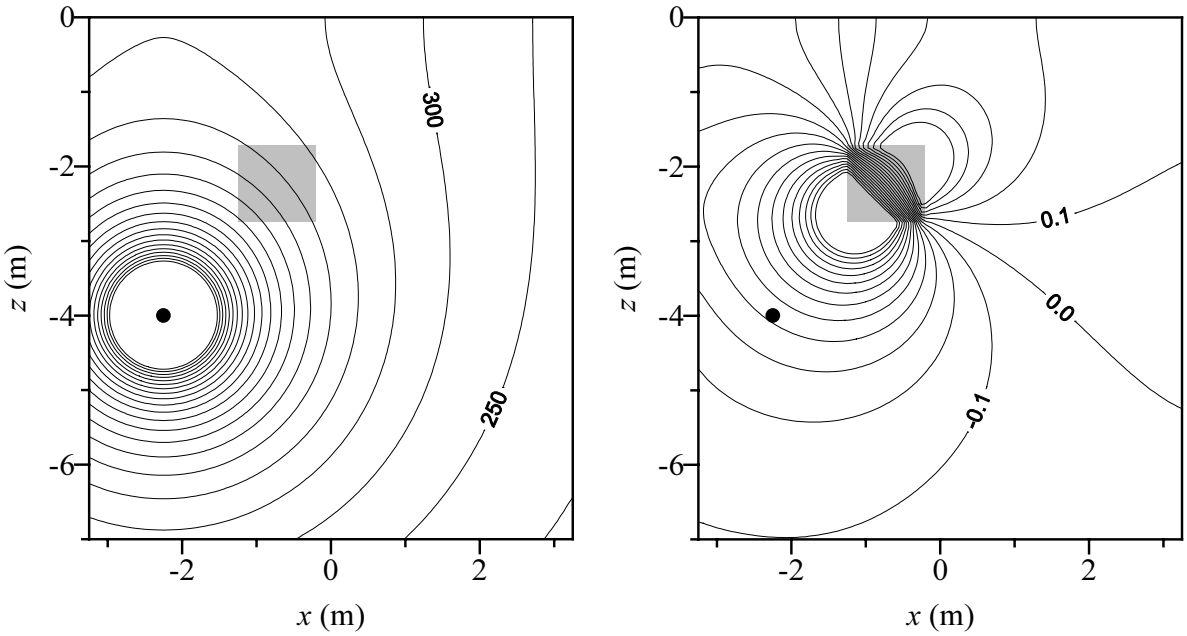

Figure 3.4: Modeled distribution of in-phase (left) and quadrature (right) component of the complex potential due to a subsurface point source (indicated by the solid circle) in the presence of a polarizable 2D block (indicated by the shaded area). The complex resistivity parameters are 100 Ωm, -50 mrad for the anomalous block and 100 Ωm, 0 mrad for the background. The potential values are given in mV, for a current of 100 mA. The underlying grid geometry corresponds to that of Figure 3.1. However, here a twice as fine model discretization has been used.

3.3 INVERSE PROBLEM

After the solution of the complex resistivity forward problem has been covered in the previous sections, now an appropriate inversion algorithm, similarly based on full complex arithmetic, is presented. As already outlined before, the algorithm is intended to meet several basic requirements. These include the capability of simulating arbitrary, complicated earth structures by means of fine model parameterizations, the general possibility to incorporate desirable model characteristics, and robustness in the presence of data errors. The general inversion approach to accomplish these objectives is addressed first, before its adaptation to the complex resistivity problem and the numerical solution of the inverse problem are discussed in detail.

3.3.1 INVERSION APPROACH

Basically, any inversion procedure aims to find a model of the subsurface distribution of the relevant physical properties explaining the given observations, i.e., measurements. However, if the earth is parameterized into a large number of model parameters (like in the tomographic approach), normally a strongly underdetermined, ill-posed problem results with an infinite number of possible solutions. This is particularly true for problems involving inherent nonuniqueness, like the resistivity problem encountered herein. In such cases, the inverse problem must be regularized by additional constraints to seek for a *unique* model exhibiting specific predefined characteristics.

Mathematically, this approach is commonly formulated as an optimization problem, where a properly designed objective function

$$\Psi(\mathbf{m}) = \Psi_{\mathrm{d}}(\mathbf{m}) + \lambda \Psi_{\mathrm{m}}(\mathbf{m}) \tag{3.35}$$

is sought to be minimized. Herein, for a given model vector $\mathbf{m}$, $\Psi_{\mathrm{d}}(\mathbf{m})$ represents the chi-squared measure of the data misfit, $\Psi_{\mathrm{m}}(\mathbf{m})$ is a model objective function containing the desired model characteristics, and λ is a real, positive number known as the regularization parameter. For N given data d_i, each contaminated by uncorrelated Gaussian noise with zero mean and individual standard deviation ε_i (in the following also simply referred to as the data error of d_i), the chi-squared measure of the data misfit is defined as

$$\Psi_{\mathrm{d}}(\mathbf{m}) = \sum_{i=1}^{N} \frac{|d_i - f_i(\mathbf{m})|^2}{|\varepsilon_i|^2}, \tag{3.36}$$

where f_i denotes the respective operator of the forward solution. The corresponding RMS error is given by

$$\varepsilon^{\mathrm{RMS}}(\mathbf{m}) = \sqrt{\frac{\Psi_\mathrm{d}(\mathbf{m})}{N}}\,. \tag{3.37}$$

The minimization of an objective function of the form of eq. (3.35) to solve an ill-posed inverse problem is also referred to as the Tikhonov approach, and in this context, the model objective function Ψ_m plays the general role of a stabilizing functional (Tikhonov and Arsenin, 1977).

Numerous DC resistivity inversion algorithms are ultimately based on the above approach, including both 2D (e.g., Sasaki, 1992; Oldenburg et al., 1993; LaBrecque et al., 1996a; Loke and Barker, 1996) and 3D (e.g., Park and Van, 1991; Sasaki, 1994; Zhang et al., 1995) implementations. Since the resistivity problem is nonlinear, the minimization of the global objective function Ψ has to be carried out in an iterative process, where normally at each step a quadratic approximation of Ψ is minimized to solve for an update of the current model. This *local* minimization is usually accompanied by a univariate line search to find the optimum value of the regularization parameter λ (e.g., deGroot-Hedlin and Constable, 1990). The iteration process is stopped when an acceptable data misfit target value Ψ_d^* is reached. From statistical theory, Ψ_d^* should be of the order of the number of (independent) data N, corresponding to an RMS value of one.

Sometimes the optimization problem is originally formulated slightly different, even if more correctly from a mathematical point of view. Rather than simply minimizing the global objective function Ψ in the described manner and assuming that the final solution is actually the minimum of Ψ_m with $\Psi_\mathrm{d} = \Psi_\mathrm{d}^*$, one may try directly to solve for the minimum of Ψ_m subject to $\Psi_\mathrm{d} = \Psi_\mathrm{d}^*$ by means of the method of Lagrange multipliers. The resulting functional to be minimized then is (e.g., Constable et al., 1987)

$$\Psi'(\mathbf{m}) = \Psi_\mathrm{m}(\mathbf{m}) + \mu\left(\Psi_\mathrm{d}(\mathbf{m}) - \Psi_\mathrm{d}^*\right), \tag{3.38}$$

where the Lagrange multiplier μ obviously corresponds inversely with the regularization parameter λ in eq. (3.35). Note that this method, strictly speaking, assumes a *fixed* value of μ during the minimization process (e.g., Parker, 1994). In practice, however, the problem is that a suitable value of μ is not known beforehand, in fact it is not even known if any value of μ may actually deliver a small enough data misfit. To overcome this difficulty, the resistivity inversion algorithms adopting this approach (e.g., Oldenburg et al., 1993) usually modify the target value Ψ_d^* at each iteration (i.e., they start the iterations with a larger value and continuously decrease it by some recipe towards the final goal) and, in addition, apply some line search technique to properly adjust μ. Then, of course, the approach of Lagrange multipliers virtually becomes equivalent to the Tikhonov approach described before, with both processes minimization of Ψ and adjustment of λ being intimately intertwined.

Apart from the actual numerical procedure to minimize the objective function, inversion algorithms based on the Tikhonov approach may differ in the choice of the stabilizing term Ψ_m. It may be defined, for instance, as the deviation from a reference model or as some kind of spatial model roughness. The latter approach (ultimately leading to an inversion type commonly referred to as smoothness-constrained, minimum-structure, or Occam's style[3]) is usually adopted if no specific prior information on the subsurface is available. Smoothing may be implemented by a first-, second-, or even higher-order differential operator, either imposed on the model itself (e.g., LaBrecque et al., 1996a) or on the model update at each iteration step (e.g., Sasaki, 1992). A discussion on different smoothing variants as applied to the DC resistivity inverse problem is given by Zhang et al. (1996). The great flexibility provided by the usage of a more general model objective function is demonstrated by Ellis and Oldenburg (1994a). They show how a proper design of Ψ_m helps biasing the resistivity inverse solution towards specific desired or expected model characteristics.

The complex resistivity inversion algorithm presented in the following is directly based on the Tikhonov approach, i.e., an objective function according to eq. (3.35) is minimized. For the purpose of this thesis, a conventional first-order spatial smoothing is adopted, i.e.,

$$\Psi_m(\mathbf{m}) = \iint \|\nabla \mathbf{m}\|^2 \, dx dz \,, \tag{3.39}$$

where $\|\ldots\|$ represents the standard L_2-norm, and ∇ is the 2D gradient operator. The numerical solution of the minimization problem, including the employed line search procedure to determine the regularization parameter λ at each inverse iteration step, is subject of the Sections 3.3.3 and 3.3.4.

3.3.2 PARAMETERS AND DATA

It seems obvious to formulate the complex resistivity inverse problem directly for complex parameters and data, i.e., to jointly invert for resistivity magnitude and phase as a complex number. An inherent advantage of such a formulation is that the inverse solution can be obtained in an elegant way using complex calculus. By the following definitions and considerations, it is shown that the inversion approach outlined in the previous section can be applied to the complex-valued problem in a straightforward manner.

---

[3] After William of Occam, whose razor cut away unnecessarily complicated or unnecessarily numerous hypotheses (Constable et al., 1987).

Within the complex resistivity inversion, log transformed parameters and data shall be used to account for the wide dynamic range of resistivity magnitude encountered in earth materials. In terms of conductivity, the model vector **m** and the data vector **d** of the inverse problem may thus be defined as

$$\begin{aligned} m_j &= \ln \sigma_j \quad (j = 1, \ldots, M) , \\ d_i &= \ln \sigma_{\mathrm{a}\,i} \quad (i = 1, \ldots, N) , \end{aligned} \tag{3.40}$$

where σ_j are the complex conductivities of the individual cells of the underlying finite-element mesh, $\sigma_{\mathrm{a}\,i}$ are the measured apparent complex conductivities, M is the number of parameters, and N is the number of measurements. The apparent conductivities are given by

$$\sigma_{\mathrm{a}\,i} = \frac{1}{G_i \, Z_i} , \tag{3.41}$$

with G_i and $Z_i = V_i / I_i$ denoting, respectively, geometric factor and transfer impedance of the i-th measurement.

Note that the complex log function in eq. (3.40) separates log magnitude and phase of its argument into real and imaginary part.[4] For instance, the real and the imaginary parts of the complex data d_i are given by $-\ln(|G_i Z_i|)$ and $-\varphi_i$, where the latter may denote the phase of $\sigma_{\mathrm{a}\,i}$.

From the equations (3.40), for the elements of the Jacobian matrix **A** of the complex inverse problem it results (by the complex version of the chain rule)

$$a_{ij} = \frac{\partial d_i}{\partial m_j} = -\frac{\sigma_j}{V_i} \frac{\partial V_i}{\partial \sigma_j} . \tag{3.42}$$

The right-hand side of eq. (3.42) is computed according to eq. (3.34).

The data misfit Ψ_{d} in eq. (3.36) contains the individual differences between the data d_i and the model responses $f_i(\mathbf{m})$, i.e., $|d_i - f_i(\mathbf{m})|$. For complex data, this quantity obviously represents the distance between the two respective points in the complex plane. The complex inversion approach thus involves the minimization of the chi-squared measure of these distances, as a part of the objective function (3.35), until the target value Ψ_{d}^* is reached.

---

[4] Since the phase values observed in the complex resistivity method are very small and, in particular, lie within the range $(-\pi, \pi]$, the complex logarithm is not ambiguous in this context but always the principal value.

It must be emphasized that although decreasing the difference between the real parts or, respectively, the imaginary parts of two complex numbers implies a smaller distance between the corresponding points in the complex plane, the inverse statement is not necessarily true, as illustrated in Figure 3.5. For extremely noisy complex resistivity data, this circumstance can place some restrictions on the quality of the inverted image of resistivity phase. This problem and how it can be overcome is addressed in Section 3.3.6.

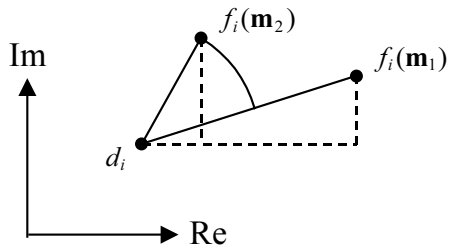

Figure 3.5: Representation of individual data misfit for two different models $\mathbf{m}_1$ and $\mathbf{m}_2$ in the complex plane. Note that for this example, $|d_i - f_i(\mathbf{m}_2)| < |d_i - f_i(\mathbf{m}_1)|$, but $|\mathrm{Im}(d_i - f_i(\mathbf{m}_2))| > |\mathrm{Im}(d_i - f_i(\mathbf{m}_1))|$.

For real-valued inverse problems, the data can vary only in one dimension, i.e., any data noise is one-dimensional. A complex number on the other hand, understood as a real vector with two independent components, real and imaginary part, may be subject to errors in two dimensions. However, for quantities depending on multiple variables, each of which contaminated by uncorrelated Gaussian noise, the denominators in the chi-squared merit function (3.36) must be extended to the respective sum of the individual variances (e.g., Press et al., 1992), scaled according to the law of propagation of errors.

For the problem encountered here, real and imaginary part are given by, respectively, log magnitude and phase of the apparent complex conductivity. Since $\left|\partial d_i / \partial \ln|Z_i|\right| = \left|\partial d_i / \partial \varphi_i\right| = 1$, the chi-squared measure of the complex data misfit may be consequently written as

$$\Psi_{\mathrm{d}}(\mathbf{m}) = \sum_{i=1}^{N} \frac{|d_i - f_i(\mathbf{m})|^2}{(\Delta \ln|Z_i|)^2 + (\Delta\varphi_i)^2}. \tag{3.43}$$

Herein, $\Delta\ln|Z_i|$ denotes the error in log magnitude of the transfer impedance, and $\Delta\varphi_i$ denotes the error in the corresponding phase value (note that, as a constant, G_i yields no contribution). Now, with the straightforward definition of a *complex* data error ε_i according to

$$\varepsilon_i = \frac{\partial d_i}{\partial \ln|Z_i|}\,\Delta\ln|Z_i| + \frac{\partial d_i}{\partial \varphi_i}\,\Delta\varphi_i = -\Delta\ln|Z_i| - \mathrm{i}\,\Delta\varphi_i \,, \tag{3.44}$$

eq. (3.43) can obviously be identified with the compact form of eq. (3.36). Note that the complex error ε_i implicitly defines a confidence region ellipse in the complex plane around the data point d_i. Thus, the definition in eq. (3.44) is not only practical but also reasonable.

3.3.3 NUMERICAL SOLUTION

To ultimately solve the complex resistivity inverse problem by complex algebra, both contributions to the global objective function (3.35), data misfit and model objective function, are first expressed as complex matrix-vector products measured by means of the complex L_2-norm[5].

The complex data errors ε_i according to eq. (3.44) may be assembled in a diagonal data weighting matrix $\mathbf{W}_\mathrm{d}$, i.e.,

$$\mathbf{W}_\mathrm{d} = \mathrm{diag}(1/\varepsilon_1, \ldots, 1/\varepsilon_N) \,. \tag{3.45}$$

Note again that the errors are assumed to be uncorrelated. With eq. (3.45), it is straightforward to write the data misfit of eq. (3.43) as

$$\Psi_\mathrm{d}(\mathbf{m}) = \left\| \mathbf{W}_\mathrm{d} \left(\mathbf{d} - \mathbf{f}(\mathbf{m}) \right) \right\|^2 \,, \tag{3.46}$$

where $\mathbf{f}$ represents the operator of the forward solution. Rewriting eq. (3.46) as

$$\left\| \mathbf{W}_\mathrm{d} \left(\mathbf{d} - \mathbf{f} \right) \right\|^2 = \left\| |\mathbf{W}_\mathrm{d}| \,\mathrm{Re}(\mathbf{d} - \mathbf{f}) \right\|^2 + \left\| |\mathbf{W}_\mathrm{d}| \,\mathrm{Im}(\mathbf{d} - \mathbf{f}) \right\|^2 \,, \tag{3.47}$$

with the real matrix $|\mathbf{W}_\mathrm{d}| = \mathrm{diag}(1/|\varepsilon_1|, \ldots, 1/|\varepsilon_N|)$, exhibits the fact that in the complex formulation it is assumed that both real and imaginary parts of $\mathbf{d}$, here represented by log magnitude and phase of the $\sigma_{\mathrm{a}i}$, are subject to the same weighting matrix. This, however, is nothing else but the inherent consequence when measuring the data misfit by means of the complex L_2-norm.

As it is shown in Appendix D, the model objective function (3.39), imposing a first-order smoothing on the complex model $\mathbf{m}$, can be expressed via a real model weighting matrix $\mathbf{W}_\mathrm{m}$ as

$$\Psi_\mathrm{m}(\mathbf{m}) = \left\| \mathbf{W}_\mathrm{m}\, \mathbf{m} \right\|^2 \,. \tag{3.48}$$

---

[5] Note that the L_2-norm of a complex vector $\mathbf{z}$ is defined via the multiplication by its complex conjugate transpose (denoted by H), i.e., $\|\mathbf{z}\|^2 = \mathbf{z}^\mathrm{H}\mathbf{z}$.

Again, eq. (3.48) implies that the same weighting matrix is assigned to the real and imaginary parts of $\mathbf{m}$, since

$$\left\| \mathbf{W}_\mathrm{m}\, \mathbf{m} \right\|^2 = \left\| \mathbf{W}_\mathrm{m}\, \mathrm{Re}(\mathbf{m}) \right\|^2 + \left\| \mathbf{W}_\mathrm{m}\, \mathrm{Im}(\mathbf{m}) \right\|^2 . \tag{3.49}$$

In many practical situations, the subsurface structures to be investigated are characterized by a preferential spatial orientation in the horizontal or vertical direction (e.g., horizontal layers, vertical dikes). Then it may be desirable to bias the inverse solution accordingly by an *anisotropic* smoothing of the model. This can be easily accomplished by separating the matrix $\mathbf{W}_\mathrm{m}$ with respect to x- and z-direction into matrices $\mathbf{W}_x$ and $\mathbf{W}_z$, respectively, and introducing two real smoothing parameters α_x and α_z (e.g., Oldenburg et al., 1993). In terms of the model objective function (3.48), it can be written (see Appendix D)

$$\mathbf{W}_\mathrm{m}^\mathrm{T} \mathbf{W}_\mathrm{m} = \alpha_x\, \mathbf{W}_x^\mathrm{T} \mathbf{W}_x + \alpha_z\, \mathbf{W}_z^\mathrm{T} \mathbf{W}_z , \tag{3.50}$$

where α_x and α_z are chosen from the interval $(0,1]$.

With the equations (3.46) and (3.48), for the global objective function to be minimized it results

$$\Psi(\mathbf{m}) = \big(\mathbf{d} - \mathbf{f}(\mathbf{m})\big)^\mathrm{H}\, \mathbf{W}_\mathrm{d}^\mathrm{H} \mathbf{W}_\mathrm{d} \big(\mathbf{d} - \mathbf{f}(\mathbf{m})\big) + \lambda\, \mathbf{m}^\mathrm{H}\, \mathbf{W}_\mathrm{m}^\mathrm{T} \mathbf{W}_\mathrm{m}\, \mathbf{m} , \tag{3.51}$$

where H denotes the complex conjugate transpose (Hermitian). Since the forward problem is nonlinear, the minimization of eq. (3.51) is performed iteratively by the Gauss-Newton method. Starting from a model $\mathbf{m}_0$, at each inverse iteration step q a quadratic approximation of Ψ at the current model $\mathbf{m}_q$ is minimized, yielding a complex linear system of equations to be solved for a new model update $\Delta\mathbf{m}_q$. In detail, one obtains the 'normal equations' (Kemna and Binley, 1996)

$$\mathbf{B}_q\, \Delta\mathbf{m}_q = \mathbf{b}_q , \tag{3.52}$$

with

$$\mathbf{B}_q = \mathbf{A}_q^\mathrm{H}\, \mathbf{W}_\mathrm{d}^\mathrm{H} \mathbf{W}_\mathrm{d}\, \mathbf{A}_q + \lambda\, \mathbf{W}_\mathrm{m}^\mathrm{T} \mathbf{W}_\mathrm{m} \tag{3.53}$$

and

$$\mathbf{b}_q = \mathbf{A}_q^\mathrm{H}\, \mathbf{W}_\mathrm{d}^\mathrm{H} \mathbf{W}_\mathrm{d} \big(\mathbf{d} - \mathbf{f}(\mathbf{m}_q)\big) - \lambda\, \mathbf{W}_\mathrm{m}^\mathrm{T} \mathbf{W}_\mathrm{m}\, \mathbf{m}_q . \tag{3.54}$$

The derivation is outlined in Appendix E. Note that in the equations (3.53) and (3.54), $\mathbf{A}_q$ is the Jacobian matrix according to eq. (3.42), evaluated at the model $\mathbf{m}_q$. The quantities $2\mathbf{B}_q$ and $-2\mathbf{b}_q$ represent approximations for the Hessian matrix and the gradient vector of $\Psi(\mathbf{m}_q)$, respectively (see Appendix E).

The use of fine model parameterizations in the tomographic inversion approach may result in several thousands of model parameters even for 2D problems, involving

computational difficulties in the direct solution of the matrix equation (3.52). One way to overcome these difficulties is to compute an approximate solution by means of iterative relaxation techniques. A very popular representative of such techniques is the method of conjugate gradients (CG), originally developed for solving linear systems (Hestenes and Stiefel, 1952) or, equivalently, for minimizing quadratic functionals (Fletcher and Reeves, 1964).

The CG technique has been variously proved to be an effective tool for the solution of large-scale, real-valued geophysical inverse problems like, for instance, in the field of seismic traveltime inversion (Scales, 1987; VanDecar and Snieder, 1994) or DC resistivity inversion (Zhang et al., 1995). Here, it shall be adopted to solve the complex linear system of equations (3.52), i.e., to minimize the quadratic approximation of the objective function (3.51) at each inverse iteration step of the Gauss-Newton method.

Since the matrix $\mathbf{B}_q$ in eq. (3.53) is Hermitian and positive definite, the complex version of the standard CG algorithm can be applied straight away (e.g., Hestenes, 1980; Morita et al., 1991). The resulting algorithm is:

$$
\begin{aligned}
&\text{calculate } \mathbf{B}_q\,,\ \mathbf{b}_q \\
&\Delta\mathbf{m}_q = 0,\ \mathbf{r}_0 = \mathbf{b}_q\,,\ \mathbf{p}_1 = \mathbf{r}_0 \\
&\text{do } k = 1, \#\,\text{CG iterations} \\
&\qquad \left.\begin{aligned} \beta_k &= \mathbf{r}_{k-1}^{\mathrm{H}}\mathbf{r}_{k-1} \big/ \mathbf{r}_{k-2}^{\mathrm{H}}\mathbf{r}_{k-2} \\ \mathbf{p}_k &= \mathbf{r}_{k-1} + \beta_k \mathbf{p}_{k-1} \end{aligned}\right\} \text{ if } k \geq 2 \\
&\qquad \alpha_k = \mathbf{r}_{k-1}^{\mathrm{H}}\mathbf{r}_{k-1} \big/ \mathbf{p}_k^{\mathrm{H}}\mathbf{B}_q\mathbf{p}_k \\
&\qquad \Delta\mathbf{m}_q = \Delta\mathbf{m}_q + \alpha_k \mathbf{p}_k \\
&\qquad \mathbf{r}_k = \mathbf{r}_{k-1} - \alpha_k \mathbf{B}_q \mathbf{p}_k \\
&\text{end do} \\
&\mathbf{m}_{q+1} = \mathbf{m}_q + \Delta\mathbf{m}_q\ .
\end{aligned}
\tag{3.55}
$$

Herein, k is the CG iteration index, $\Delta\mathbf{m}_q$ is the estimate of the solution vector with residual $\mathbf{r}_k$, $\mathbf{p}_k$ is the CG relaxation direction, and α_k, β_k are the corresponding step lengths. Apart from the computation of α_k and β_k, the complex CG algorithm (3.55) is identical to that implemented by Mackie and Madden (1993) to solve the 3D magnetotelluric inverse problem.

To improve the convergence properties of the CG algorithm, in addition a diagonal scaling of the matrix $\mathbf{B}_q$ is used for preconditioning (Pini and Gambolati, 1990). Note that the diagonal elements of $\mathbf{B}_q$ are positive real numbers since the system is positive definite.

From theory, the CG method must have converged after at most M iterations, with M being the number of model parameters, i.e., unknowns. However, here the solution vector $\Delta\mathbf{m}_q$ represents only a model update within the iterative Gauss-Newton process. For this purpose, the knowledge of a reasonable approximation of $\Delta\mathbf{m}_q$ is sufficient. In the implemented complex resistivity inversion algorithm, the CG iterations are being stopped when the normalized squared norm of the residual vector,

$$\varepsilon_k^{\mathrm{CG}} = \frac{\mathbf{r}_{k-1}^{\mathrm{H}}\mathbf{r}_{k-1}}{\mathbf{r}_0^{\mathrm{H}}\mathbf{r}_0}, \tag{3.56}$$

reaches the value 10^{-4}, typically after $M/40$ to $M/20$ iterations. It was found that a larger number of iterations does not effectively improve the resulting data misfit after updating the model according to the approximate CG solution.

As outlined above, the procedure employed to minimize the (nonquadratic) objective function Ψ is a combination of the complex-valued CG method (for minimizing a local, quadratic approximation of Ψ) with the standard Gauss-Newton method. Consequently, within the inversion process one has to distinguish between the *inner* CG iterations (index k) to solve for a model update and the *outer* Gauss-Newton iterations (index q) to ultimately solve for the model minimizing Ψ. Note that this approach requires the solution of the forward problem [i.e., the computation of $\mathbf{f}(\mathbf{m}_q)$ and $\mathbf{A}_q$] only at each outer Gauss-Newton step to determine $\mathbf{B}_q$ and $\mathbf{b}_q$.

There also exists another approach to minimize nonquadratic functionals like Ψ by the CG technique alone, going back to Polak and Ribière (1969). Herein, at each CG relaxation step the model itself is updated, i.e., $\mathbf{m}_{k+1} = \mathbf{m}_k + \alpha_k \mathbf{p}_k$ [cf. the corresponding line in the algorithm (3.55)], where the step length α_k is chosen to minimize Ψ as a function of α_k, i.e., a line search is performed. The new gradient of $\Psi(\mathbf{m}_{k+1})$ is directly evaluated and used to determine the subsequent CG direction $\mathbf{p}_{k+1}$. Thus, this approach involves only a single iteration cycle (the outer Gauss-Newton iterations vanish) at the price of having to calculate the gradient vector, virtually given by eq. (3.54), at each CG step (note that the Hessian is not exploited at all). The connection between the combined Gauss-Newton/CG method and the Polak-Ribière method is discussed in Hestenes (1980).

The Polak-Ribière method has also been applied to nonlinear geophysical inverse problems. For instance, it was used by Ellis and Oldenburg (1994b) for 3D DC resistivity inversion and by Mora (1987) for 2D seismic inversion. In particular, Mora (1987) showed how to incorporate the Hessian information within a sophisticated CG preconditioner.

3.3.4 REGULARIZATION PARAMETER AND STEP-LENGTH DAMPING

As already outlined in Section 3.3.1, at each inverse (i.e., Gauss-Newton) iteration step an optimum value of the regularization parameter λ has to be found. For this purpose, a univariate search is performed and the data misfit Ψ_d is evaluated as a function of λ. The implemented procedure finds the maximum value of λ (locally) minimizing $\Psi_\mathrm{d}(\lambda)$ or, respectively, yielding the desired target misfit Ψ_d^*. This approach is similar to that originally employed by deGroot-Hedlin and Constable (1990) and later adopted by, e.g., Oldenburg et al. (1993) and LaBrecque et al. (1996a).

In this thesis, the line search is carried out by successively solving eq. (3.52) with different trial values λ_l of the regularization parameter. After each time an additional forward modeling is performed to determine the resulting data RMS error $\varepsilon^{\mathrm{RMS}}(\lambda_l)$. The search begins at the optimum value of λ of the previous Gauss-Newton iteration. The subsequent trial values are then chosen according to a formula

$$\lambda_{l+1} = \lambda_l \, h\left[\varepsilon^{\mathrm{RMS}}(\lambda_l)\right], \tag{3.57}$$

until the minimum of $\varepsilon^{\mathrm{RMS}}(\lambda)$ has been found or the target misfit is reached. In eq. (3.57), the real, positive scalar function $h[\ldots]$ depends upon the current data RMS error in a way that it decreases λ_l if $\varepsilon^{\mathrm{RMS}}(\lambda_l) > 1$ and increases λ_l if $\varepsilon^{\mathrm{RMS}}(\lambda_l) < 1$.[6] For the explicit choice of h, in particular accounting for a finer adjustment of λ towards the end of the inversion process, it is referred to Appendix F.

Following the suggestion of Newman and Alumbaugh (1997), an adequate starting value λ_0 at the first inverse iteration step may be estimated from the row sums of the matrix product $\mathbf{A}^{\mathrm{H}} \mathbf{W}_\mathrm{d}^{\mathrm{H}} \mathbf{W}_\mathrm{d} \mathbf{A}$. Such a choice properly scales the regularizing term $\lambda \mathbf{W}_\mathrm{m}^{\mathrm{T}} \mathbf{W}_\mathrm{m}$ in eq. (3.53) at the beginning of the inversion process. However, whereas Newman and Alumbaugh (1997) use the maximum absolute row value which occurs, for the problem considered herein five times the corresponding mean value has been found to be sufficiently large. Taking in addition the smoothing parameters α_x and α_z into account, it is

$$\lambda_0 = \frac{2}{\alpha_x + \alpha_z} \frac{5}{M} \sum_{m=1}^{M} \left| \sum_{j=1}^{M} \sum_{i=1}^{N} \frac{\overline{a}_{im} a_{ij}}{\overline{\varepsilon}_i \varepsilon_i} \right|, \tag{3.58}$$

where $\overline{}$ denotes complex conjugation.

---

[6] Note that $\varepsilon^{\mathrm{RMS}} = 1$ corresponds with $\Psi_\mathrm{d} = \Psi_\mathrm{d}^*$ if Ψ_d^* is taken to be the statistically expected value, i.e., the number of independent data N (provided that the data errors are normally distributed and the standard deviations ε_i are correctly chosen).

The solution vector $\Delta\mathbf{m}_q$ of the matrix equation (3.52) minimizes a quadratic approximation of Ψ at the current model $\mathbf{m}_q$, obtained by linearizing the forward problem $\mathbf{f}$ at that point. Since the problem actually is nonlinear, it might happen that updating $\mathbf{m}_q$ by the full step $\Delta\mathbf{m}_q$ causes the true local minimum of Ψ to be overshot. A common approach to prevent from overshooting, also referred to as step-length damping, is to step only partly into the direction of $\Delta\mathbf{m}_q$ (e.g., LaBrecque et al., 1996a), i.e.,

$$\mathbf{m}_{q+1} = \mathbf{m}_q + s\,\Delta\mathbf{m}_q \,, \tag{3.59}$$

where s denotes the step length with $s \in (0,1]$.

In the developed inversion algorithm, step-length damping is implemented as follows. Once the optimum value of λ has been found, which implies that $\Psi(s{=}1) = \Psi(\mathbf{m}_q + \Delta\mathbf{m}_q)$ has been calculated, a second forward modeling is run for $s = 0.5$ to evaluate $\Psi(s{=}0.5) = \Psi(\mathbf{m}_q + 0.5\Delta\mathbf{m}_q)$. Since $\Psi(s{=}0) = \Psi(\mathbf{m}_q)$ is known anyway, it is now possible to fit a parabola to the three points $\Psi(s{=}0)$, $\Psi(s{=}0.5)$, and $\Psi(s{=}1)$ as a function of s. Finally, the step length $s_{\min}$ corresponding to the smallest value of the parabola in the range $s \in (0,1]$ is chosen to ultimately update the model according to eq. (3.59). Note that if $s_{\min} \neq 1$, this normally implies that the forward solution has to be carried out once again.

3.3.5 ROBUST INVERSION

In the presented complex resistivity inversion algorithm the standard L_2-norm is being used as the measure of data misfit and model structure. The approach of minimizing the objective function Ψ is thus inherently related to the family of least-squares methods, which represent an efficient means of parameter estimation if the data errors are normally distributed and the correct variances are known. However, geophysical measurements are inevitably subject to errors of various sources and nature,[7] and seldom their true statistical distribution is known. Therefore, the error description by means of estimated standard deviations is often far from being correct, in particular in the presence of data outliers.

An efficient procedure to account for incorrect data noise estimates in the L_2-formulated DC resistivity inversion problem was suggested by LaBrecque and Ward (1990) on the basis of a robust estimation method originally described in

[7] Errors in complex resistivity measurements may be due to, for instance, electrode effects (poor galvanic coupling, polarization effects), incomplete removal of electromagnetic coupling, cultural and telluric noise, or simply instrumental errors. When inverting the data, additional errors arise directly from the limited accuracy in the numerical forward solution, especially when presuming the true earth to be 2D. Discussions on the particular characteristics of error distributions in ERT data sets can be found in Binley et al. (1995) and LaBrecque et al. (1996a).

Mosteller and Tukey (1977). It is characterized by the iterative correction of the individual error estimates at each Gauss-Newton step of the inversion. As recently stated by Farquharson and Oldenburg (1998), this approach represents a merger of the iteratively reweighted least-squares method, generally used to incorporate robust (non-L_2) measures of misfit,[8] with the standard Gauss-Newton method. Here, the scheme of LaBrecque and Ward (1990) is applied to the complex data errors ε_i of eq. (3.44).

Let χ_q denote the vector of the individual data misfits at the q-th inverse iteration step, i.e.,

$$\chi_{i,q} = \frac{d_i - f_i(\mathbf{m}_q)}{\varepsilon_{i,q}}. \tag{3.60}$$

Then the new error estimates for the $(q+1)$-th inverse iteration are determined by the three-step process

$$\begin{aligned} \varepsilon'_i &= \varepsilon_{i,q}\,\sqrt{|\chi_{i,q}|}\,, \\ \varepsilon''_i &= \varepsilon'_i\,\frac{\|\chi'\|_1}{\|\chi_q\|_1}\,, \\ \varepsilon_{i,q+1} &= \begin{cases} \varepsilon_{i,q} & \text{if } |\varepsilon''_i| \le |\varepsilon_{i,q}| \\ \varepsilon''_i & \text{if } |\varepsilon''_i| > |\varepsilon_{i,q}| \end{cases}, \end{aligned} \tag{3.61}$$

where the temporary misfit vector χ' is given by replacing $\varepsilon_{i,q}$ in eq. (3.60) by ε'_i, and $\|\ldots\|_1$ denotes the L_1-norm. Note that, compared to the L_2-measure, the L_1-measure is much more insensitive to existing outliers (e.g., Claerbout and Muir, 1973). In the first step of the scheme (3.61), the current error estimates $\varepsilon_{i,q}$ are altered according to the corresponding individual data misfit. Step two represents a normalization of the new values in order to keep the L_1-measure of the overall misfit at the original level. Finally, the third step ensures that the error magnitudes are at the most increased by the procedure, never decreased. In all, the scheme properly adjusts the error estimates of those data being significantly poorly fit by the current model $\mathbf{m}_q$.

The efficiency of this method when being used within a DC resistivity tomographic inversion algorithm is demonstrated in Morelli and LaBrecque (1996). Even in cases of underestimating the true error level by a factor of 10 or in the presence of

---

[8] A recommendable review on robust methods in linear inverse theory is given by Scales and Gersztenkorn (1987), covering the general idea of using L_p-measures with $1 \le p < 2$ (inclusive of the special case $p = 1$, resulting in least-absolute-deviations inversion), the practical implementation in the iteratively reweighted least-squares algorithm, and in particular, the history of robust inversion.

large systematic errors (e.g., due to misconnecting two electrodes), the robust scheme yields excellent, stable reconstruction results.

3.3.6 FINAL PHASE IMPROVEMENT

The joint inversion of resistivity magnitude and phase by means of complex calculus is based on the standard complex L_2-norm as the measure of data misfit and model structure. As an inherent consequence, the complex inversion algorithm basically seeks to minimize (in a least-squares sense) individual distances between two points in the complex plane, either in data or model space.

Now, for complex resistivity data the misfit in log magnitude (the real component) is typically one order of magnitude larger than the misfit in phase (the imaginary component), where the latter is measured in rad. Accordingly, the individual noise levels of log magnitude and phase often differ by about a factor of 10. For instance, the log magnitudes may be contaminated by random Gaussian noise with a standard deviation of $\mathrm{Re}(\varepsilon_i) = 0.05$ (which corresponds to a relative error in magnitude of 5 %), whereas the noise level for the phase values may be given by $\mathrm{Im}(\varepsilon_i) = 5\,\mathrm{mrad} = 0.005\,\mathrm{rad}$. Therefore, the individual confidence region ellipses in the complex plane, described by the complex data errors ε_i, are generally elongated in the real direction.

For error ellipses with extremely bad aspect ratios (e.g., in the case of relatively noisy data magnitudes), it may happen that the complex misfit is already brought down by the complex inversion process to some acceptable value although the phase fit itself is still rather poor (see Figure 3.5). As already mentioned in Section 3.3.2, this would result in poor quality phase images.

An obvious approach to attack this problem, if evident, is to run additional inversion iterations purely for the phase – that is while keeping the recovered distribution of resistivity magnitude fixed – once the complex inversion process has converged. Such a procedure thus represents a conventional real-valued inversion to improve the image of resistivity phase provided by the complex inverse solution. In detail this means that at the end of the complex inversion the phase values $-\varphi_i$ are taken as the new data (which are modeled in the same way as before from the current complex resistivity distribution) and a new inverse problem is iteratively solved for an update of the phase values of the complex model at each iteration. The corresponding inversion algorithm, however, is directly obtained from the presented complex version by simply replacing the relevant quantities in all above equations according to:[9]

---

[9] Note that $\mathrm{Re}(a_{ij}) = \partial\,\mathrm{Im}(d_i)/\partial\,\mathrm{Im}(m_j)$ [cf. equation (3.29)].

$$\begin{aligned} m_j &\rightarrow \mathrm{Im}(m_j) \quad , \\ f_i &\rightarrow \mathrm{Im}(f_i) \quad , \\ d_i &\rightarrow \mathrm{Im}(d_i) \quad , \\ \varepsilon_i &\rightarrow \mathrm{Im}(\varepsilon_i) \quad , \\ a_{ij} &\rightarrow \mathrm{Re}(a_{ij}) \quad , \\ \Delta m_j &\rightarrow \mathrm{Im}(\Delta m_j) \, . \end{aligned} \tag{3.62}$$

Therefore, this final step in the overall inversion process, in the following also referred to as final phase improvement, is easily implemented using the same subroutines as for the full complex inversion. Note that the general inversion approach, however, remains unchanged (including aspects like regularization, step-length damping, robust error estimation, stopping criterion, etc.).

The efficiency of the above procedure is being demonstrated in the next chapter within the scope of the comprehensive investigation of the complex resistivity inversion by means of synthetic model examples.

3.4 SUMMARY

In this chapter, an algorithm for the 2D tomographic inversion of complex resistivity data was presented. The algorithm is based on the finite-element method for forward modeling and a regularized Gauss-Newton approach to solve the inverse problem, with both parts being formulated in terms of complex arithmetic.

Since all electromagnetic effects are neglected, the forward problem can be reduced to a simple Poisson equation for a point source analogous to the conventional DC case. By carrying out a Fourier transform with respect to the assumed strike direction, a complex-valued, purely 2D Helmholtz equation is deduced, which is then discretized by means of the FE method subject to the given boundary conditions. Except for the surface, where homogeneous Neumann conditions are imposed, all grid boundaries are of mixed type, taking the asymptotic behavior of the complex potential adequately into account. Singularity removal is implemented in order to keep the modeling errors near the electrodes at a minimum. A complex version of the Cholesky method is used to solve the resultant FE matrix equation for the secondary potential attributing to inhomogeneities in the underlying conductivity distribution. The complex resistivity response for an arbitrary multipole electrode configuration is finally obtained by application of the inverse Fourier transform and appropriate superposition. The corresponding complex sensitivities are efficiently calculated via the principle of reciprocity.

The inversion procedure uses log transformed complex parameters and data to jointly invert for resistivity magnitude and phase at a given measurement frequency. The objective function being minimized is composed of the complex L_2-measures of data misfit and first-order model roughness, with both terms being balanced by means of a regularization parameter. Due to the nonlinearity of the forward problem, the minimization results in an iterative Gauss-Newton scheme, where at each step a complex linear system of equations is solved for a model update by means of the conjugate-gradient method. Moreover, at each inverse iteration step a univariate search is performed to find the maximum value of the regularization parameter which locally minimizes the data misfit function or, respectively, yields the desired target misfit. In addition, a robust data reweighting scheme may be applied in the presence of poor data noise estimates. The optimum step length into the model update direction is determined by means of three-point parabolic interpolation to prevent the algorithm from overshooting. The inverse iteration process is stopped when the desired data misfit target value is reached. However, to overcome a possible lack of resolution in resistivity phase due to large errors in the magnitude data, the inversion process may be continued for the phase alone. This results in a conventional real-valued inverse problem, with the magnitude distribution from the complex solution being used in the (still complex) forward model.

4 SYNTHETIC MODEL EXAMPLES

In order to investigate the efficiency of the complex resistivity inversion developed in the previous chapter, three different synthetic models were derived representing typical problems that may be encountered in the different fields of application. The models were deliberately designed to keep a reasonable balance between exhibiting some realistic complexity on the one hand and, nonetheless, being sufficiently simple to clearly point out the respective characteristics of the inversion scheme on the other hand.

As an example for environmental applications, the first model represents a contamination scenario involving two overlapping contaminant plumes, each of which characterized by an individual electrical signature. The two plumes may be given, for instance, by specific components of a complex subsurface contamination (e.g., soluble and insoluble components). The second model describes a typical lithologic situation as being of interest in many hydrogeological applications. It consists of two clay layers (or lenses) which are embedded in a sandy aquifer. To address a typical problem in mineral exploration as well, model three finally represents a dipping fracture or shear zone within an overburden-covered host rock, exhibiting a characteristic complex resistivity response due to, for instance, the presence of a significant amount of net-textured sulfide mineralization. Whereas the first two models are considered for a single frequency only, the third model was set up to be frequency-dependent in order to investigate the feasibility of recovering intrinsic spectral parameters by means of tomographic complex resistivity inversion.

4.1 CONTAMINANT PLUME MODEL

For cases of combined organic and inorganic subsurface contamination the measurement of resistivity magnitude alone may give inadequate information to identify each plume, since the conductive characteristic of an inorganic substance dissolved in the pore water is often likely to hide the resistive signature of a non-aqueous organic. By analyzing the system, however, as a distribution of complex resistivity, the phase response may provide additional information to delineate the two contaminants (see Section 2.6.2).

In order to demonstrate the complex resistivity inversion for such a problem, the first synthetic model was derived to represent a realistic contamination scenario in which an electrically conductive inorganic contaminant plume, controlled by hydraulic gradients, followed a different pathway to a dense, gravity driven, resistive organic plume. Unlike the inorganic, the organic contamination additionally may give rise to an increased IP effect in terms of a significant change in resistivity phase. In its essentials, the dual plume model was already presented in Kemna and Binley (1996). Figure 4.1 shows the slightly modified version being used in this thesis.

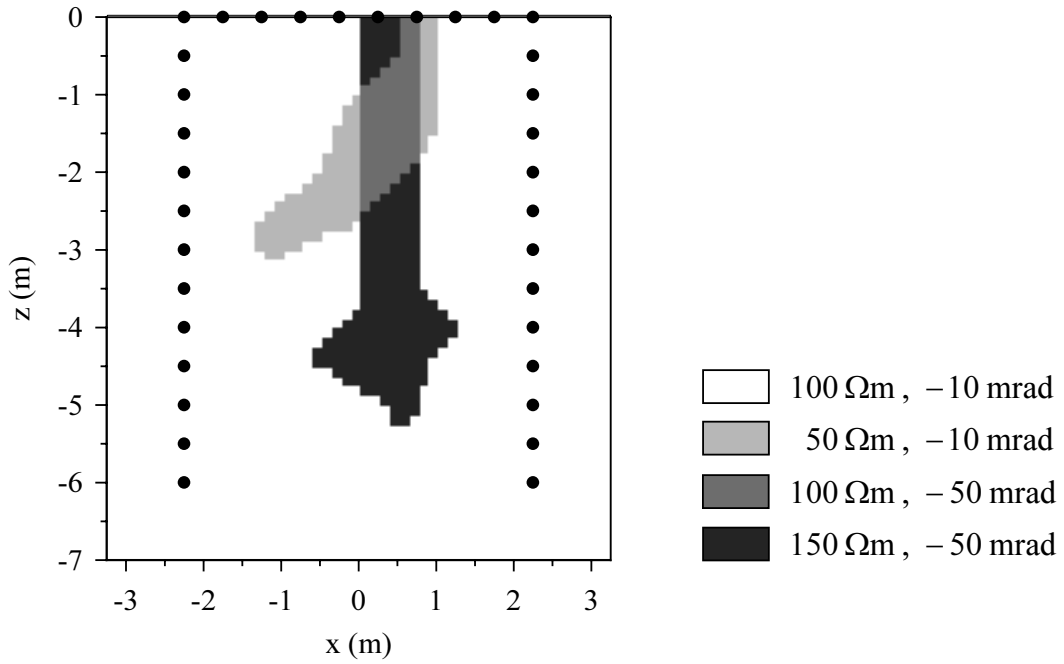

Figure 4.1: Definition of the contaminant plume model. The solid circles indicate the position of electrodes.

The electrode setup consists of 34 electrodes arranged in two boreholes and at the surface (see Figure 4.1). A finite-element mesh with $52 \times 56 = 2912$ elements was used to model a data set of altogether 404 different dipole-dipole measurements. The data set was obtained by including all possible combinations with a fixed dipole length of two electrode separations for both current injection and measurement dipoles (reciprocal configurations were disregarded). In practice, this choice represents a reasonable compromise between signal strength and resolution.[1] To avoid relatively large as well as small voltage magnitudes, respectively, configurations with both dipoles being less than two electrodes apart and those with a geometric factor greater

[1] Discussions on different electrode configurations that may be used in ERT data sets can be found in, for example, Sasaki (1992), Zhou and Greenhalgh (1997), and Sullivan and LaBrecque (1998).

than 10^5 m were left out. The resultant 404 modeled transfer impedances, each of which consisting of magnitude and phase, then acted as input to the inversion procedure.

According to early ERT studies (e.g., Sasaki, 1992; Shima, 1992), for all inversions in this thesis a regular parameterization characterized by two model cells per electrode separation is used. In general, however, for a smoothness-constraint regularization as applied herein, there are no lower restrictions on the model cell size placed by numerical stability aspects. The employed parameterization rather represents a compromise between the highest possible geometrical freedom of the model on the one hand (see, e.g., discussion in Oldenburg and Li, 1994) and the computational requirements of the inversion, intimately related to the total number of parameters M, on the other hand. For the present example, the inversion mesh is identical to that of Figure 3.1, with $M = 26 \times 28 = 728$, and thus coarser than the mesh originally used to generate the synthetic data.

As the starting model of the inversion always a homogeneous distribution is used, with its value determined from the arithmetic mean of the log-transformed apparent complex resistivity input data.

NOISE-FREE INVERSION

To study the efficiency of the complex resistivity inversion procedure in the optimum case of perfect measurements, a first inversion was performed without adding noise to the synthetic data. However, in order to account for possible modeling errors introduced by the finite-element solution itself (see Figure 3.3), uniform complex data errors ε_i corresponding to 1.5 % relative error in magnitude and 1 mrad absolute error in phase were assumed within the inversion to evaluate the data misfit. Note that these tolerances also define the level to which the data are sought to be fit by the inversion process. Due to the 2D character of the contaminant plume model geometry, no directional bias was imposed on the model roughness, i.e., $\alpha_x = \alpha_z = 1$ was chosen. Moreover, the iterative reweighting of the data according to the robust error estimation scheme (see Section 3.3.5) was disabled and no extra final-phase-improvement step (see Section 3.3.6) was carried out.

Figure 4.2 provides insight into the iterative evolution of the resultant inversion process. It displays the behavior of the regularization parameter λ, the data misfit Ψ_d, and the model roughness Ψ_m as the individual constituents of the global objective function ultimately being minimized by the inversion. Note that the major decrease of Ψ_d, and correspondingly increase of Ψ_m, takes place within the first four inverse iterations. Figure 4.3 illustrates the typical convergence behavior of the conjugate gradient method being used to calculate the model update at each inverse iteration step. Accordingly, the residual is not continuously being decreased, but the convergence curve occasionally exhibits single relaxation directions where the residual

again increases. Normally, however, the subsequent relaxation step immediately compensates for this effect.

The resultant complex resistivity image, obtained after 11 iterations of the inversion algorithm, is shown in Figure 4.4a. It can be seen that the essential features of the contaminant plume model are recovered reasonably well. Of course, due to the smoothness constraint within the inversion, the contours of the plumes are blurred to some extent, but nevertheless their general geometrical shape is clearly recognizable. Also, nearly the true parameter contrast has been reached in both phase and even magnitude, although the latter distribution is characterized by relatively sharp changes between conductive and resistive areas. The loss of the lowest small 'nose' of the dense, sinking plume at about $z \approx -5$ m must be attributed to the well-known decrease of resolution of crosshole ERT surveys with depth and towards the center of the image plane (e.g., Ramirez et al., 1993; LaBrecque et al., 1996a). This aspect is addressed in some more detail within the scope of the second synthetic model example in Section 4.2.

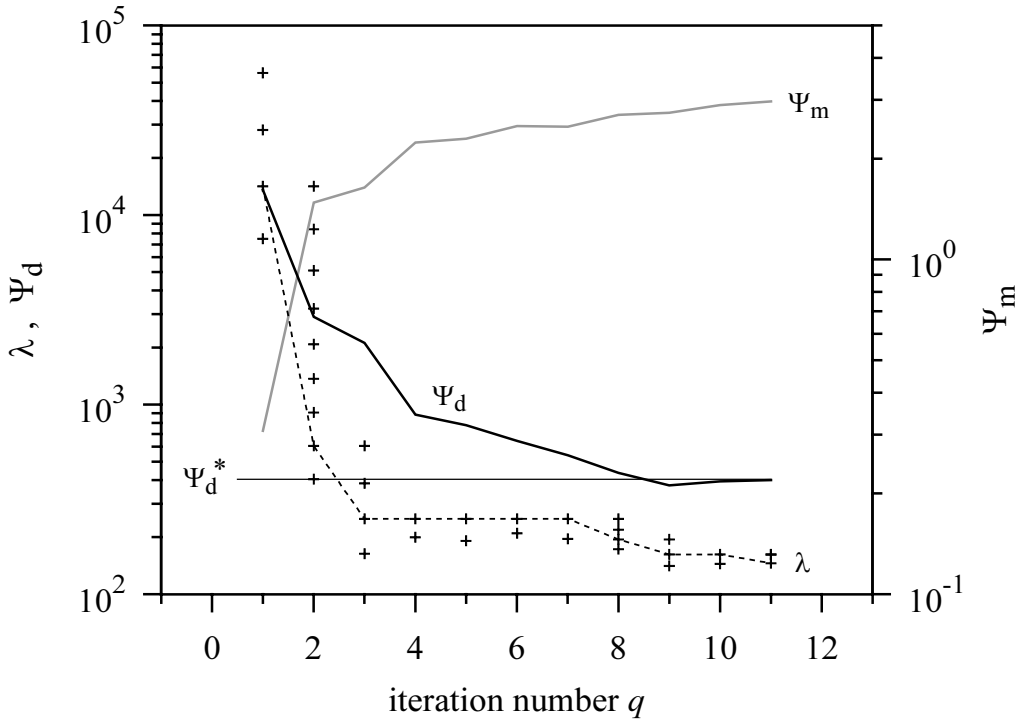

Figure 4.2: Iterative evolution of data misfit Ψ_d (thick solid black line), optimum regularization parameter λ (dashed line), and first-order model roughness Ψ_m (gray line) during the inversion leading to the result shown in Figure 4.4a. The obelisks indicate the sequence of regularization parameter trial values λ_l at each inverse iteration step, and the horizontal line marks the data misfit target value $\Psi_d^* = N = 404$, corresponding with $\varepsilon^{RMS} = 1$.

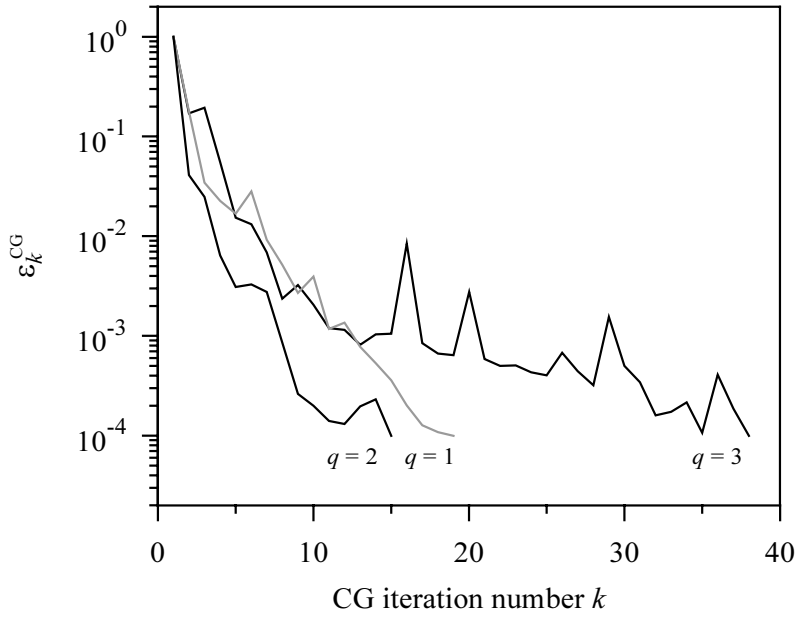

Figure 4.3: Convergence behavior of the complex conjugate gradient algorithm to solve for the model update at each inverse iteration step, showing the normalized squared norm of the CG residual vector ε_k^{CG} against the number of CG iterations k. The three exemplary convergence curves correspond to the first three inverse iterations of Figure 4.2, as indicated by the index q. Note that the CG iterations are being stopped when ε_k^{CG} reaches the value 10^{-4}.

A final remark on the occurrence of slight grid artifacts, as for instance between $x \approx -2$ m and $x \approx -0.5$ m at the top of the phase image in Figure 4.4a, may be added. As pointed out by Zhang et al. (1996), grid artifacts may be related to the type of smoothing imposed by the stabilizing model objective function. With respect to the suppression of such effects they state that a higher-order smoothing might be superior to the first-order smoothing adopted in this thesis.

INVERSION WITH NOISY DATA

To simulate somewhat more realistic conditions encountered in the field, zero-mean Gaussian noise was added to the magnitudes and, independently, to the phase values of the synthetic transfer impedances. The standard deviations were set to 5 % and 5 mrad for magnitude and phase, respectively. Note that the latter value corresponds to 12.5 % of the overall phase contrast present in the target model.

For the inversion, the correct noise levels were assigned to the complex data errors ε_i. All other adjustments, however, were left as in the previous paragraph. The inversion result, obtained after only four inverse iterations, is displayed in Figure 4.4b. The images compare remarkably well with those of Figure 4.4a (note that the same color scales were used), reflecting the robustness of the inversion procedure in the presence of data noise.

The reconstructed images in the case of noise-contaminated data may represent a realistic result gained by complex resistivity inversion for a dual plume contamination field problem. Compared to the conventional DC resistivity approach the advantage of the complex resistivity method for such problems is obvious. The inverted image of resistivity magnitude alone does not, as stated earlier, give a precise picture of the connectivity of the two contaminant bodies, however, when used in conjunction with the phase image there is clear delineation of both plumes.

FINAL PHASE IMPROVEMENT

As outlined in Section 3.3.6, the presence of large errors in the data magnitudes may not only give rise to poor inversion results in terms of resistivity magnitude, but may also badly affect the recovered phase images. To illustrate this situation, the inversion from the previous paragraph was repeated with the synthetic input data contaminated by 20 % Gaussian noise in magnitude and, as before, 5 mrad Gaussian noise in phase. Again, the data were fit to the correct noise level, i.e., uniform complex data errors ε_i with $\mathrm{Re}(\varepsilon_i) = 0.2$ and $\mathrm{Im}(\varepsilon_i) = 0.005$ (rad) were assumed within the inversion. Notice the enormous dominance of the magnitude misfit in the complex data misfit function (3.43), being sought to be minimized by the inversion procedure.

Due to the high noise level the complex inversion algorithm already converged after only two iterations. Figure 4.4c shows the resultant distributions of resistivity magnitude and phase. Compared with Figure 4.4b, the magnitude image clearly exhibits loss of resolution, as must have been expected. Whereas the conductive plume is still recognizable, the existence of the resistive plume is no longer evident. However, although the same amount of noise was added to the underlying phase data as in the previous example, the phase distribution of the target model is now comparatively poorly resolved with respect to both connectivity of the polarizable anomaly as well as phase value contrast.

The respective results obtained by subsequently carrying out additional phase inversion iterations, i.e., continuing fitting the phase data to their misfit target value while keeping the distribution of resistivity magnitude unchanged (see Section 3.3.6), are shown in Figure 4.4d. In both cases, 5 % and 20 % data magnitude noise, two more iterations were required to meet the (new) stopping criterion. However, whereas for 5 % magnitude noise there is no major difference between the phase images obtained with and without the final phase inversion steps (cf. Figure 4.4b), Figure 4.4d reveals significant improvement in resolution if the data magnitudes are contaminated by 20 % noise (cf. Figure 4.4c).

As already explained before, the reason for the decreased phase resolution of the complex inversion procedure that may occur in the presence of noisy magnitude data, is the different influence of magnitude and phase misfit on the overall data misfit as measured by the complex L_2-norm. It must be emphasized though that this problem

represents an inherent consequence of inverting complex resistivity data by means of a regularized inversion approach completely based on complex algebra. However, the example given above clearly demonstrates that, if necessary, loss of resolution in resistivity phase can be effectively overcome with little extra effort by continuing the inversion process purely for the phase once the complex algorithm has converged.

Finally, two more remarks may be added.

First, in the above examples the correct noise levels were assumed to be known – which is not always the case when working with true field data. However, as demonstrated elsewhere (Morelli and LaBrecque, 1996), even if only poor noise estimates are available, reasonable inversion results are obtained by activating the iterative error adjustment procedure (see Section 3.3.5).

Second, a rough idea of the computational requirements of the complex resistivity inversion algorithm may be given. In general, of course, these are strongly dependent on the numbers of electrodes, measurements, and model parameters. However, the inversion leading to the result shown in Figure 4.4b took approximately 44 minutes on a Pentium® II, 400 MHz processor and required about 12 MB of memory. Altogether four inverse iteration steps were performed involving a total number of 31 forward model calculations.

Within the following model examples, the principles applied to generate the synthetic dipole-dipole data sets as well as to create the modeling and inversion grids are the same as in this section and thus not explicitly addressed again. Moreover, for all inversions again a homogeneous starting model was used (geometric mean of the apparent complex resistivities) and the correct noise levels were specified by means of uniform complex data errors.

→

Figure 4.4: Recovered distribution of complex resistivity by inverting the synthetic data computed from the contaminant plume model of Figure 4.1. a) Resistivity magnitude (left) and phase (right) for noise-free data. b) Resistivity magnitude (left) and phase (right) for data magnitudes and phase values contaminated by, respectively, 5 % and 5 mrad Gaussian noise. Same color scales as in a). c) Resistivity magnitude (left) and phase (right) for data magnitudes and phase values contaminated by, respectively, 20 % and 5 mrad Gaussian noise. d) Resistivity phase after carrying out additional, pure phase inversion iterations for the cases of 5 %, 5 mrad data noise (left) and 20 %, 5 mrad data noise (right), corresponding to, respectively, b) and c).

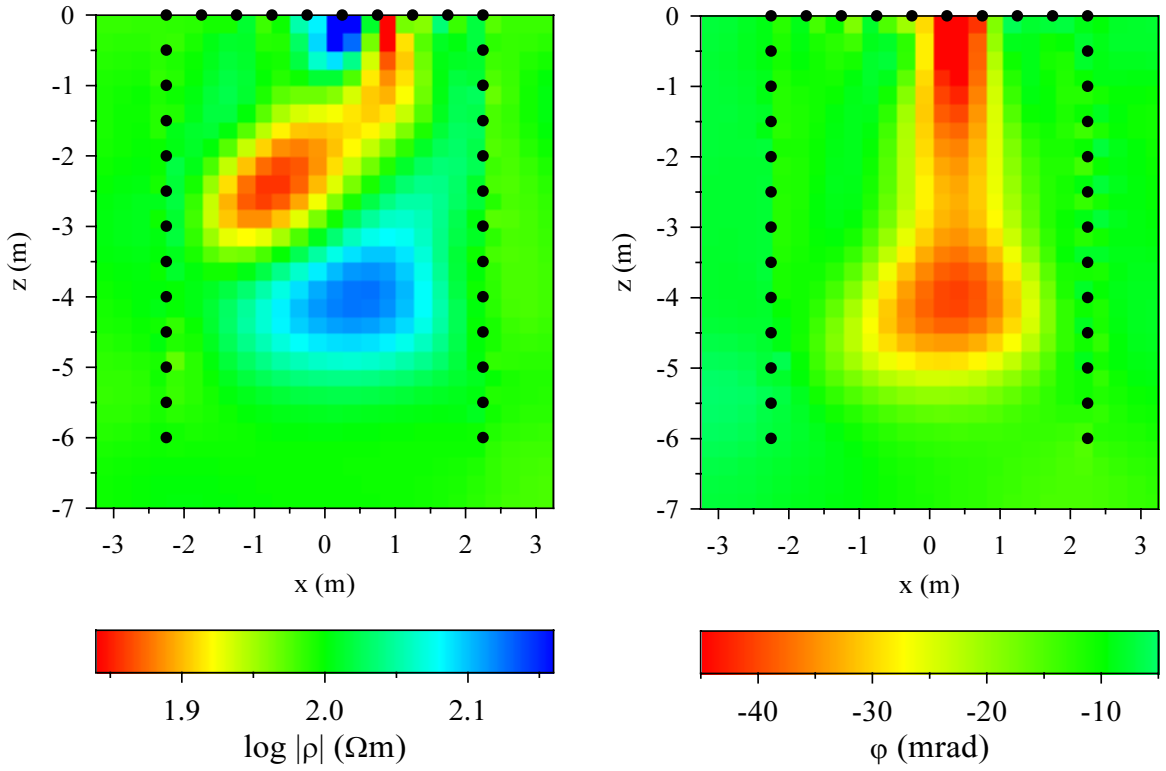

a)

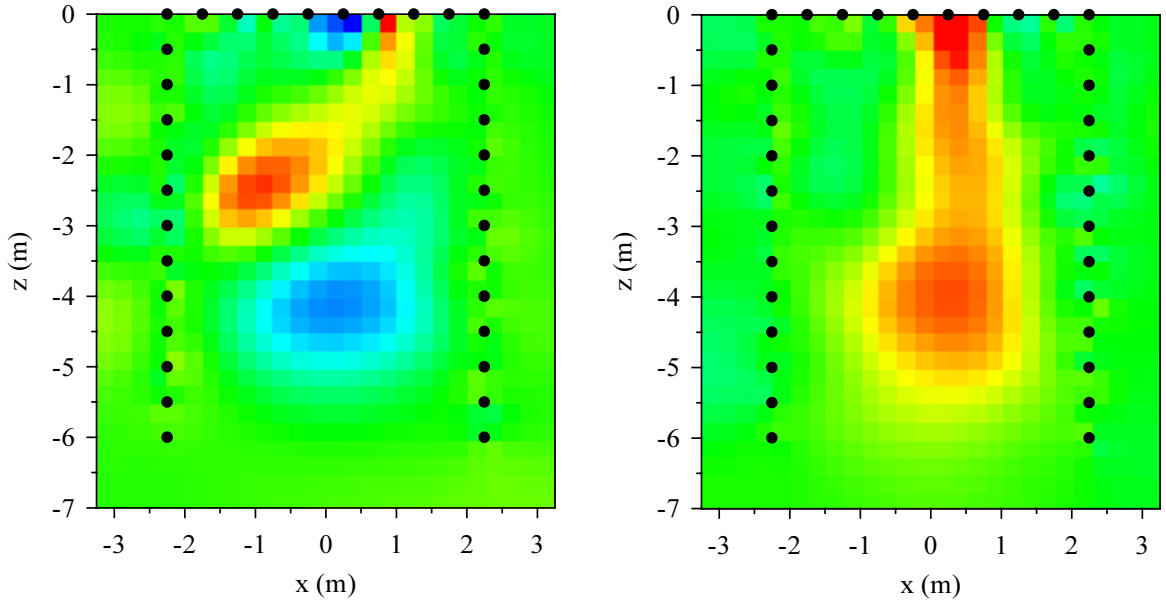

b)

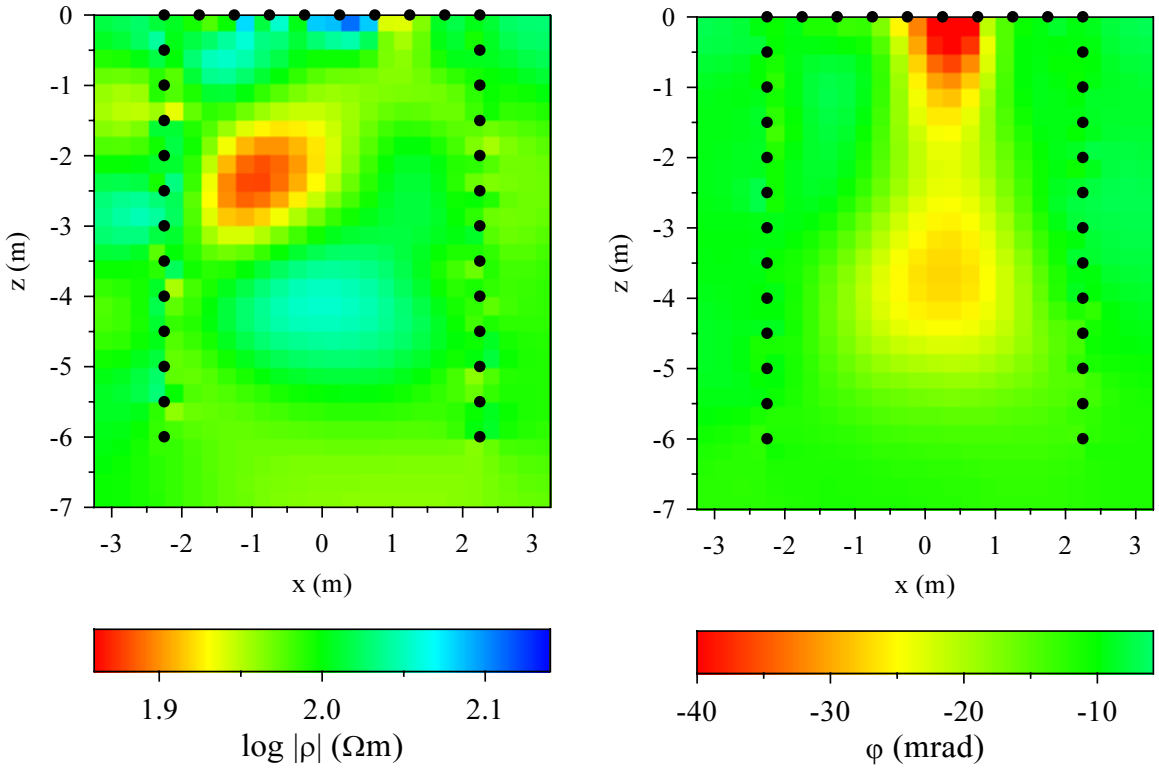

c)

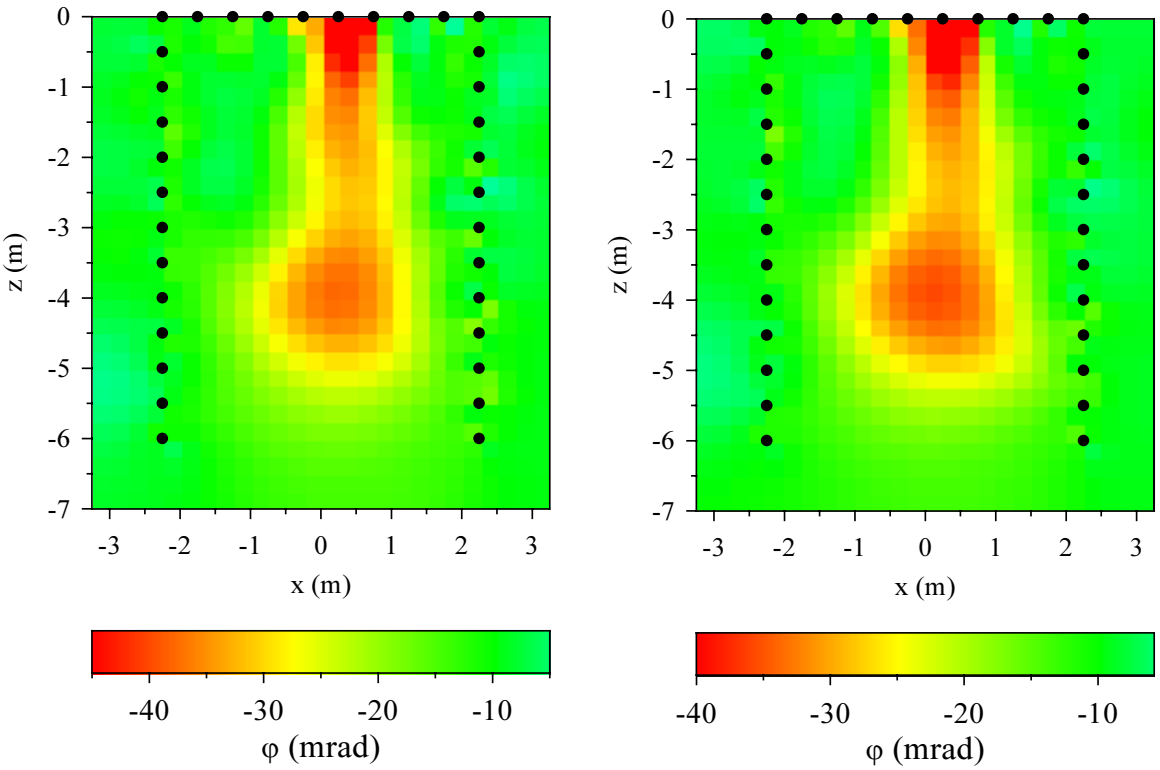

d)

Figure 4.4 (Continued).

4.2 HORIZONTAL LAYER MODEL

The basic problem faced in ground-water prospecting or hydrogeological site characterization in general is the identification, delineation, and discrimination of aquifers and aquitards. In the case of clastic, loose sediments this typically means to determine depth, thickness, and lateral extent of lower permeable clay or silt layers in contrast to higher permeable sands or gravels, because the corresponding stratification is predominantly responsible for the hydrogeological conditions (e.g., ground-water table, direction of ground-water flow, etc.). Since the membrane polarization effect in porous rocks is strongly related to pore space and grain size characteristics and, thus, also to hydraulic rock properties (see Section 2.6.2), the measurement of IP in the complex resistivity method represents an important complement to conventional DC resistivity surveys in the above regard. Therefore, a synthetic model was derived to illustrate the possibilities and limitations of the developed complex resistivity inversion algorithm in a representative, layered situation.

The model consists of two conductive, polarizable layers – representing more or less clayey/sandy silts – embedded in a comparatively resistive and lower-polarizable background – representing clay-free sands, perhaps not fully saturated (see Figure 4.5). To simulate some natural variations in sedimentation, the background itself consists of two units, a top layer (sand in a loose packing) and the actual half-space below (sand with a higher grade of compaction and thus lower porosity). Moreover, both resistive as well as both conductive units are assumed to differ slightly in their respective complex resistivity values. Note also that in contrast to the upper conductive layer, which is continuous, the lower one has a lens feature since extending only half way across the model plane.

As in the previous section, the electrodes defining the tomographic survey plane are located at the surface as well as inside two boreholes. However, in order to examine the dependence of image resolution on borehole separation, here three different crosshole geometries with z/x - aspect ratios of 2:1, 3:2, and 1:1 were set up, resulting in 31, 33, and 37 electrodes, respectively (see Figure 4.5). For each crosshole geometry a synthetic dipole-dipole data set was modeled using a finite-element mesh with $64 \times 56 = 3584$ elements. The procedure applied for the generation of the different measurement configurations is described in Section 4.1. For the present example, however, only those measurements were considered as input to the inversion with transfer resistances greater than $10^{-3}\ \Omega$ (reasonable signal strength) and absolute phase shifts less than the arbitrarily chosen value of 35 mrad. Note that the latter value approximately corresponds to the maximum (absolute) intrinsic phase shift that can be typically expected for loose sediments as represented by the present model (e.g., Vanhala, 1997; see Figure 2.6). The resultant data sets for the three electrode arrangements consist of 296, 343, and 479 measurements, respectively. For the

inversion, the magnitude and phase values of these data sets were contaminated by, respectively, 5 % and 3 mrad Gaussian noise.

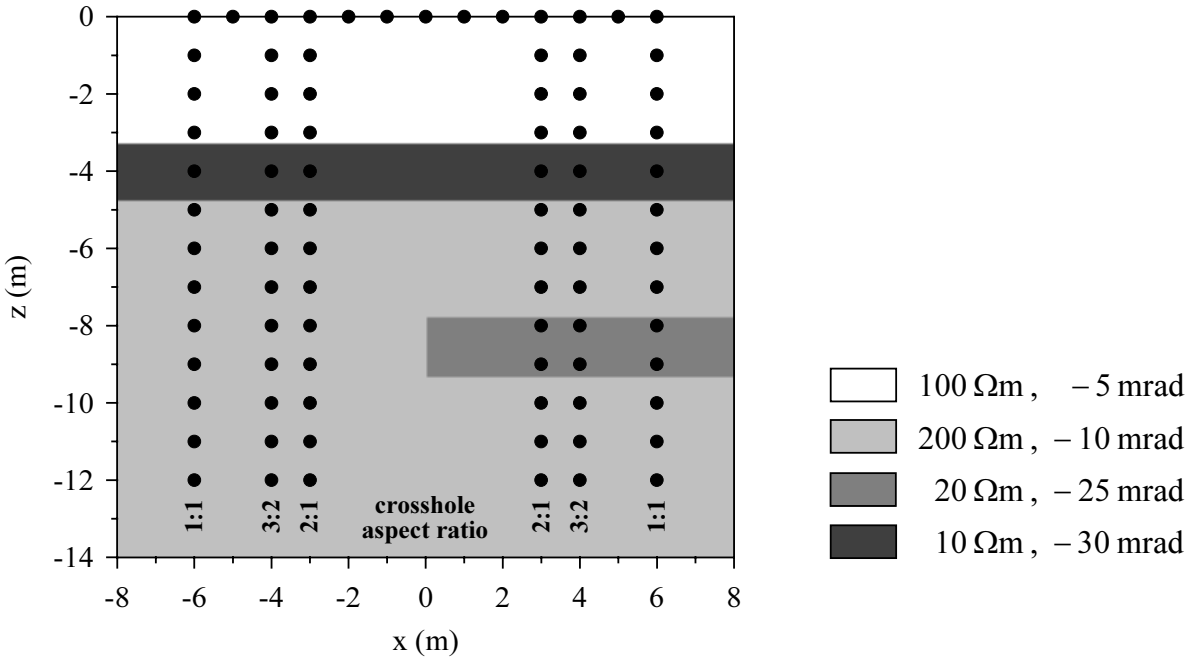

Figure 4.5: Definition of the horizontal layer model. The solid circles indicate the position of electrodes for three different crosshole image planes with z/x-aspect ratios of 2:1, 3:2, and 1:1. For each plane, only the electrodes in the two respective boreholes and the corresponding surface electrodes between them are being considered.

In the inversion, a regular parameterization with $32 \times 28 = 896$ model cells was used, i.e., two model cells per electrode separation. Note that, hence, the parameterization grid does not coincide with the true layer boundaries (cf. Figure 4.5). Consequently, the model discontinuities cannot be exactly represented in the inversion. Further, with respect to their vertical extension the conductive layers correspond to no more than two complete model cell rows, suggesting that the underlying finite-element discretization is rather poor with regard to the given parameter contrast in terms of resistivity magnitude. Since it was observed that these circumstances cause the magnitudes of some data points to be inaccurately modeled in the inversion (a fact obviously not taken into account by the assumed uniform data weighting terms), all the following inversions were carried out using both robust error estimation (see Section 3.3.5) as well as final phase improvement (see Section 3.3.6). Note that this approach is particularly attractive from a practical viewpoint, because it avoids the troublesome beforehand discarding of individual measurement configurations that may give rise to numerical problems in the inversion.

INVERSION FOR ASPECT RATIO 2:1

For the first crosshole surveying geometry with aspect ratio 2:1, the inversion was performed twice using two different types of model smoothing. In addition to the isotropic smoothing given by $\alpha_x = \alpha_z = 1$, an anisotropic smoothing with emphasis in the horizontal direction was applied because of the layered character of the target model. For this purpose, the smoothing parameters were set to $\alpha_x = 1$ and $\alpha_z = 0.1$ (see Oldenburg and Li, 1994). The corresponding inversion results in the region between the two involved boreholes are shown in Figure 4.6a.

The images of resistivity magnitude clearly reflect the upper conductive layer. In consideration of the fact that the parameterization does not coincide with the actual layer boundaries, the unit is reasonably well recovered in terms of depth, thickness, and parameter contrast. The lower conductive layer, however, is comparatively poorly resolved. This is due to several reasons. First, it takes up less volume in the subsurface than the continuous upper layer and, thus, has relatively less impact on the data set. Second, it is twice as resistive as the conductive layer above, resulting in a somewhat weaker contrast with the background. Besides these factors involving model geometry and parameter contrast, however, the most influencing factor is due to a characteristic of the method itself in that resolution decreases with increasing distances from electrodes – an aspect which is addressed again at the end of this section.

When comparing the inverted distributions of resistivity magnitude for the different choices of the smoothing parameters α_x and α_z, it is obvious that the anisotropic smoothing, imposing an increased penalty against variation in the horizontal direction, yields an image much closer to the target model. In particular, the typical, well-known distortion effects occurring in crosshole ERT images of layered earth models (e.g., Daily and Ramirez, 1995; LaBrecque et al., 1996a; Yi et al., 1997) are suppressed to some extent. Using anisotropic smoothing, the upper conductive layer actually appears as a continuous, uniform feature rather than as a convex lens.

The resultant images of resistivity phase basically exhibit the same characteristics as the magnitude images. Therefore, most of the above discussion applies here analogously. However, the improvement by applying greater smoothing in the horizontal direction is even more significant for the phase. For isotropic smoothing, the signature of the upper polarizable layer becomes extremely blurred towards the center of the image plane while the left end of the lower polarizable layer even appears erroneously bent upwards. With the anisotropic smoothing, on the other hand, both units are reasonably reconstructed. Note again that the comparatively feeble appearance of the lower polarizable layer must be attributed, in part, to the weaker underlying phase contrast.

It shall be emphasized that the discrepancies between the two inversion results express the fundamental problem of nonuniqueness inherent in resistivity surveys. However, in many practical situations certain a-priori information on the principal

spatial orientation of the subsurface structures is available. This is particularly true for hydrogeological applications, often dealing with a horizontally stratified earth. As the inversion example demonstrates, it is then recommendable to bias the inverse solution accordingly by means of an appropriate choice of α_x and α_z.

INVERSION FOR ASPECT RATIOS 3:2 AND 1:1

According to the results of the previous paragraph, for the two other crosshole aspect ratios the inversion was directly performed using an anisotropic smoothing with $\alpha_z/\alpha_x = 0.1$.

Figure 4.6b shows the recovered distribution of complex resistivity for the electrode layout with aspect ratio 3:2. For this example, an additional inversion using a twice as fine parameterization was performed in order to illustrate the general independence of the virtual character of the inversion result from the underlying model cell size. The corresponding phase image is included in Figure 4.6b. It compares reasonably well to the phase distribution obtained for the coarser model grid, expressing the insensitivity of the inversion procedure with respect to parameterization. Basically, the inverted images of resistivity magnitude and phase reveal the principal characteristics of the target model. Like for the smaller borehole separation with aspect ratio 2:1, the upper conductive, polarizable layer is clearly delineated. However, the lower layer does no more appear to extend half way across the image plane but only one-third, indicating the decreased resolution in the center between the wells (cf. Figure 4.6a).

Finally, the inversion result for the borehole separation as large as the borehole depth (aspect ratio 1:1) is displayed in Figure 4.6c. The continuous upper layer is still sharply resolved in resistivity magnitude, although with some loss in conductive contrast, but already exhibits a somewhat swelled and blurred character in the phase image. However, whereas there is still some indication for the presence of the lower conductive lens in the magnitude image, the phase only shows a general slight increase in polarizability in the whole lower part of the image plane – a fact which must be attributed to an insufficient resolving power in this region. It is thus obvious that the general resolution pattern in the image plane of crosshole complex resistivity surveys should be carefully taken into account to avoid an erroneous interpretation of the inversion results.

APPRAISAL OF IMAGE RESOLUTION

As stressed by the last example in the previous paragraph, when interpreting crosshole resistivity inversion results one must be aware of the variation in resolution throughout the image plane. Numerous factors such as electrode layout, data acquisition scheme, data accuracy, subsurface resistivity distribution, inversion approach (including parameterization and model constraints), etc. are responsible for the ultimate

resolution achieved in crosshole ERT surveys. Some basic characteristics, however, may be estimated by means of a simple sensitivity analysis or, more correctly from a mathematical point of view, by the explicit computation of the parameter resolution matrix as used in classic inversion theory[2] (see, e.g., Meju, 1994).

Whereas the latter approach is readily applicable to resistivity inverse problems in 1D and 2D situations with only a few model parameters (Inman, 1975; Tripp et al., 1984), it has been impractical for finely parameterized inversion schemes for a long time due to computational expense. In view of today's computer resources, however, recently Alumbaugh and Newman (1998) investigated the use of the parameter resolution matrix for image appraisal in 2D and 3D nonlinear tomographic inversion. Their work is based on an earlier approach of Ramirez et al. (1995), who suggested the evaluation of solely the diagonal elements of the matrix. In particular, Alumbaugh and Newman (1998) demonstrate how to calculate an estimation of the parameter resolution matrix when conjugate gradient techniques are employed to solve the inverse problem and, thus, the generalized inverse matrix is not explicitly available.

However, in the following an indirect approach for the appraisal of image resolution, based on a simple sensitivity analysis, is used as a computationally inexpensive and hence practical alternative. Rather than directly calculating how the model parameters are resolved by the data, one can examine how the data set is actually influenced by the respective complex resistivities of the model cells, or in other words, how specific areas of the imaging region are 'covered' by the data. Obviously a poorly covered region is unlikely to be well resolved and, thus, coverage may give some crude indication for resolution. It must be emphasized, however, that good coverage does not necessarily imply high resolution, but rather represents a favoring factor. Analogous to seismic tomography, where ray coverage is given by the sum of the respective ray segments in each model cell, coverage in ERT surveys may be defined as the sum of the absolute sensitivities over all measurements (e.g., Kemna, 1995). However, due to the close connection with the inverse problem's Hessian matrix, here the sum of the squared absolute sensitivities is used as the measure of data coverage. Weighting each contribution according to the corresponding data error, one thus has for the coverage of the j-th model cell:

---

[2] By assuming that the complex resistivity inverse problem is approximately linear in the vicinity of the solution, the corresponding parameter resolution matrix $\mathbf{R}$ may be calculated analogous to linear inverse problems according to (e.g., Meju, 1994)

$$\mathbf{R} = \left(\mathbf{A}^{\mathrm{H}} \mathbf{W}_{\mathrm{d}}^{\mathrm{H}} \mathbf{W}_{\mathrm{d}} \mathbf{A} + \lambda \mathbf{W}_{\mathrm{m}}^{\mathrm{T}} \mathbf{W}_{\mathrm{m}} \right)^{-1} \mathbf{A}^{\mathrm{H}} \mathbf{W}_{\mathrm{d}}^{\mathrm{H}} \mathbf{W}_{\mathrm{d}} \mathbf{A} .$$

Note that $\mathbf{R}$ shows how the model parameters are resolved by the data. In practice, however, it should be used carefully since, using the cautionary words of Meju (1994), "a perfect resolution does not imply in every respect an accurate or reliable model".

$$\sum_{i=1}^{N} \frac{\overline{a}_{ij}\, a_{ij}}{\overline{\varepsilon}_i\, \varepsilon_i} = \left(\mathbf{A}^{\mathrm{H}}\, \mathbf{W}_{\mathrm{d}}^{\mathrm{H}}\, \mathbf{W}_{\mathrm{d}}\, \mathbf{A} \right)_{jj} . \tag{4.1}$$

Note that for an unconstrained inverse problem (corresponding to $\lambda = 0$), $(\mathbf{A}^{\mathrm{H}}\, \mathbf{W}_{\mathrm{d}}^{\mathrm{H}}\, \mathbf{W}_{\mathrm{d}}\, \mathbf{A})^{-1}$ represents the parameter covariance matrix describing the uncertainties of the estimated parameters (e.g., Meju, 1994). Thus, in some way a contrary behavior of the variance of the j-th parameter and the coverage of the corresponding model cell is plausible.

Figure 4.7 shows the coverage of the crosshole image plane by the ERT measurements for the three different borehole separations with aspect ratios 2:1, 3:2, and 1:1, respectively. The displayed distributions were calculated on the basis of the final inversion results of Figure 4.6. The general geometrical pattern of coverage reveals the well-known decrease towards the center and the bottom of the image plane, indicating loss of resolution in the inverse solution. Note that the slight increase of coverage in the vicinity of the two conductive layers reflects the current channeling therein according to the principles of current flow. Recalling the afore-mentioned deficiencies of the inversion in recovering the true target model, Figure 4.7 suggests that ERT surveys should – as a rough guideline – be designed in such a manner that the coverage according to eq. (4.1), normalized by the maximum value, exceeds 10^{-3} in the area of major interest. For the present example, this would imply use of an electrode setup with a z/x-aspect ratio no smaller than 3:2.

In any case, the analysis of coverage on the basis of the measurements' sensitivities represents a useful approach for a first assessment of image quality in (complex) resistivity tomography.

→

Figure 4.6: Recovered distribution of complex resistivity by inverting the synthetic data computed from the horizontal layer model of Figure 4.5. Prior to inversion 5 % and 3 mrad Gaussian noise was added to, respectively, the data magnitudes and phase values. Note that only the region between the two involved boreholes is shown. a) Resistivity magnitude (left) and phase (right) for the image plane with aspect ratio 2:1 using isotropic smoothing ($\alpha_z/\alpha_x = 1$) and an anisotropic smoothing with emphasis in the horizontal direction ($\alpha_z/\alpha_x = 0.1$). b) Resistivity magnitude (left) and phase (middle) for the image plane with aspect ratio 3:2 using anisotropic smoothing with emphasis in the horizontal direction ($\alpha_z/\alpha_x = 0.1$). In addition, the resultant phase image for a finer parameterization is shown (right), where the same grid is used as for the computation of the synthetic data set. The color scales are the same as in a). c) Resistivity magnitude (left) and phase (right) for the image plane with aspect ratio 1:1 using anisotropic smoothing with emphasis in the horizontal direction ($\alpha_z/\alpha_x = 0.1$). The color scales are the same as in a).

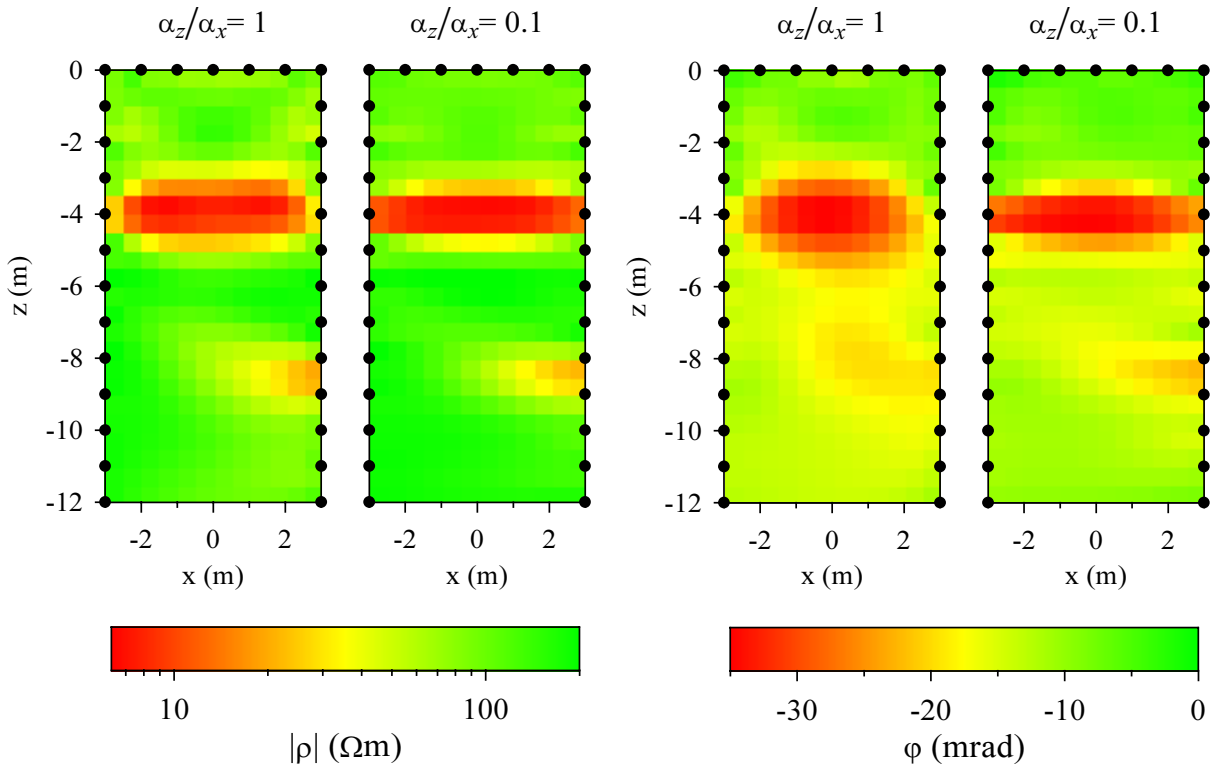

a)

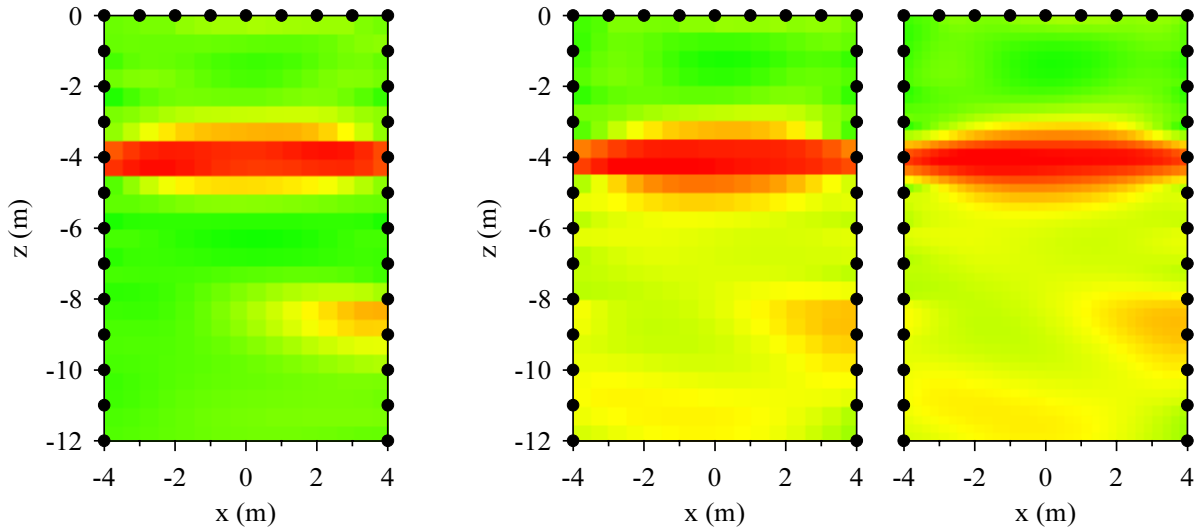

b)

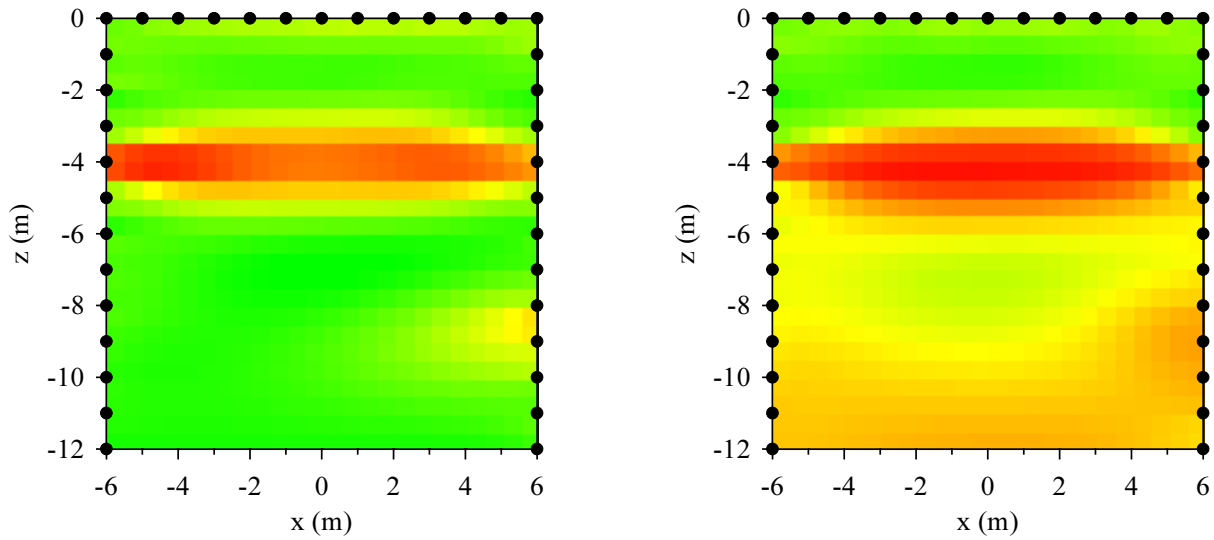

c)

Figure 4.6 (Continued).

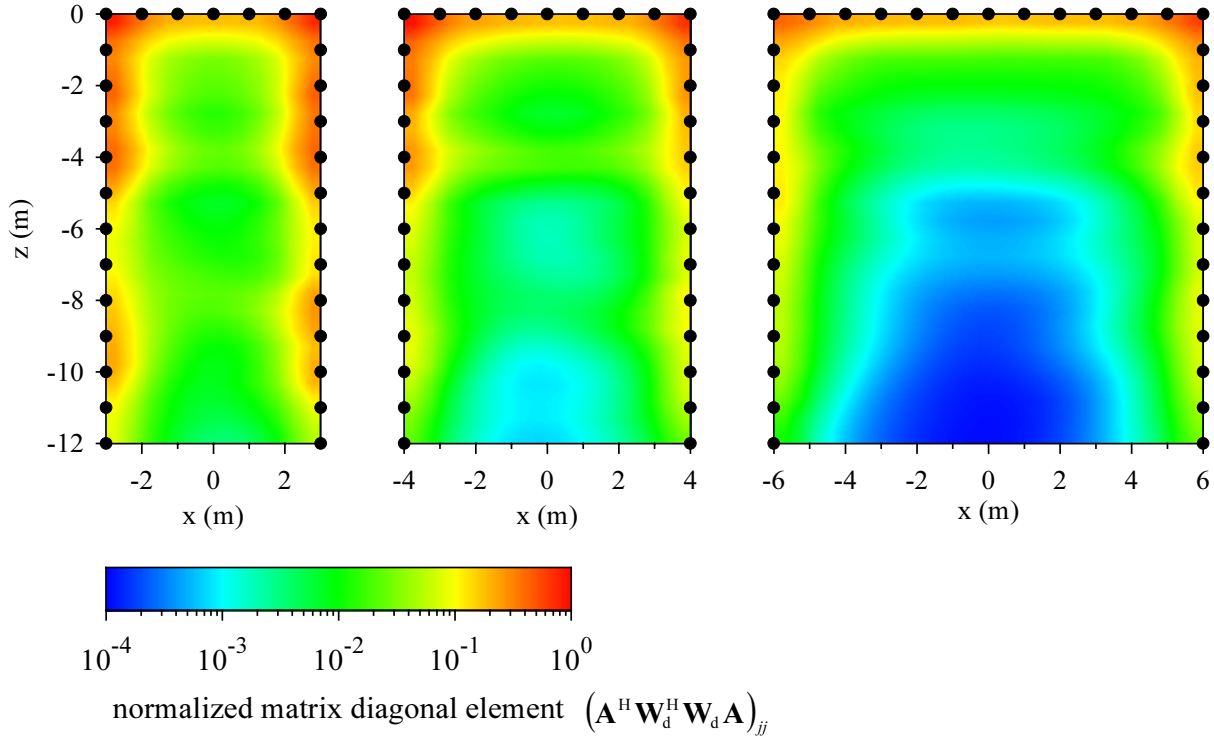

Figure 4.7: Coverage of the crosshole image plane by the tomographic measurements for the three different survey geometries, corresponding to the inversion results of Figure 4.6 for $\alpha_z/\alpha_x = 0.1$. Note that all images are normalized by the same maximum value and, thus, are quantitatively comparable.

4.3 MINERALIZATION ZONE MODEL

Because of the pronounced polarization effects occurring in mineralized rocks at the interfaces between electronic conducting mineral grains and the pore fluid, the IP method is probably most effectively applied for mineral exploration. The general intensity of the IP response and, in particular, spectral IP characteristics have been proved to help in assessing various mining-related aspects of considerable economical interest. As already discussed in Section 2.4.2, the spectral IP response of mineralized rocks is adequately described by the Cole-Cole model

$$\rho(\omega) = \rho_0 \left\{ 1 - m \left[1 - \frac{1}{1 + (i\omega\tau)^c} \right] \right\}, \tag{4.2}$$

with the four parameters DC resistivity ρ_0, chargeability m, time constant τ, and frequency exponent c. Note that for the purpose of this section, eq. (2.13) has been rewritten using eq. (2.24). Roughly speaking, m, τ, and c are related to the amount of mineralization, the dominant mineral grain size, and the type (or degree) of mineralization, respectively, and thus can be used to discriminate a mineral deposit according to its structure (see Section 2.6.1).

Whereas throughout the previous synthetic model examples only a single frequency was considered, in this section a frequency-dependent model is defined representing a realistic geological situation that might be encountered in mineral exploration. Based on the assumption of multifrequency measurements, the objective here is to investigate the suitability of complex resistivity tomography to recover intrinsic spectral IP characteristics described in terms of the Cole-Cole model in eq. (4.2). Besides the characterization of mineral deposits with respect to mineral concentration, type, and grain size, however, such a procedure may also yield useful hydrogeological information by, for instance, discriminating between mineralized and fluid-filled fractures.

The derived synthetic model is associated with a narrow, dipping fracture or shear zone bearing a significant amount of net-textured or even veined sulfide mineralization. It occurs within a lower-polarizable host bedrock exhibiting only minor amounts of disseminated mineralization (see Figure 4.8). In contrast to the surrounding host rock, the highly-mineralized fracture zone may constitute an exploitable deposit. The entire rock formation is covered by a conductive sedimentary overburden, in addition giving rise to some non-metallic polarizability characterized by relatively low intensity and little frequency dispersion. For each of the three structural areas intrinsic Cole-Cole parameters were adopted which represent typical values for the associated rock types (see Table 4.1). The dipping zone of higher mineralization grade is described by a strong IP amplitude, a moderate frequency dependence, and a large time constant, in

contrast to the host rock with lower chargeability, a somewhat more pronounced dispersive character, and a small time constant as typical for finely disseminated mineralization. Furthermore, it is assumed that the bulk resistivity of the host rock is reduced in the fracture zone on the account of electronic conduction phenomena. The spectral behavior corresponding to the assumed Cole-Cole parameter sets is illustrated in Figure 4.9.

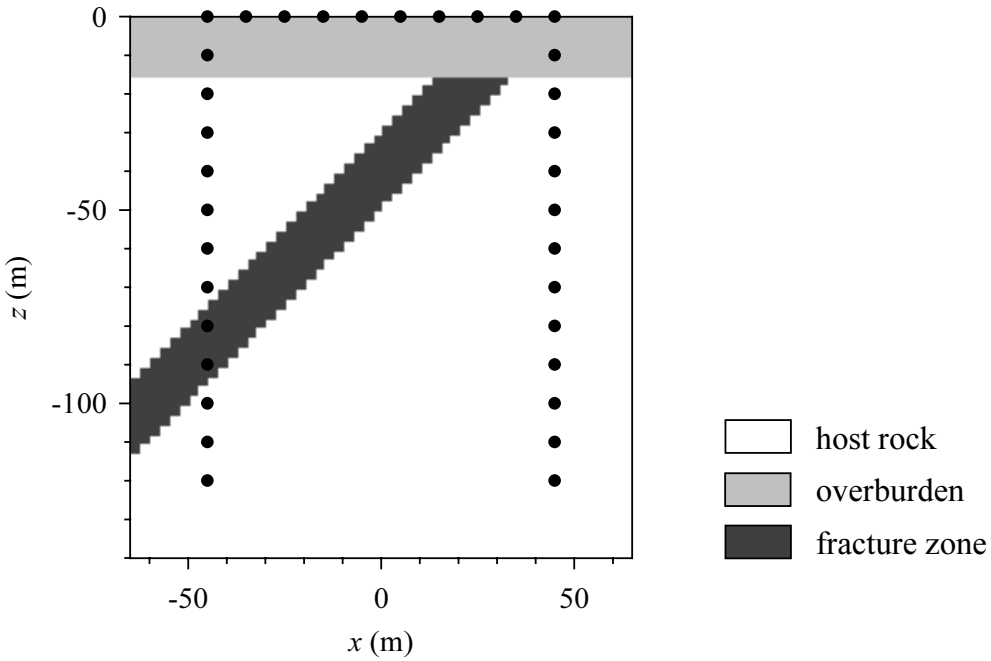

Figure 4.8: Definition of the mineralization zone model. The Cole-Cole parameters of the three different structural areas, characterizing the intrinsic spectral complex resistivity behavior, are listed in Table 4.1. For illustration, the respective phase spectra are plotted in Figure 4.9 in the considered frequency range. The solid circles again indicate the position of electrodes.

The model grids used for the computation of the synthetic data sets and the inversion, respectively, as well as the employed electrode setup and the tomographic measurement scheme are identical to those of Section 4.1. However, for the present example altogether seven different measurement frequencies covering the range from 1/64 Hz to 64 Hz are considered. The frequencies were chosen to be equally spaced on logarithmic scale, i.e., two adjacent values constantly differ by a factor of four. For each frequency a separate data set was modeled on the basis of the corresponding complex resistivity distribution (note again that in the modeling algorithm electromagnetic effects are neglected). The measurement configurations were subject to the same rejection criteria as in Section 4.1, extended by the demand of a minimum transfer resistance of 10^{-2} Ω. The resultant data sets, each of which comprising about 370 impedance measurements, were again contaminated by Gaussian noise to simulate

field data errors. In order to account for the presence of larger errors at higher frequencies, associated with the rise of electromagnetic coupling effects occurring in real field situations, the standard deviations of the noise in magnitude and phase were set to 5 % and 5 mrad for $f \leq 4\,\text{Hz}$, 7 % and 7 mrad for $f = 16\,\text{Hz}$, and finally, 10 % and 10 mrad for $f = 64\,\text{Hz}$, respectively. For analogous reasons as in Section 4.2, the inversions referred to in the following were performed with both robust error estimation and final phase improvement.

	ρ_0 (Ωm)	m	τ (s)	c
overburden (non-metallic polarizability)	100	0.25	10^{-2}	0.1
host rock (disseminated mineralization)	1000	0.1	$10^{-1.5}$	0.4
fracture zone (net-textured / veined mineralization)	500	0.4	10^{1}	0.3

Table 4.1: Intrinsic Cole-Cole parameters being used to calculate the complex resistivity values of the mineralization zone model of Figure 4.8. Note that the parameters were chosen to reasonably correspond with the associated geological sources of IP.

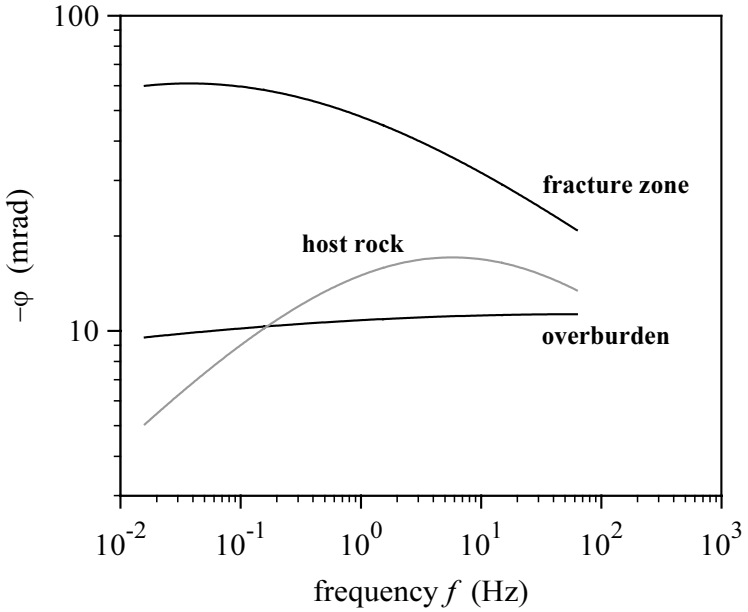

Figure 4.9: Phase spectra corresponding to the Cole-Cole parameters of Table 4.1. The curves exhibit the spectral IP characteristics of the mineralization zone model of Figure 4.8. Note that the displayed frequency range is assumed to be covered by the complex resistivity measurements.

SINGLE-FREQUENCY INVERSION

The noise-contaminated multifrequency data sets were inverted by successive application of the developed single-frequency complex resistivity inversion algorithm. Note that the procedure, at this stage, does not require the specification of the underlying relaxation model. In fact, the evaluation at a certain frequency is completely independent of the measurements at other frequencies.

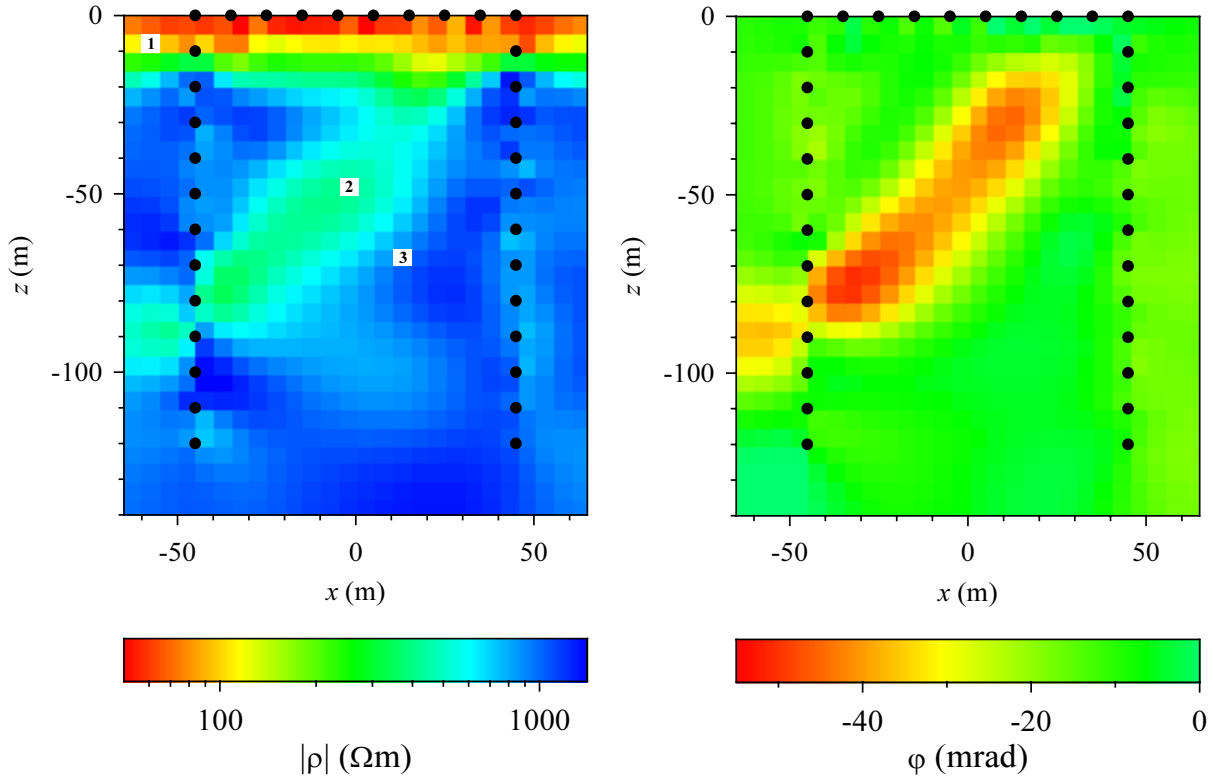

Figure 4.10: Recovered distribution of complex resistivity by inverting the synthetic data at $f = 0.25\,\mathrm{Hz}$ computed from the mineralization zone model of Figure 4.8. Prior to inversion 5 % and 5 mrad Gaussian noise was added to, respectively, the data magnitudes and phase values. The three marked model cells in the left image indicate the spatial origin of the exemplary phase spectra of Figure 4.11.

As an example of the inversion results, Figure 4.10 shows the recovered distribution of complex resistivity at $f = 0.25\,\mathrm{Hz}$. Already the image of resistivity magnitude alone does provide essential information about the general geological situation. The conductive overburden is clearly discriminated from the resistive bedrock, and also some indication for the existence of a dipping lower-resistive zone is given. Although the presence of noise has led to minor local disturbances in the image (in particular in the vicinity of the electrodes), the mean absolute values in the different structural areas compare reasonably well to those of the target model. Even though some uncertainty is left in the magnitude image with respect to the fracture zone, the image of resistivity

phase provides ultimate evidence. The region of high polarizability is remarkably well resolved, in particular in view of the fact that the assumed noise level of 5 mrad corresponds to more than 10 % of the overall phase contrast in the target model at the considered frequency (cf. Figure 4.9).

In conjunction, the images of resistivity magnitude and phase reveal the basic characteristics of the underlying mineralization zone model. This holds for both the geometrical form and arrangement of the structural features as well as the corresponding conduction and polarization properties in general. However, the information obtained by the single-frequency measurements is not sufficient for a further, more subtle characterization of the indicated mineralization.

COLE-COLE ANALYSIS

Given complex resistivity inversion results at a range of measurement frequencies it is possible to examine spectral variations in the recovered model parameters. If an appropriate relaxation model is adopted, even intrinsic spectral IP parameters may be deduced, as being demonstrated in the following for the present model example.

For each of the parameter cells a Cole-Cole model was fitted to the complex resistivity values provided by the multifrequency inversions. Since the Cole-Cole model response depends nonlinearly upon the Cole-Cole parameters τ and c, the model fitting was accomplished by means of a nonlinear least-squares inversion procedure, using simple Marquardt-regularization (see Pelton et al., 1984). For details of the implementation as being used herein it is referred to Appendix G. For illustration, Figure 4.11 shows the phase response of the fitted Cole-Cole models for three exemplary model cells corresponding to overburden, host rock, and fracture zone, respectively. It is seen that the essential characteristics of the original phase spectra in Figure 4.9 are reasonably recovered, in particular to a degree allowing clear discrimination of the curves. Note also that although the validity of the Cole-Cole model was tacitly presupposed, its appropriateness is likewise suggested from the inverted phase values alone – at least as far as the host rock and the fracture zone are concerned.

In order to gain insight into the uncertainty and correlation of the estimated Cole-Cole parameters, each of the Cole-Cole fits was performed along with the computation of the resultant parameter covariance matrix (see Appendix G). In general, the DC resistivity ρ_0 and, with some restriction, the time constant τ represent the most independent parameters in the inversion (strictly speaking this holds for $\ln\rho_0$ and $\ln\tau$ actually being used in the inversion), whereas the chargeability m and the frequency exponent c were found to be most strongly correlated (see Table 4.2). The poorest inversion results were obtained for model cells from the overburden. This, however, might virtually have been expected from the flat phase spectrum in this region, giving

only few indication for a maximum (the decisive feature in the Cole-Cole model), and the therefore often indefinite trend in the underlying phase values (see Figure 4.11).

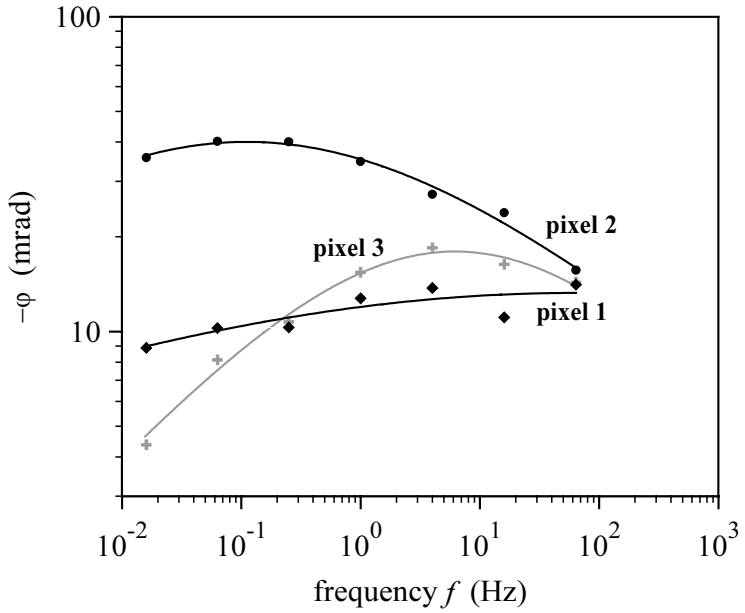

Figure 4.11: Intrinsic phase spectra for three exemplary model cells (see Figure 4.10) as recovered from the multifrequency data by means of tomographic complex resistivity inversion. Note that the selected model cells correspond to the different structural areas of the target model (see Figure 4.9). The solid curves show the phase response of the Cole-Cole models fitted to the respective inversion results.

pixel 2	$\ln\rho_0$	m	$\ln\tau$	c
$\ln\rho_0$	1			
m	0.33	1		
$\ln\tau$	0.32	0.86	1	
c	-0.30	-0.95	-0.82	1

pixel 3	$\ln\rho_0$	m	$\ln\tau$	c
$\ln\rho_0$	1			
m	0.07	1		
$\ln\tau$	0.01	-0.50	1	
c	-0.06	-0.88	0.48	1

Table 4.2: Correlation coefficients of the fitted Cole-Cole parameters for two of the exemplary phase spectra in Figure 4.11, corresponding to fracture zone (pixel 2) and host rock (pixel 3), respectively.

As a whole, the Cole-Cole analyses of the individual model cells provide continuous images of the intrinsic parameters ρ_0, m, τ, and c. Due to some degree of uncertainty in the fitted parameters along with the circumstance that each model cell was analyzed separately (i.e., without any coupling to adjacent cells), the resultant images turned out to be relatively rough though. However, a smooth image appearance may be readily achieved by the subsequent application of appropriate spatial filtering. For this purpose, the so-called α-trimmed mean filter by Gersztenkorn and Scales

(1988) was adopted, which represents a merger of mean and median filtering balanced via a scalar $\alpha \in [0, 0.5]$. Note that, in contrast to mean filtering ($\alpha = 0$), by median filtering ($\alpha = 0.5$) individual outliers are removed from the image without destroying sharp structural features or loosing parameter contrast. Here, the α-trimmed mean filter was applied with $\alpha = 0.3$, using a filter window of 3×3 model cells. The filtered Cole-Cole parameter images are shown in Figure 4.12.

The distribution of ρ_0 in Figure 4.12a distinctly delineates the given geological setup. Compared to the resistivity magnitude result of Figure 4.10, a clear improvement of image quality can be stated. This is, of course, due to two reasons. First, spatial filtering has now been applied, and second, Figure 4.12a in some way represents a merger of the individual noise-contaminated magnitude images at the different frequencies, consequently exhibiting a better signal-to-noise ratio (note that at each frequency a different ensemble of random numbers was used to represent the statistical errors). However, in addition to the geometrical delineation, Figure 4.12 now provides the possibility to characterize the type of mineralization in more detail. It thus yields essential new information as against the single-frequency results. From the characteristic time constant in Figure 4.12c, the dipping fracture zone is clearly discriminated. The corresponding values generally exceed $10^{0.5}$ s, in contrast to average values around $10^{-1.5}$ s for the host rock and less than $10^{-1.8}$ s for the overburden. In practice, from the approximate relation (2.34), one would thus estimate the mean grain size of the associated electronic conducting particles in the host rock and the fracture zone at about 0.3 mm and >3 mm, respectively. Additional textural information on the mineralization might be obtained from the distribution of the frequency exponent. In conjunction with the images of resistivity phase and the time constant, providing basic structural identification, the image of c in Figure 4.12d suggests a broader frequency dispersion in the fracture zone ($c \approx 0.3$) than in the host rock ($c > 0.35$). In a real situation, this would indicate a higher degree of mineralization in the fracture zone, involving polarization phenomena at more various spatial scales. In addition, Figure 4.12d exhibits the negligible frequency dispersion in the overburden ($c < 0.15$), typical for sedimentary rocks. Finally, it shall be noted that also the chargeability image in Figure 4.12b reveals the dipping polarizable structure. For the present example, however, the image only contains redundant (but nevertheless confirming) information on the subsurface structure – although in practice, chargeability might be best suited for a quantitative appraisal of mineral concentration.

→

Figure 4.12: a-d) Distribution of the intrinsic Cole-Cole parameters ρ_0, m, τ, and c as obtained by means of a pixel-wise Cole-Cole analysis of the multifrequency complex resistivity inversion results (cf. Table 4.1). Note that since each model cell was analyzed separately, appropriate filtering was applied to the images in order to suppress individual outliers. In the blanked areas, the nonlinear inversion procedure associated with the Cole-Cole model fitting did not converge to an acceptable degree.

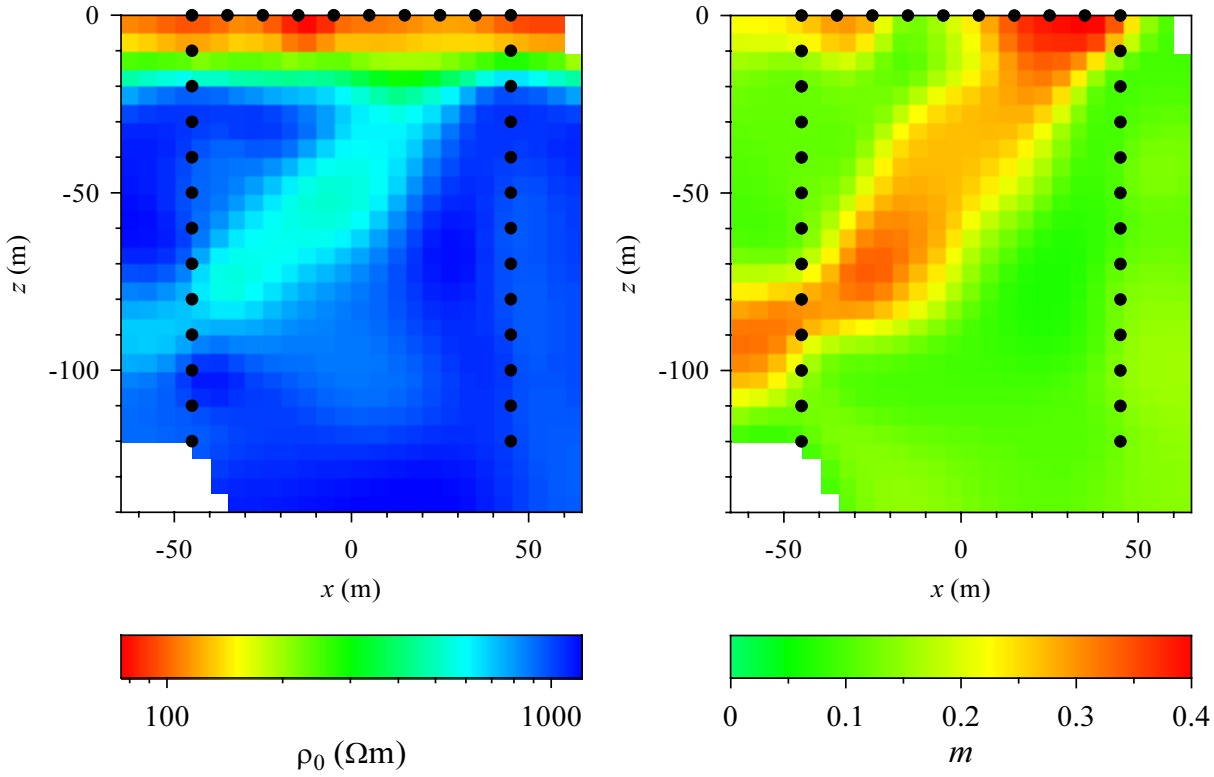
0
-50
-100
z (m)
-50
0
50
x (m)
100
1000
ρ0 (Ωm)
a)
0
-50
-100
z (m)
-50
0
50
x (m)
0
0.1
0.2
0.3
0.4
m
b)

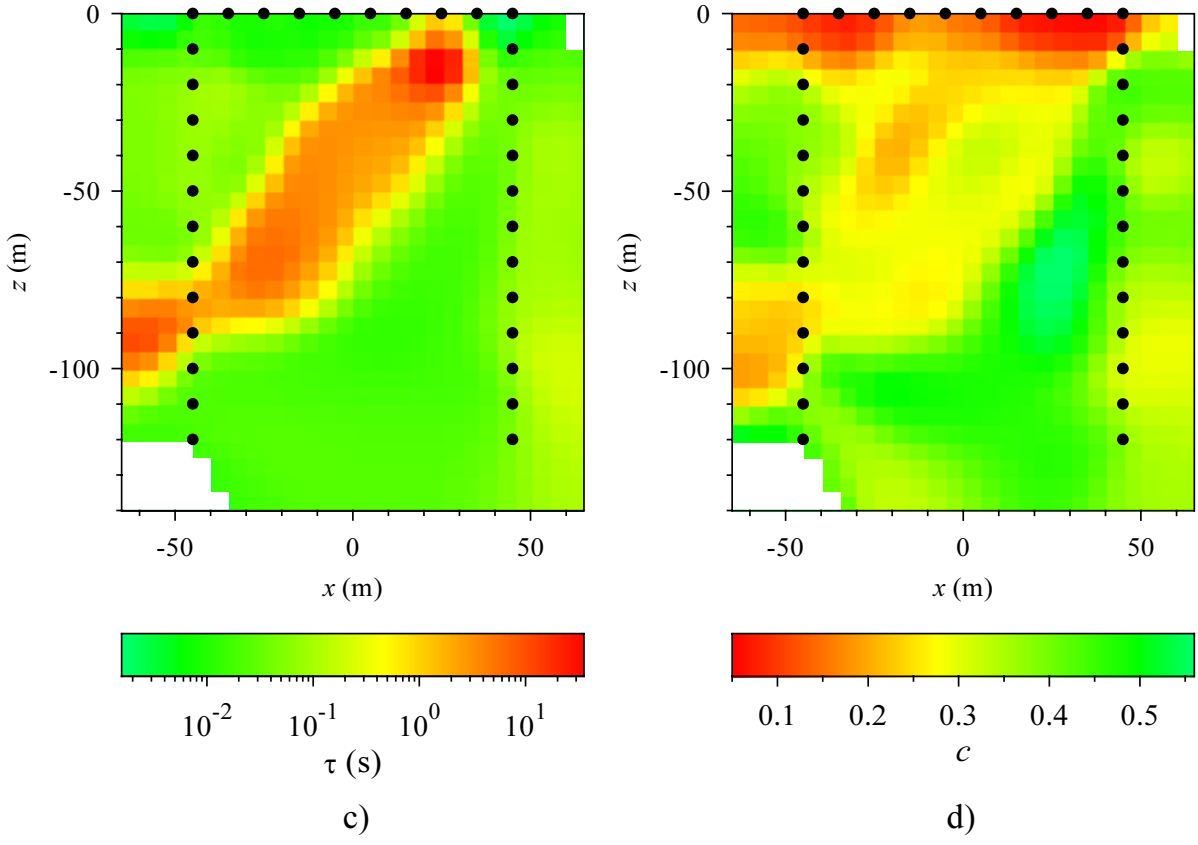
0
-50
-100
z (m)
-50
0
50
x (m)
10-2
10-1
100
101
τ (s)
c)
0
-50
-100
z (m)
-50
0
50
x (m)
0.1
0.2
0.3
0.4
0.5
c
d)

In all, the recovered Cole-Cole parameter images demonstrate the general feasibility of determining spectral IP parameters from given complex resistivity tomography results at multiple measurement frequencies. Besides the geometrical delineation of polarizable structures, the procedure may thus pave the way for source discrimination and characterization in a tomographic sense. Undoubtedly, this opens new perspectives in the geoelectrical exploration of, for instance, mineral deposits.

4.4 SUMMARY

In the preceding sections, the complex resistivity inversion algorithm developed in Chapter 3 was extensively investigated by means of synthetic model examples. The models were deliberately chosen to represent typical subsurface situations in the different fields of principal application of the method.

With the first model example of a dual contaminant plume, described by complementary conductive and polarizable properties, the general behavior of the inversion algorithm in the case of both noise-free and noise-contaminated data was examined. Different levels of noise were separately, but simultaneously, imposed on the data magnitudes and phase values in order to in particular gain insight into the magnitude-phase interaction during the inversion process and the resultant impact on the recovered images. In this context, the carrying-out of additional inverse iterations purely for the phase, a technique herein referred to as final phase improvement, was shown to be effective to overcome qualitative deficiencies in the phase image incident to extremely noisy magnitude data. Overall, the inversion algorithm proved capable of adequately recovering the assumed target model. As the inversion results indicate, complex resistivity tomography may not only be successfully applied to detect and map subsurface contamination, but also to differentiate organic and inorganic contaminant components according to their distinctive electrical signature.

Next, a horizontally stratified model was assumed as to investigate the potential of the inversion procedure in a typical near-surface sedimentary environment. The model may represent an alternated bedding of sands and silts, the arrangement of which often being of interest in hydrogeological studies. Using conventional isotropic smoothing, the recovered images of resistivity magnitude and phase were found to exhibit some geometrical distortion of the true layered conditions. The corresponding artifacts are well-known for crosshole ERT algorithms imposing L_2-smoothness on the model and point out the fundamental problem of nonuniqueness inherent in the method. By means of appropriate anisotropic smoothing, however, the inversion may be biased towards the expected model characteristics. With the choice of a vertical smoothing one order of magnitude smaller than in the horizontal direction ($\alpha_z/\alpha_x = 0.1$), a reasonable conformity with the target model could be achieved without substantially

wiping out the lateral image variations. In order to furthermore examine the influence of the borehole separation on the resolving power of the inversion, altogether three different survey geometries with z/x - aspect ratios of 2:1, 3:2, and 1:1 were simulated. The concept of sensitivity-based coverage was introduced as a simple means to quantitatively assess image resolution, with the ultimate goal of recognizing poorly resolved areas in the imaging plane. From the discrepancies between the target model and the respective inversion results for the different crosshole geometries, a minimum normalized coverage of 10^{-3} was inferred to be desirable to avoid misinterpretation. Accordingly, a minimum aspect ratio of 3:2 proved to be necessary to reasonably resolve the essential features of the horizontal layer model. However, being aware of these inherent limitations of the method, the results clearly demonstrate the general suitability of complex resistivity tomography also for hydrogeological site characterization.

The third model being used for numerical investigation was designed to represent a situation frequently faced in mineral exploration. A fracture or shear zone within a host rock was supposed to bear a significant amount of mineralization, causing a distinct IP signature. In contrast to the other synthetic model examples, the mineralization zone model was supplied with spectral properties by adopting appropriate Cole-Cole parameters for the different structural areas. However, even with single-frequency data alone, the general geological situation could be inferred from the complementary information provided by the images of resistivity magnitude and phase. On the basis of the inversion results at multiple measurement frequencies, moreover an attempt was made to recover the intrinsic Cole-Cole parameters by fitting a Cole-Cole model to the inverted complex resistivity values for each model cell. The resultant images reveal the assumed Cole-Cole parameters to a considerable extent. However, some areas are only poorly resolved due to a weak frequency dispersion and, thus, uncertainty and often strong correlation of the Cole-Cole parameters (in particular of chargeability and frequency exponent). Nevertheless, the evaluation of the intrinsic spectral parameters, achievable by applying the complex resistivity inversion algorithm to multifrequency data sets, enabled a further characterization of the IP source type. This suggests an enormous potential of the inversion method especially for mineral exploration.

5 FIELD APPLICATIONS

As indicated by the synthetic model studies in the previous chapter, complex resistivity tomography is supposed to provide valuable information for subsurface investigation in various situations. However, like any geophysical technique, the method must ultimately prove its suitability in real field applications, where the conditions are generally incomparably harder than in controlled lab-scale experiments or even numerical simulations. Only if the practical value of the method can be convincingly demonstrated, it may actually become a geophysical tool routinely employed by scientists and engineers working in the different fields of possible application.

Whereas so far, as already outlined previously, only few publications exist which are concerned with the theory of combined tomographic resistivity and IP inversion, the situation with respect to corresponding field applications is even worse – in particular with regard to complex resistivity, i.e., spectral IP surveys. One of the key objectives of this thesis was the application of the developed inversion procedure to real field data in order to assess the possibilities and limitations of complex resistivity tomography in practice. The results of these applications, together with all relevant background information, are summarized in the present chapter.

To study the method in different situations, field data from two surveys for different purposes are considered. The first example describes a complex resistivity survey conducted for environmental site characterization at a hydrocarbon-contaminated former fuel depot (Section 5.1). The second example, on the other hand, is from an IP tomography test survey for mineral exploration (Section 5.2). In addition to the actual objective of investigation, the presented surveys differ in the underlying geological environment, the target depth of exploration, as well as in fundamental survey parameters such as electrode arrangement and tomographic measurement scheme. Thus, in conjunction, both case histories are hoped to give a fair impression of what can be gained from complex resistivity tomography in realistic situations.[1]

[1] Parts of the results presented in this chapter were already published in Kemna et al. (1999) in association with this thesis.

5.1 ENVIRONMENTAL SITE CHARACTERIZATION

The first field survey presented in this chapter was entirely designed and conducted within the scope of this thesis. The ultimate objective of the survey was to evaluate the suitability of complex resistivity tomography for the detection and delineation of subsurface organic contamination in an unconsolidated sedimentary environment. Both the resultant electrical signature and the subsurface distribution and migration pattern of contaminants are strongly dependent upon the nature of the given contaminant as well as the underlying geological situation itself. A general site characterization, including lithologic and hydrogeological aspects, is therefore essential for the understanding of contamination problems and, thus, represented an additional, not less important objective of the conducted survey.

First, in Section 5.1.1 a brief description of the test site along with the associated contamination problem is given. Section 5.1.2 then contains details on electrode setup and data acquisition of the conducted complex resistivity survey. Since spectral data were collected up to relatively high frequencies, prior to inversion an inductive coupling removal scheme had to be applied, which is outlined in Section 5.1.3. After that, Section 5.1.4 covers some aspects concerning the employed inversion procedure before, eventually, the inversion results are presented and extensively discussed in Section 5.1.5. As an attempt at a more sophisticated interpretation, Sections 5.1.6 and 5.1.7 address, respectively, the Cole-Cole analysis of the spectral inversion results and the estimation of hydraulic permeability. Finally, a summary is given in Section 5.1.8.

5.1.1 SITE DESCRIPTION

The test site is a kerosene-contaminated former military tank farm near to the Strasbourg-Entzheim airport in France. Although some parts of the tank farm are still in use today for storage purposes, principal contamination of the site occurred during the period of intensive operation as a jet fuel (kerosene) depot in the years from its installation in 1957 until the early seventies. Besides occasional spillage accidents, incident to pumping or other transport operations, which may have caused massive short-term releases of jet fuel, the underground has been continuously contaminated over a long time due to slow leakage of underground storage tanks and pipelines.

Geologically, the test area is characterized by a sequence of alluvial sediments associated with the rivers Rhine and Bruche in the east and the north, respectively. The stratigraphic situation at the site, inferred from recent drillings, is sketched in Figure 5.1. Below a top loessic layer, about 1.5 m thick, follow sands and gravels in which, at a depth of approximately 9 m, a nearly 1 m thick clayey silt layer is embedded just above the water table.

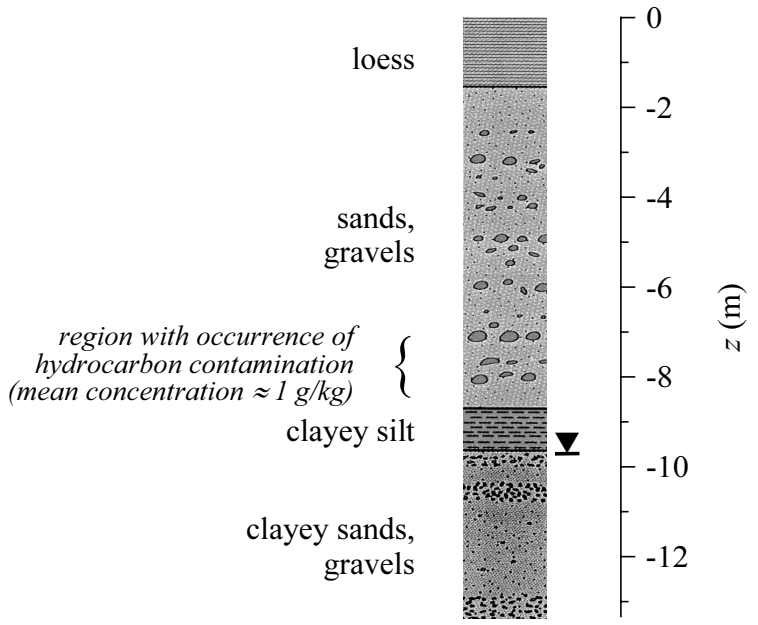

Figure 5.1: Lithologic stratification at the contaminated test site as determined from cored drillings. In addition, also the occurrence of hydrocarbon contamination as proved by chemical sample analyses[2] and the ground-water table is shown.

The jet fuel contamination was expected to having followed the typical migration pattern of light non-aqueous phase liquids (LNAPLs)[3]. Generally, an LNAPL moves downwards through the unsaturated (vadose) zone under the force of gravity until it either hits a lower-permeable formation or the ground-water table. From there lateral spreading takes place in the down-hill direction of the present lithologic barrier or (hydraulically driven) in the direction of ground-water flow (see Figure 5.2). In the latter case, due to soluble components, dissolved contaminant plumes may also develop, capable of polluting the ground water in a large area.

At the Entzheim site this scenario was confirmed by an extensive investigation programme conducted in the years 1972 to 1977, which included the installation of multiple monitoring wells (Duprat et al., 1979). Concerning the horizontal spread of contaminant it was found that an area of approximately 400 000 m^2 had already been affected by the pollutant. As expected, the contaminant plume had extended in the direction of ground-water flow. Whereas most of the contaminated area was characterized by kerosene at residual saturation, yet 80 000 m^2 exhibited mobile

---

[2] Data provided by the Institut Français du Pétrole (IFP), Paris, France.

[3] By definition, *light* non-aqueous phase liquids are less dense than water, in contrast to *dense* non-aqueous phase liquids (DNAPLs) which have densities greater than water. An overview on the distribution and migration characteristics of non-aqueous phase liquids in the subsurface may be found in Domenico and Schwartz (1998) and Fetter (1999).

hydrocarbon on the top of the low-permeable clayey silt layer and the water table right below (see Figure 5.1). Water sample analyses also proved the presence of dissolved contaminant fractions. Principal constituents thereof revealed to be aromatic hydrocarbons such as naphthalene and BTX (benzene, toluene, xylene), with concentrations amounting up to several hundreds mg/l.

Application of complex resistivity tomography was hoped to give more detailed insight into the subsurface contaminant distribution and migration pattern, in particular with a view to the influencing role of both silt layer and ground water.

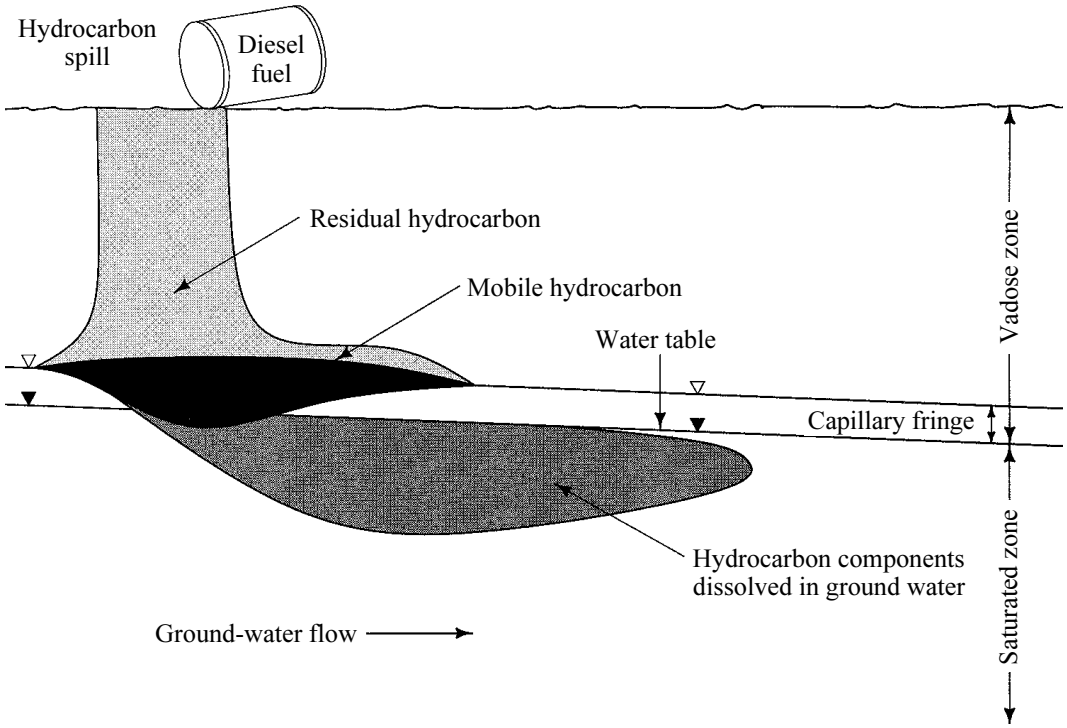

Figure 5.2: Subsurface distribution of an LNAPL spill. After Fetter (1999).

5.1.2 ELECTRODE SETUP AND DATA ACQUISITION

For the tomographic measurements four, about 13 m deep, boreholes were drilled at the test site. The separation between two adjacent boreholes was about 8 m, resulting in a crosshole aspect ratio of roughly 3:2. Herewith a reasonable coverage of the corresponding image planes was expected (see Section 4.2). The exact locations of the boreholes were selected on the basis of a previously conducted EM31[4] survey, with a view to avoiding any proximity to underground storage tanks, pipelines, or other

[4] Electromagnetic induction instrument by Geonics, Ltd., Mississauga, Canada, for ground conductivity measurements from the surface.

subsurface objects capable of negatively affecting the electrical measurements. The boreholes were equipped with 16 equally spaced electrodes[5], with an electrode separation of 0.75 m. In addition to the borehole electrodes, 10 electrodes were placed at the surface between any respective borehole pair selected for data acquisition. Thus each tomographic plane was surrounded by altogether 42 electrodes.

Although complex resistivity crosshole data were basically collected for all combinations of two adjacent boreholes, for the purpose of this thesis only a single image plane is considered for which broad-band spectral data acquisition and analysis was performed. The selected plane, however, is supposed to be representative because of the virtually layered character of the given subsurface environment. The electrode arrangement for the considered image plane is shown in Figure 5.3. Note that the lithologic log of Figure 5.1 corresponds to the left borehole thereof.

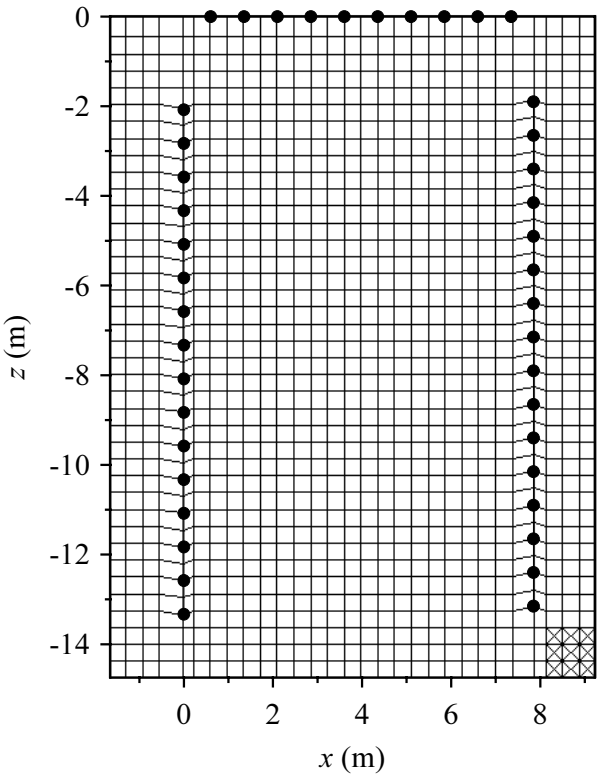

Figure 5.3: Setup of borehole and surface electrodes (indicated by the solid circles) at the test site. Also shown is the parameterization of the tomographic image plane as employed in the inversion. The underlying finite-element discretization is indicated in the bottom right corner.

In August 1997, spectral complex resistivity data were collected at seven discrete current injection frequencies, ranging from 2^{-3} Hz to 2^{13} Hz. A modular, PC-controlled

[5] For details concerning the technical implementation of the electrodes see Göbel (1998).

ERT data acquisition system by ZERO[6] was used, consisting of a battery-powered square-wave transmitter (ZT-30), a 16 bit multichannel receiver (GDP-32), and a multiplexer (MX-30) for electrode selection. Details on the system can be found in Daily et al. (1996).

The predefined set of measured electrode configurations comprised all possible dipole-dipole combinations with a fixed dipole length of two electrode separations (see Section 4.1). With regard to a reasonable estimation of the individual data errors, each measurement was repeated by use of its reciprocal configuration, i.e., with switched current and potential dipoles. This resulted in a total number of approximately 700 ($350 + 350$) measurements for the considered image plane.

5.1.3 INDUCTIVE COUPLING REMOVAL

Besides the resistive coupling of grounded electrode pairs exploited in the complex resistivity method, with increasing measurement frequency ω inductive coupling between the transmitter and receiver circuits becomes more and more effective. Inductive coupling, also referred to as electromagnetic (EM) coupling, strongly affects the shape of the observed impedance spectra and, hence, may lead to an erroneous interpretation of spectral IP effects if not taken into account.

Since electromagnetic induction is being neglected within the applied tomographic inversion procedure (see Chapter 3), any EM coupling effects in the measured multifrequency data needed to be removed prior to inversion. The employed removal technique is outlined in this section. The technique in particular requires the description of the IP response by means of a spectral relaxation model, which is thus addressed first.

MODEL DESCRIPTION OF THE IP RESPONSE

By analyzing the collected data set it was found that, in general, the phase values show some systematic variation with frequency even at lowest measurement frequencies (see Figure 5.4). Since here EM coupling effects are supposed to be negligible, this low-frequency dispersion is attributed to IP.

Obviously the Cole-Cole model represents an appropriate relaxation model which accounts for the observed phase characteristics in the low-frequency range (see Section 2.4). It was therefore adopted herein for the description of the IP contribution $Z_{\mathrm{ip}}(\omega)$ to the overall impedance $Z(\omega) = V(\omega)/I(\omega)$. Employing the Cole-Cole model in the form of eq. (4.2), $Z_{\mathrm{ip}}(\omega)$ is thus written as

$$Z_{\mathrm{ip}}(\omega) = R_0 \left(1 - r_{\mathrm{ip}}(\omega)\right), \tag{5.1}$$

[6] Zonge Engineering and Research Organization, Inc., Tucson, USA.

with

$$r_{\mathrm{ip}}(\omega) = m_{\mathrm{a}} \left[1 - \frac{1}{1 + (\mathrm{i}\,\omega\tau_{\mathrm{a}})^{c_{\mathrm{a}}}} \right]. \tag{5.2}$$

In eq. (5.1), R_0 denotes the DC resistance, which might be expressed as an apparent resistivity $\rho_{0\mathrm{a}} = G R_0$, using the geometric factor G of the given electrode configuration. Note that likewise the three other Cole-Cole parameters chargeability m_{a}, time constant τ_{a}, and frequency exponent c_{a} merely represent apparent quantities.

It shall be emphasized that the *apparent* spectral IP response in complex resistivity data originated from *intrinsic* Cole-Cole relaxation characteristics in the ground must not necessarily obey the Cole-Cole model. Strictly speaking this is only true for relatively simple geological settings, such as a finite polarizable body in a non-polarizable host rock (e.g., Luo and Zhang, 1998). However, often the shape of the observed spectra is very similar to a Cole-Cole model, which then represents a reasonable (and commonly used) approximation. Comprehensive discussions on the relationship between intrinsic Cole-Cole spectra and the resultant apparent spectra may be found in Guptasarma (1984), Liu and Vozoff (1985), Soininen (1985), and more recently, Luo and Zhang (1998). The latter authors in particular derived quantitative relations between the respective Cole-Cole parameters, yet only for simple and thus restrictive earth models.

DECOUPLING APPROACHES

The theory of EM coupling as of interest in complex resistivity surveys (see, e.g., Wait, 1959; Sumner, 1976) is in principle based on the well-known formulas for the mutual impedance between two lengths of wire on the earth (see, e.g., Sunde, 1968). Model calculations for collinear dipoles over a uniform or layered half-space (Millett, 1967; Dey and Morrison, 1973; Hohmann, 1973) have shown that in many situations of practical relevance inductive coupling initially, for ω increasing from zero, gives rise to an increase of the observed phase lag (see Figure 5.4a). By convention, this normal type of coupling is referred to as *positive*.

In general, inductive coupling may be expressed as a separate contribution $Z_{\mathrm{em}}(\omega)$ to the measured impedance, adding to the resistivity/IP term $Z_{\mathrm{ip}}(\omega)$, i.e.,

$$Z(\omega) = Z_{\mathrm{ip}}(\omega) + Z_{\mathrm{em}}(\omega). \tag{5.3}$$

The ultimate objective of EM coupling removal is thus to isolate $Z_{\mathrm{ip}}(\omega)$ from $Z_{\mathrm{em}}(\omega)$.

Simple EM coupling removal schemes are based on a power-series representation of the phase spectrum, normally using information at three frequencies (three-point

decoupling), where either a constant or linearly with log frequency varying IP phase is assumed (Hallof, 1974; Coggon, 1984; Liu, 1984).

A more sophisticated approach was originally introduced by Pelton et al. (1978a) on the basis of a Cole-Cole model description of the spectral IP response. They empirically found that in the relevant frequency range, i.e., less than 10 kHz, EM coupling spectra may be reasonably approximated by the low-frequency portion of another Cole-Cole dispersion term, that is in the case of positive coupling (e.g., Major and Silic, 1981)

$$Z_{\mathrm{em}+}(\omega) = -R_0\, r_{\mathrm{em}+}(\omega)\,, \tag{5.4}$$

with

$$r_{\mathrm{em}+}(\omega) = m_+ \left[1 - \frac{1}{1 + (\mathrm{i}\,\omega\tau_+)^{c_+}} \right]. \tag{5.5}$$

Accordingly, the nature of positive EM coupling effects is characterized by three additional Cole-Cole parameters m_+, τ_+, and c_+. Whereas m_+ may essentially vary within a similar range as its IP counterpart m_a, that is between 0 and 1, typical values are $m_+ > 0.5$ (Hallof and Pelton, 1980). The parameters τ_+ and c_+, however, are found to be significantly different from the corresponding IP parameters τ_a and c_a. Here, typical IP values of $10^{-3}\ \mathrm{s} < \tau_\mathrm{a} < 10^{3}\ \mathrm{s}$ and $0.1 < c_\mathrm{a} < 0.6$ (see Sections 2.4.2 and 2.6.1) stand opposite typical EM coupling values of, respectively, $10^{-6}\ \mathrm{s} < \tau_+ < 10^{-3}\ \mathrm{s}$ and $0.8 < c_+ \leq 1$ (Hallof and Pelton, 1980; Major and Silic, 1981). This fact manifests the basis for a successful distinction of both IP and EM coupling Cole-Cole contributions in apparent complex resistivity spectra.

It may be noted that Pelton et al. (1978a) originally proposed a multiplicative connection of the two Cole-Cole dispersions in $Z_\mathrm{ip}(\omega)$ and $Z_{\mathrm{em}+}(\omega)$, rather than the additive variant according to eq. (5.3). However, since

$$\begin{aligned} Z_\mathrm{ip}(\omega) + Z_{\mathrm{em}+}(\omega) &= R_0 \left(1 - r_\mathrm{ip}(\omega) - r_{\mathrm{em}+}(\omega)\right) \\ &\approx R_0 \left(1 - r_\mathrm{ip}(\omega)\right)\left(1 - \tfrac{1}{1-m_\mathrm{a}}\, r_{\mathrm{em}+}(\omega)\right) \end{aligned} \tag{5.6}$$

for $\tau_+ \ll \tau_\mathrm{a}$ (Major and Silic, 1981), both formulations lead to essentially the same decoupling results provided the dispersions are well separated. As pointed out by Brown (1985) though, from a theoretical point of view the additive approach is preferable.

Whereas over a moderately resistive earth normally positive EM coupling effects are observed, in the presence of good conductors coupling often exhibits an opposite spectral behavior in that the apparent phase lag decreases with increasing frequency (Hallof and Pelton, 1980). For a positive (i.e., normal) apparent IP effect, this so-called

negative EM coupling may in particular give rise to a sign reversal in the measured phase spectrum (see Figure 5.4b).

In order to account for negative coupling effects, Hallof and Pelton (1980) suggested to expand the expression for the EM coupling response from eq. (5.4) by an additional Cole-Cole dispersion term $r_{\mathrm{em}-}(\omega)$ with opposite sign, i.e.,

$$Z_{\mathrm{em}}(\omega) = -R_0\left(r_{\mathrm{em}+}(\omega) - r_{\mathrm{em}-}(\omega)\right), \tag{5.7}$$

with

$$r_{\mathrm{em}-}(\omega) = m_-\left[1 - \frac{1}{1+\left(\mathrm{i}\omega\tau_-\right)^{c_-}}\right] \tag{5.8}$$

and $m_- \geq 0$. Herein, the descriptive parameters m_-, τ_-, and c_- in principle vary within the same ranges as the parameters m_+, τ_+, and c_+, respectively, in eq. (5.5). In particular τ_- and c_- are thus likewise different from typical IP values.

If with increasing frequency initially positive and subsequently negative coupling is present in the phase spectrum (i.e., $\tau_- < \tau_+$), which is the most frequent type of a combined effect, often $\omega\tau_- \ll 1$ is found for the considered frequency range. Then the approximation $r_{\mathrm{em}-}(\omega) \approx \mathrm{i}\omega\tau_-$ holds for the special case $m_- = 1$ and $c_- = 1$, and $Z_{\mathrm{em}}(\omega)$ in eq. (5.7), with $c_+ = 1$, yields exactly the coupling formula given by Brown (1985). His derivation, however, is based on a reasonable, if greatly simplified, physical model and in that, as Brown (1985) states, may provide some theoretical legitimation to the use of the merely empirical coupling expression defined by eqs. (5.5), (5.7), and (5.8).

A final remark shall be added, following a critical discussion by Wait and Gruszka (1986) on this subject. Undoubtedly, the removal of EM coupling effects is essential for a conscientious interpretation of spectral IP data. However, any approximate decoupling scheme inevitably bears some inherent limitations from a theoretical point of view (alas no others are readily available to date). Therefore, either of these schemes should always be applied with care.

EMPLOYED PROCEDURE

In the present case, positive and negative coupling effects as well as combinations of both are found in the data, not seldom involving enormous phase changes. The various effects may be attributed to, first, the large number of different measurement geometries; using crosshole, in-hole, and hole-to-surface electrode configurations; and second, the presence of the low-resistive silt layer which is supposed to strongly affecting the inductive response.

Therefore, the general EM coupling expression of Hallof and Pelton (1980) has been adopted herein. Accordingly; using eqs. (5.1), (5.3), and (5.7); the overall mutual impedance is described by

$$Z(\omega) = R_0 \left(1 - r_{\mathrm{ip}}(\omega) - r_{\mathrm{em}+}(\omega) + r_{\mathrm{em}-}(\omega)\right). \tag{5.9}$$

This model provides a great flexibility and is hence capable of explaining all different types of coupling effects present in the data, such as phase reversals or combined positive and negative effects.

The implemented decoupling procedure is based on a Marquardt-type least-squares inversion to fit the model above to the observed spectral impedance data. In order to remove EM coupling from the entire tomographic data set, the model fitting was performed for each individual measurement configuration. Input to the inversion were the geometric mean values of the respective normal and reciprocal impedances, each comprising magnitude and phase, given at the different measurement frequencies ω_k. The inversion routine then returned estimates of the IP and EM coupling Cole-Cole parameters, the corresponding correlation matrix (providing insight into uncertainty and ambiguity in the inverted model), as well as the final data misfit as a quality measure. A comprehensive description of the inversion procedure and its implementation is given in Appendix G.

Depending on the individual character of the inductive signature in the phase spectrum (where effects are most diagnostic), either a single positive or negative coupling term ($m_+ > 0$, $m_- = 0$ or $m_+ = 0$, $m_- > 0$) or actually a combination of both ($m_+ > 0$, $m_- > 0$) was taken into account. For the latter case, however, both amplitude factor and frequency exponent of the higher-frequency response were held fixed ($m_- = 1$, $c_- = 1$ or $m_+ = 1$, $c_+ = 1$) in order to reasonably reduce the total number of unknowns in the inversion.

Once estimates of the two parameter sets describing $Z_{\mathrm{ip}}(\omega)$ and $Z_{\mathrm{em}}(\omega)$ were found, the decoupled data $Z_{\mathrm{ip}}(\omega_k)$ were simply computed by subtracting the inductive contribution from the original data $Z(\omega_k)$, i.e.,

$$Z_{\mathrm{ip}}(\omega_k) = Z(\omega_k) - Z_{\mathrm{em}}(\omega_k). \tag{5.10}$$

Note that at this stage, the actual model description of the IP effect in terms of the Cole-Cole model (5.2) is not of primary interest, but only the discrimination of IP and EM coupling effects. Thus any correlation between inverted Cole-Cole parameters corresponding to the same type of response, either IP or EM, does virtually not affect the final decoupling result (see last paragraph in Appendix G).

→

Figure 5.4: Exemplary apparent resistivity magnitude (left) and phase (right) spectra as observed at the test site. Circles and triangles indicate original data using normal and reciprocal measurement configuration, respectively. The thin solid curve shows the response of the fitted compound (IP and EM coupling) Cole-Cole model. The thick solid curve shows the IP response alone. Details on the employed decoupling procedure are given in the text. a) Positive EM coupling effect. b) Negative EM coupling effect.

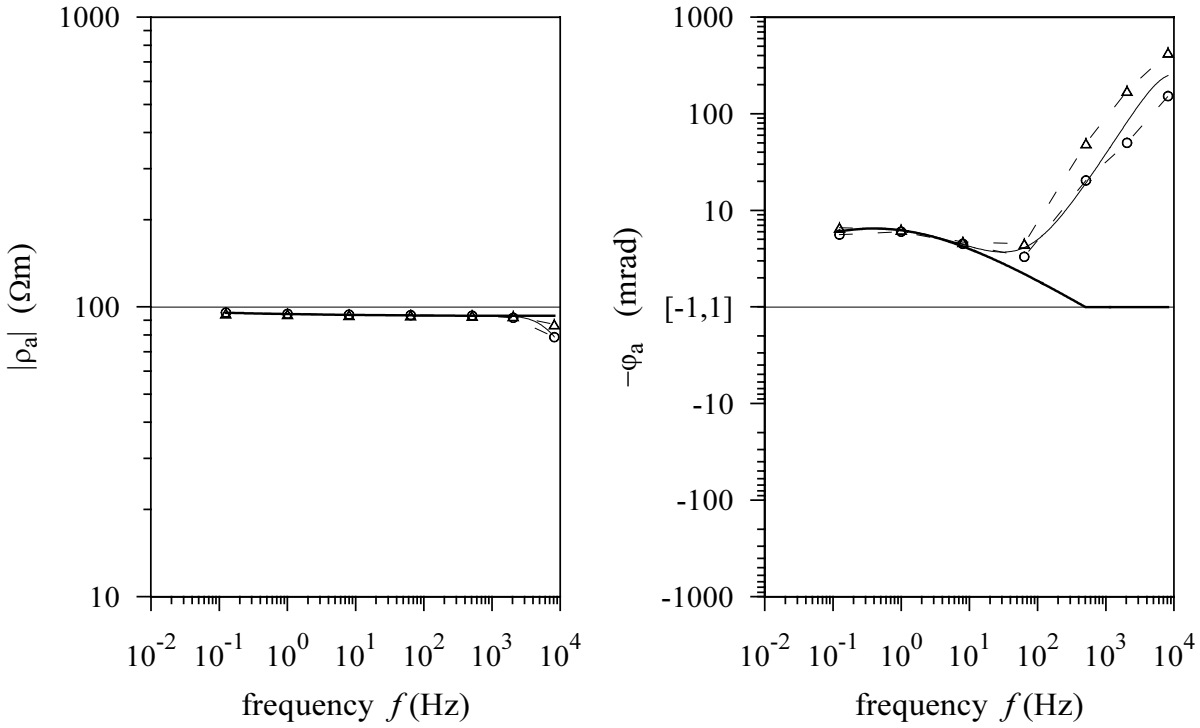
1000
100
10
$|\rho_a|$ (Ωm)
10^{-2} 10^{-1} 10^{0} 10^{1} 10^{2} 10^{3} 10^{4}
frequency f (Hz)
1000
100
10
[-1,1]
-10
-100
-1000
$-\varphi_a$ (mrad)
10^{-2} 10^{-1} 10^{0} 10^{1} 10^{2} 10^{3} 10^{4}
frequency f (Hz)

a)

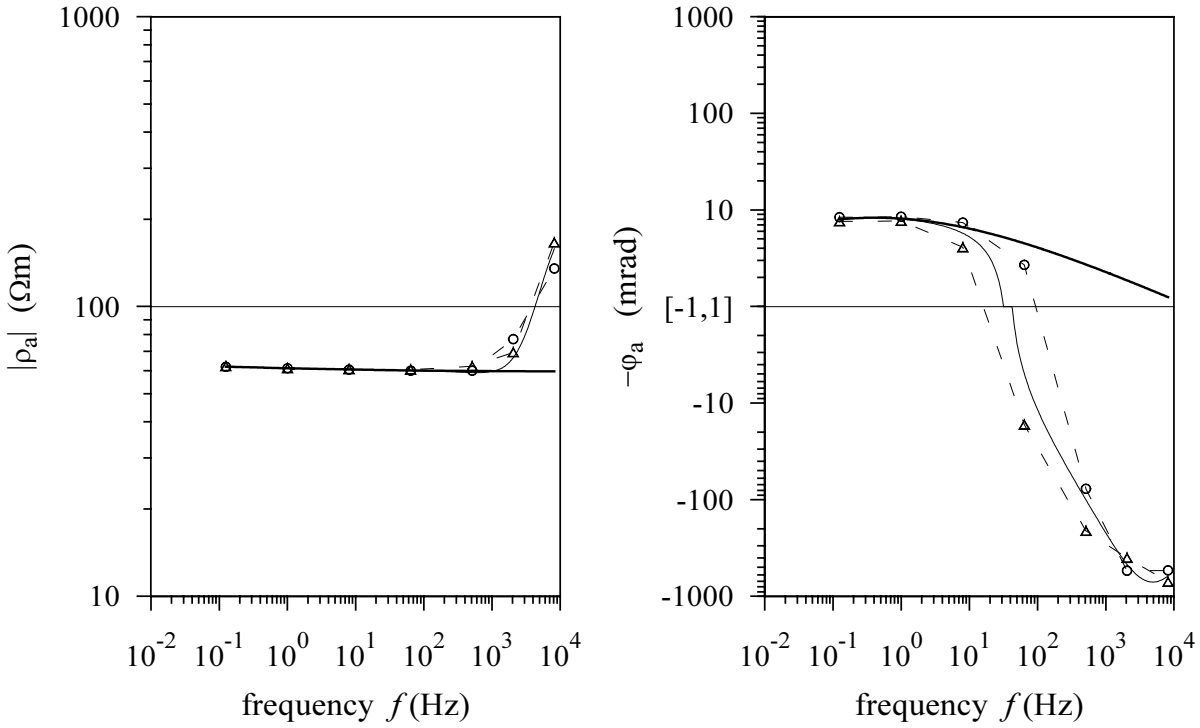
1000
100
10
$|\rho_a|$ (Ωm)
10^{-2} 10^{-1} 10^{0} 10^{1} 10^{2} 10^{3} 10^{4}
frequency f (Hz)
1000
100
10
[-1,1]
-10
-100
-1000
$-\varphi_a$ (mrad)
10^{-2} 10^{-1} 10^{0} 10^{1} 10^{2} 10^{3} 10^{4}
frequency f (Hz)

b)

Figure 5.4 shows typical apparent complex resistivity spectra as measured at the test site along with the obtained decoupling results after applying the above procedure. It can be seen that inductive coupling begins to dominate the spectral response at frequencies between 10 Hz and 100 Hz. In general, however, the phase at 64 Hz was also found to be caused, to a significant degree, by IP and, hence, up to this frequency decoupling results are considered as acceptable. Above 64 Hz, the phase behavior must be principally attributed to EM coupling, and consequently, the corresponding IP phase values are rather poorly resolved. For this reason, only the decoupled data sets at the lower measurement frequencies up to 64 Hz were actually used for complex resistivity tomography.

5.1.4 INVERSION PROCEDURE

After electromagnetic coupling effects had been removed from the multifrequency complex resistivity data, using the technique outlined in the previous section, the individual single-frequency data sets at 0.125 Hz, 1 Hz, 8 Hz, and 64 Hz subsequently acted as input to the tomographic inversion procedure.

For the inversion, the considered image plane was parameterized into 1131 model cells (see Figure 5.3), employing a standard finite-element mesh characterized by two model cells per electrode separation (see Section 4.1). In particular, the mesh was set up to account for any deviations of the borehole electrode positions from the desired regular grid.

To obviate any problems involved with an underestimation of data noise or the presence of individual data outliers, all inversions were carried out in the robust mode, i.e., with iterative reweighting of the individual data (see Section 3.3.5). Furthermore, each inversion was completed by final phase improvement (see Section 3.3.6) to avoid any loss of resolution in the resultant phase images (see Section 4.1). For all inversions a homogeneous starting model was used, the value of which given by the geometric mean of the input apparent complex resistivities.

Initially, individual data errors ε_i were obtained by rescaling the differences between original normal and reciprocal data, $\Delta d_i = d_{i\,\mathrm{nor}} - d_{i\,\mathrm{rec}}$, to some adequate noise level $\varepsilon_{\mathrm{lev}}$ according to

$$\varepsilon_i = \varepsilon_{\mathrm{lev}} \frac{\Delta d_i}{|\Delta d|_{\mathrm{mean}}}. \tag{5.11}$$

Herein, $|\Delta d|_{\mathrm{mean}}$ is the geometric mean of the $|\Delta d_i|$. For the complex inversions, a uniform value $\varepsilon_{\mathrm{lev}} = 0.05$ (equivalent to a 5 % magnitude error) was adjusted for all frequencies. For final phase improvement, however, $\varepsilon_{\mathrm{lev}}$ was set to 2 mrad for 0.125 Hz and 1 Hz, 5 mrad for 8 Hz, and 10 mrad for 64 Hz. This choice was assumed

to reasonably account for an increase of the phase error level in the decoupled data sets with increasing frequency, associated with EM coupling removal.

In view of the expected layered character of the subsurface structure (see Section 5.1.1), anisotropic model smoothing with emphasis in the horizontal direction was applied throughout the inversions. According to the synthetic model results of Section 4.2, a ratio $\alpha_z/\alpha_x = 0.1$ was supposed to be appropriate. In this context it is also worth noting that for the present case, the geology is indeed adequately represented by means of a two-dimensional model, as tacitly presumed in the inversion.

5.1.5 INVERSION RESULTS

Before actually inspecting the multifrequency inversion results with respect to spectral characteristics, first the general distribution of resistivity magnitude and phase, as similarly recovered for all considered measurement frequencies, shall be discussed.

SINGLE-FREQUENCY RESULTS

As a representative example, Figure 5.5 shows the recovered distribution of complex resistivity at the lowest measurement frequency $f = 0.125\,\mathrm{Hz}$.

It is evident that the resistivity magnitude image basically reflects the lithologic stratification at the test site as known from the cored drillings. The conductive (15-35 Ωm) clayey silt layer at a depth of approximately 9 m is clearly delineated, with both depth and thickness corresponding remarkably well with the recovered drill cores. The saturated, clayey sand/gravel formation below the silt layer is characterized by medium resistivities (35-80 Ωm). As expected, the unsaturated sand/gravel region above the silt layer exhibits distinctly higher resistivities (100-1400 Ωm). In this context, also notice the general, slight increase of resistivity magnitude towards the boreholes, suggesting some loss of resolution of the inversion towards the center of the image plane (see Section 4.2). Finally, due to the high content of clay minerals, the top loessic layer again produces a relatively conductive signature (20-70 Ωm).

If at all, the hydrocarbon contamination is expected to show resistive characteristics (see Section 2.6.2). Therefore, the nearly 1 m thick, weakly resistive (250-450 Ωm) anomaly directly above the silt layer may be associated with the occurrence of kerosene in this region (cf. Figure 5.1). However, there is no ultimate evidence for this interpretation from the resistivity magnitude image alone.

A quantitative comparison between the inverted resistivity curve with depth and the resistivity log obtained from lab measurements on core samples taken from one of the involved boreholes is shown in Figure 5.6. In principle, the displayed curves exhibit a very similar behavior, in particular reflecting the same lithologic boundaries. This fact underlines that, in addition to qualitative imaging, the inversion actually

provides accurate quantitative information. The slight shift of the lab curve towards higher resistivities, especially in the saturated zone, can be attributed to some drying up of the probes during transport and storage prior to electrical analysis. Note that the smooth character of the inverted resistivity curve is due to the applied regularization in the inversion.

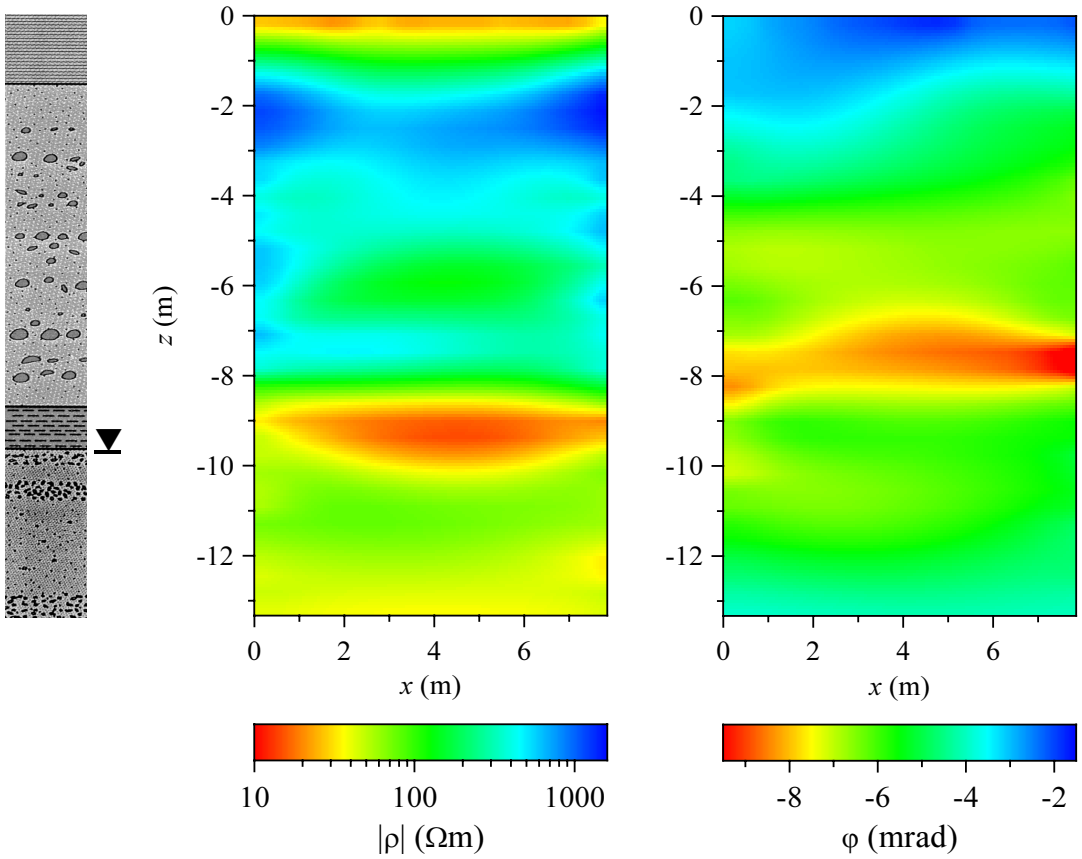

Figure 5.5: Complex resistivity inversion result at $f = 0.125$ Hz, showing distribution of resistivity magnitude (left) and phase (right) in the tomographic image plane. Note that only the region between the boreholes is displayed (cf. Figure 5.3). For comparison, also the lithologic log from Figure 5.1 is shown, actually corresponding to the left borehole.

The reconstructed image of resistivity phase in Figure 5.5 provides additional structural information on the subsurface. The lowest phase lags occur within the top loessic layer (1.5-3.5 mrad). With diminishing clay mineral content and increasing dominant pore size initially membrane polarization effects are enhanced (see Section 2.6.2). Accordingly, the (clayey) sand/gravel regions are characterized by higher phase shifts (typically 4-7 mrad), whereas the clayey silt layer again constitutes a local, if very weak, anomaly of lower polarizability. Note that the decrease of absolute phase values towards greater depths (> 11 m) might be an artifact due to an insufficient image resolution (see Section 4.2).

Although, all in all, the observed polarization effects are rather small, the phase image clearly reveals a continuous, roughly 1 m thick layer of increased polarizability (7.5-10 mrad) just on top of the silt layer (coinciding with the weak resistive anomaly in the magnitude image). According to the typical LNAPL distribution pattern as well as the results of the chemical core sample analyses (see Section 5.1.1), this distinct anomaly is expected to be an effect of the hydrocarbon contamination.[7]

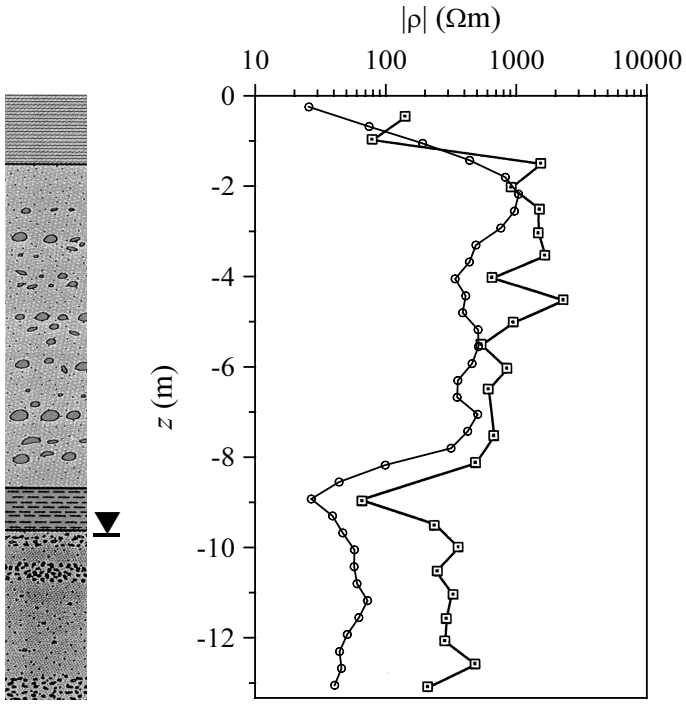

Figure 5.6: Resistivity log as determined by complex resistivity tomography (circles) in comparison to resistivity measurements conducted on recovered core samples[8] (squares). Note that the core samples as well as the shown lithologic log, replotted from Figure 5.1, actually correspond to the left borehole of the crosshole image plane. The displayed inverted resistivity values represent an exemplary pixel column, 0.5 m apart from the left borehole, of the tomographic inversion result from Figure 5.5.

To support this interpretation, however, an additional complex resistivity survey was conducted in an unpolluted area up-gradient of the tank farm, basically exhibiting the same geology as at the contaminated test site. The corresponding magnitude and phase inversion results thus served as reference images from a 'clean' region. In

[7] Note that a possible increase of partial water saturation above the low-permeable silt layer would be unlikely to explaining the observations: With increasing water content the phase lag typically decreases (see Section 2.6.2).

[8] Data provided by the Institut Français du Pétrole (IFP), Paris, France.

particular, this reference survey proved the absence of the afore-mentioned increased IP effect directly above the silt layer at the uncontaminated site (see Figure 5.7). This result also indicates that the phase anomaly is likely to be caused by the contamination. Note, however, that a different phase behavior is also observed within the silt layer itself (see Figure 5.7). It therefore appears that the silt horizon is affected by the contamination as well, albeit to a minor degree.

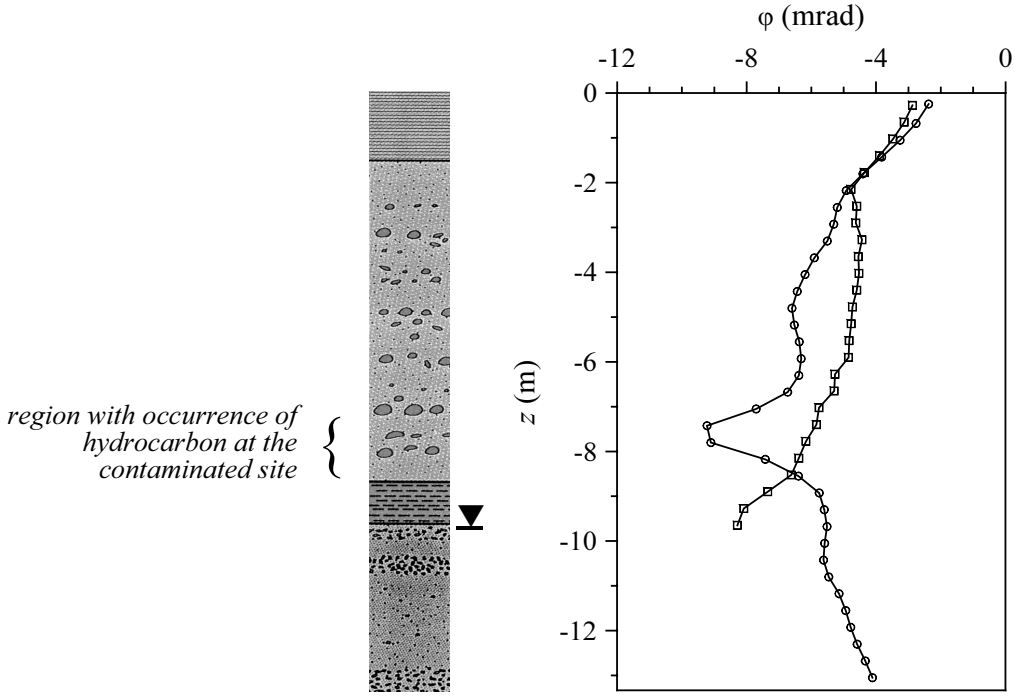

Figure 5.7: Vertical distribution of resistivity phase at the contaminated test site (circles) and an uncontaminated reference site (squares) as determined by complex resistivity tomography. The displayed curves represent exemplary pixel columns of the respective tomographic images (cf. Figure 5.5). Note that at the reference site, the exploration depth is less due to a slightly different electrode setup. The lithologic log, replotted from Figure 5.1, however, reflects the geology at both sites.

A possible explanation of the increased IP effect in the sand/gravel layer might be that, even at residual saturation, the contaminant – as a non-aqueous phase liquid – to some extent obstructs the pore passages. Due to this, the influence of any existing double layers on ion mobility may be increased, ultimately resulting in stronger membrane polarization effects (see Section 2.3.2). Similar observations of an increased IP effect in a sand/gravel environment due to the presence of a subsurface jet fuel plume are reported by Morgan et al. (1999). Note, however, that the numerous laboratory measurements on soil and rock samples to date have revealed a wide palette of different possible effects of hydrocarbons on the conduction and polarization properties (see Section 2.6.2). These depend on aspects such as contaminant type,

water content, clay content, and pore space characteristics. Presently, it is therefore difficult to reliably predict the electrical signature of such contaminants in a given geological environment.

The presented complex resistivity inversion result, with complementary information provided by magnitude and phase, demonstrates the potential of the method for environmental site characterization – in particular comprising the delineation of hydrocarbon contamination – even if only a single current injection frequency is available. For the present case, the lithologic stratification is reflected by the magnitude image, whereas the phase image gives clear indication regarding the subsurface distribution of the jet fuel contamination. The latter interpretation is inferred from results from chemical sample analyses and an in-situ reference survey over an unpolluted underground. Accordingly, the kerosene has accumulated on top of the low-permeable clayey silt layer, forming a continuous, about 1 m thick contaminated layer. Mean contaminant concentrations in this region were determined to about 1 g/kg. It is not clear, however, how far the contamination has penetrated through the silt layer itself until finally reaching the ground-water table below – the ultimate barrier for an LNAPL. Complex clay-organic reactions may have taken place (e.g., King and Olhoeft, 1989) affecting both chemical and electrical characteristics and, hence, making contaminant identification difficult.

SPECTRAL RESULTS

As already mentioned earlier, a particular objective of the conducted test survey was to investigate the general possibility of resolving any characteristic changes of the subsurface electrical properties with frequency by means of multifrequency complex resistivity tomography. Accordingly, the inversion was successively applied to the different decoupled, single-frequency data sets ranging from 0.125 Hz to 64 Hz. The corresponding inversion results are three-dimensionally visualized in Figure 5.8.

The slices of resistivity magnitude in Figure 5.8 reveal only minor variation with frequency. They exhibit lateral rather than spectral changes, suggesting that the principal frequency dependence of resistivity magnitude is, if at all, beyond the resolution of the method. An exception is observed at the slice at 1.5 m depth, which shows some systematic increase of resistivity with increasing frequency, especially in the middle of the image plane. Nevertheless, basically an identical stratification can be inferred from the 64 Hz as from the 0.125 Hz result.[9]

---

[9] Note that if only resistivity magnitude would have been of interest (as in conventional ERT), the survey could have been conducted at a relatively high frequency – avoiding time-consuming and thus expensive low-frequency measurements – without loosing essential geological information.

The corresponding slices of resistivity phase, however, are much more diagnostic with respect to spectral characteristics. A clear dispersive behavior is found for nearly all depths. Within the top loessic layer the phase lag almost steadily increases with increasing frequency, indicating that the responsible relaxation phenomena operate at relatively high frequencies. For depths greater than 10 m, in the saturated sand/gravel region, just the opposite behavior can be recognized, namely a light decrease of polarizability towards higher frequencies. The spectral behavior of most of the slices, however, is characterized by a more or less sharp and significant phase maximum (in terms of absolute values) occurring within the covered frequency range.

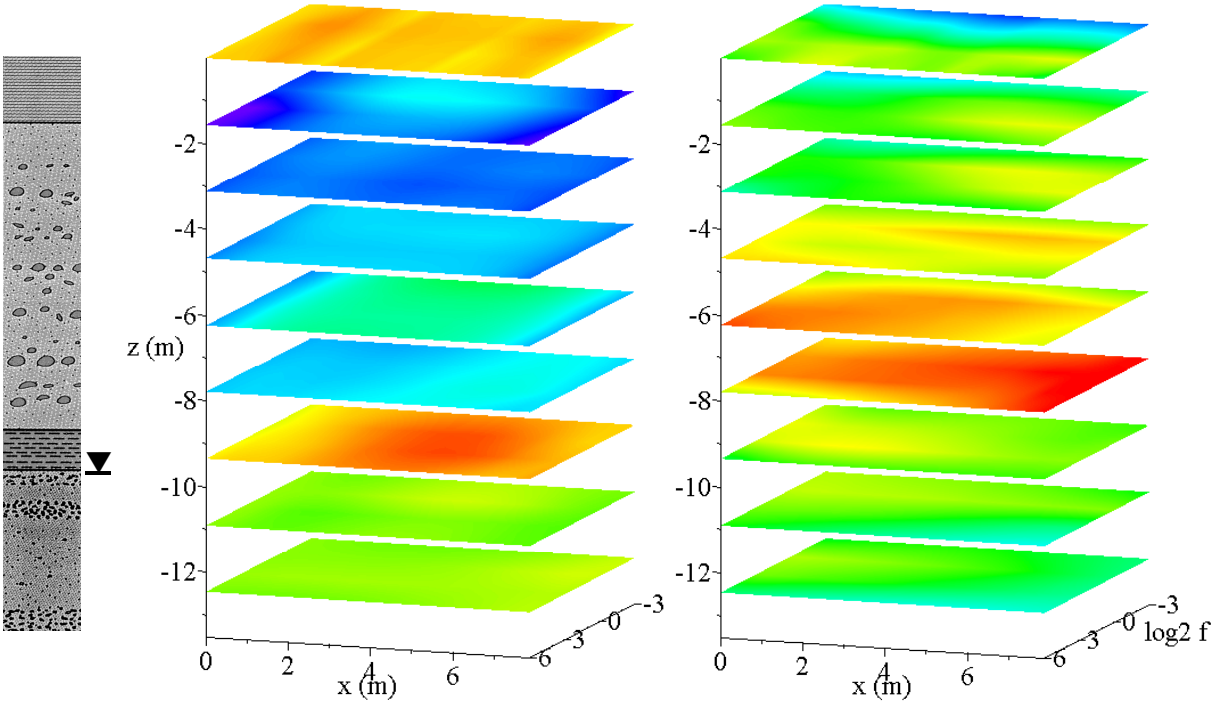

Figure 5.8: Frequency dependence of resistivity magnitude (left) and phase (right) in the tomographic image plane as determined by multifrequency complex resistivity inversion. The slices show the horizontal variation between the boreholes (cf. Figure 5.5) as well as the interpolated spectral variation from 0.125 Hz to 64 Hz at different depth levels. Note that the frequency axis is descending, i.e., frequency decreases into the paper plane (labels are in $\log_2$ of the frequency in Hz). The underlying color scales are the same as in Figure 5.5.

Obviously, the multifrequency phase inversion results contain additional structural information not available with a single-frequency approach. For instance, the phase maxima may be directly related to characteristic relaxation times of the associated polarization processes (see Section 2.4). Such an interpretation, however, requires the quantitative analysis of the spectral results on the basis of an appropriate relaxation model, which is addressed in the following section.

5.1.6 COLE-COLE ANALYSIS

In order to assess the observed frequency dispersion quantitatively and, moreover, connect it with specific pore space characteristics, the multifrequency inversion results were analyzed by means of the Cole-Cole relaxation model. Note that the Cole-Cole model has already been adopted to describe the spectral behavior of the underlying data within the context of EM coupling removal (see Section 5.1.3).

The analysis was accomplished by fitting a Cole-Cole model to the inverted complex resistivity values for each model cell in the tomographic image plane (see Section 4.3 and Appendix G). By this, tomographic images of the intrinsic Cole-Cole parameters were obtained, fully describing the dispersive character in the complex resistivity inversion results. In particular the images of the time constant τ and the frequency exponent c were hoped to provide more insight into structural characteristics and are thus discussed below.

TIME CONSTANT

The Cole-Cole time constant is directly related to the spatial scale at which the relaxation processes take place in the pore space and, consequently, contains indirect grain size information (see Section 2.6.2). This fact is clearly reflected in Figure 5.9a, showing the resultant τ image for the present survey. Smallest values (< 0.02 s) are found near the surface, corresponding to the high portion of silt-sized particles characteristic for loess. Beneath, medium time constants (0.02-0.1 s) characterize the (unsaturated) sand/gravel formation with clearly larger grains. Note that Figure 5.9a suggests some variability of the mean grain size in this region.

Strictly speaking, τ may only be associated with the electrically effective part of the pore space. Besides pore space geometry, however, this is strongly dependent on the actual degree of water saturation. At residual saturation, i.e., in the (upper) vadose zone, water is adhesively held only within a small film around the grains (the so-called pendular ring), consequently implying comparatively small relaxation times. For fully saturated conditions, on the other hand, the entire pores are made available for relaxation phenomena, suggesting a shift thereof towards larger time constants. These circumstances are likely to be responsible for the significant increase of τ in the saturated sand/gravel region below the silt layer (> 0.15 s) and, as compared to the top loessic layer, within the silt layer itself (typically 0.1 s). Note that again low credibility should be assigned to the decrease of τ towards the lower edge of the image (see Section 5.1.5).

Finally, Figure 5.9a exhibits increased τ values in a thin layer directly on top of the silt layer. Following the interpretation of Section 5.1.5, this anomaly is likely to be an effect of the contamination, indicating that the contaminant predominantly affects the wider parts of the pore space.

FREQUENCY EXPONENT

In contrast to the time constant τ, determining the position of the Cole-Cole phase maximum along the frequency axis, its broadness is described by the frequency exponent c. As already outlined elsewhere (see Section 2.6.2 and Appendix A), for sedimentary rocks c may be regarded as an indirect measure of grain size sorting. A broad grain size distribution should normally likewise originate a broad spectral dispersion, due to relaxation phenomena simultaneously occurring at various spatial scales. According to Figure 5.9b, the loessic layer exhibits the largest c values (> 0.4), i.e., the sharpest dispersion, in conformity with the relatively good sorting of loess. Lowest values of c (< 0.2) occur within the unsaturated sand/gravel region, indicating a rather poor sorting therein.

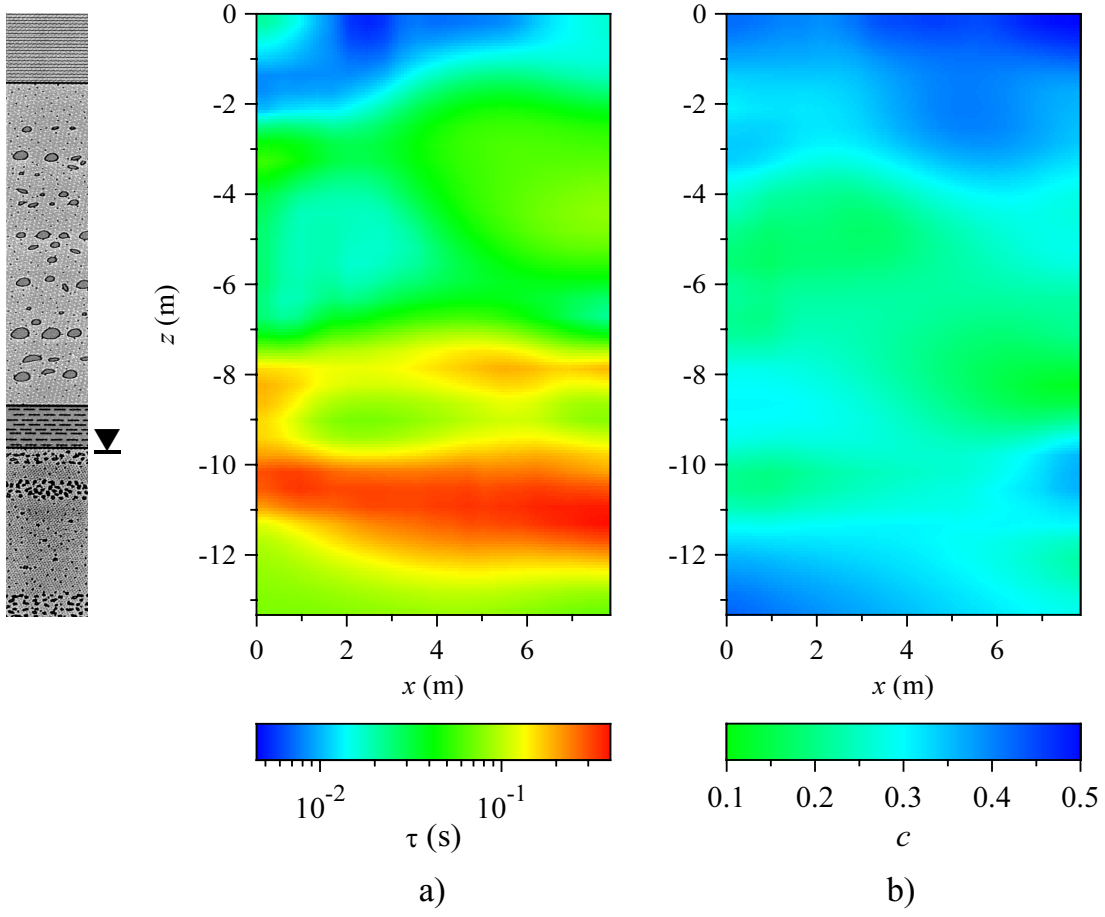

Figure 5.9: Distribution of intrinsic Cole-Cole parameters as obtained by means of a pixel-wise Cole-Cole analysis of the multifrequency complex resistivity inversion results of Figure 5.8. Note that only the region between the boreholes is shown. a) Time constant τ. b) Frequency exponent c.

In order to verify the postulated correlation of frequency exponent and grain size sorting, recovered core samples from the site were subject to granulometric analyses, the results of which were then compared with the tomographic inversion results of Figure 5.9b. As an example, Figure 5.10 and Figure 5.11 show, respectively, the ascertained grain size distribution for a sample from the silt layer and the inverted phase spectrum for a corresponding model cell of the tomographic image plane. Also plotted in Figure 5.11 is the fitted Cole-Cole model response, with corresponding parameters given in Table 5.1.

The spread of the log grain size distribution may be expressed as the deviation $\log_{10}(r_{90}/r_{10})$, where r_{10} and r_{90} are the grain sizes at which the log grain size cumulative frequency equals 10 % and 90 %, respectively (see Appendix A). For the sample of Figure 5.10, the values $2r_{10} \approx 3\,\mu m$ and $2r_{90} \approx 60\,\mu m$ were found, resulting in $\log_{10}(r_{90}/r_{10}) \approx 1.3$. Based on the approximate relation (A.3), on the other hand, from the corresponding frequency exponent in Table 5.1, $c \approx 0.33$, the spread of log grain size distribution is estimated to $1/2c \approx 1.5$. Thus, the electrically (and in-situ) determined result is in fair accordance with the true value obtained from granulometric lab analysis.

Although only of exemplary character, the above consideration suggests the general possibility of assessing grain size sorting from the recovered frequency dispersion. For the present survey, however, the frequency band of barely three decades covered by the spectral measurements is relatively narrow (in view of the typically broad dispersion of sedimentary rocks), and consequently, the frequency exponent in Figure 5.9b is rather poorly resolved. This fact is also reflected by the generally strong correlation between c and chargeability m in the fitted Cole-Cole models (see Table 5.1). Furthermore, much more research is actually required to thoroughly derive and prove quantitative relations between granulometric and spectral IP parameters suitable for practical use. The simple relation employed herein is only of approximative nature and may have restrictions in certain situations.

ρ_0 (Ωm)	m	τ (s)	c
23	0.05	0.10	0.33

	$\ln\rho_0$	m	$\ln\tau$	c
$\ln\rho_0$	1			
m	0.04	1		
$\ln\tau$	0.02	0.38	1	
c	-0.03	-0.96	-0.37	1

Table 5.1: Fitted Cole-Cole parameters (left) and correlation coefficients thereof (right) for the exemplary phase spectrum in Figure 5.11.

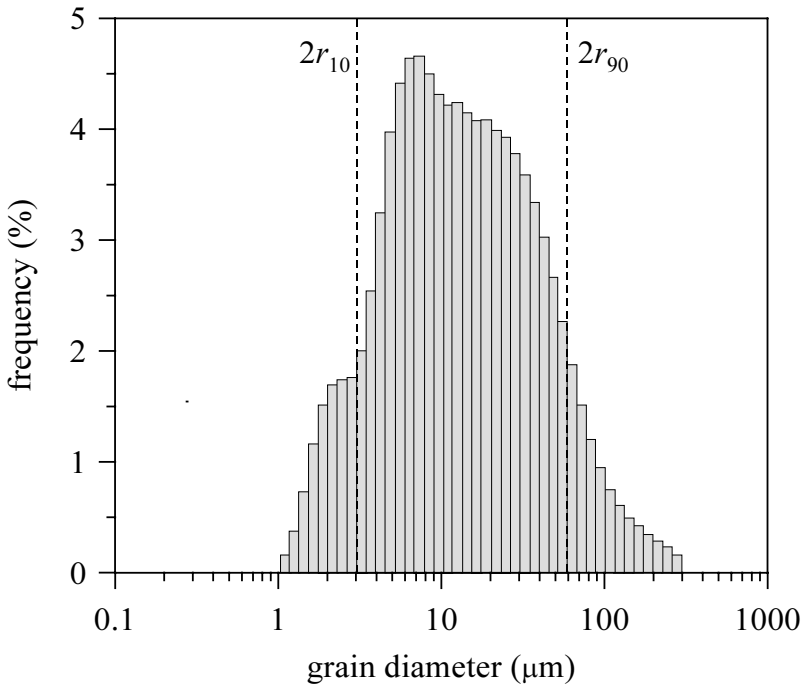

Figure 5.10: Grain-size distribution for a recovered core sample from the clayey silt layer as determined by granulometric measurements.[10] Note that the dashed lines indicate the grain sizes which have a cumulative frequency on logarithmic scale of 10 % and 90 %, respectively, serving as a measure of the spread of the distribution.

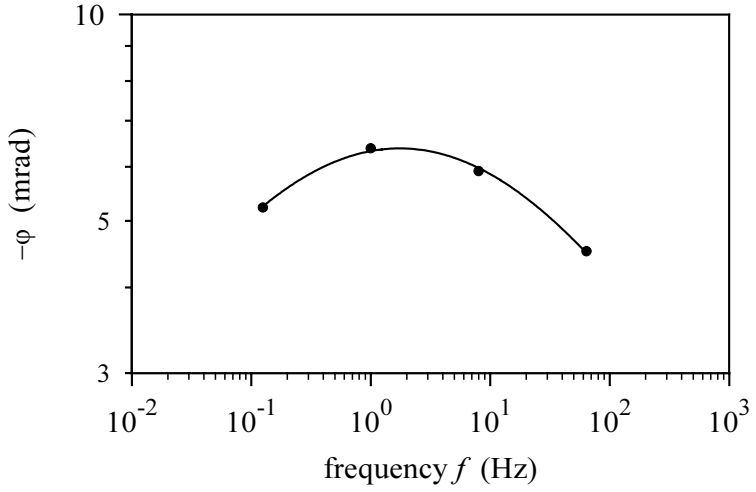

Figure 5.11: Exemplary intrinsic phase spectrum, showing multifrequency inversion results (circles) and fitted Cole-Cole model response (solid curve), for a representative model cell from a depth corresponding to the granulometric analysis of Figure 5.10.

[10] Data provided by the Institut Français du Pétrole (IFP), Paris, France.

In summary, it must be stated that, in conjunction, the tomographic images of the Cole-Cole parameters τ and c permit a clear distinction of the different structural regions in the subsurface. Moreover, they give valuable information on specific pore space characteristics, including dominant grain size and grain size distribution as well as water saturation and contaminant occurrence.

5.1.7 HYDRAULIC PERMEABILITY ESTIMATION

Within Section 2.6.2, methods were outlined for the estimation of one of the key parameters in hydrogeology, the hydraulic permeability K, by means of complex resistivity measurements. So far, however, the method has been principally restricted to laboratory studies on rock or soil samples or simple field surveys such as electrical soundings (e.g., Börner et al., 1996). Moreover, as far as the field applications are concerned, the published results unfortunately lack in ultimate conviction of the approach.

On the basis of the complex resistivity inversion scheme developed in this thesis, however, it is in principle possible to apply the proposed intrinsic relations in a tomographic way at the field scale. By this, a continuous image of in-situ permeability, characterized by a comparatively high spatial resolution, may be non-invasively gained. Since for the present case history a comprehensive spectral data set is available, it has been an obvious concern herein to compare the results of such an approach with the known hydrogeological situation.

Although in principle, plausible relations between K and spectral IP parameters can be derived on the basis of a Cole-Cole model description [see eq. (2.41)], these are yet only of qualitative character. For this reason, herein the quantitative relation (2.44), inferred from the fractal pore space model by Pape et al. (1987), was adopted for permeability analysis.

According to eq. (2.45), the needed surface area to pore volume ratio, S_{por}, may be estimated from the imaginary component of complex conductivity at a reference frequency. Strictly speaking, however, this approach presumes the validity of the constant-phase-angle relaxation model (see Section 2.4.3). Consequently, for the purpose of this section the actual frequency dependence of resistivity phase was ignored, and only a representative constant value acted as input to the analysis. For simplicity, this was assumed to be given by the recovered phase at 0.125 Hz (see Figure 5.5).

Besides S_{por}, likewise the formation factor F is required as essential input to eq. (2.44). The calculation thereof, however, can be readily accomplished by means of eq. (2.42), employing complex bulk conductivity, both pore water conductivity and saturation, σ_{w} and S_{w}, as well as saturation exponent n and the parameter $l = \mathrm{Im}(\sigma_{\mathrm{int}})/\mathrm{Re}(\sigma_{\mathrm{int}})$. The latter describes the actual separation of interfacial

conductivity σ_{int} into real and imaginary part (see Section 2.3.2). Although in general σ_w may vary considerably, for the present study it was assumed to be constant. A mean value of $\sigma_w \approx 108\,\mathrm{mS/m}$, with a standard deviation of $21\,\mathrm{mS/m}$, was determined from measurements in three boreholes. The parameters n and l are unfortunately not as directly measurable. Therefore, typical values for loose sediments must be adopted as a reasonable approximation. The values chosen here were $n = 2$ and $l = 0.1$ (see Section 2.3 and Börner et al., 1996).

Obviously, a significant uncertainty in the formation factor is due to the degree of water saturation in the different stratigraphic units [see eq. (2.42)]. Hence, a simple but realistic saturation model $S_w(z)$ was derived as to roughly reflect the expected situation with depth z (see Figure 5.12).

Whereas the saturated zone below the ground-water table is defined by a uniform value $S_w = 1$, within the unsaturated vadose zone three different regions are distinguished. These are the upper *pendular zone*, actually exhibiting residual (irreducible) water saturation; the lower *capillary zone*, with almost $S_w \approx 1$ due to the presence of capillary water; and finally a transition zone between – the so-called *funicular zone*, characterized by a steady increase of S_w with increasing depth (see, e.g., Fetter, 1999). Note that the choice $S_w = 1$ presumes that water represents the only phase in the pore space. For the sake of simplicity, any residual air or kerosene saturation in the capillary or saturated zone is ignored. This is justified, however, since water must be attributed the decisive role with respect to electrolytic (in-phase) conduction and, thus, the determination of F.

The capillary rise in unconsolidated sediments typically varies from more than 1 m for silts to less than 0.1 m for very coarse sands (see, e.g., Fetter, 1999). Accordingly, the capillary zone is expected to extend slightly beyond the clayey silt layer into the upper sand/gravel region. Above, a 1.5 m thick funicular zone is assumed, characterized by a simple linear behavior of $S_w(z)$, until finally a uniform residual saturation of $S_{wr} = 0.3$ is reached in the pendular zone (see Figure 5.12).

On the basis of the afore-mentioned parameters and values, permeability was estimated for each model cell in the tomographic image plane from the complex resistivity inversion result at 0.125 Hz (see Figure 5.5). The resultant distribution is shown in Figure 5.12.

From a comparison with the lithologic log, it is evident that, in principle, the recovered image reflects the given sedimentary sequence. Both clayey silt layer and top loessic layer, for instance, are clearly delineated in terms of lower permeability values. However, in addition to pure qualitative imaging, Figure 5.12 likewise reveals valuable quantitative information. The absolute values correspond remarkably well

with typical permeabilities for the different sediment types (see, e.g., Hölting, 1996). For the silt and the loessic layer, K ranges from 10^{-2} d to less than 10^{-1} d.[11] Thus both layers must be hydrogeologically considered as *low permeable*. On the other hand, the sand/gravel sections are principally characterized by K values between 10^{-1} d and 10^{1} d, a range which is commonly referred to as *permeable*. Note in this context that Figure 5.12 suggests considerable vertical variation within the upper sand/gravel region.

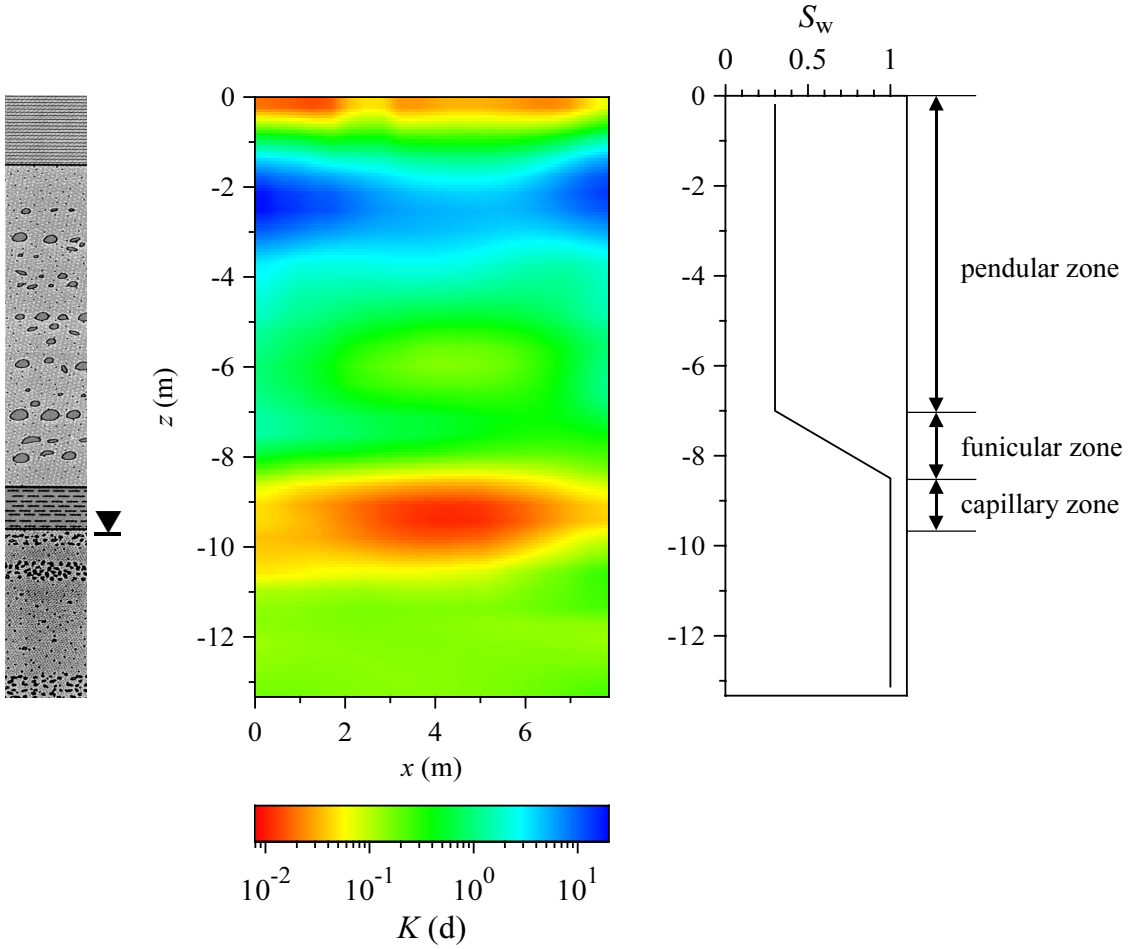

Figure 5.12: Distribution of hydraulic permeability as estimated from the complex resistivity inversion result at $f = 0.125\,\text{Hz}$ (see Figure 5.5). Note that only the region between the boreholes is displayed. Details on the employed estimation procedure are given in the text. Besides the corresponding lithologic log from Figure 5.1 (left-hand side), also the assumed variation of water saturation with depth is shown (right-hand side).

[11] It is common to measure permeability in *darcies* (d), where $1\,\text{d} \approx 1\,\mu\text{m}^2$. In hydrogeology, often also the hydraulic conductivity K_f is used, which is, however, readily obtained from the corresponding K value using the conversion $1\,\text{d} \approx 10^{-5}$ m/s (see, e.g., Schön, 1996).

Obviously, Figure 5.12 provides additional information regarding the hydrogeological characterization of the site. Attributing credibility to the estimated permeability values, the clayey silt layer does not represent a long-term hydraulic barrier – neither for water nor for the hydrocarbon contaminant plume (note that $K < 10^{-3}$ d for *very-low-permeable* sediments; see, e.g., Hölting, 1996). This conclusion, however, is in full accordance with the actual situation at the site, since dissolved contaminant components have been detected in the ground water below (see Section 5.1.1).

The present example proves the general feasibility of successful permeability estimation from complex resistivity data under realistic field conditions. With the availability of tomographic inversion schemes, such as those developed in this thesis, theoretical relations between intrinsic hydraulic and electrical characteristics can be effectively extended to the field scale. This fact, however, again underlines the great potential of complex resistivity tomography with respect to hydrogeological problems.

5.1.8 SUMMARY

In the preceding sections, a complex resistivity tomography survey conducted at a kerosene-contaminated jet fuel depot was described, as an example for the application of the method for environmental purposes. Aspects addressed in this context included survey design, data pre-processing, employed inversion procedure, discussion and interpretation of the inversion results, and finally, more advanced analysis techniques such as extraction of relaxation characteristics and hydraulic permeability estimation. Besides the investigation of the (hydro)geological situation, the survey was in particular intended to prove the method's capability of delineating subtle electrical contrasts associated with the presence of hydrocarbon contamination under real field conditions. A critical evaluation hereof was possible due to the availability of comprehensive information on the subsurface environment from other sources (e.g., monitoring wells, cored drillings, soil and water sample analyses).

Although several boreholes were actually equipped with electrodes and used for tomographic data collection, the presentation herein focussed on a single, yet representative, image plane. For the considered plane, measurements were taken at a set of current injection frequencies, ranging from 0.125 Hz to 8192 Hz, with a view to examining spectral IP characteristics. Due to the occurrence of EM coupling effects with increasing frequency, however, an indispensable requirement prior to inversion was the application of an appropriate decoupling scheme. Therefore, an effective and flexible procedure, based on a Cole-Cole model description of both IP and (low-frequency) EM response, was adapted and implemented for tomographic use. The approach proved capable of removing the various types of effects observed in the data, such as, for instance, combined positive and negative coupling. Up to 64 Hz, the

decoupled data sets successively acted as input to the tomographic inversion algorithm, resulting in complex resistivity images over multiple frequencies.

The lithologic stratification at the site was found to be reasonably delineated by the resistivity magnitude images, showing the alternation of comparatively conductive layers – representing loess and clayey silts, respectively – and more resistive layers – representing sands and gravels with variable degrees of cementation, compaction, and water saturation. Quantitatively, the inverted resistivities agree fairly well with measurements conducted on corresponding core samples. However, the multifrequency magnitude results exhibit no significant spectral dispersion. The images of resistivity phase, on the other hand, provide additional subsurface information in terms of both single-frequency and spectral results. In particular, given the chemical sample analyses, the phase is supposed to reveal a clear signature of the contamination. Following this interpretation, kerosene has accumulated on top of the low-permeable silt layer, constituting a continuous layer of increased pollution.

Further valuable insight into specific structural characteristics arose from the interpretation of the dispersive (phase) behavior. As to demonstrate the benefits of a quantitative spectral analysis, an appropriate relaxation model – the Cole-Cole model – was fitted to the individual model cell inversion results. The resultant images of intrinsic Cole-Cole parameters were interpreted by utilizing assumed relationships with intrinsic granulometric and hydraulic properties. In view of the correlation with dominant grain size, for instance, the time constant result reveals a reasonable lithologic discrimination and, given the log information, even identification of the sedimentary sequence throughout the tomographic image plane. Moreover, the recovered image suggests that the contaminant principally affects the larger pores within the sand/gravel formation. On the other hand, the significance of the frequency exponent with respect to the quantification of grain size sorting was outlined. An exemplary comparison with granulometric analysis results proved the practicability of such an approach in principle. Finally, a recently proposed way of estimating hydraulic permeability from complex resistivity was tomographically applied, in order to assess its ultimate value at the field scale. The obtained permeability image agrees remarkably well with the given subsurface situation, in particular it reveals characteristic absolute values.

The presented field data example demonstrates that complex resistivity tomography may provide valuable information about the structural and hydraulic nature of the subsurface in a sedimentary environment. The results prove the general feasibility of assessing both pore space and pore fluid characteristics in a tomographic way and, in that, underline the practical value of the method with respect to a variety of environmental problems.

5.2 MINERAL EXPLORATION

To demonstrate the efficiency of complex resistivity tomography for the purpose of mineral exploration, for which the IP method has been traditionally applied with success, in the following sections a typical field data example is presented. As compared to many environmental problems associated with rather shallow targets, often less than 10 m deep, mineral applications are generally characterized by extensive geological structures, normally implying exploration depths greater than 100 m. In addition to the spatial scale, they may differ substantially in the intrinsic electrical characteristics since typically involving different rock types. In view of these aspects, the given mineral exploration example is also intended to underline the universal applicability of the developed inversion procedure.

It is emphasized that the considered field survey was actually conducted by the Metal Mining Agency of Japan, Tokyo (Katayama et al., 1998), who kindly provided the raw data for utilization within this thesis.

In the following sections, first a general description of the site is given, addressing geology and occurring mineralization (Section 5.2.1), followed by some information on electrode setup and data acquisition of the tomographic survey (Section 5.2.2). The complex resistivity inversion results are then presented and discussed in Section 5.2.3, in particular with respect to the anticipated geological model, before concluding with a brief summary in Section 5.2.4.

5.2.1 SITE DESCRIPTION

The tomographic IP survey considered herein was conducted at the Flying Doctor Prospect in the south-eastern Broken Hill area in New South Wales, Australia. The following information on the general geological setting in the area was basically extracted from the corresponding chapter in Tyne and Webster (1988) and the comprehensive report by Burton (1994).

The Broken Hill area, approximately 50 km by 70 km in size, hosts one of the world's biggest known base-metal deposits. Before discovered in 1883 and, from that time on, extensively being mined, the main sulfide ore bodies – the so-called Broken Hill Main Lode – contained an estimated 280 million tons of Pb-Zn-Ag ore in several overlapping lenses or lodes. Since productiveness of the main Broken Hill mines is limited, however, in recent times intensive effort has been directed towards the exploration of new base-metal deposits in the area as well as of extensions to the known ore bodies. The Flying Doctor Prospect, located only few kilometers along strike from the major ore bodies, represents such an extension. It is considered to be most prospective in the region for the development of massive sulfide mineralization

and, hence, mining thereof may occur in the future to supplement production from the Broken Hill Main Lode.

Geologically, the Broken Hill Block, with an age of about 1700 Ma, belongs to the early to middle Proterozoic. It was subjected to regional prograde metamorphism around 1600 Ma ago, followed by widespread readjustment in the form of retrograde schist zones around 520 Ma ago. In addition, multiple major fold generations have caused massive structural deformation of the block. Within the south-eastern area, the sulfide deposits occur principally within the so-called Broken Hill Group, which basically consists of a sequence of metasediments, metasedimentary gneisses, and metamorphosed volcanic/volcaniclastic rocks. Most recent interpretations presume a syngenetic origin of the deposits. Herein, the lode horizons are regarded as chemical sediments deposited in a marine environment from metal-rich brines. However, the cutting discussion by Stevens (1996) and White et al. (1996) may express the still controversial debate amongst researches on many (fundamental) aspects regarding the genesis of the Broken Hill Block.

At the Flying Doctor Prospect, two separate lode horizons are present: the main lode horizon in about 1000 m depth (interpreted as the direct extension of the Broken Hill Main Lode) and the upper lode horizon in less than 150 m depth (probably a structural repetition of the main horizon). Both lode horizons represent variable packages of lode rock types (commonly quartz gahnite, garnet quartzite, and garnet sandstone), containing Pb-Zn-Ag sulfide mineralization in form of individual lenses and shoots. Mineralization comprises predominantly galenite and sphalerite, as well as minor chalcopyrite, pyrrhotite, and pyrite, and occurs commonly as disseminations, in massive form as patches, irregular vein-like masses, or reticular networks.

The anticipated geological setting at the Flying Doctor Prospect, showing the upper lode horizon, is sketched in Figure 5.13. The indicated position of the sulfide deposit is mainly based on results from an extensive drilling programme, accompanied by geophysical logging, which has been conducted over the last decades. These investigations clearly revealed distinct sulfide lenses, virtually representing zones of high sulfide concentration with an admixture of gangue material. Accordingly, the sulfide deposit is located near the boundary between a quartzitic gneiss, the actual host rock (belonging to the Broken Hill Group), and a retrograde schist zone, the so-called Globe Vauxhall Shear Zone. It is expected to bear 300 000 t of subeconomic mineralization with estimated grades of 7 % Pb, 2.4 % Zn, and 60 g/t Ag.

A final remark may be added on the model representation in Figure 5.13. Since the underlying investigations actually only yielded selective information along individual boreholes, form and extent of the deposit as indicated – even if plausible from the general geological situation – represent no more than an expected model derived by inter-/extrapolation. In fact, there is no ultimate evidence, for instance, for the continuation of the sulfide zone up to the surface. Neither an obvious gossanous

outcrop exists, nor did geophysical surface measurements indicate the presence of localized high sulfide concentrations in the shallow subsurface (see Tyne and Webster, 1988).

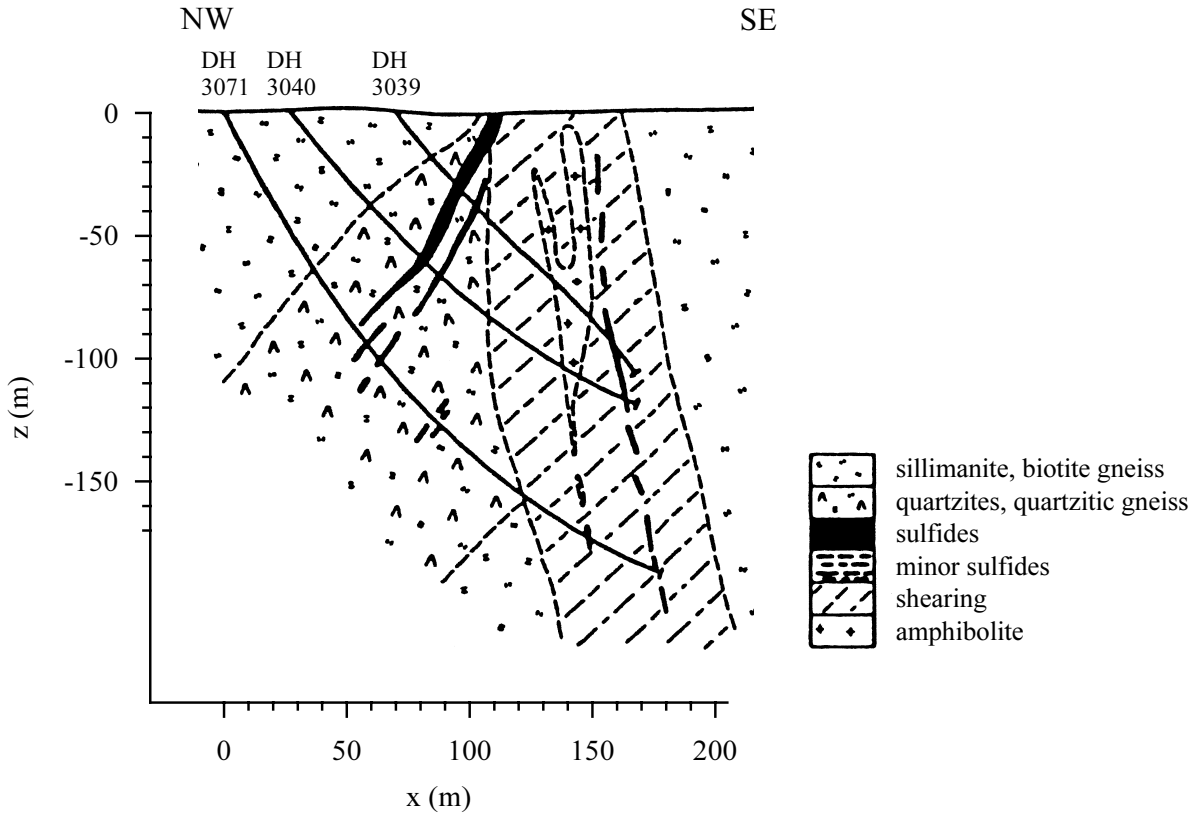

Figure 5.13: Anticipated geological section at the Flying Doctor Prospect, south-eastern Broken Hill area, serving as a test site for complex resistivity tomography. The model was derived from geophysical logging results in the three indicated boreholes (solid curves) under consideration of the general geological situation in the area. After Tyne and Webster (1988).

5.2.2 Electrode Setup, Data Acquisition, and Inversion Procedure

In July 1997, the MMAJ[12] conducted an IP tomography test survey at the Flying Doctor Prospect in order to examine the applicability of the technique for mineral exploration in the upper lode horizon (Katayama et al., 1998). Since previous borehole measurements had revealed a polarizable nature of the sulfide lenses (Tyne and Webster, 1988), IP tomography was expected to yield a better geometrical delineation

[12] Metal Mining Agency of Japan, Tokyo, Japan.

of the deposit as well as to help in recognizing variations in the degree of mineralization.

For the tomographic survey, three existing exploration drill holes (DH 3071, DH 3040, and DH 3039) were utilized for placing electrodes in the subsurface. The roughly coplanar drill holes (lateral planar deviation < 3 %) spread a vertical image plane approximately perpendicular to the presumed strike direction of the sulfide deposit. The employed electrode cables were arranged such as to realize a uniform separation of 10 m between adjacent electrode positions, with electrode depths up to 170 m. An additional line of surface electrodes completed the setup in the survey plane, totally comprising 67 potential and 26 current electrodes (see Figure 5.14). The borehole and surface electrodes were made of lead and stainless steel, respectively (Katayama, 1998, pers. com.).

The employed PC-controlled data acquisition system by MMAJ is based on the McOHM-21 by OYO[13]. It consists of a battery-powered transmitter, optionally supplemented by a generator-driven external booster, a 16 bit 10-channel receiver, and a multiplexer for electrode selection. Automatic data collection is executed according to a predefined measurement protocol. More details on the system may be found in Arai (1997). For the present survey, more than 1200 independent pole-dipole configurations were measured, using a square-wave current with 50 % duty cycle and a pulse length of 2 s. For each configuration, full transient data were recorded at a sampling rate of 250 Hz, and signals were stacked over two cycles as a compromise between improved signal-to-noise ratio and yet efficient acquisition speed (Katayama, 1998, pers. com.).

Whereas the MMAJ intended a more conventional time-domain analysis of the tomographic data set on the basis of integral chargeability (Katayama et al., 1998), within the scope of this thesis an attempt was made at a frequency-domain interpretation in terms of complex resistivity. For this purpose, the recorded current and voltage time series, $I(t)$ and $V(t)$, respectively, were individually Fourier-transformed according to eqs. (2.31) and (2.32). Subsequently, the corresponding transfer impedance spectra $Z(\omega) = V(\omega)/I(\omega)$ were derived and evaluated at the fundamental frequency of the employed square wave, $f_0 = 0.125\,\mathrm{Hz}$. Uncertain signals, however, with a voltage amplitude less than 0.2 mV or an associated geometric factor greater than 10^6 m, were disregarded, so that the resultant data set acting as input to the tomographic inversion procedure eventually comprised about 1000 measurements.

---

[13] OYO Corporation, Tokyo, Japan.

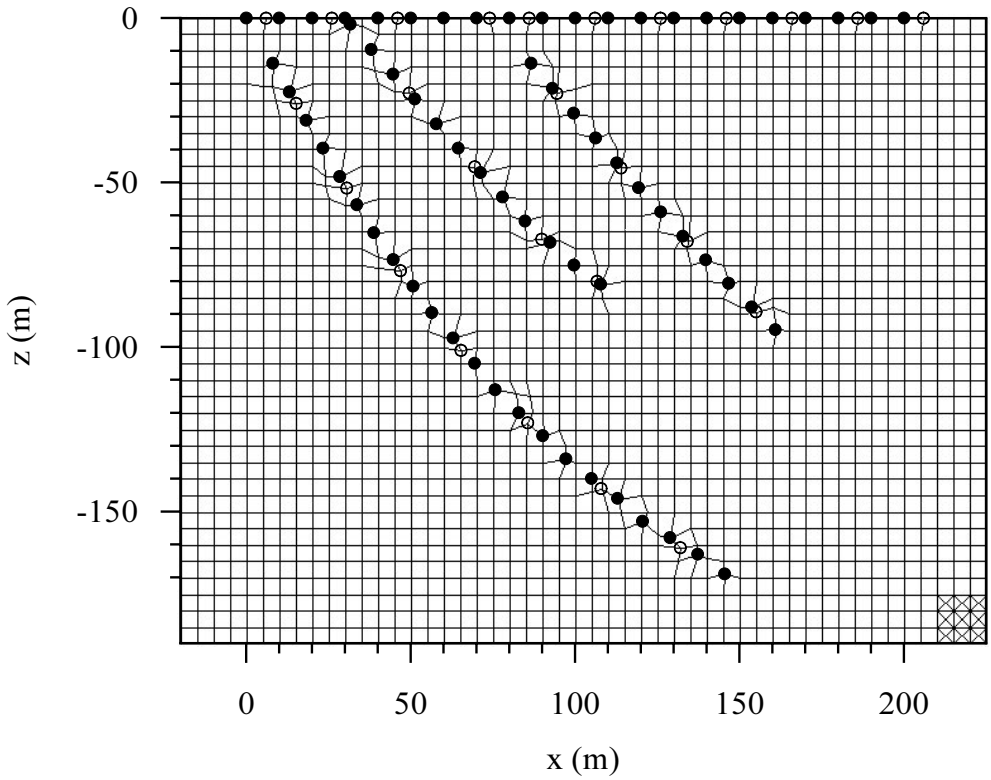

Figure 5.14: Setup of borehole and surface electrodes for the complex resistivity tomography survey at the Flying Doctor Prospect. Solid and open circles indicate, respectively, position of potential and current electrodes. Note that the three utilized drill holes are identical with those of Figure 5.13. Also shown is the parameterization of the tomographic image plane as employed in the inversion. The underlying finite-element discretization is indicated in the bottom right corner.

For the inversion, a standard parameterization of the survey plane into about 1800 model cells was used. Some irregularities, however, were incorporated into the underlying finite-element mesh as to account for the exact electrode positions, in particular in the boreholes (see Figure 5.14). For analogous reasons as in Section 5.1.4, the inversion was carried out in the robust mode (iterative data reweighting) and, furthermore, completed by final phase improvement. In contrast to the previous case history, however, isotropic model smoothing was employed and uniform data errors of 25 % in magnitude and 5 mrad in phase were initially adjusted. These error levels were found to let the inversion process readily converge. As the starting model again a homogeneous distribution was used (geometric mean of the given apparent complex resistivities).

Note finally that, as mentioned earlier, the tomographic image plane lies perpendicular to the assumed strike direction of the principal subsurface geological structures (lode horizon, shear zone, etc.; see Figure 5.13). Since strike length of the sulfide deposit is moreover expected to exceed 250 m (Burton, 1994), a two-dimensional inversion approach, as applied herein, actually represents a reasonable approximation.

5.2.3 INVERSION RESULTS

The inverted distributions of resistivity magnitude and phase in the tomographic image plane are shown in Figure 5.15. Both images reveal several structural characteristics in the subsurface which in principle correspond with the expected geological situation.

The magnitude image, with resistivities varying over more than two orders of magnitude, permits a first distinction of different geological formations. The right-hand side of the image ($x > 120$ m) exhibits only minor, smooth variation of resistivity, with average values around 100-300 Ωm. The slight but steady increase towards greater depths may be attributed to a general increase of compaction incident to an increasing lithostatic load. The corresponding region coincides roughly with the position of the Globe Vauxhall Shear Zone as interpolated from the drilling results (cf. Figure 5.13). There is no evidence, however, for the presence of embedded amphibolites, which in fact may be due to the absence of a significant electrical contrast associated therewith.

In the north-western part of the image ($x < 80$ m), the near-surface region is found to be of different character, showing very low resistivities (< 30 Ωm). Below this conductive zone, resistivity increases rapidly with depth, almost reaching 1500 Ωm underneath borehole DH 3071 (at $x < 20$ m). This section corresponds to the upper sillimanite / biotite gneiss (cf. Figure 5.13), characterized by strong weathering in the first 10-20 m (Tyne and Webster, 1988).

The center part of the image plane reveals a rather inhomogeneous character due to the presence of several smaller-scale features. Most dominant thereof is the distinct, highly conductive ($\approx 10\,\Omega$m) anomaly between boreholes DH 3040 and DH 3039 (at $x \approx 100$ m). According to Figure 5.13, this zone belongs to the quartzites / quartzitic gneiss formation, actually hosting the sulfide lode horizon. The overall dipping character of the host rock becomes evident when likewise interpreting the bilateral transition towards lower resistivities underneath drill hole DH 3071 as a change from sillimanite / biotite gneiss to quartzites / quartzitic gneiss (cf. Figure 5.13).

In conformity with previous electrical logging results (see Tyne and Webster, 1988), the conductive anomaly at $x \approx 100$ m is assumed to delineate zones of highest sulfide concentrations in the lode horizon. The minor magnitude variations therein, however, might not only reflect varying concentrations but could also indicate changes in the structural nature of the mineralization, basically ranging from a rather disseminated to an almost massive type (see Section 5.2.1). Note finally that although sulfides have been actually intersected in the lower borehole DH 3071, a corresponding conductive signature is missing at all in the recovered magnitude image. Principally, however, the inverted magnitude values are remarkably consistent with previous electrical logging results (see Tyne and Webster, 1988).

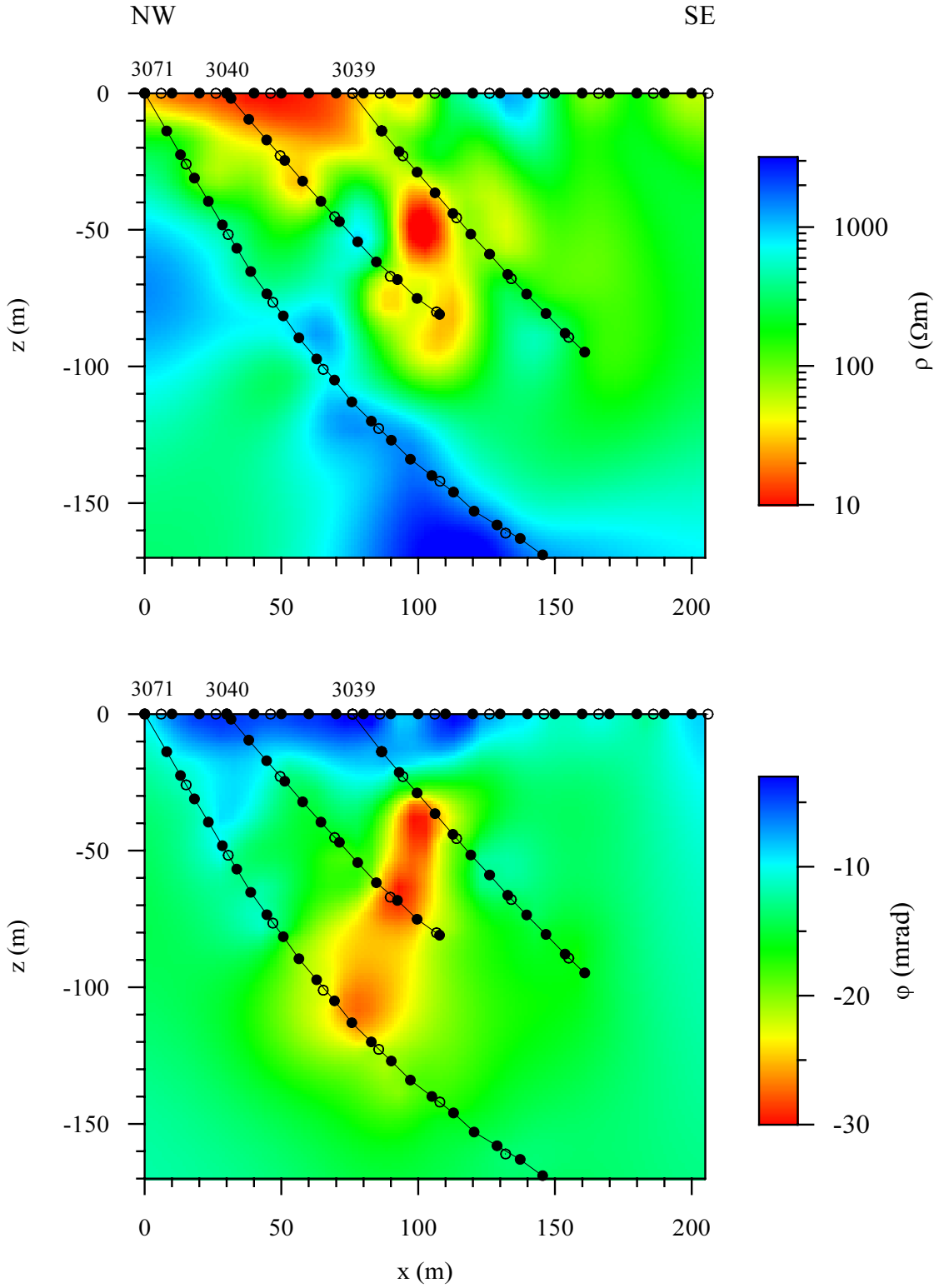

Figure 5.15: Complex resistivity inversion result, showing distribution of resistivity magnitude (top) and phase (bottom). Solid and open circles indicate, respectively, position of potential and current electrodes. Note that the tomographic image plane corresponds to the anticipated geological section of Figure 5.13.

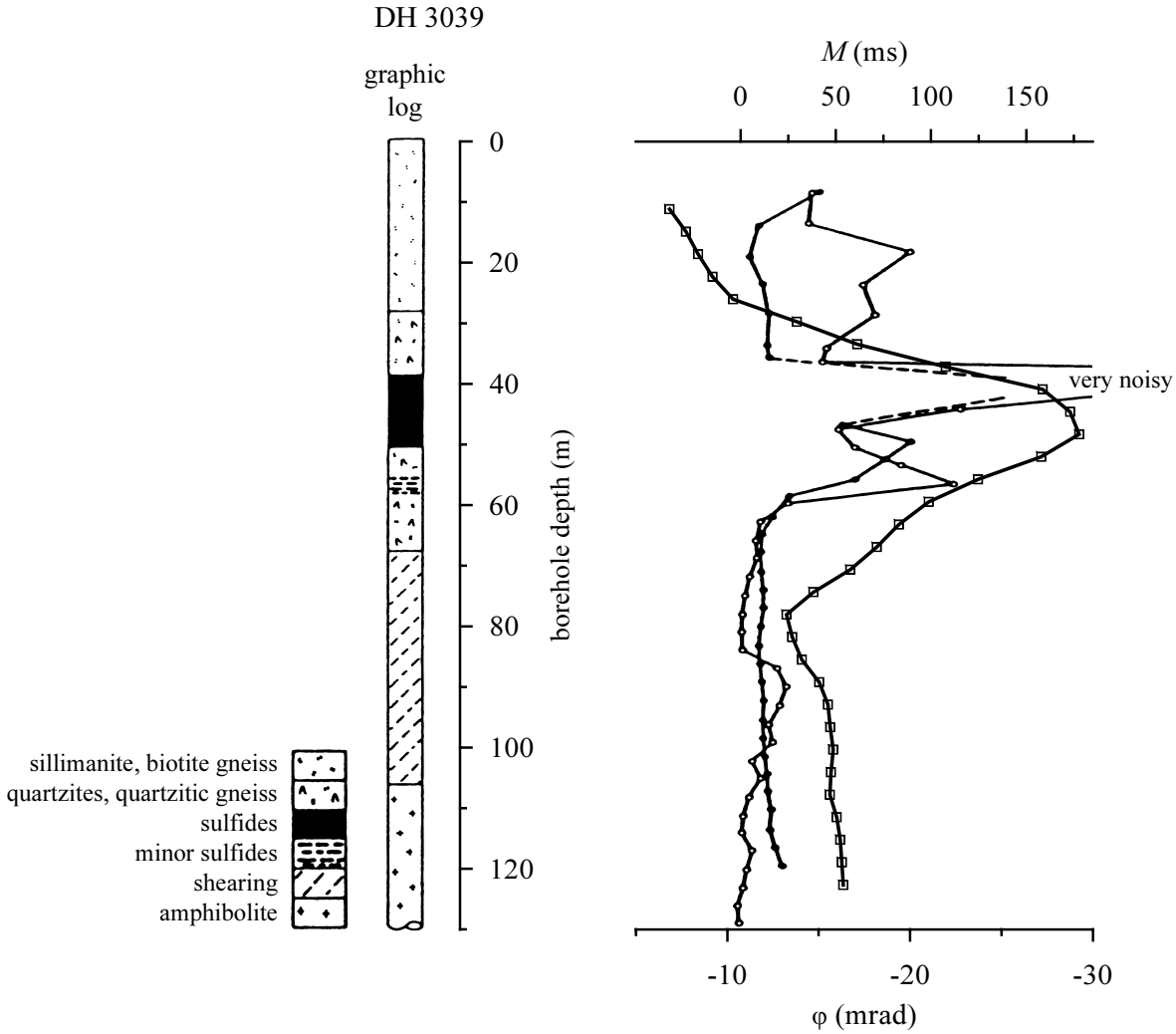

Figure 5.16: Stratigraphy[14] in drill hole DH 3039 (left) in comparison to determined IP amplitude with borehole depth (right). The curves of chargeability (circles) and resistivity phase (squares) represent, respectively, the IP log[14] as obtained by electrical borehole measurements and the corresponding IP variation as extracted from the complex resistivity inversion result of Figure 5.15. Note that quantitatively, the two IP parameters may only be compared with reservation since, apart from their inherent distinctness, chargeability is strongly dependent upon the employed definition (e.g., concerning timing parameters; see Section 2.5.2).

Compared to the image of resistivity magnitude, the inverted phase distribution reveals somewhat different structural characteristics and, thus, provides complementary information. Most of the image shows a relatively uniform, moderate background IP response in the range of 10-20 mrad (absolute values), perhaps with a slight increase within the quartzites / quartzitic gneiss formation (cf. Figure 5.13). An

[14] Adapted from Tyne and Webster (1988).

exception represents the low-polarizable (< 10 mrad) zone of weathered sillimanite / biotite gneiss in the north-western part of the image ($x < 130$ m). Undoubtedly most conspicuous, however, is the continuous, steeply dipping zone of increased polarizability (> 25 mrad) extending from the upper drill hole DH 3039 (at $x \approx 100$ m) to the lower drill hole DH 3071 (at $x \approx 80$ m) half way across the image plane. The position of this distinct anomaly coincides well with the principal sulfide intersections found along the three boreholes (cf. Figure 5.13), as illustrated by Figure 5.16 for the upper well DH 3039.

Since previous IP logging has clearly revealed a polarizable nature of the sulfides (see Figure 5.16), the zone of high IP response is supposed to delineate the occurrence of sulfide mineralization in the lode horizon. Accordingly, the sulfide deposit reaches about 100 m in plunge length and is almost confined by the boreholes DH 3071 and DH 3040. Due to limited resolution, however, the tomographic procedure is incapable of actually discriminating several discrete sulfide lenses, either of each again being composed of thin massive sulfide bands and interfingering gangue material, as verified by the drillings (Tyne and Webster, 1988).

Traditionally, the metal factor MF is often used in mineral exploration to assess the amount of mineralization. However, as outlined earlier (see Section 2.5.2), it may be directly related to the imaginary component of complex conductivity $\mathrm{Im}(\sigma)$ – a quantity independent of the electrolytic (in-phase) conduction in the pore spaces and thus most diagnostic for the degree of electrode polarization at the mineral-solution interfaces. For the present case, the resultant $\mathrm{Im}(\sigma)$ distribution is shown in Figure 5.17. The image delineates the zones of highest sulfide concentrations in the lode horizon clearer than resistivity magnitude (cf. Figure 5.15). The conductive anomaly associated with strong weathering near the surface, which is due to in-phase conduction mechanisms, now almost disappears.

In conjunction, the complex resistivity inversion result provides a clear delineation of the sulfide deposit and, in addition, reveals specific structural variation thereof. Whereas the phase image reflects the overall extent of principal mineralization in terms of high polarizability, the magnitude image indicates conductive zones of highest (and thus economically most promising) sulfide concentrations. In unison, both images show a homogeneous signature of the Globe Vauxhall Shear Zone and a 10-25 m thick weathering layer at the top of the gneissic rock formation in the north-west.

Contrary to the anticipated geological situation (see Figure 5.13), from Figure 5.15 the sulfide lenses do apparently not continue up to the surface but seem to vanish just above the upper drill hole DH 3039. In fact, this result may explain why several geophysical surface methods (e.g., resistivity, IP, self potential), previously applied over the deposit, have actually failed in proving a near-surface sulfide body (see Tyne and Webster, 1988). The disappearance of the distinct electrical response may be, in

part, also due to oxidation and other weathering processes within the mineralized zone, increasingly gaining in importance towards the surface. Note that the abrupt disappearance of the polarizable feature is unlikely to be due to an insufficient image resolution. This may become evident from Figure 5.18, showing the coverage of the image plane by the tomographic measurements, earlier introduced as a simple means for appraising image resolution (see Section 4.2). In the relevant regions, the normalized values lie clearly above 10^{-3}, which was earlier found to be the order of a critical threshold (see Section 4.2).

In view of the above results, the presented field example in particular exposes the fundamental problem of deriving a continuous geological model from borehole information alone, which may readily lead to essential misinterpretations (e.g., by erroneously extrapolating). With tomographic geophysical techniques, like the one developed in this thesis, such problems may be effectively overcome and, thus, these methods may contribute significantly to a reliable geological model. For the present case, by application of complex resistivity tomography a detailed image of the subsurface sulfide deposit could be achieved.

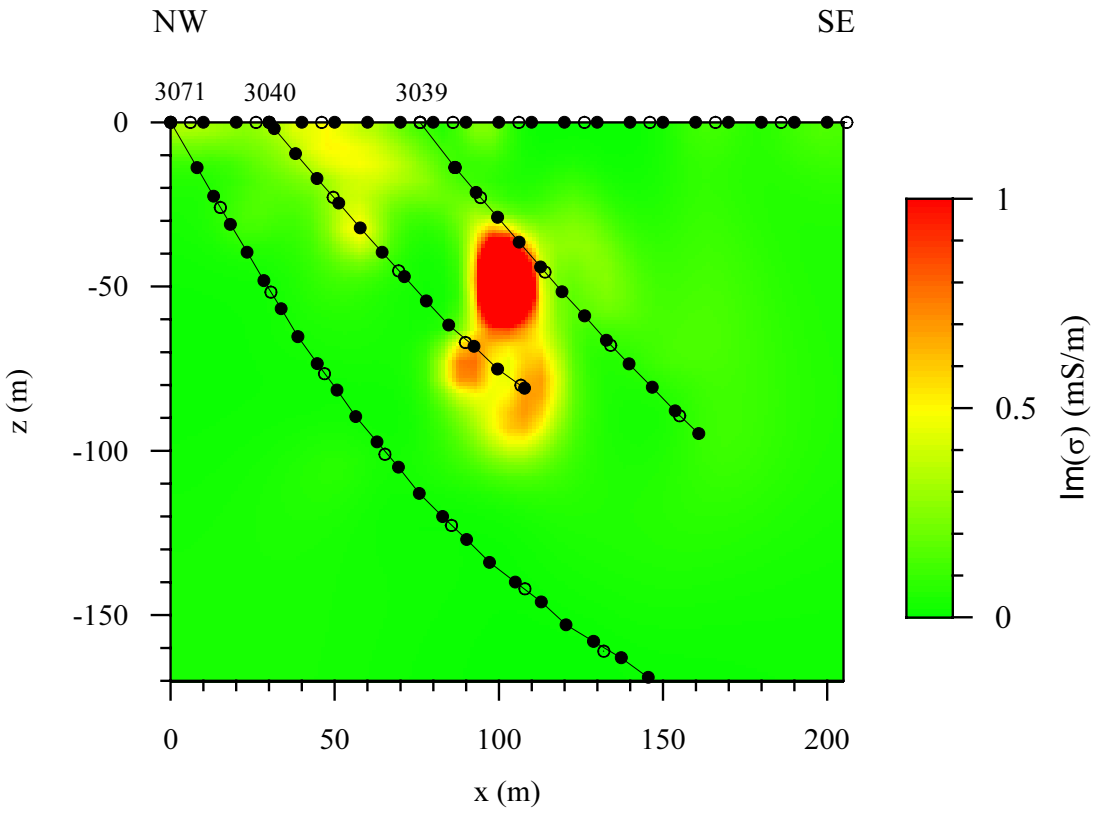

Figure 5.17: Distribution of the imaginary component of complex conductivity as obtained from the complex resistivity inversion result of Figure 5.15. Solid and open circles indicate, respectively, position of potential and current electrodes.

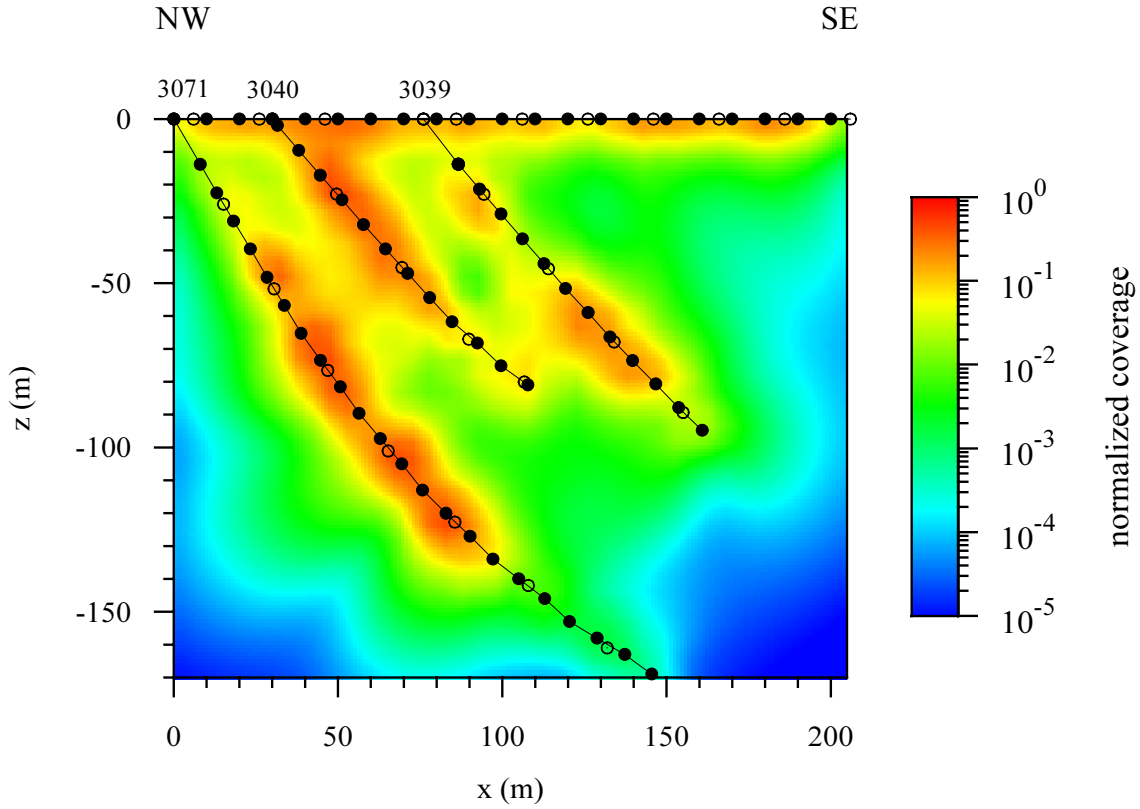

Figure 5.18: Normalized coverage of the image plane by the tomographic measurements according to eq. (4.1), corresponding to the complex resistivity inversion result of Figure 5.15.

5.2.4 SUMMARY

In the preceding sections, a field application of complex resistivity tomography over a sulfide deposit was presented in order to demonstrate the usefulness of the method for mineral exploration in realistic situations. The field data are from a test survey conducted at the Flying Doctor Prospect in the south-eastern Broken-Hill area, Australia. Detailed a-priori information on the geological setting at the site, available from previous exploration drillings and geophysical logging results, enabled a critical assessment of the method's efficiency with respect to the delineation and characterization of the sulfide mineralization zone.

For the tomographic survey, electrodes in three existing boreholes and at the surface were used, spreading an image plane perpendicular to the presumed strike direction of the deposit. Since full transient current and voltage signals were originally recorded, the data set could be converted into the frequency domain, enabling the subsequent application of the developed inversion procedure at the fundamental frequency of the employed square wave.

The inverted images of resistivity magnitude and phase reveal valuable subsurface information which, in principle, correlates well with the anticipated geological model. For instance, a weathering zone is clearly imaged, and even the alternation of different gneissic rock formations can be recognized partly. Most important, however, is the information on the sulfide deposit itself. Whereas the magnitude image indicates only zones of highest sulfide concentrations, i.e., of primary economical interest, the phase image delineates the principal occurrence of sulfide mineralization. Both the character of the electrical signature and the position of the deposit in the tomographic image plane is in absolute agreement with previous electrical logging results. Rather unexpected, on the other hand, is the relatively sharp disappearance of the characteristic IP response in the dip direction. In particular, this result suggests an abrupt ending or, at least, significant chemical alteration (e.g., due to oxidation) of the mineralization long before reaching the surface – in opposition to the originally assumed geological situation.

In summary, the presented field study demonstrates that complex resistivity tomography is capable of providing valuable information on location, extent, and structural characteristics of subsurface mineral deposits. The method is applicable in practical situations and, in particular, may substantially complement traditional exploration techniques, such as drillings and geophysical logging, with regard to the derivation of a detailed and reliable geological model. This potential suggests a bright perspective for the method in the general field of mineral exploration.

6 SUMMARY AND CONCLUSIONS

A new procedure for complex resistivity tomography has been developed and extensively investigated through a number of applications.

The thesis was motivated by two circumstances becoming evident in the early to mid nineties: first, the major advance of electrical resistivity tomography (ERT) as a powerful, high-resolution imaging technique – in particular for hydrogeological and environmental purposes; and second, proven by numerous laboratory studies, the enormous extent of structural information (e.g., grain size and pore fluid characteristics) generally contained in spectral complex resistivity data. Attempts to account for complex resistivity within modern imaging techniques such as ERT, however, have been rare. Consequently, so far there have been only few possibilities to utilize the lab-proven relationships effectively at the field scale. This again has significantly weakened their ultimate practical value. In order to overcome this deficiency, the main objective of this thesis was the development of an efficient (2D) tomographic inversion algorithm universally applicable to complex resistivity data sets.

As the basis of the new procedure, an appropriate forward modeling needed to be developed. To meet the requirements of a flexible approach (e.g., in terms of arbitrary geometries), the finite-element (FE) technique was adapted for this purpose. Unlike existing FE modeling codes for the conventional DC (i.e., real-valued) resistivity problem, in this thesis complex linear FE equations were derived from an extension of the underlying variational principle to a complex form. With the additional implementation of asymptotic boundary conditions and singularity removal, an accurate routine resulted for the computation of the complex resistivity response for arbitrary coplanar tomographic electrode configurations (permitting both surface and borehole electrodes). Analogous to the conventional DC case, the utilization of the reciprocity principle led to an efficient way of calculating the corresponding complex sensitivities with respect to the individual elements, which are required in a gradient-type inversion approach.

Due to the general ill-posedness of the tomographic complex resistivity inverse problem, a spatially regularized inversion approach was chosen in which the inversion process is controlled by means of a model smoothness constraint. This technique is well-established in inverse problems and, in particular, has been widely demonstrated to yield satisfactory results in conventional ERT. To account for the mathematical

nature of the considered problem, however, in this thesis the approach was extended to a new, complex form. As an inherent consequence of the approach, the inversion yields tomographic images of both resistivity magnitude and phase simultaneously. In the underlying optimization problem, data misfit and model roughness, each of which being measured in terms of the complex L_2-norm, are jointly minimized to find the 'smoothest' model which fits the data to an acceptable degree. Because of the non-linearity of the forward problem, the model search is performed iteratively, by means of a combination of the standard Gauss-Newton technique and the conjugate-gradient method. The balance between data misfit and model roughness is controlled by a regularization parameter, the optimum value of which is determined at each inverse iteration step. With a view to practical applications, a robust iterative data reweighting scheme was adopted. By this, stable inversion results are produced even in the presence of individual data outliers or in the case of uncertainty regarding the actual data noise level. For extremely noisy magnitude data, the phase image quality may be improved by running subsequent inverse iterations solely for the phase once the complex algorithm has converged.

Due to its flexibility and robustness, the developed algorithm is applicable to arbitrary tomographic electrode arrangements and measurement schemes. Besides typical crosshole geometries, likewise complex resistivity data from pure surface arrays may be interpreted (see Binley et al., 1998). Moreover, although this thesis was restricted to two-dimensional applications, the approach may be analogously extended to three dimensions, as recently done by Shi et al. (1998) and Yang et al. (2000). Of course, several aspects related to the inversion approach in general or its implementation in detail are open to procedural alternatives or extensions. Routh et al. (1998), for instance, proposed an inversion scheme which directly solves for spectral Cole-Cole parameters. In this thesis, the inversion is formulated in (more general) terms of complex resistivity, and no presumption is made on the underlying relaxation model. Insight into spectral characteristics may be obtained by a multifrequency application of the procedure. Presently, however, each measurement frequency is considered individually, i.e., any information from other available frequencies is disregarded within the inversion process. Since electrical properties may be expected to vary only smoothly with frequency, a full spectral complex resistivity approach, controlled by some additional regularization in the frequency dimension, appears to be a promising future development. A final remark may be added on the complex formulation of the inversion as proposed herein. In principle, a joint inversion of resistivity magnitude and some appropriate IP quantity (such as resistivity phase) is also possible by means of a decoupled, real-valued algorithm. However, apart from the inherent compactness of the complex approach (which one may agree to bear some mathematical elegance), it was, in fact, recently shown to be superior to more conventional approaches in terms of IP image resolution (Ramirez et al., 1999).

To investigate the capabilities of the new inversion procedure in a theoretical manner, different synthetic models were derived in this thesis that reflect potential practical applications.

The first such model represents a subsurface pollution scenario involving a dual contaminant plume which is characterized by complementary conductive and polarizable properties. Herewith, the general behavior of the complex inversion algorithm was examined, in particular in the presence of data noise. The second model simulates a layered sequence of sands and silts, as typical for a near-surface sedimentary environment. This model was particularly used to demonstrate the appropriateness of anisotropic model smoothing to bias the inverse solution towards, for instance, horizontal model characteristics. Moreover, different crosshole electrode arrangements were examined with regard to the general influence of borehole separation on the quality of the inversion result. In this context, the concept of sensitivity-based coverage was pointed out as a simple means to quantitatively appraise image resolution in the tomographic survey plane. Unlike the first two synthetic studies, the third model was supplied with full spectral complex resistivity properties. It represents a dipping mineralization zone – a situation often encountered in mineral exploration applications. In view of the associated rock types, the Cole-Cole relaxation model was adopted to describe the frequency dependence within the different structural units. Assuming measurements over a range of input frequencies, the feasibility was investigated to reconstruct the respective spectra by means of successive single-frequency applications of the tomographic inversion scheme.

From the synthetic model results, the new tomographic inversion algorithm proved capable, in principle, of recovering given distributions of resistivity magnitude and phase reasonably well – both qualitatively and quantitatively. In conjunction, the presented model examples suggest the general applicability of the method for various practical purposes. These may range from contaminant plume delineation, over hydrogeological site characterization, to the more classic field of mineral exploration. Whereas single-frequency applications provide valuable, complementary information in terms of resistivity magnitude and phase, a multifrequency approach even enables access to additional, spectral characteristics.

In order to verify the supposed potential of complex resistivity tomography also in practical situations, the thesis was likewise concerned with two different field applications.

In the first case study, spectral complex resistivity tomography was applied at a military jet fuel depot, former activities at which have resulted in kerosene contamination of the subsurface. The survey was entirely designed and conducted within the scope of this thesis with a view to several objectives. First, the method's usefulness for environmental applications at the field scale should be proved in principle – in particular regarding the mapping of subsurface hydrocarbon

contamination. Based on laboratory results at the core scale, the latter application has been widely suggested in the past but so far, also due to the lack of appropriate imaging techniques, had not been convincingly demonstrated in a realistic, crosshole field experiment. Second, the general possibility of resolving spectral IP characteristics by means of complex resistivity tomography should be examined and, furthermore, the suitability of a recently proposed scheme for hydraulic permeability estimation should be tested within a tomographic approach. Again, the last two issues had not been addressed previously in a complex resistivity field survey. A critical evaluation of the method's efficiency in the above regards was possible due to the availability of comprehensive subsurface information from other sources. Explicitly, the analysis steps and the respective results were as follows:

The reconstructed images of resistivity magnitude and phase were found to provide complementary information on the subsurface environment. Whereas the magnitude image principally reflects the given sedimentary sequence, the phase image gives clear indication for the presence of kerosene contamination and, by this, permits valuable insight into the contaminant distribution and migration pattern. The successive application of the inversion algorithm to the acquired multifrequency data yielded tomographic images of complex resistivity over a range of frequencies. Prior to the spectral analysis, however, inductive coupling was removed from the data by means of an effective decoupling procedure (which was adapted for tomographic purposes within the scope of this thesis). In order to properly assess the recovered spectral characteristics, a Cole-Cole relaxation model was fitted to the individual model cell inversion results. Thus, the approach ultimately resulted in tomographic images of the intrinsic Cole-Cole parameters. The Cole-Cole time constant and frequency exponent proved to reveal additional structural information regarding dominant grain size and grain size sorting, respectively. In this context, a simple, approximate relation between the Cole-Cole frequency exponent and grain size sorting was proposed. Finally, the tomographic estimation of in-situ hydraulic permeability was also successful. The determined values were found to be in fair agreement with the associated sediment types.

By the second field data example, the efficiency of the new inversion procedure for the purpose of mineral exploration was demonstrated. Full transient data from a tomographic IP survey, conducted over a steeply dipping sulfide deposit, were transformed into the frequency domain and, afterwards, processed by means of the developed algorithm. The resultant complex resistivity distribution was compared with the anticipated geological model inferred from previous exploration drillings and geophysical logging results. Accordingly, the magnitude image indicates only zones of highest sulfide concentrations, whereas the phase image sharply delineates the principal occurrence of sulfide mineralization within the metamorphic host rock. With the tomographic inversion result, continuous structural information on the deposit is

available, contributing to a much better understanding of the actual geological situation.

In summary, the synthetic and field studies presented in this thesis prove an enormous potential of complex resistivity tomography for practical applications. In the hydrogeological field, it may provide insight into the structural and hydraulic nature of sedimentary environments. Here, images of grain size and pore fluid characteristics as well as an estimate of hydraulic permeability should be achievable. With respect to environmental pollution problems, the method may play a major role in detecting, delineating, monitoring, or even identifying subsurface contamination. For instance, organic and inorganic contaminant components may be differentiated due to their distinctive electrical signature. In mineral exploration applications, complex resistivity tomography may yield valuable information on location, extent, or structural characteristics (e.g., composition) of mineral deposits. The environmental and economic significance of the above capabilities is obvious.

With respect to the various applications, however, the ultimate value of complex resistivity tomography strongly depends upon the validity and reliability of the utilized relations between the observed electrical phenomena and the relevant structural characteristics. For instance, the close connection of the characteristic (Cole-Cole) time constant and the spatial scale at which the associated relaxation processes take place in the pore space was repeatedly outlined in this thesis. Although certainly providing some sort of grain or pore size information, the *electrically* effective part of the pore space may be significantly different from the *hydraulically* effective part which, however, may be the focus of interest in practical applications. This example elucidates that, without doubt, much more fundamental research is still required to investigate further the underlying electrical and structural properties with the view of establishing reliable and practical relations between the respective characteristic quantities. Together with the availability of appropriate tomographic inversion schemes, such as the one developed in this thesis, it will then become possible in future to effectively combine the benefits of high-resolution imaging with improved source characterization capabilities. This obviously opens a bright perspective for the complex resistivity tomography method in any of the indicated fields of potential application.

REFERENCES

ABRAMOWITZ, M., and STEGUN, I. A., 1984, Handbook of mathematical functions: Dover Publ., Inc.

ALUMBAUGH, D. L., and NEWMAN, G. A., 1998, Image appraisal for 2D and 3D electromagnetic inversion: 68th Ann. Internat. Mtg., Soc. Expl. Geophys., Expanded Abstracts, 456-460.

ANDERSON, W. L., 1979, Numerical integration of related Hankel transforms of orders 0 and 1 by adaptive digital filtering: Geophysics, **44**, 1287-1305.

ARAI, E., 1997, Development of the IP tomography system and field testing in the Seta area, Japan: 67th Ann. Internat. Mtg., Soc. Expl. Geophys., Expanded Abstracts, 1961-1964.

ARCHIE, G. E., 1942, The electrical resistivity log as an aid in determining some reservoir characteristics: Trans. Am. Inst. Min. Metall. Eng., **146**, 54-62.

BEARD, L. P., HOHMANN, G. W., and TRIPP, A. C., 1996, Fast resistivity/IP inversion using a low-contrast approximation: Geophysics, **61**, 169-179.

BERG, R. R., 1970, Method for determining permeability from reservoir rock properties: Trans. Gulf Coast Section, Soc. Econ. Paleont. Mineral., Am. Assn. Petr. Geol., **20**, 303-317.

BERTIN, J., and LOEB, J., 1976, Experimental and theoretical aspects of induced polarization, vol. 1 and 2: Gebrüder Borntraeger.

BINLEY, A. M., RAMIREZ, A. L., and DAILY, W. D., 1995, Regularised image reconstruction of noisy electrical resistance tomography data, *in* Beck, M. S., Hoyle, B. S., Morris, M. A., Waterfall, R. C., and Williams, R. A., Eds., Process tomography – 1995: Proc. 4th Workshop Eur. Concerted Action Process Tomography, 401-410.

BINLEY, A. M., SHAW, B., and HENRY-POULTER, S., 1996, Flow pathways in porous media – electrical resistance tomography and dye staining image verification: Meas. Sci. Tech., **7**, 384-390.

BINLEY, A. M., ERIKSEN, A., GASCOYNE, J., NGUYEN, T., and KEMNA, A., 1998, Spectral characteristics at a former industrial site using complex resistivity: Proc. 4th Mtg. Environmental and Engineering Geophysics, Environ. Eng. Geophys. Soc., Eur. Section, 1-4.

BLEIL, D. F., 1953, Induced polarization – a method of geophysical prospecting: Geophysics, **18**, 636-661.

BÖRNER, F. D., 1991, Untersuchungen zur komplexen elektrischen Leitfähigkeit von Gesteinen im Frequenzbereich von 1 mHz bis 10 kHz: Ph.D. dissertation, Freiberg Univ. of Mining and Technology.

BÖRNER, F. D., and SCHÖN, J. H., 1991, A relation between the quadrature component of electrical conductivity and the specific surface area of sedimentary rocks: The Log Analyst, **32**(5), 612-613.

BÖRNER, F. D., GRUHNE, M., and SCHÖN, J. H., 1993, Contamination indications derived from electrical properties in the low frequency range: Geophys. Prosp., **41**, 83-98.

BÖRNER, F. D., SCHOPPER, J. R., and WELLER, A., 1996, Evaluation of transport and storage properties in the soil and groundwater zone from induced polarization measurements: Geophys. Prosp., **44**, 583-601.

BÖTTCHER, C. J. F., and BORDEWIJK, P., 1978, Theory of electric polarization, vol. II – Dielectrics in time-dependent fields: Elsevier Science Publ. Co., Inc.

BROWN, R. J., 1985, EM coupling in multifrequency IP and a generalization of the Cole-Cole impedance model: Geophys. Prosp., **33**, 282-302.

BURTON, G. R., 1994, Metallogenic studies of the Broken Hill and Euriowie Blocks, New South Wales, vol. 3 – Mineral deposits of the south-eastern Broken Hill Block: Bulletin no. 32(3), Geol. Surv. New South Wales, Dept. Mineral Resources.

CLAERBOUT, J. F., and MUIR, F., 1973, Robust modeling with erratic data: Geophysics, **38**, 826-844.

COGGON, J. H., 1971, Electromagnetic and electrical modeling by the finite element method: Geophysics, **36**, 132-155.

COGGON, J. H., 1984, New three-point formulas for inductive coupling removal in induced polarization: Geophysics, **49**, 307-309.

COLE, K. S., and COLE, R. H., 1941, Dispersion and absorption in dielectrics: J. Chem. Phys., **9**, 341-351.

CONSTABLE, S. C., PARKER, R. L., and CONSTABLE, C. G., 1987, Occam's inversion – a practical algorithm for generating smooth models from electromagnetic sounding data: Geophysics, **52**, 289-300.

DAHLIN, T., and LOKE, M. H., 1997, Quasi-3D resistivity imaging – mapping of three dimensional structures using two dimensional DC resistivity techniques: Proc. 3rd Mtg. Environmental and Engineering Geophysics, Environ. Eng. Geophys. Soc., Eur. Section, 143-146.

DAILY, W. D., RAMIREZ, A. L., LABRECQUE, D. J., and NITAO, J., 1992, Electrical resistivity tomography of vadose water movement: Water Resources Res., **28**, 1429-1442.

DAILY, W. D., RAMIREZ, A. L., LABRECQUE, D. J., and BARBER, W., 1995, Electrical resistance tomography experiments at the Oregon Graduate Institute: J. Appl. Geophys., **33**, 227-237.

DAILY, W. D., and RAMIREZ, A. L., 1995, Electrical resistance tomography during in-situ trichloroethylene remediation at the Savannah River Site: J. Appl. Geophys., **33**, 239-249.

DAILY, W. D., RAMIREZ, A. L., and ZONGE, K., 1996, A unique data acquisition system for electrical resistance tomography: Proc. Symp. Application of Geophysics to Engineering and Environmental Problems, Environ. Eng. Geophys. Soc., 743-751.

DAILY, W. D., RAMIREZ, A. L., and JOHNSON, R., 1998, Electrical impedance tomography of a perchloroethylene release: J. Environ. Eng. Geophys., **2**, 189-201.

DEGROOT-HEDLIN, C., and CONSTABLE, S. C., 1990, Occam's inversion to generate smooth, two-dimensional models from magnetotelluric data: Geophysics, **55**, 1613-1624.

DE LIMA, O. A. L., and ARAUJO, F. F. S., 1996, Subsurface contaminant tracking by ground-penetrating radar and spectral induced polarization: 66th Ann. Internat. Mtg., Soc. Expl. Geophys., Expanded Abstracts, 924-927.

DEY, A., and MORRISON, H. F., 1973, Electromagnetic coupling in frequency and time-domain induced-polarization surveys over a multilayered earth: Geophysics, **38**, 380-405.

DEY, A., and MORRISON, H. F., 1979, Resistivity modelling for arbitrarily shaped two-dimensional structures: Geophys. Prosp., **27**, 106-136.

DISSADO, L. A., and HILL, R. M., 1984, Anomalous low-frequency dispersion: J. Chem. Soc. Faraday Trans., **80**, 291-319.

DOMENICO, P. A., and SCHWARTZ, F. W., 1998, Physical and chemical hydrogeology: John Wiley & Sons, Inc.

DRASKOVITS, P., HOBOT, J., VERÖ, L., and SMITH, B. D., 1990, Induced-polarization surveys applied to evaluation of groundwater resources, Pannonian Basin, Hungary, *in* Fink, J. B., McAlister, E. O., Sternberg, B. K., Wieduwilt, W. G., and Ward, S. H., Eds., Induced polarization: Soc. Expl. Geophys., 379-396.

DUDÁS, J., NIESNER, E., and VERÖ, L., 1991, Resistivity and IP parameters used for hydrogeologic purposes and differentiation between nonmetallic minerals: Geophys. Trans., **36**, 81-92.

DUPRAT, A., SIMLER, L., and VALENTIN, J., 1979, Contamination de la nappe phréatique par les hydrocarbures à Entzheim, *in* Duprat, A., Simler, L., and Valentin, J., Nappe phréatique de la plaine du Rhin en Alsace: Louis Pasteur Univ. of Strasbourg, Mémoire no. 60, Science géologique, 201-216.

ELLIS, R. G., and OLDENBURG, D. W., 1994, Applied geophysical inversion: Geophys. J. Internat., **116**, 5-11.

ELLIS, R. G., and OLDENBURG, D. W., 1994, The pole-pole 3-D DC-resistivity inverse problem – a conjugate-gradient approach: Geophys. J. Internat., **119**, 187-194.

FALKENHAGEN, H., 1971, Theorie der Elektrolyte: Hirzel.

FARQUHARSON, C. G., and OLDENBURG, D. W., 1998, Non-linear inversion using general measures of data misfit and model structure: Geophys. J. Internat., **134**, 213-227.

FETTER, C. W., 1999, Contaminant hydrogeology: Prentice-Hall, Inc.

FINK, J. B., MCALISTER, E. O., STERNBERG, B. K., WIEDUWILT, W. G., and WARD, S. H., Eds., 1990, Induced polarization: Soc. Expl. Geophys.

FLETCHER, R., and REEVES, C. M., 1964, Function minimization by conjugate gradients: The Computer Journal, **7**, 149-154.

FRANGOS, W., 1990, Stable-oscillator phase IP systems, *in* Fink, J. B., McAlister, E. O., Sternberg, B. K., Wieduwilt, W. G., and Ward, S. H., Eds., Induced polarization: Soc. Expl. Geophys., 79-90.

FRYE, K. M., LESMES, D. P., and MORGAN, F. D., 1998, The influence of pore fluid chemistry on the induced polarization response of rocks and soils: Proc. Symp. Application of Geophysics to Engineering and Environmental Problems, Environ. Eng. Geophys. Soc., 771-780.

FULLER, B. D., and WARD, S. H., 1970, Linear system description of the electrical parameters of rocks: IEEE Trans. Geosci. Electron., **GE-8**, 7-18.

GERSZTENKORN, A., and SCALES, J. A., 1988, Smoothing seismic tomograms with alpha-trimmed means: Geophys. J. Internat., **92**, 67-72.

GESELOWITZ, D. B., 1971, An application of electrocardiographic lead theory to impedance plethysmography: IEEE Trans. Biomed. Eng., **BME-18**, 38-41.

GÖBEL, P., 1998, Erkundung kokereispezifischer Untergrundkontaminationen auf Altstandorten mit Hilfe ausgewählter ingenieurgeophysikalischer Methoden: Ph.D. dissertation, Tech. Univ. Clausthal.

GRAHAME, D. C., 1947, The electrical double layer and the theory of electrocapillarity, Chem. Rev., **41**, 441-501.

GRAHAME, D. C., 1952, Mathematical theory of the faradaic admittance: J. Electrochem. Soc., **99**, 370C-385C.

GUPTASARMA, D., 1984, True and apparent spectra of buried polarizable targets: Geophysics, **49**, 171-176.

HALLOF, P. G., 1964, A comparison of the various parameters employed in the variable-frequency induced-polarization method: Geophysics, **29**, 425-433.

HALLOF, P. G., 1974, The IP phase measurement and inductive coupling: Geophysics, **39**, 650-665.

HALLOF, P. G., and PELTON, W. H., 1980, The removal of inductive coupling effects from spectral IP data: 50th Ann. Internat. Mtg., Soc. Expl. Geophys., Expanded Abstracts, Session M.21, 2681-2724.

HASEGAWA, N., SHIMA, H., and SAKURAI, K., 1996, An application of two-dimensional IP image profiling to characterization of an active fault: 66th Ann. Internat. Mtg., Soc. Expl. Geophys., Expanded Abstracts, 928-931.

HESTENES, M. R., and STIEFEL, E., 1952, Methods of conjugate gradients for solving linear systems: J. Res. Nat. Bur. Standards, **49**, 409-436.

HESTENES, M. R., 1980, Conjugate direction methods in optimization: Springer-Verlag New York, Inc.

HOHMANN, G. W., 1973, Electromagnetic coupling between grounded wires at the surface of a two-layer earth: Geophysics, **38**, 854-863.

HOHMANN, G. W., 1988, Numerical modeling for electromagnetic methods of geophysics, *in* Nabighian, M. N., Ed., Electromagnetic methods in applied geophysics, vol. I – Theory: Soc. Expl. Geophys., 313-363.

HOHMANN, G. W., 1990, Three-dimensional IP models, *in* Fink, J. B., McAlister, E. O., Sternberg, B. K., Wieduwilt, W. G., and Ward, S. H., Eds., Induced polarization: Soc. Expl. Geophys., 150-178.

HÖLTING, B., 1996, Hydrogeologie: Ferdinand Enke.

ILICETO, V., SANTARATO, G., and VERONESE, S., 1982, An approach to the identification of fine sediments by induced polarization laboratory measurements: Geophys. Prosp., **30**, 331-347.

INMAN, J. R., 1975, Resistivity inversion with ridge regression: Geophysics, **40**, 798-817.

ISEKI, S., and SHIMA, H., 1992, Induced-polarization tomography – a crosshole imaging technique using chargeability and resistivity: 62nd Ann. Internat. Mtg., Soc. Expl. Geophys., Expanded Abstracts, 439-442.

JIN, J., 1993, The finite element method in electromagnetics: John Wiley & Sons, Inc.

JOHNSON, I. M., 1984, Spectral induced polarization parameters as determined through time-domain measurements: Geophysics, **49**, 1993-2003.

JONSCHER, A. K., 1981, A new understanding of the dielectric relaxation of solids: J. Mat. Sci., **16**, 2037-2060.

KATAYAMA, H., ARAI, E., SUZUKI, T., and YOKOKAWA, K., 1998, IP tomography test survey in the Barrier Main Lode, Broken Hill, Australia: Expl. Geophys., **29**, 433-439.

KEMNA, A., 1995, Tomographische Inversion des spezifischen Widerstandes in der Geoelektrik: diploma thesis, Univ. of Cologne.

KEMNA, A., and BINLEY, A. M., 1996, Complex electrical resistivity tomography for contaminant plume delineation: Proc. 2nd Mtg. Environmental and Engineering Geophysics, Environ. Eng. Geophys. Soc., Eur. Section, 196-199.

KEMNA, A., RÄKERS, E., and BINLEY, A. M., 1997, Application of complex resistivity tomography to field data from a kerosene-contaminated site: Proc. 3rd Mtg. Environmental and Engineering Geophysics, Environ. Eng. Geophys. Soc., Eur. Section, 151-154.

KEMNA, A., RÄKERS, E., and DRESEN, L., 1999, Field applications of complex resistivity tomography: 69th Ann. Internat. Mtg., Soc. Expl. Geophys., Expanded Abstracts, 331-334.

KING, T. V. V., and OLHOEFT, G. R., 1989, Mapping organic contamination by detection of clay-organic processes: Proc. Conf. Petroleum Hydrocarbons and Organic Chemicals in Ground Water – Prevention, Detection, and Restoration, Nat. Water Well Assn., 627-640.

KLEIN, J. D., BIEGLER, T., and HORNE, M. D., 1984, Mineral interfacial processes in the method of induced polarization: Geophysics, **49**, 1105-1114.

KULENKAMPFF, J. M., 1994, Die komplexe elektrische Leitfähigkeit poröser Gesteine im Frequenzbereich von 10 Hz bis 1 MHz – Einflüsse von Porenstruktur und Porenfüllung: Ph.D. dissertation, Tech. Univ. Clausthal.

LABRECQUE, D. J., and WARD, S. H., 1990, Two-dimensional cross-borehole resistivity model fitting, *in* Ward, S. H., Ed., Geotechnical and environmental geophysics, vol. III: Soc. Expl. Geophys., 51-74.

LABRECQUE, D. J., 1991, IP tomography: 61st Ann. Internat. Mtg., Soc. Expl. Geophys., Expanded Abstracts, 413-416.

LABRECQUE, D. J., MILETTO, M., DAILY, W. D., RAMIREZ, A. L., and OWEN, E., 1996a, The effects of noise on Occam's inversion of resistivity tomography data: Geophysics, **61**, 538-548.

LABRECQUE, D. J., MORELLI, G., and LUNDEGARD, P., 1996b, 3-D electrical resistivity tomography for environmental monitoring: Proc. Symp. Application of Geophysics to Engineering and Environmental Problems, Environ. Eng. Geophys. Soc., 723-732.

LABRECQUE, D. J., RAMIREZ, A. L., DAILY, W. D., BINLEY, A. M., and SCHIMA, S., 1996c, ERT monitoring of environmental remediation processes: Meas. Sci. Tech., **7**, 375-383.

LE MÉHAUTÉ, A., and CRÉPY, G., 1983, Introduction to transfer and motion in fractal media: Solid States Ionics, **9/10**, 17-30.

LEWIS, R. J. G., 1985, The determination of spectral parameters with pulse-train induced polarization: Geophysics, **50**, 870-871.

LI, Y., and OLDENBURG, D. W., 1997, 3D inversion of induced polarization data: Univ. of Arizona, Dept. of Mining and Geological Engineering, High-Resolution Geophysics Workshop, Expanded Abstract.

LIU, S., 1984, A new IP decoupling scheme: Expl. Geophys., **15**, 99-112.

LIU, S., and VOZOFF, K., 1985, The complex resistivity spectra of models consisting of two polarizable media of different intrinsic properties: Geophys. Prosp., **33**, 1029-1062.

LIU, S. H., 1985, Fractal model for the ac response of a rough interface: Phys. Rev. Lett., **55**, 529-532.

LOCKNER, D. A., and BYERLEE, J. D., 1985, Complex resistivity measurements of confined rock: J. Geophys. Res., **90**(B), 7837-7847.

LOKE, M. H., and BARKER, R. D., 1996, Rapid least-squares inversion of apparent resistivity pseudosections by a quasi-Newton method: Geophys. Prosp., **44**, 131-152.

LOWRY, T., ALLEN, M. B., and SHIVE, P. N., 1989, Singularity removal – a refinement of resistivity modeling techniques: Geophysics, **54**, 766-774.

LUO, Y., and ZHANG, G., 1998, Theory and application of spectral induced polarization: Soc. Expl. Geophys., Geophys. Mono., **8**.

MACKIE, R. L., and MADDEN, T. R., 1993, Three-dimensional magnetotelluric inversion using conjugate gradients: Geophys. J. Internat., **115**, 215-229.

MADDEN, T. R., and CANTWELL, T., 1967, Induced polarization, a review, *in* Hansen, D. A., Heinrichs, Jr., W. E., Holmer, R. C., MacDougall, R. E., Rogers, G. R., Sumner, J. S., and Ward, S. H., Eds., Mining geophysics, vol. II: Soc. Expl. Geophys., 373-400.

MAJOR, J., and SILIC, J., 1981, Restrictions on the use of Cole-Cole dispersion models in complex resistivity interpretation: Geophysics, **46**, 916-931.

MARSHALL, D. J., and MADDEN, T. R., 1959, Induced polarization, a study of its causes: Geophysics, **24**, 790-816.

MEJU, M. A., 1994, Geophysical data analysis – understanding inverse problem theory and practice: Soc. Expl. Geophys., Course Notes, **6**.

MILLETT, JR., F. B., 1967, Electromagnetic coupling of collinear dipoles on a uniform half-space, *in* Hansen, D. A., Heinrichs, Jr., W. E., Holmer, R. C., MacDougall, R. E., Rogers, G. R., Sumner, J. S., and Ward, S. H., Eds., Mining geophysics, vol. II: Soc. Expl. Geophys., 401-419.

MORA, P., 1987, Nonlinear two-dimensional elastic inversion of multioffset seismic data: Geophysics, **52**, 1211-1228.

MORELLI, G., and LABRECQUE, D. J., 1996, Advances in ERT modeling: Eur. J. Environ. Eng. Geophys., **1**, 171-186.

MORGAN, F. D., SCIRA-SCAPPUZZO, F., SHI, W., RODI, W., SOGADE, J., VICHABIAN, Y., and LESMES, D. P., 1999, Induced polarization imaging of a jet fuel plume: Proc. Symp. Application of Geophysics to Engineering and Environmental Problems, Environ. Eng. Geophys. Soc., 541-548.

MORITA, N., KUMAGAI, N., and MAUTZ, J. R., 1991, Integral equation methods for electromagnetics: Artech House.

MOSTELLER, F., and TUKEY, J. W., 1977, Data analysis and regression: Addison-Wesley Publ. Co.

NELSON, P. H., and VAN VOORHIS, G. D., 1973, Letter to the Editor regarding the paper "Complex resistivity spectra of porphyry copper mineralization": Geophysics, **38**, 984.

NELSON, P. H., HANSEN, W. H., and SWEENEY, M. J., 1982, Induced-polarization response of zeolitic conglomerate and carbonaceous siltstone: Geophysics, **47**, 71-88.

NELSON, P. H., 1994, Permeability-porosity relationships in sedimentary rocks: The Log Analyst, **35**(3), 38-61.

NEWMAN, G. A., and ALUMBAUGH, D. L., 1997, Three-dimensional massively parallel electromagnetic inversion – I. Theory: Geophys. J. Internat., **128**, 345-354.

NOBES, D. C., 1996, Troubled waters – environmental applications of electrical and electromagnetic methods: Kluwer Academic Publ., Surveys in Geophysics, **17**, 393-454.

OGILVY, A. A., and KUZMINA, E. N., 1972, Hydrogeologic and engineering-geologic possibilities for employing the method of induced potentials: Geophysics, **37**, 839-861.

OLDENBURG, D. W., MCGILLIVRAY, P. R., and ELLIS, R. G., 1993, Generalized subspace methods for large-scale inverse problems: Geophys. J. Internat., **114**, 12-20.

OLDENBURG, D. W., and LI, Y., 1994, Inversion of induced polarization data: Geophysics, **59**, 1327-1341.

OLDENBURG, D. W., LI, Y., and ELLIS, R. G., 1997, Inversion of geophysical data over a copper gold porphyry deposit – a case history for Mt. Milligan: Geophysics, **62**, 1419-1431.

OLHOEFT, G. R., 1981, Electrical properties of rocks, *in* Touloukian, Y. S., Judd, W. R., and Roy, R. F., Eds., Physical properties of rocks and minerals: McGraw-Hill, Inc., 257-297.

OLHOEFT, G. R., 1985, Low-frequency electrical properties: Geophysics, **50**, 2492-2503.

OLHOEFT, G. R., 1986, Direct detection of hydrocarbon and organic chemicals with ground penetrating radar and complex resistivity: Proc. Conf. Petroleum Hydrocarbons and Organic Chemicals in Ground Water – Prevention, Detection, and Restoration, Nat. Water Well Assn., 284-305.

OLHOEFT, G. R., 1992, Geophysical detection of hydrocarbon and organic chemical contamination: Proc. Symp. Application of Geophysics to Engineering and Environmental Problems, Soc. Eng. Min. Expl. Geophys., 587-595.

ORISTAGLIO, M. L., and WORTHINGTON, M. H., 1980, Inversion of surface and borehole electromagnetic data for two-dimensional electrical conductivity models, Geophys. Prosp., **28**, 633-657.

PAPE, H., RIEPE, L., and SCHOPPER, J. R., 1982, A pigeon-hole model for relating permeability to specific surface: The Log Analyst, **23**(1), 5-13.

PAPE, H., RIEPE, L., and SCHOPPER, J. R., 1987, Theory of self-similar network structures in sedimentary and igneous rocks and their investigation with microscopical and physical methods: J. Microscopy, **148**, 121-147.

PAPE, H., and SCHOPPER, J. R., 1988, Relations between physically relevant geometrical properties of a multi-fractal porous system, *in* Unger, K. K., Rouquerol, J., Sing, K. S. W., and Kral, H., Eds., Characterization of porous solids: Elsevier Science Publ. Co., Inc., 473-482.

PAPE, H., and VOGELSANG, D., 1996, Fractal evaluation of induced polarization logs in the KTB-Oberpfalz HB: Bundesanstalt für Geowissenschaften und Rohstoffe / Geologische Landesämter in der Bundesrepublik Deutschland, Geologisches Jahrbuch, **54**(E), 3-27.

PARK, S. K., and VAN, G. P., 1991, Inversion of pole-pole data for 3-D resistivity structure beneath arrays of electrodes: Geophysics, **56**, 951-960.

PARKER, R. L., 1994, Geophysical inverse theory: Princeton Univ. Press.

PATNODE, H. W., and WYLLIE, M. R. J., 1950, The presence of conductive solids in reservoir rocks as a factor in electric log interpretation: Trans. Am. Inst. Min. Metall. Eng., **189**, 47-52.

PELTON, W. H., WARD, S. H., HALLOF, P. G., SILL, W. R., and NELSON, P. H., 1978a, Mineral discrimination and removal of inductive coupling with multifrequency IP: Geophysics, **43**, 588-609.

PELTON, W. H., RIJO, L., and SWIFT, JR., C. M., 1978b, Inversion of two-dimensional resistivity and induced-polarization data: Geophysics, **43**, 788-803.

PELTON, W. H., SILL, W. R., and SMITH, B. D., 1983, Interpretation of complex resistivity and dielectric data, part I: Geophys. Trans., **29**, 297-330.

PELTON, W. H., SILL, W. R., and SMITH, B. D., 1984, Interpretation of complex resistivity and dielectric data, part II: Geophys. Trans., **30**, 11-45.

PINI, G., and GAMBOLATI, G., 1990, Is a simple diagonal scaling the best preconditioner for conjugate gradients on supercomputers?: Adv. Water Resources, **13**, 147-153.

POLAK, E., and RIBIERE, G., 1969, Note sur la convergence de méthodes de directions conjuguées: Revue Française d'Informatique et de Recherche Opérationnelle, **16**(R1), 35-43.

PRESS, W. H., TEUKOLSKY, S. A., VETTERLING, W. T., and FLANNERY, B. P., 1992, Numerical recipes in FORTRAN – the art of scientific computing: Cambridge Univ. Press.

PRIDMORE, D. F., HOHMANN, G. W., WARD, S. H., and SILL, W. R., 1981, An investigation of finite-element modeling for electrical and electromagnetic data in three dimensions: Geophysics, **46**, 1009-1024.

QUERALT, P., POUS, J., and MARCUELLO, A., 1991, 2-D resistivity modeling – an approach to arrays parallel to the strike direction: Geophysics, **56**, 941-950.

RAMIREZ, A. L., DAILY, W. D., LABRECQUE, D. J., OWEN, E., and CHESNUT, D., 1993, Monitoring an underground steam injection process using electrical resistance tomography: Water Resources Res., **29**, 73-87.

RAMIREZ, A. L., DAILY, W. D., and NEWMARK, R. L., 1995, Electrical resistance tomography for steam injection monitoring and process control: J. Environ. Eng. Geophys., **0**, 39-51.

RAMIREZ, A. L., DAILY, W. D., BINLEY, A. M., LABRECQUE, D. J., and ROELANT, D., 1996, Detection of leaks in underground storage tanks using electrical resistance methods: J. Environ. Eng. Geophys., **1**, 189-203.

RAMIREZ, A. L., DAILY, W. D., BINLEY, A. M., and LABRECQUE, D. J., 1999, Electrical impedance tomography of known targets: J. Environ. Eng. Geophys., **4**, 11-26.

RIJO, L., 1977, Modelling of electric and electromagnetic data: Ph.D. thesis, Univ. of Utah.

RINK, M., and SCHOPPER, J. R., 1974, Interface conductivity and its implication to electric logging: Trans. 15th Ann. Logging Symp., Soc. Prof. Well Log Analysts, 1-15.

RODI, W. L., 1976, A technique for improving the accuracy of finite element solutions for magnetotelluric data: Geophys. J. Roy. Astr. Soc., **44**, 483-506.

ROUTH, P. S., OLDENBURG, D. W., and LI, Y., 1998, Regularized inversion of spectral IP parameters from complex resistivity data: 68th Ann. Internat. Mtg., Soc. Expl. Geophys., Expanded Abstracts, 810-813.

RUFFET, C., GUÉGUEN, Y., and DAROT, M., 1991, Complex conductivity measurements and fractal nature of porosity: Geophysics, **56**, 758-768.

RUFFET, C., DAROT, M., and GUÉGUEN, Y., 1995, Surface conductivity in rocks – a review: Kluwer Academic Publ., Surveys in Geophysics, **16**, 83-105.

SASAKI, Y., 1989, Two-dimensional joint inversion of magnetotelluric and dipole-dipole resistivity data: Geophysics, **54**, 254-262.

SASAKI, Y., 1992, Resolution of resistivity tomography inferred from numerical simulation: Geophys. Prosp., **40**, 453-463.

SASAKI, Y., 1994, 3-D resistivity inversion using the finite-element method: Geophysics, **59**, 1839-1848.

SCALES, J. A., 1987, Tomographic inversion via the conjugate gradient method: Geophysics, **52**, 179-185.

SCALES, J. A., and GERSZTENKORN, A., 1987, Robust methods in inverse theory, *in* Lines, L. R., and Scales, J. A., Eds., Geophysical imaging: Soc. Expl. Geophys., 25-50.

SCHIMA, S., LABRECQUE, D. J., and MILETTO, M., 1993, Tracking fluid flow in the unsaturated zone using cross-borehole resistivity and IP: Proc. Symp. Application of Geophysics to Engineering and Environmental Problems, Environ. Eng. Geophys. Soc., 527-543.

SCHÖN, J. H., 1996, Physical properties of rocks – fundamentals and principles of petrophysics: Elsevier Science Ltd., Handbook of geophysical exploration, Seismic Exploration, **18**.

SCHOPPER, J. R., KULENKAMPFF, J. M., and DEBSCHÜTZ, W. G., 1997, Grenzflächenleitfähigkeit, *in* Knödel, K., Krummel, H., and Lange, G., Eds., Handbuch zur Erkundung des Untergrundes von Deponien und Altlasten, Band 3 – Geophysik: Springer-Verlag Berlin, 992-995.

SCHWARZ, H. R., 1991, Methode der finiten Elemente: Teubner.

SEIGEL, H. O., 1959, Mathematical formulation and type curves for induced polarization: Geophysics, **24**, 547-565.

SEIGEL, H. O., VANHALA, H., and SHEARD, S. N., 1997, Some case histories of source discrimination using time-domain spectral IP: Geophysics, **62**, 1394-1408.

SHERIFF, R. E., 1991, Encyclopedic dictionary of exploration geophysics: Soc. Expl. Geophys.

SHI, W., RODI, W., and MORGAN, F. D., 1998, 3-D induced polarization inversion using complex electrical resistivities: Proc. Symp. Application of Geophysics to Engineering and Environmental Problems, Environ. Eng. Geophys. Soc., 785-794.

SHIMA, H., 1992, 2-D and 3-D resistivity image reconstruction using crosshole data: Geophysics, **57**, 1270-1281.

SHUEY, R. T., and JOHNSON, M., 1973, On the phenomenology of electrical relaxation in rocks: Geophysics, **38**, 37-48.

SLATER, L. D., BROWN, D., and BINLEY, A. M., 1996, Determination of hydraulically conductive pathways in fractured limestone using cross-borehole electrical resistivity tomography: Eur. J. Environ. Eng. Geophys., **1**, 35-52.

SLATER, L. D., ZAIDMAN, M. D., BINLEY, A. M., and WEST, L. J., 1997, Electrical imaging of saline tracer migration for the investigation of unsaturated zone transport mechanisms: Hydrology and Earth System Sci., **1**, 291-302.

SOININEN, H., 1984, Inapplicability of pulse train time-domain measurements to spectral induced polarization: Geophysics, **49**, 826-827.

SOININEN, H., 1985, The behavior of the apparent resistivity phase spectrum in the case of two polarizable media: Geophysics, **50**, 810-819.

SOININEN, H., and VANHALA, H., 1996, Mapping oil contamination in glacial sediments by the spectral induced polarization method: Proc. Symp. Application of Geophysics to Engineering and Environmental Problems, Environ. Eng. Geophys. Soc., 1007-1015.

STERNBERG, B. K., and OEHLER, D. Z., 1990, Induced-polarization hydrocarbon surveys – Arkoma Basin case histories, *in* Fink, J. B., McAlister, E. O., Sternberg, B. K., Wieduwilt, W. G., and Ward, S. H., Eds., Induced polarization: Soc. Expl. Geophys., 354-378.

STERNBERG, B. K., 1991, A review of some experience with the induced-polarization/resistivity method for hydrocarbon surveys – successes and limitations: Geophysics, **56**, 1522-1532.

STEVENS, B. P. J., 1996, Contributed remarks on the paper "Broken Hill area, Australia, as a Proterozoic fold and thrust belt – implications for the Broken Hill base-metal deposit": Trans. Inst. Min. Metall. (Section B: Appl. Earth Sci.), 105, B89-90.

STOLLAR, R. L., and ROUX, P., 1975, Earth resistivity surveys – a method for defining ground-water contamination: Ground Water, **13**(2), 145-150.

STURROCK, J. T., LESMES, D. P., and MORGAN, F. D., 1998, The influence of micro-geometry on the hydraulic permeability and the induced polarization response of sandstones: Proc. Symp. Application of Geophysics to Engineering and Environmental Problems, Environ. Eng. Geophys. Soc., 859-867.

STURROCK, J. T., LESMES, D. P., and MORGAN, F. D., 1999, Permeability estimation using spectral induced polarization measurements: Proc. Symp. Application of Geophysics to Engineering and Environmental Problems, Environ. Eng. Geophys. Soc., 409-416.

SULLIVAN, E., and LABRECQUE, D. J., 1998, Optimization of ERT surveys: Proc. Symp. Application of Geophysics to Engineering and Environmental Problems, Environ. Eng. Geophys. Soc., 571-581.

SUMNER, J. S., 1976, Principles of induced polarization for geophysical exploration: Elsevier Science Publ. Co., Inc.

SUNDE, E. D., 1968, Earth conduction effects in transmission systems: Dover Publ., Inc.

TELFORD, W. M., GELDART, L. P., and SHERIFF, R. E., 1990, Applied geophysics: Cambridge Univ. Press.

TIKHONOV, A. N., and ARSENIN, V. Y., 1977, Solutions of ill-posed problems: W. H. Winston and Sons.

TOMBS, J. M. C., 1981, The feasibility of making spectral IP measurements in the time domain: Elsevier Science Publ. Co., Inc., Geoexploration, **19**, 91-102.

TOWLE, J. N., ANDERSON, R. G., PELTON, W. H., OLHOEFT, G. R., and LABRECQUE, D. J., 1985, Direct detection of hydrocarbon contaminants using the induced-polarization method: 55th Ann. Internat. Mtg., Soc. Expl. Geophys., Expanded Abstracts, 145-147.

TRIPP, A. C., HOHMANN, G. W., and SWIFT, JR., C. M., 1984, Two-dimensional resistivity inversion: Geophysics, **49**, 1708-1717.

TYNE, E. D., and WEBSTER, S. S., 1988, Surface and borehole electrical surveys at the Flying Doctor Prospect, Broken Hill – a case study: Geological Survey Report no. GS1988/101, Geol. Surv. New South Wales, Dept. Mineral Resources.

VACQUIER, V., HOLMES, C. R., KINTZINGER, P. R., and LAVERGNE, M., 1957, Prospecting for ground water by induced electrical polarization: Geophysics, **22**, 660-687.

VANDECAR, J. S., and SNIEDER, R., 1994, Obtaining smooth solutions to large, linear, inverse problems: Geophysics, **59**, 818-829.

VANHALA, H., SOININEN, H., and KUKKONEN, I., 1992, Detecting organic chemical contaminants by spectral-induced polarization method in glacial till environment: Geophysics, **57**, 1014-1017.

VANHALA, H., and PELTONIEMI, M., 1992, Spectral IP studies of Finnish ore prospects: Geophysics, **57**, 1545-1555.

VANHALA, H., and SOININEN, H., 1995, Laboratory technique for measurement of spectral induced polarization response of soil samples: Geophys. Prosp., **43**, 655-676.

VANHALA, H., 1996, Monitoring the integrity of liner construction using induced polarization: Proc. Symp. Application of Geophysics to Engineering and Environmental Problems, Environ. Eng. Geophys. Soc., 1017-1026.

VANHALA, H., 1997, Mapping oil-contaminated sand and till with the spectral induced polarization (SIP) method: Geophys. Prosp., **45**, 303-326.

VANHALA, H., 1999, Estimation of ore-mineral grain-size distribution by spectral induced polarisation measurements – a laboratory study: 61st Ann. Internat. Mtg., Eur. Assn. Expl. Geophys., Session 2032.

VAN VOORHIS, G. D., NELSON, P. H., and DRAKE, T. L., 1973, Complex resistivity spectra of porphyry copper mineralization: Geophysics, **38**, 49-60.

VINEGAR, H. J., and WAXMAN, M. H., 1984, Induced polarization of shaly sands: Geophysics, **49**, 1267-1287.

WAIT, J. R., 1959, The variable-frequency method, *in* Wait, J. R., Ed., Overvoltage research and geophysical applications: Pergamon Press, Inc., 29-49.

WAIT, J. R., 1982, Geo-electromagnetism: Academic Press Inc.

WAIT, J. R., 1984, Relaxation phenomena and induced polarization: Elsevier Science Publ. Co., Inc., Geoexploration, **22**, 107-127.

WAIT, J. R., and GRUSZKA, T. P., 1986, On electromagnetic coupling "removal" from induced polarization surveys: Elsevier Science Publ. Co., Inc., Geoexploration, **24**, 21-27.

WARD, S. H., and FRASER, D. C., 1967, Conduction of electricity in rocks, *in* Hansen, D. A., Heinrichs, Jr., W. E., Holmer, R. C., MacDougall, R. E., Rogers, G. R., Sumner, J. S., and Ward, S. H., Eds., Mining geophysics, vol. II: Soc. Expl. Geophys., 197-223.

WARD, S. H., 1990, Resistivity and induced polarization methods, *in* Ward, S. H., Ed., Geotechnical and environmental geophysics, vol. I: Soc. Expl. Geophys., 147-189.

WARD, S. H., STERNBERG, B. K., LABRECQUE, D. J., and POULTON, M. M., 1995, Recommendations for IP research: The Leading Edge, **14**, 243-247.

WAXMAN, M. H., and SMITS, L. J. M., 1968, Electrical conductivities in oil-bearing shaly sands: Soc. Petr. Eng. J., **8**, 107-122.

WELLER, A., and BÖRNER, F. D., 1996, Measurements of spectral induced polarization for environmental purposes: Environ. Geology, **27**, 329-334.

WELLER, A., SEICHTER, M., and KAMPKE, A., 1996a, Induced-polarization modelling using complex electrical conductivities: Geophys. J. Internat., **127**, 387-398.

WELLER, A., GRUHNE, M., SEICHTER, M., and BÖRNER, F. D., 1996b, Monitoring hydraulic experiments by complex conductivity tomography: Eur. J. Environ. Eng. Geophys., **1**, 209-228.

WHITE, S. H., ROTHERY, E., LIPS, A. L. W., and BARCLAY, T. J. R., 1996, Authors' reply on contributed remarks on the paper "Broken Hill area, Australia, as a Proterozoic fold and thrust belt – implications for the Broken Hill base-metal deposit": Trans. Inst. Min. Metall. (Section B: Appl. Earth Sci.), 105, B90-98.

WONG, J., 1979, An electrochemical model of the induced-polarization phenomenon in disseminated sulfide ores: Geophysics, **44**, 1245-1265.

YANG, X., and LABRECQUE, D. J., 2000, Three-dimensional complex resistivity tomography: Proc. Symp. Application of Geophysics to Engineering and Environmental Problems, Environ. Eng. Geophys. Soc., 897-906.

YI, M., KIM, J., CHUNG, S., and CHO, I., 1997, The borehole effect in imaging the earth using resistivity tomography: 59th Ann. Internat. Mtg., Eur. Assn. Expl. Geophys., Session P079.

YONG, R. N., MOHAMED, A. M. O., and WARKENTIN, B. P., 1992, Principles of contaminant transport in soils: Elsevier Science Publ. Co., Inc.

YUVAL, and OLDENBURG, D. W., 1996, DC resistivity and IP methods in acid mine drainage problems – results from the Copper Cliff mine tailings impoundments: J. Appl. Geophys., **34**, 187-198.

ZHANG, J., MACKIE, R. L., and MADDEN, T. R., 1995, 3-D resistivity forward modeling and inversion using conjugate gradients: Geophysics, **60**, 1313-1325.

ZHANG, J., RODI, W., MACKIE, R. L., and SHI, W., 1996, Regularization in 3-D DC resistivity tomography: Proc. Symp. Application of Geophysics to Engineering and Environmental Problems, Environ. Eng. Geophys. Soc., 687-694.

ZHOU, B., and GREENHALGH, S. A., 1997, A synthetic study on crosshole resistivity imaging using different electrode arrays: Expl. Geophys., **28**, 1-5.

ZONGE, K. L., SAUCK, W. A., and SUMNER, J. S., 1972, Comparison of time, frequency, and phase measurements in induced polarization: Geophys. Prosp., **20**, 626-648.

APPENDICES

A: GRAIN SIZE SORTING AND COLE-COLE EXPONENT

For a clastic sedimentary rock, the spread of the log grain size distribution as used by Berg (1970) is defined as $\ln(r_{90}/r_{10})$. Herein, r_{10} and r_{90} denote the grain sizes which have a cumulative frequency on logarithmic scale of 10 % and 90 %, respectively. For a log-normal distribution of grain sizes about the median value r_{grain}, this 80 % interval is approximately equal to the width at half-maximum, which shall be denoted by $\Delta_{\ln r}$.

Assuming a relation $\tau \sim r_{\text{grain}}^2$ between the time constant τ of a Cole-Cole-type electrical response and the median grain size (see Section 2.6.2), one may therefore write

$$\ln(r_{90}/r_{10}) \approx \Delta_{\ln r} \approx \frac{1}{2}\Delta_{\ln \tau} \,. \tag{A.1}$$

In eq. (A.1), $\Delta_{\ln \tau}$ now represents the width at half-maximum of the relaxation time distribution corresponding to the underlying Cole-Cole model (see Section 2.4.2).

As illustrated in Figure 2.2b, the width of the relaxation time distribution is implicitly related to the Cole-Cole exponent c. From a numerical analysis for the relevant range $0.1 < c < 0.6$, it was found that this relation is reasonably described by the equation

$$\Delta_{\ln \tau} \approx 2.3\, c^{-1.2} \,. \tag{A.2}$$

Thus, in a first approximation, eqs. (A.1) and (A.2) may be simplified to $\ln(r_{90}/r_{10}) \approx 1/c$ or – more convenient for practical purposes –

$$\log_{10}(r_{90}/r_{10}) \approx 1/2c \,, \tag{A.3}$$

relating the spread of the grain size distribution, i.e., grain size sorting, with the resultant electrical frequency dispersion.

Finally it may be noted that eq. (A.3) is in good agreement with grain size distributions and complex resistivity spectra published by Vanhala (1997) and Vanhala (1999) for, respectively, different silt and mineralized rock samples. Deviations occur

in cases where the frequency exponent is only poorly resolved by the spectral phase behavior. Then, however, the validity of a Cole-Cole model description is questionable due to negligible spectral dispersion.

B: REARRANGEMENT OF FINITE-ELEMENT FUNCTIONAL

Before the stationarity requirement $\delta F = 0$ is applied to the complex FE functional F in order to deduce the linear FE equations, any terms in the original expression (3.20) containing second derivatives of the unknown function $\widetilde{\phi}_s$ need to be reduced to first derivatives, since the former are not well-defined for a linear elemental approximation as being used within this thesis.

By partial integration and the application of Gauss' integral theorem, one finds the complex identities

$$\iint_A \partial_x \left(\Delta\sigma\, \partial_x \widetilde{\phi}_p\right) \widetilde{\phi}_s \, dx dz = \oint_C \left(\Delta\sigma\, \partial_x \widetilde{\phi}_p\right) \widetilde{\phi}_s \, n_x \, ds - \iint_A \left(\Delta\sigma\, \partial_x \widetilde{\phi}_p\right)\left(\partial_x \widetilde{\phi}_s\right) dx dz \qquad \text{(B.1)}$$

and

$$\iint_A \partial_z \left(\Delta\sigma\, \partial_z \widetilde{\phi}_p\right) \widetilde{\phi}_s \, dx dz = \oint_C \left(\Delta\sigma\, \partial_z \widetilde{\phi}_p\right) \widetilde{\phi}_s \, n_z \, ds - \iint_A \left(\Delta\sigma\, \partial_z \widetilde{\phi}_p\right)\left(\partial_z \widetilde{\phi}_s\right) dx dz \,, \qquad \text{(B.2)}$$

where n_x and n_z denote the components of the outward normal in x- and z-direction, respectively. Note that the left-hand sides of eqs. (B.1) and (B.2) represent contributions to the FE functional (3.20).

Now, since

$$n_x\, \partial_x \widetilde{\phi}_p + n_z\, \partial_z \widetilde{\phi}_p = \partial_n \widetilde{\phi}_p \qquad \text{(B.3)}$$

and moreover, from the equations (3.8), (3.17), and (3.19),

$$\Delta\sigma\, \partial_n \widetilde{\phi}_p = -\Delta\beta\, \widetilde{\phi}_p \,, \qquad \text{(B.4)}$$

with $\Delta\beta = \beta - \beta_0$, adding up both identities (B.1) and (B.2) yields

$$\begin{aligned} &\iint_A \left[\partial_x \left(\Delta\sigma\, \partial_x \widetilde{\phi}_p\right) + \partial_z \left(\Delta\sigma\, \partial_z \widetilde{\phi}_p\right)\right] \widetilde{\phi}_s \, dx dz \\ &\qquad = -\oint_C \Delta\beta\, \widetilde{\phi}_p\, \widetilde{\phi}_s \, ds - \iint_A \Delta\sigma \left[\left(\partial_x \widetilde{\phi}_p\right)\left(\partial_x \widetilde{\phi}_s\right) + \left(\partial_z \widetilde{\phi}_p\right)\left(\partial_z \widetilde{\phi}_s\right)\right] dx dz \,. \end{aligned} \qquad \text{(B.5)}$$

Substituting eq. (B.5) into eq. (3.20) and, finally, splitting the integration according to the domain discretization, i.e.,

$$\begin{aligned} \iint_A \begin{Bmatrix} \sigma \\ \Delta\sigma \end{Bmatrix} \dots dxdz \quad &\rightarrow \quad \sum_{j=1}^{N_e} \begin{Bmatrix} \sigma_j \\ \Delta\sigma_j \end{Bmatrix} \iint_{A_j} \dots dxdz \,, \\ \oint_C \begin{Bmatrix} \beta \\ \Delta\beta \end{Bmatrix} \dots ds \quad &\rightarrow \quad \sum_{j=1}^{N_b} \begin{Bmatrix} \beta_j \\ \Delta\beta_j \end{Bmatrix} \int_{C_j} \dots ds \,, \end{aligned} \tag{B.6}$$

obviously results in the expression for the FE functional given in eq. (3.21).

C: EVALUATION OF INVERSE FOURIER INTEGRAL

The procedure used to evaluate the inverse Fourier integral (3.31) is based on the approach of LaBrecque et al. (1996a). Since the asymptotic behavior of the transformed potential $\widetilde{\phi}(k)$ for small and large arguments is different, the integral is split into two parts to which, respectively, adequate numerical integration techniques are then applied, i.e.,

$$\int_0^\infty \widetilde{\phi}(k)\, dk = \int_0^{k_0} \widetilde{\phi}(k)\, dk + \int_{k_0}^\infty \widetilde{\phi}(k)\, dk \,, \tag{C.1}$$

with some characteristic wavenumber k_0.

According to eq. (3.10), the (primary) transformed potential is proportional to the modified Bessel function $\mathrm{K}_0(u)$, with $u = kr$. Here, r denotes the representative radial distance from the (image) source. The corresponding asymptotic behavior is given by (Abramowitz and Stegun, 1984)

$$\begin{aligned} u \rightarrow 0 \;&:\; \mathrm{K}_0(u) \sim -\ln u \,, \\ u \rightarrow \infty \;&:\; \mathrm{K}_0(u) \sim \mathrm{e}^{-u} \big/ \sqrt{u} \,. \end{aligned} \tag{C.2}$$

To overcome the singularity in the integrand at zero, the change of variable $k' = (k/k_0)^{1/2}$ is made in the first integral of the right-hand side of eq. (C.1). The resulting nonsingular integral, with integrand $g(k') = 2k_0 k' \widetilde{\phi}(k)$, is evaluated by conventional N_G-point Gaussian quadrature (Press et al., 1992), yielding appropriate abscissa k'_n with corresponding weights w'_n. Summing up both steps, it is

$$\int_0^{k_0} \widetilde{\phi}(k)\, dk = \int_0^1 g(k')\, dk' = \sum_{n=1}^{N_\mathrm{G}} w'_n\, g(k'_n) = \pi \sum_{n=1}^{N_\mathrm{G}} w_n\, \widetilde{\phi}(k_n) \,, \tag{C.3}$$

where $k_n = k_0 k'^2_n$ and $w_n = 2k_0 k'_n w'_n / \pi$.

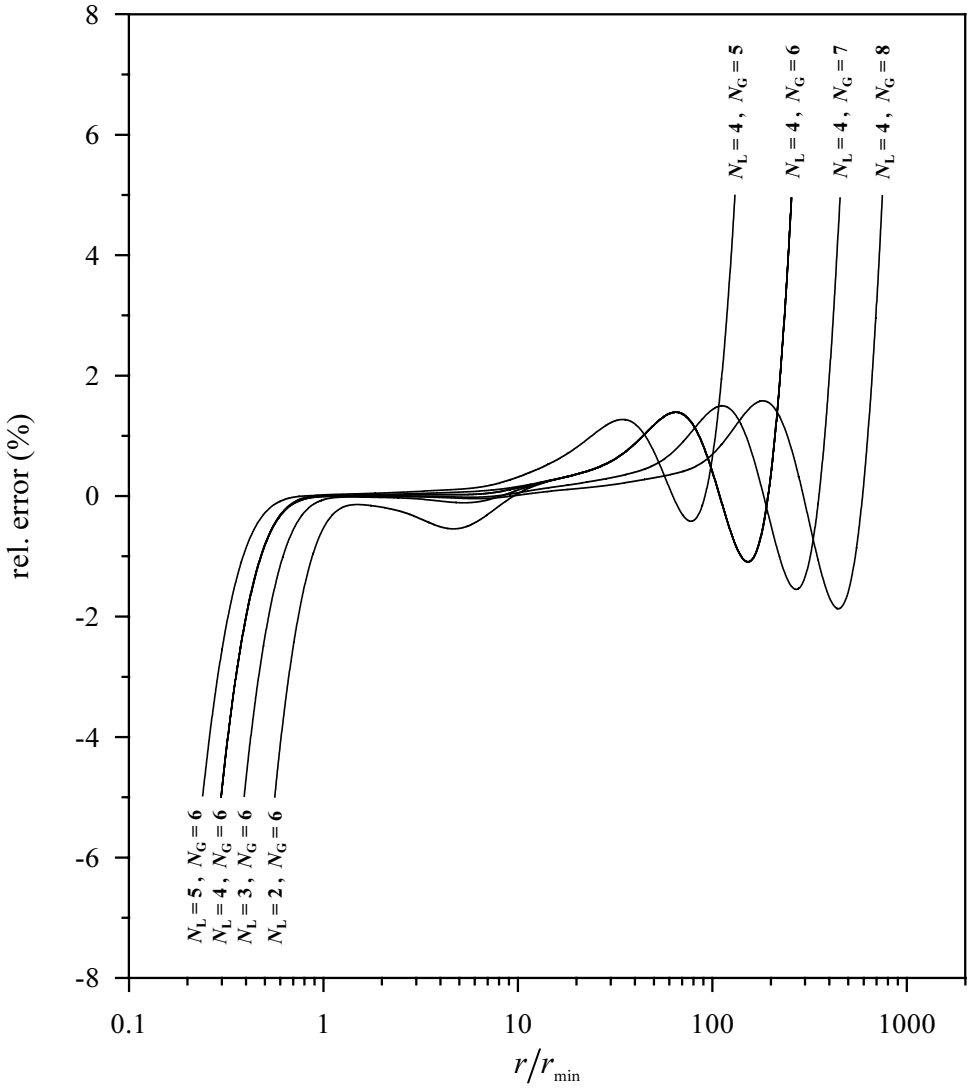

Figure C.1: Relative error in the inverse Fourier transform according to eqs. (C.3) and (C.4) against the normalized distance $r/r_{\min}$ from the current source for a surface electrode over a homogeneous half-space and $k_0 = 1/(2r_{\min})$. As indicated, the different curves represent different choices of the number of abscissa N_G and N_L in the Gauss and Laguerre integration formulas, respectively. Note that a minimum value of $N_L = 4$ prevents the formation of an additional 'dent' within the region where errors are relatively small, and that increasing N_G is basically more effective to broaden the valid range of the integration than increasing N_L.

From the relations (C.2), it is seen that the behavior of $\widetilde{\phi}(k)$ for large arguments is characterized by an exponential decrease. Therefore, the upper integration in eq. (C.1) is performed using a N_L - point Laguerre-type formula (Press et al., 1992). Analogous to eq. (C.3), one finds

$$\int_{k_0}^{\infty} \widetilde{\phi}(k)\, dk = \int_{0}^{\infty} \mathrm{e}^{-k'}\, g(k')\, dk' = \sum_{n=1}^{N_L} w'_n\, g(k'_n) = \pi \sum_{n=1}^{N_L} w_n\, \widetilde{\phi}(k_n)\,, \qquad \text{(C.4)}$$

with the rescaled abscissa and weights, respectively, $k_n = k_0 (k'_n + 1)$ and $w_n = k_0 \, \mathrm{e}^{k'_n} \, w'_n / \pi$. Note that in eq. (C.4), after substitution of $k' = k/k_0 - 1$, the new function $g(k') = k_0 \, \mathrm{e}^{k'} \, \widetilde{\phi}(k)$ is temporarily defined.

The integration bound k_0 has to be specified in relation to the spatial scale of the considered problem. A characteristic quantity in this regard is given by the minimum distance between corresponding transmitting and receiving electrodes within the underlying set of measurement configurations, denoted by $r_{\min}$. The number of employed abscissa in the integration formulas determines the valid range of the integration in terms of the distance from the source. From a numerical analysis for a homogeneous half-space, it was found that the variable choice

$$N_{\mathrm{G}} = int[6 \log(r_{\max} / r_{\min})], \tag{C.5}$$

together with $N_{\mathrm{L}} = 4$ and $k_0 = 1/(2 r_{\min})$, guarantees an error of less than 0.5 % in the inverse Fourier integration for distances ranging from $r_{\min}$ to $r_{\max}$ (see Figure C.1). Herein, $r_{\max}$ denotes the maximum distance between source and receiver electrodes as being of interest within the survey.

Obviously, combination of both integration parts according to eq. (C.1) results in the overall expression (3.32).

D: Parameterization of Model Roughness

The model objective function of eq. (3.39) imposes a first-order smoothing on the complex model $\mathbf{m}$. Since the model is given as a parameterization into M rectangular cells, the double integral can be replaced by a sum and the squared L_2-norm may be expanded according to

$$\Psi_{\mathrm{m}}(\mathbf{m}) = \sum_{j=1}^{M} \left(\left| \frac{\Delta m_j}{\Delta x_j} \right|^2 + \left| \frac{\Delta m_j}{\Delta z_j} \right|^2 \right) \Delta x_j \, \Delta z_j \; . \tag{D.1}$$

With the denotations explained in Figure D.1, eq. (D.1) is rewritten as

$$\begin{aligned} \Psi_{\mathrm{m}}(\mathbf{m}) &= \sum_{j=1}^{M} \left(\left| \frac{m_j - m_{\mathrm{R}\,j}}{\Delta x_{\mathrm{R}\,j}} \right|^2 \Delta x_{\mathrm{R}\,j} \, \Delta z_j + \left| \frac{m_j - m_{\mathrm{D}\,j}}{\Delta z_{\mathrm{D}\,j}} \right|^2 \Delta x_j \, \Delta z_{\mathrm{D}\,j} \right) \\ &= \mathbf{m}^{\mathrm{H}} \, \mathbf{W}_x^{\mathrm{T}} \, \mathbf{W}_x \, \mathbf{m} + \mathbf{m}^{\mathrm{H}} \, \mathbf{W}_z^{\mathrm{T}} \, \mathbf{W}_z \, \mathbf{m} \, , \end{aligned} \tag{D.2}$$

where the real matrices $\mathbf{W}_x$ and $\mathbf{W}_z$ are implicitly defined via

$$(\mathbf{W}_x\,\mathbf{m})_j = \begin{cases} \sqrt{\Delta z_j / \Delta x_{\mathrm{R}\,j}}\;(m_j - m_{\mathrm{R}\,j}) & \text{if } m_{\mathrm{R}\,j} \text{ exists} \\ 0 & \text{otherwise} \end{cases},$$
$$(\mathbf{W}_z\,\mathbf{m})_j = \begin{cases} \sqrt{\Delta x_j / \Delta z_{\mathrm{D}\,j}}\;(m_j - m_{\mathrm{D}\,j}) & \text{if } m_{\mathrm{D}\,j} \text{ exists} \\ 0 & \text{otherwise} \end{cases}, \qquad \text{(D.3)}$$

for $j = 1, \ldots, M$.

Introducing extra smoothing parameters α_x and α_z finally yields

$$\begin{aligned} \Psi_{\mathrm{m}}(\mathbf{m}) &= \mathbf{m}^{\mathrm{H}} \left(\alpha_x\,\mathbf{W}_x^{\mathrm{T}}\,\mathbf{W}_x + \alpha_z\,\mathbf{W}_z^{\mathrm{T}}\,\mathbf{W}_z \right) \mathbf{m} \\ &= \left\| \mathbf{W}_{\mathrm{m}}\,\mathbf{m} \right\|^2 , \end{aligned} \qquad \text{(D.4)}$$

with the real model weighting matrix $\mathbf{W}_{\mathrm{m}}$ according to eq. (3.50). Note that $\mathbf{W}_{\mathrm{m}}^{\mathrm{T}}\,\mathbf{W}_{\mathrm{m}}$ is symmetric and positive definite.

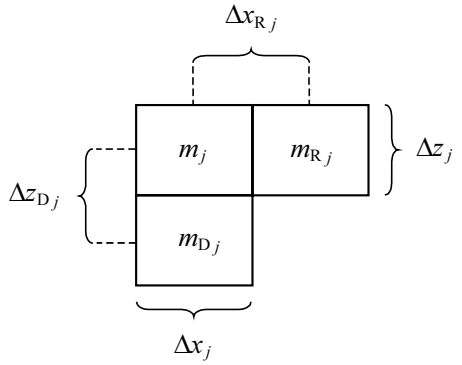

Figure D.1: Parameters as being used to express the first-order roughness of the model $\mathbf{m}$, according to Oldenburg et al. (1993). Shown is the j-th model cell together with the neighboring cells $m_{\mathrm{R}\,j}$ and $m_{\mathrm{D}\,j}$ in the right and downwards direction, respectively.

E: DERIVATION OF COMPLEX NORMAL EQUATIONS

A quadratic approximation of the objective function Ψ about the model $\mathbf{m}_q$ is given by means of a Taylor series expansion up to second order. Using complex algebra, one obtains

$$\Psi(\mathbf{m}_q + \Delta\mathbf{m}_q) \approx \Psi_q + \frac{\partial \Psi_q}{\partial \mathbf{m}} \Delta\mathbf{m}_q + \frac{1}{2} \Delta\mathbf{m}_q^{\mathrm{H}} \frac{\partial}{\partial \mathbf{m}^{\mathrm{H}}} \frac{\partial \Psi_q}{\partial \mathbf{m}} \Delta\mathbf{m}_q , \qquad \text{(E.1)}$$

with the abbreviations $\Psi_q = \Psi(\mathbf{m}_q)$ and

$$\frac{\partial}{\partial \mathbf{m}} = \left(\frac{1}{2}\frac{\partial}{\partial \mathrm{Re}(m_1)} + \frac{\mathrm{i}}{2}\frac{\partial}{\partial \mathrm{Im}(m_1)}, \quad \cdots \quad , \frac{1}{2}\frac{\partial}{\partial \mathrm{Re}(m_M)} + \frac{\mathrm{i}}{2}\frac{\partial}{\partial \mathrm{Im}(m_M)} \right)^{\mathrm{H}} \tag{E.2}$$

[note that $\partial \ldots / \partial \mathbf{m}^{\mathrm{H}} = (\partial \ldots / \partial \mathbf{m})^{\mathrm{H}}$]. For the model perturbation $\Delta \mathbf{m}_q$ minimizing the approximation (E.1), one finds the requirement

$$\frac{\partial \Psi}{\partial \Delta \mathbf{m}_q} = \frac{\partial \Psi_q}{\partial \mathbf{m}} + \Delta \mathbf{m}_q^{\mathrm{H}} \frac{\partial}{\partial \mathbf{m}^{\mathrm{H}}} \frac{\partial \Psi_q}{\partial \mathbf{m}} = 0 \,, \tag{E.3}$$

or equivalently

$$\frac{\partial}{\partial \mathbf{m}} \frac{\partial \Psi_q}{\partial \mathbf{m}^{\mathrm{H}}} \Delta \mathbf{m}_q = - \frac{\partial \Psi_q}{\partial \mathbf{m}^{\mathrm{H}}} \,. \tag{E.4}$$

Now, carrying out the differentiation for Ψ_q according to eq. (3.51) yields

$$\frac{\partial \Psi_q}{\partial \mathbf{m}^{\mathrm{H}}} = -2\, \mathbf{A}_q^{\mathrm{H}}\, \mathbf{W}_{\mathrm{d}}^{\mathrm{H}}\, \mathbf{W}_{\mathrm{d}} \left(\mathbf{d} - \mathbf{f}(\mathbf{m}_q) \right) + 2\lambda\, \mathbf{W}_{\mathrm{m}}^{\mathrm{T}}\, \mathbf{W}_{\mathrm{m}}\, \mathbf{m}_q \tag{E.5}$$

and, furthermore,

$$\frac{\partial}{\partial \mathbf{m}} \frac{\partial \Psi_q}{\partial \mathbf{m}^{\mathrm{H}}} \approx 2\, \mathbf{A}_q^{\mathrm{H}}\, \mathbf{W}_{\mathrm{d}}^{\mathrm{H}}\, \mathbf{W}_{\mathrm{d}}\, \mathbf{A}_q + 2\lambda\, \mathbf{W}_{\mathrm{m}}^{\mathrm{T}}\, \mathbf{W}_{\mathrm{m}} \,, \tag{E.6}$$

where $\mathbf{A}_q = \frac{\partial \mathbf{f}}{\partial \mathbf{m}}(\mathbf{m}_q)$ and, in eq. (E.6), the second derivatives $\frac{\partial}{\partial \mathbf{m}^{\mathrm{H}}} \frac{\partial \mathbf{f}}{\partial \mathbf{m}}(\mathbf{m}_q)$ are neglected (i.e., a linearized version of $\mathbf{f}$ is used). Finally, substituting the equations (E.5) and (E.6) into the local minimization requirement (E.4) yields the complex linear system of equations given in eqs. (3.52) through (3.54).

It shall be noted that the resulting system of equations may be equivalently obtained by directly substituting the linearization $\mathbf{f}(\mathbf{m}_q + \Delta \mathbf{m}_q) = \mathbf{f}(\mathbf{m}_q) + \mathbf{A}_q \Delta \mathbf{m}_q$ into the objective function and, subsequently, equating its first derivative to zero.

F: VARIATION OF REGULARIZATION PARAMETER

The univariate search for the optimum value of the regularization parameter λ at each inverse iteration step is realized by successively changing a trial value λ_l according to eq. (3.57) and observing the resulting data misfit. Depending on whether the data RMS error $\varepsilon^{\mathrm{RMS}}(\lambda_l)$ is greater or less than one, the trial value is, respectively, decreased or increased in order to loosen or tighten the regularization by the model objective function. It appears reasonable to adjust the step width between two consecutive trial values λ_l and λ_{l+1} in dependence upon the stage of the overall inversion process. At

the beginning larger changes make sense, whereas a fine adjustment should take place towards the end.

Let h_i and h_f $(0 < h_\mathrm{i} < h_\mathrm{f} < 1)$ denote, respectively, the *initial* and the *final* factor by which λ_l shall be decreased at the beginning and at the end of the inversion process (an increase of λ_l may be realized by multiplication by the respective inverse value). In terms of data misfit, describing the progress of the inversion, h_i thus corresponds with the RMS error of the starting model, $\varepsilon_0^{\mathrm{RMS}}$, while h_f corresponds with the target value $\varepsilon^{\mathrm{RMS}} = 1$.

The function $h(\varepsilon^{\mathrm{RMS}})$ in eq. (3.57) is now defined by linearly interpolating between the points

$$h_\mathrm{i} = h(\varepsilon_0^{\mathrm{RMS}}), \quad h_\mathrm{f} = \lim_{\varepsilon^{\mathrm{RMS}} \to 1+} h(\varepsilon^{\mathrm{RMS}}) \tag{F.1}$$

on double logarithmic scales. Taking the possible sign of $\ln \varepsilon^{\mathrm{RMS}}$ into account (to either decrease or increase λ_l), it results

$$h(\varepsilon^{\mathrm{RMS}}) = h_\mathrm{f}^{\,\mathrm{sgn}\left(\ln \varepsilon^{\mathrm{RMS}}\right)} \left(h_\mathrm{i}/h_\mathrm{f}\right)^{\ln \varepsilon^{\mathrm{RMS}}/\ln \varepsilon_0^{\mathrm{RMS}}}, \tag{F.2}$$

where it is assumed that $\varepsilon_0^{\mathrm{RMS}} > 1$, $\varepsilon^{\mathrm{RMS}} > 0$, and $\ln \varepsilon_0^{\mathrm{RMS}} > |\ln \varepsilon^{\mathrm{RMS}}|$.

For the inversions performed within the scope of this thesis, the values $h_\mathrm{i} = 0.5$ and $h_\mathrm{f} = 0.9$ have been used, normally resulting in less than five trial values λ_l to determine the optimum value of λ.

G: COLE-COLE MODEL FITTING

In the following the employed procedure for fitting a Cole-Cole model to a given set of spectral complex resistivity data is outlined. Strictly speaking, the model may be composed of one or even more Cole-Cole dispersion terms, depending on whether the procedure is applied to extract *intrinsic* Cole-Cole parameters from multifrequency complex resistivity tomography results (see Sections 4.3 and 5.1.6) or to remove EM coupling from multifrequency field data given in terms of *apparent* complex resistivity spectra (see Section 5.1.3). However, mathematically both objectives are similar and, thus, can be achieved using the same algorithm.

To start with, the Cole-Cole functions of eqs. (4.2) and (5.9) are written in the general form

$$\rho(\omega) = \rho_0 \left(1 - \sum_{l=1}^{L} r_l(\omega)\right), \tag{G.1}$$

with the DC resistivity ρ_0 and one to three Cole-Cole dispersion terms

$$r_l(\omega) = m_l \left[1 - \frac{1}{1 + (\mathrm{i}\,\omega\tau_l)^{c_l}} \right], \tag{G.2}$$

each comprising chargeability m_l, time constant τ_l, and Cole-Cole exponent c_l. For $L = 1$, eq. (G.1) solely describes the spectral IP effect, whereas for $2 \le L \le 3$, one or two additional Cole-Cole dispersion terms are included to account for EM coupling effects present in the complex resistivity data (note that for negative EM coupling the opposite sign has been absorbed into m_l).

Due to the nonlinearity in eq. (G.2) with respect to τ_l and c_l, the model fitting is performed by means of a nonlinear inversion routine. Here, a conventional real-valued least-squares approach with Marquardt regularization is used. The implementation is based on the corresponding subroutine from Press et al. (1992). It may be noted that the inversion approach is similar to that already employed by Pelton and colleagues for Cole-Cole model fitting, which is described in some more detail in Pelton et al. (1984).

Depending on whether one, two, or three Cole-Cole dispersion terms are needed to adequately describe the spectral behavior of the given complex resistivity data, the model vector $\mathbf{x}$ in the inversion consists of four, seven, or ten parameters, respectively.[1] Schematically, $\mathbf{x}$ is defined as

$$\mathbf{x} = \left(\ln\rho_0 ; m_1, \ln\tau_1, c_1 ; m_2, \ln\tau_2, c_2 ; \ldots \right)^{\mathrm{T}} . \tag{G.3}$$

Whereas m_l and c_l are kept linear in the parameterization, ρ_0 and τ_l are employed in log scale due to their wide dynamical range. The data vector $\mathbf{y}$ is assembled by the log magnitude and phase values of the complex resistivity data, given at several measurement frequencies ω_k, according to

$$\mathbf{y} = \left(\ln|\rho(\omega_1)|, \ln|\rho(\omega_2)|, \ldots ; \varphi(\omega_1), \varphi(\omega_2), \ldots \right)^{\mathrm{T}} \tag{G.4}$$

(note again that $\rho = |\rho|\, \mathrm{e}^{\mathrm{i}\varphi}$). The corresponding forward modeling operator $\mathbf{f}$ is implicitly defined through eqs. (G.1) and (G.2).

At each iteration step q of the inversion, the resultant normal equations

$$\left(\mathbf{J}_q^{\mathrm{T}} \mathbf{W}_{\mathrm{y}}^{\mathrm{T}} \mathbf{W}_{\mathrm{y}} \mathbf{J}_q + \lambda \mathbf{I} \right) \Delta\mathbf{x}_q = \mathbf{J}_q^{\mathrm{T}} \mathbf{W}_{\mathrm{y}}^{\mathrm{T}} \mathbf{W}_{\mathrm{y}} \left(\mathbf{y} - \mathbf{f}(\mathbf{x}_q) \right) \tag{G.5}$$

---

[1] To reduce the total number of unknowns, sometimes the fixation of certain parameters in the inversion is useful or even necessary if data are only available at a relatively small number of measurement frequencies. For instance, in many cases the choice $c_l = 1$ for $l > 1$ represents a sufficient approximation of the EM coupling frequency dispersion (e.g., Hallof and Pelton, 1980; see Section 5.1.3).

are solved for an update $\Delta\mathbf{x}_q$ of the current model $\mathbf{x}_q$. In eq. (G.5), $\mathbf{J}_q$ denotes the Jacobian, $\mathbf{W}_y$ a data weighting matrix, λ the regularization parameter, and $\mathbf{I}$ the identity matrix. The partial derivatives $\partial y_i/\partial x_j$, required to build up $\mathbf{J}_q$, are readily obtained by computing the partial derivatives $\partial\rho/\partial x_j$ via complex calculus and, subsequently, making use of the relations

$$\frac{\partial \ln|\rho|}{\partial x_j} = \frac{1}{2\,\overline{\rho}\rho}\left(\frac{\partial\overline{\rho}}{\partial x_j}\rho + \overline{\rho}\frac{\partial\rho}{\partial x_j}\right) \tag{G.6}$$

and

$$\frac{\partial\varphi}{\partial x_j} = \mathrm{i}\left(\frac{\partial \ln|\rho|}{\partial x_j} - \frac{1}{\rho}\frac{\partial\rho}{\partial x_j}\right). \tag{G.7}$$

In eq. (G.6), $\overline{\ }$ again denotes complex conjugation. From eqs. (G.1) and (G.2), for $\partial\rho/\partial x_j$ the following expressions are found:

$$\begin{aligned}
\frac{\partial\rho}{\partial \ln\rho_0} &= \rho\,, \\
\frac{\partial\rho}{\partial m_l} &= \rho_0\left[\frac{1}{1+(\mathrm{i}\omega\tau_l)^{c_l}} - 1\right], \\
\frac{\partial\rho}{\partial \ln\tau_l} &= a_l\, c_l\,, \\
\frac{\partial\rho}{\partial c_l} &= a_l \ln(\mathrm{i}\omega\tau_l), \quad \text{with } a_l = -\frac{\rho_0 m_l (\mathrm{i}\omega\tau_l)^{c_l}}{\left[1+(\mathrm{i}\omega\tau_l)^{c_l}\right]^2}\,.
\end{aligned} \tag{G.8}$$

For the solution of eq. (G.5) simple Gauss-Jordan elimination is used. Note that after each inverse iteration step, λ is either decreased or increased by a factor of ten depending on whether the data misfit could be reduced or not (see Press et al., 1992). Satisfactory convergence is considered to be achieved after five consecutive successful iterations with a relative RMS error improvement of less than 2 %.

The data errors are assumed to be uncorrelated and, thus, $\mathbf{W}_y$ is a diagonal matrix with each element being given by the inverse of the respective individual error estimate. However, to strengthen the importance of the phase data within the inversion, their weights may be in addition increased against the magnitude weights by multiplication by a constant factor. By numerical tests, it was found that a factor of five yields a reasonable balance between the influence of magnitude and phase data and, hence, was applied herein. The decisive role of the phase in Cole-Cole model fitting was also pointed out by Luo and Zhang (1998). They report that the Cole-Cole

parameters (ρ_0 excluded) obtained from a single phase spectrum inversion are generally very close to those of joint inversion of magnitude and phase spectra.

If the inversion procedure is used to remove EM coupling effects from apparent complex resistivity spectra, the individual error estimates are derived from the discrepancies between the respective data values measured in normal and reciprocal electrode configuration. On the other hand, if the algorithm is applied to intrinsic complex resistivity spectra provided by complex resistivity tomography results, the errors are estimated from the mean noise levels in the underlying data sets.

A reasonable starting model $\mathbf{x}_0$ for the inversion can be estimated from the general shape of the given complex resistivity spectra. When working with more than one Cole-Cole dispersion term, one should moreover take the typically expected, distinctive parameter ranges of the respective Cole-Cole parameters in the IP and the EM term(s) into account (see Section 5.1.3). An exemplary starting model for $L = 2$ may be given by $\rho_0 = |\rho(\omega_{\min})|$, $m_1 = 0.5$, $\tau_1 = 1/\omega_{\min}$, $c_1 = 0.25$; and $m_2 = \pm 1$ (positive or negative EM coupling), $\tau_2 = 1/\omega_{\max}$, $c_2 = 1$; with typical minimum and maximum measurement frequencies being of the order of $\omega_{\min}/2\pi \approx 0.1\,\mathrm{Hz}$ and $\omega_{\max}/2\pi \approx 10\,\mathrm{kHz}$, respectively.

In order to assess uncertainty and correlation of the resultant Cole-Cole parameters, the parameter covariance matrix

$$\mathbf{Cov}(\mathbf{x}) = \left(\mathbf{J}^{\mathrm{T}}\,\mathbf{W}_{\mathrm{y}}^{\mathrm{T}}\,\mathbf{W}_{\mathrm{y}}\,\mathbf{J}\right)^{-1} \tag{G.9}$$

is evaluated at the end of the inversion process. Whereas the j-th diagonal element of $\mathbf{Cov}(\mathbf{x})$ is directly related to the variance of the j-th parameter x_j, the coefficient

$$r_{jm} = \frac{cov_{jm}}{\sqrt{cov_{jj}\,cov_{mm}}} \tag{G.10}$$

describes the correlation between the uncertainty in x_j and x_m, with cov_{jm} denoting the j,m-th element of $\mathbf{Cov}(\mathbf{x})$. Note that for the particular purpose of EM coupling removal, where the primary objective is not the assignment of certain Cole-Cole parameters but simply the separation of IP and EM effects, basically only the *cross*-correlation between the two parameter sets belonging to $l = 1$ (IP) and $l > 1$ (EM) is of importance. Any *intra*-correlation between parameters belonging to the same Cole-Cole dispersion term does merely provide information on the ambiguity in the mathematical description of either of these effects.

LIST OF SYMBOLS AND ABBREVIATIONS

a	proportionality constant
a_{ij}	matrix element
a_j, a_l	scalar variables
A	area of considered region
A_j	finite element
$\mathbf{A}$, $\mathbf{A}_q$	Jacobian matrix
b	exponent of constant-phase-angle model
$\mathbf{b}$, $\mathbf{b}_q$	right-hand side vector
$\mathbf{B}$	magnetic induction
$\mathbf{B}_q$	matrix in the inverse problem
c, c_l	exponent of Cole-Cole model
c_a	apparent Cole-Cole exponent
c_k	Fourier coefficient
c_+, c_-	Cole-Cole exponent of positive, negative EM coupling
cov_{jm}	element of parameter covariance matrix
$\mathbf{c}$	vector
C	boundary of considered region
C_j	boundary element
$\mathbf{Cov}$	parameter covariance matrix
CG	*conjugate gradient*
CPA	*constant phase angle*
d_i	data
$\mathbf{d}$	data vector
D	fractal dimension of pore surface
$\mathbf{D}$	dielectric displacement
DC	*direct current*
DNAPL	*dense non-aqueous phase liquid*
$\mathbf{E}$	electric field
EM	*electromagnetic*
ERT	*electrical resistivity tomography*
f	frequency
f_dc	DC forward modeling operator
f_i	forward modeling operator
f_0	fundamental frequency of time-domain waveform
$\mathbf{f}$	forward modeling operator

F	formation factor
FE	frequency effect
F	finite-element functional
FE	*finite element*
g	scalar function
g, g_j	scalar variables
G, G_i	geometric factor
h	scalar function
$h_\mathrm{i}, h_\mathrm{f}$	parameters to adjust the regularization parameter
$\mathbf{H}$	magnetic field
i, j, k, l, m, n	index variables
i	imaginary unit
I, I_i	electric current
$\mathbf{I}$	identity matrix
Im	imaginary part
IP	*induced polarization*
$\mathbf{j}$	electric current density
$\mathbf{j}_\mathrm{s}$	source current density
$\mathbf{J}, \mathbf{J}_q$	Jacobian matrix
k	conjugate-gradient iteration index
k, k', k_0	wavenumber
k_n, k'_n	abscissa for inverse Fourier integration
K	hydraulic permeability
K_f	hydraulic conductivity
K_0	modified Bessel function of order zero
K_1	modified Bessel function of first order
l	imaginary part to real part ratio of interfacial conductivity
L	number of Cole-Cole dispersion terms in spectral model
$\mathbf{L}$	lower triangular matrix
$\mathcal{L}$	Laplace transform
LNAPL	*light non-aqueous phase liquid*
m	cementation exponent
m, m_j, m_l	chargeability
m_a	apparent chargeability
m_j	model parameter
m_+, m_-	amplitude factor of positive, negative EM coupling
$\mathbf{m}, \mathbf{m}_q$	model vector
$\mathbf{m}_0$	starting model
M	integral chargeability
M	number of parameters
MF	metal factor

n	saturation exponent
n	boundary outward normal
N	number of data
N_e	number of finite elements
N_b	number of boundary elements
N_G, N_L	number of abscissa for Gauss, Laguerre integration
N_n	number of nodes
N_p	number of pulses
N_s	number of samples per period of time-domain waveform
$\mathbf{p}_k$	relaxation direction in the conjugate gradient algorithm
P	Cauchy principal value
PFE	percent frequency effect
$\mathbf{P}$	polarization
q	Gauss-Newton iteration index
r, r_-	radial distance from the source
r_+	radial distance from the image source
r_eff	effective hydraulic radius
$r_{\mathrm{em}+}$, $r_{\mathrm{em}-}$, r_ip, r_l	Cole-Cole dispersion terms
r_grain	grain size
r_{jm}	parameter correlation coefficient
r_min, r_max	minimum, maximum source-receiver distance
r_{10}, r_{90}	grain size at which the cumulative frequency on log scale is 10 %, 90 %
$\mathbf{r}$	position vector
$\mathbf{r}_k$	residual vector in the conjugate gradient algorithm
$\mathbf{r}_\mathrm{s}$	source position vector
R	transfer function of receiver system
R_0	DC resistance
$\mathbf{R}$	parameter resolution matrix
Re	real part
RMS	*root-mean-square*
s, s_min	step length
S_por	specific surface area to pore volume ratio
S_w	water saturation
$S_{\mathrm{w\,r}}$	residual saturation
$\mathbf{S}$	finite-element matrix
$\mathbf{S}_{1j}$, $\mathbf{S}_{2j}$, $\mathbf{S}_{3j}$	element matrices
SIP	*spectral induced polarization*
SIRT	*simultaneous iterative reconstruction technique*
t, t'	time
t_1, t_2	bounds of time interval

T	pulse length of time-domain current waveform
u, u'	scalar variables
V, V_i	voltage
V_p	primary voltage
V_s	secondary voltage
w_n, w_n'	weights for inverse Fourier integration
$\mathbf{W}_\mathrm{d}, \mathbf{W}_\mathrm{y}$	data weighting matrix
$\mathbf{W}_\mathrm{m}$	model weighting matrix
$\mathbf{W}_x, \mathbf{W}_z$	model weighting matrix in x-, z - direction
x, y, z	Cartesian coordinates
$x_\mathrm{s}, y_\mathrm{s}, z_\mathrm{s}$	source coordinates
x_j, x_m	model parameter
$\mathbf{x}, \mathbf{x}_q$	model vector
$\mathbf{x}_0$	starting model
X	scalar variable
y_i	data
$\mathbf{y}$	data vector
$\mathbf{z}$	complex vector
Z, Z_i	transfer impedance
Z_em	impedance on account of electromagnetic induction
Z_ip	impedance on account of induced polarization
α	filtering parameter
α_k, β_k	step lengths in the conjugate gradient algorithm
α_x, α_z	smoothing parameters
β, β_j, β_0	boundary parameter
δ	Dirac delta function
Δd_i	difference between normal and reciprocal data
$\Delta_{\ln r}, \Delta_{\ln \tau}$	spread of log grain size, relaxation time distribution
$\Delta \ln \lvert Z_i \rvert$	error in log magnitude of transfer impedance
Δm_j	difference between model parameters of adjacent cells
$\Delta \mathbf{m}_q, \Delta \mathbf{x}_q$	model update
Δt	sampling interval
$\Delta x_j, \Delta z_j$	increment in x-, z - direction
$\Delta\beta, \Delta\beta_j$	perturbation of boundary parameter
$\Delta\sigma, \Delta\sigma_j$	perturbation of conductivity
$\Delta\varphi_i$	phase error
ε	dielectric permittivity
$\varepsilon_i, \varepsilon_{i,q}$	data error
$\varepsilon_k^{\mathrm{CG}}$	error in the conjugate gradient solution
ε_lev	error level

$\varepsilon^{\mathrm{RMS}}$	root-mean-square error
$\varepsilon_0^{\mathrm{RMS}}$	root-mean-square error of starting model
ε_0	zero-frequency asymptote of permittivity
ε_∞	infinite-frequency asymptote of permittivity
κ	index variable
$\lambda, \lambda_l, \lambda_0$	regularization parameter
μ	Lagrange multiplier
ν	saturation exponent
ρ	electrical resistivity
ρ_a	apparent resistivity
ρ_n	resistivity magnitude at reference frequency
ρ_0	zero-frequency asymptote of resistivity
ρ_∞	infinite-frequency asymptote of resistivity
σ, σ_j	electrical conductivity
$\sigma_\mathrm{a}, \sigma_{\mathrm{a}\,i}$	apparent conductivity
σ_el	electrolytic conductivity
$\sigma_\mathrm{dc}, \sigma_{\mathrm{dc}\,j}$	DC conductivity
σ_int	interfacial conductivity
σ_ip	effective conductivity in the presence of polarization
σ_w	conductivity of pore solution
σ_0	reference conductivity
σ_∞	infinite-frequency asymptote of conductivity
τ, τ', τ_l	time constant
τ_a	apparent time constant
τ_+, τ_-	time constant of positive, negative EM coupling
φ	phase of resistivity
φ_a	apparent phase
φ_peak	(negative) value of phase maximum
ϕ, ϕ_i	electric potential
$\widetilde{\phi}, \widetilde{\phi}_i$	transformed potential
$\widetilde{\phi}_\mathrm{p}, \widetilde{\phi}_{\mathrm{p}\,i}$	primary potential
$\widetilde{\phi}_\mathrm{s}, \widetilde{\phi}_{\mathrm{s}\,i}$	secondary potential
Φ	porosity
$\widetilde{\Phi}, \widetilde{\Phi}_\mathrm{p}, \widetilde{\Phi}_\mathrm{s}$	discrete vector of transformed potentials
$\chi_{i,q}$	individual data misfit
χ_q	vector of individual data misfits
Ψ, Ψ', Ψ_q	global objective function
Ψ_d	chi-squared measure of data misfit
Ψ_d^*	target value of data misfit
Ψ_m	model objective function
$\omega, \omega', \omega_k$	angular frequency

ω_{min} , ω_{max}	minimum, maximum frequency
ω_{peak}	frequency where phase maximum occurs
ω_0	reference frequency
ω_1, ω_2	bounds of frequency interval

Bisher sind in der Reihe

Berichte des Instituts für Geophysik der Ruhr-Universität Bochum

Reihe A

folgende Bände erschienen:

Nr. 1: **L. Dresen**
Modellseismische Untersuchungen zum Problem der Ortung oberflächennaher Hohlräume in Festgestein.
Mai 1972

Nr. 2: **R. Schepers**
Bearbeitungsverfahren zur Bestimmung oberflächennaher Strukturen aus Einkanal-Reflexionsseismogrammen bei senkrechtem Einfall.
Juli 1972

Nr. 3: **S. Freystätter**
Modellseismische Untersuchungen zur Anwendung von Flözwellen für die untertägige Vorfelderkundung im Steinkohlenbergbau.
Juni 1974

Nr. 4: **F. Rummel**
Experimentelle Untersuchungen zum Bruchvorgang in Gesteinen.
Januar 1975

Nr. 5: **H. Rüter**
Anwendung reflexionsseismischer Verfahren bei der Erkundung oberflächennaher horizontal geschichteter Lockergesteine.
Februar 1975

Nr. 6: **R. Pelzing**
Untersuchungen zur Ortung von Herden seismischer Ereignisse, dargestellt an Beispielen aus einem Stationsnetz im Ruhrbergbaugebiet.
Juni 1978

Nr. 7: **C.-H. Hsieh**
Ortung verdeckter Bergwerksschächte mit Hilfe von Rayleigh-Wellen.
Januar 1979

Nr. 8: **G. Ullrich**
Stapelung, Migration und Dekonvolution von Reflexionsseismogrammen aus zyklisch geschichteten Untergrundstrukturen mit tektonischen Störungen.
Juni 1979

Nr. 9: **U. Bleil**
Die Magnetisierung der ozeanischen Kruste. Ein Beitrag zum Vine-Matthews-Modell nach Ergebnissen mariner Tiefbohrungen.
Dezember 1981

Nr. 10: **H.-J. Alheid**
Untersuchungen von Bruch und Scherprozessen im Granit und Serpentinit bei hohen Drücken und Temperaturen.
Dezember 1981

Nr. 11: **W. Hanka**
Analyse breitbandiger Oberflächenwellen – eine Möglichkeit zur seismischen Diskriminierung.
Februar 1982

Nr. 12: **H. Sommer**
Untersuchungen zur Ortung oberflächennaher Hohlräume mit gravimetrischen Verfahren.
Januar 1983

Nr. 13: **R.-B. Winter**
Bruchmechanische Gesteinsuntersuchungen mit dem Bezug zu hydraulischen Frac-Versuchen in Tiefbohrungen.
Dezember 1983

Nr. 14: **C. Kerner**
Untersuchungen an zweidimensionalen analogen und numerischen Modellen zur Transmission und Reflexion von Love- und Rayleigh-Flözwellen.
Januar 1984

Nr. 15: **K.-G. Hinzen**
Vergleich von Herdflächenlösungen und Momententensoren.
Januar 1984

Nr. 16: **N. Weinreich**
Magnetische Untersuchungen neogener pelagischer Sedimente des zentralen Äquatorialpazifik.
Februar 1985

Nr. 17: **V. Spieß**
Analyse und Interpretation zwei- und dreidimensionaler mariner magnetischer Anomalien.
November 1985

Nr. 18: **J. Meister**
Möglichkeiten und Grenzen hybriden und seismischen Modellierens.
November 1985

Nr. 19: **R.-G. Ferber**
Berechnung der zeitlichen Entwicklung der Felder transienter Wellen in geschichteten elastischen Medien.
März 1986

Nr. 20: **R. Jung**
Erzeugung eines großflächigen künstlichen Risses im Falkenberger Granit durch hydraulisches Spalten und Untersuchung seiner mechanischen und hydraulischen Eigenschaften.
April 1986

Nr. 21: **J. Baumgärtner**
Anwendung des Hydraulic-Fracturing-Verfahrens für Spannungsmessungen im geklüfteten Gebirge dargestellt anhand von Meßergebnissen aus Tiefbohrungen in der Bundesrepublik Deutschland, Frankreich und Zypern.
April 1987

Nr. 22: **W. Müller**
Experimentelle und numerische Untersuchungen zur Rißausbreitung im anisotropen Gestein in der Nähe von Grenzflächen.
Juni 1987

Nr. 23: **M. Joswig**
Methoden zur automatischen Erfassung und Auswertung von Erdbeben in seismischen Netzen und ihre Realisierung beim Aufbau des lokalen BOCHUM UNIVERSITY GERMANY – Netzes.
Juli 1987

Nr. 24: **R. Elsen**
Die Ortung oberflächennaher Hohlräume mit Verfahren der Geoelektrik.
November 1987

Nr. 25: **M. Redanz**
Waveletextraktion und Inversion von Reflexionsseismogrammen zur Ableitung von akustischen Impedanzen.
Juli 1988

Nr. 26: **G. Möhring-Erdmann**
Experimentelle und numerische Untersuchungen zur Entstehung von Bohrlochrandausbrüchen.
März 1989

Nr. 27: **E. Räkers**
Seismoakustische Ereignisse in Steinkohleflözen als Hilfe zur Erkennung von Abbaubereichen mit erhöhten Gebirgsdrücken.
Juni 1989

Nr. 28: **M. Breitzke**
Ein Normalmodensummations- und Frequenz-Wellenzahl-Verfahren zur Modellierung, Rekompression und Migration dispersiver Flözwellen.
Februar 1990

Nr. 29: **D. Krollpfeifer**
Experimentelle modellseismische Untersuchungen zum gezielten Anschießen von Flözstrukturen mit P- und SV-Wellen.
November 1990

Nr. 30: **H. Krummel**
Rechnergestützte Verfahren der seismischen Stratigraphie.
Januar 1991

Nr. 31: **E. Rybacki**
Experimentelle Festigkeitsuntersuchungen an inhomogen-anisotropen Gneisen und Granuliten bei hohen Drücken und Temperaturen.
Januar 1991

Nr. 32: **S. Menger**
Experimentelle und numerische Untersuchungen zum Problem der Dezentrierung beim Akustischen Bohrloch Televiewer.
Dezember 1991

Nr. 33: **B. Lehmann**
Modellseismische Untersuchungen zur Transmissions- und Reflexions-Tomographie unter Verwendung der Gauß-Beam-Methode.
Januar 1992

Nr. 34: **E. Al-Tarazi**
Investigation and assessment of seismic hazard in Jordan and its vicinity.
November 1992

Nr. 35: **F. Roth**
Modellierung von Vorgängen an Verwerfungen mit Hilfe der Dislokationstheorie.
Dezember 1992

Nr. 36: **C. Schneider**
Erkundung des Untergrundes von Deponien und Altlasten mit Rayleigh-Oberflächenwellen.
Juli 1993

Nr. 37: **M. Kemper**
Migration bohrlochseismischer Ereignisse.
Dezember 1993

Nr. 38: **T. Yu**
Numerische Modellierungen zur Untersuchung des Einflusses von lokalen Irregularitäten auf die Ausbreitung von Love-Wellen in geschichteten Medien.
Dezember 1993

Nr. 39: **U. Casten**
Untertagegravimetrie zur in situ Bestimmung des Gesteinsparameters Dichte und zur Erfassung bergbauinduzierter Dichteänderungen.
September 1994

Nr. 40: **C. Bönnemann**
Bestimmung seismischer Geschwindigkeiten aus Steilwinkelreflexionen im p-t-Bereich.
Mai 1995

Nr. 41: **H. Schulte-Theis**
Automatische Lokalisierung und Clusteranalyse regionaler Erdbeben.
Juni 1995

Nr. 42: **J. Wüster**
Diskrimination von Erdbeben und Sprengungen im Vogtlandgebiet und Nordwest-Böhmen.
Mai 1995

Nr. 43: **M. Janik**
Experimente zur seismischen Nutzung des Bohrgeräusches an der Kontinentalen Tiefbohrung der Bundesrepublik Deutschland (KTB).
Juli 1995

Nr. 44: **D. Orlowsky**
Erhöhung des Auflösungsvermögens der Common Mid Point- (CMP-) Refraktionsseismik durch eine Kombination mit der Generalized Reciprocal Method (GRM).
Januar 1996

Nr. 45: **B. Dombrowski**
3D-modeling, analysis and tomography of surface wave data for engineering and environmental purposes.
Februar 1996

Nr. 46: **A. Liebig**
Zweidimensionale geoelektrische Inversion als Teil einer integrierten geophysikalischen Auswertung zur Erkundung oberflächennaher Schichten.
Juni 1996

Nr. 47: **Y. Jia**
Bestimmung der scheinbaren Dämpfung seismischer Wellen in der europäischen Lithosphäre.
Juli 1996

Nr. 48: **J. Renner**
Experimentelle Untersuchungen zur Rheologie von Coesit.
Juli 1996

Nr. 49: **L. te Kamp**
Numerische Modellierungen von Rißwechselwirkungen.
Juli 1996

Nr. 50: **R. Misiek**
Surface waves: Application to lithostructural interpretation of near-surface layers in the meter and decameter range.
November 1996

Nr. 51: **G. Bokelmann**
Seismological constraints on anisotropy of the Earth's crust with emphasis on array methods.
April 1997

Nr. 52: **I. Heyde**
Integrierte Interpretation gravimetrischer und magnetischer Daten am Beispiel KTB.
Mai 1999

Nr. 53: **M. Joswig**
Raum-zeitliche Seismizitätsanalysen mit Methoden zur Handhabung von unvollständigem Wissen.
Dezember 1999

Nr. 54: **T. Stöcker**
Local spectral analysis and synthesis for seismic signal processing.
Juli 2000

Nr. 55: **M. Knapmeyer**
Abbildung seismischer Diskontinuitäten in der südlichen Ägäis mit migrierten Receiver Functions.
Juli 2000